UNIVERSITY OF LIEGE
FACULTY OF APPLIED SCIENCES
ArGEnCo DEPARTMENT

Integration of near-surface geophysical, geological and hydrogeological data with multiple-point geostatistics in alluvial aquifers

by

Thomas J. HERMANS

Civil Engineer in Mining and Geology, University of Liege, 2010

Submitted to the ArGEnCo Department on February 2014 in partial fulfillment of the requirements for the degree of

Doctor of Philosophy

in Applied Sciences at the University of Liege, Belgium

Jury

Nguyen Frédéric (Supervisor)	Pr. Dr. Ir., University of Liege, ArGEnCo Department, GEO^3, Applied Geophysics
Dassargues Alain (President)	Pr. Dr. Ir., University of Liege, ArGEnCo Department, GEO^3, Hydrogeology and Environmental Geology
Brouyère Serge	Dr. Ir., University of Liege, ArGEnCo Department, GEO^3, Hydrogeology and Environmental Geology
Collin Frédéric	Pr. Dr. Ir., University of Liege, ArGEnCo Department, GEO^3, Geotechnics
Javaux Mathieu	Pr. Dr. Ir., Catholic University of Louvain-la-Neuve, Earth and Life Institute
Kemna Andreas	Pr. Dr. Ir., Bonn University, Steinmann-Institute, Applied Geophysics
Irving James	Pr. Dr. Ir., University of Lausanne, Applied and Environmental Geophysics Group

To Kim, my loving wife.

"It is in the game"

EA Sports

Abstract

Alluvial plains constitute essential geological bodies for environmental studies such as contaminated sites remediation, low-enthalpy geothermal energy or groundwater resources. The heterogeneity of these deposits governs flow processes and needs to be quantified. A proper description of such complex deposits requires an integrated approach combining geological, geophysical and hydrogeological data. Solving such spatial inverse problems in the Earth Sciences remains a considerable challenge given the large number of parameters to invert for, the non-linearity of forward models and, as a result, the ill-posedness of the problem. Geostatistics is therefore needed to specify prior models, more particularly, information to control the spatial features of the inverse solutions.

Two-point geostatistical approaches have been developed to describe the heterogeneity of one geological formation but fail to reproduce the heterogeneity of fluvial deposits with multiple facies. Multiple-point statistics (MPS) introduced the training image (TI) concept to replace the variogram within an extended sequential simulation framework. The use of geophysics to constrain such simulations has been studied in the petroleum industry with wave-based methods (seismic reflection), but little research has been done to assess the use of near-surface potential methods to condition MPS in environmental studies.

In this work, we propose to integrate geological (borehole logs), geophysical (electrical resistivity tomography (ERT) profiles) and hydrogeological (hydraulic heads) data within MPS models on the alluvial plain of the Meuse River, Belgium.

Potential-based geophysical methods being integrative, they suffer from a relatively poor resolution. We first study how we can improve the informative content of geophysical inversion by including prior information in the ERT inverse problem. Three methods are tested and compared in several field cases, namely the reference model inversion, the structural inversion and the regularized geostatistical inversion. If every method has advantages and drawbacks, the best suited method for the considered problem is the regularized geostatistical method. Electromagnetic borehole logs enable to derive the vertical correlation length of electrical resistivity in the deposits and to subsequently use it to constrain the inversion. In addition to the knowledge of the bedrock position, it enables to retrieve an electrical resistivity distribution of the deposits close to direct observations. This ensures that geophysical models will be informative to constrain MPS simulations.

Given the lack of geological and sedimentological data to build accurate TIs, a data base of TIs is built using several different parameters and scenarios. They are all based on a three facies description: clay/loam, sand and gravel corresponding to low, intermediate and

high hydraulic conductivity. Then, we develop a methodology to verify the consistency of independently-built TIs with geophysical data. Our methodology starts by creating subsurface models with each TI. From these models we create synthetic geophysical data and from this synthetic data, synthetic inverted models. These models are now compared with a single inverted model obtained from the field survey, allowing for our definition of what is "consistent". To that extent, we calculate the Euclidean distance between any two inverted models as well as field data and visualize the results in a 2D or 3D space using multidimensional scaling (MDS). With this technique, it is possible to verify if field cases fall in the distribution represented by synthetic cases, and thus are consistent with them. In a second step, we present a cluster analysis on the MDS-map to highlight which parameters are the most sensitive for the construction of TI. Based on this analysis, a probability of each geological scenario is computed through kernel smoothing of the densities in reduced projected metric space.

The integration of hydrogeological data is made through a stochastic inversion method: the probability perturbation method (PPM), using MPS constrained with geophysical data to generate models. The PPM algorithm automatically seeks solutions fitting both hydrogeological data and training-image based geostatistical constraints. Only geometrical features of the model are affected by the perturbation, i.e. we do not attempt to directly find the optimal value of hydrogeological parameters (chosen *a priori*), but the optimal spatial distribution of facies whose prior distribution is quantified in a training image.

Tracing experiments may be used to further constrain hydrogeological models. ERT has proven its ability to monitor salt tracer tests, but few studies have investigated its performances in thermal tracing experiments. In this study, we demonstrate the ability of surface and crosshole ERT to image quantitatively temperature changes during heat injection experiments. Such resistivity data provides important information to improve hydrogeological models. Our study proves that ERT, especially crosshole ERT, is a reliable tool to follow thermal tracing experiments. It also confirms that ERT should be included to in situ techniques to characterize heat transfer in the subsurface and to monitor geothermal resources exploitation.

Keywords: Multiple-point statistics, hydrogeological inversion, probability perturbation method, electrical resistivity tomography, regularized inversion, prior information, temperature monitoring, time-lapse ERT, alluvial aquifers.

Résumé

Les plaines alluviales sont des environnements géologiques essentiels pour des études environnementales telles que la dépollution de sites contaminés, l'énergie géothermique de faible enthalpie ou les ressources en eau souterraine. L'hétérogénéité de ces dépôts gouverne les processus d'écoulement et doit être quantifiée. Une bonne description de ces dépôts complexes nécéssite une approche intégrée combinant des données géologique, géophysique et hydrogéologique. Résoudre de tels problèmes en Sciences de la Terre reste un challenge considérable au vu du nombre important de paramètres à inverser et de la non-linéarité des modèles directs. En conséquence, le problème est généralement mal posé. Les géostatistiques sont donc nécessaires pour spécifier des modèles *a priori*, ou plus particulièrement, pour contrôler les caractéstiques spatiales des solutions.

Les géostatistiques à 2 points ont été développées pour décrire l'hétérogénéité d'une formation géologique, mais ne parviennent pas à reproduire l'hétérogénéité de dépôts fluviatiles à faciès multiples. Les géostatistiques multipoints (MPS) introduisent l'image d'entraînement (TI) pour remplacer le variogramme dans un système de simulations séquentielles. L'utilisation de la géophysique pour contraindre ces simulations a été étudiée dans l'industrie pétrolière avec des méthodes d'onde (sismique réflexion), mais peu de recherches ont évalué les méthodes géophysiques potentielles pour contraindre les simulations MPS.

Dans cette thèse, nous proposons d'intégrer des données géologiques (logs de forage), géophysiques (tomographie de résistivité électrique (ERT)) et hydrogéologiques (mesures piézométriques) dans des modèles MPS de la plaine alluviale de la Meuse en Belgique.

Les méthodes géophysique potentielles sont intégratives, elles souffrent d'une résolution relativement faible. Nous étudions en premier lieu comment l'on peut améliorer le contenu informatif des inversions géophysiques en incorporant de l'information *a priori* dans le problème ERT inverse. Trois méthodes sont testées et comparées dans plusieurs cas réels: l'inversion avec modèle de référence, l'inversion structurelle et l'inversion géostatistique régularisée. Si chaque méthode a des avantages et des inconvénients, la méthode la plus adéquate dans le problème considéré est l'inversion géostatistique régularisée. Des logs électromagnétiques permettent de déduire la longueur de corrélation verticale de la résistivité électrique des dépôts qui est utilisée pour contraindre l'inversion. En plus de la connaissance de la position du bedrock, cela permet de retrouver une distribution de résistivité électrique proche des observations directes. Cela assure que les modèles géophysiques seront informatifs pour contraindre les simulations MPS.

Vu le manque de données géologiques et sédimentologiques pour construire des TIs pré-

cises, une base de données est créée en utilisant différents scénarios. Ceux-ci sont basés sur une description par trois faciès : argile, sable et gravier, correspondant respectivement à une conductivité hydraulique faible, intermédiaire et élevée. Ensuite, nous développons une méthodologie afin de vérifier la compatibilité des TIs avec les données géophysiques. Des modèles du sous-sol sont extraits des TIs et des données géophysiques synthétiques sont simulées, puis inversées pour obtenir des modèles synthétiques inverses. Ceux-ci sont ensuite comparés avec un modèle inverse obtenu par inversion de données de terrain, qui sert de référence pour définir la compatibilité. Nous calculons alors la distance entre tous les différents modèles deux à deux et visualisons les résultats en 2D ou 3D via la méthode du "multidimensional scaling" (MDS). Cette technique permet de vérifier si le modèle inverse de terrain est compris dans la distribution des modèles synthétiques, et donc s'ils sont compatibles. La carte MDS ainsi obtenue est analysée par clustering pour mettre en évidence les paramètres les plus sensibles dans la construction des TIs. La probabilité de chaque scénario est aussi calculée.

L'intégration de données hydrogéologiques est réalisée par une méthode stochastique d'inversion : la méthode de perturbation des probabilités (PPM). Elle utilise les simulations MPS, contraintes par la géophysique, pour générer des modèles. L'algorithme PPM recherche automatiquement les solutions respectant à la fois les contraintes géostatistiques et les données hydrogéologiques. Les perturbations itératives affectent uniquement les caractéristiques géométriques des modèles, et non la valeur des paramètres hydrogéologiques qui sont choisis *a priori*. Le but est d'optimiser la distribution spatiale des faciès dont la distribution *a priori* est quantifiée dans la TI.

Les expériences de traçage thermique sont de plus en plus communes en hydrogéologie pour estimer les paramètres gouvernant les transferts de chaleur et pour étudier les réservoirs géothermiques. L'ERT a prouvé ses capacités pour suivre des tests de traçage salin, mais peu d'études ont investigué ses performances en traçage thermique. Dans ce travail, nous démontrons l'aptitude de l'ERT de surface et de forage pour imager quantitativement les changements de température durant des tests d'injection de chaleur. Les données de résistivité apportent une information importante pour améliorer les modèles hydrogéologiques. Notre étude prouve que l'ERT est un outil fiable pour suivre des expériences de traçage thermique. Elle confirme également que l'ERT devrait être intégrée aux méthodes in-situ pour caractériser les transferts de chaleur dans le sous-sol et pour le suivi de réservoirs géothermiques.

Mots-clés: géostatistiques multipoints, inversion hydrogéologique, méthode de perturba-

tion des probabilités, tomographie de résistivité électrique, inversion régularisée, information *a priori*, suivi de température, aquifère alluvial.

Acknowledgments

A PhD is a very long road: you know where you start, you know where you want to go, but you do not really know how to reach your final objective. Most often, the straight line is not possible, you need to take tortuous pathways. A few times during this four (or even more) year project, you get lost or you are aware that you are walking round and round. You feel discouraged and you do not know how you are going to find your way. Sometimes, you can find it alone, following your intuition, you understand what you have to do to get back on track. Sometimes, you need someone to show you the way, hidden behind the fog. I would like to thank all the people who helped me find my way during this PhD.

First of all, I would like to thank my wife, Kim, to who this thesis is dedicated. She never stopped encouraging me. Even before the beginning of the PhD, when I was writing the proposal, she was already my first supporter, believing in me more than I was believing in myself. She has always shown me how important I was at her eyes, how great I was doing my job, and how lucky I was, doing an exciting job as a researcher, doing a job I like, a job which is at the same time a passion.

Kim has been the lighthouse in my life for almost nine years now. Our relationship evolves in parallel with my academic life. We started to see each other just before I passed the entrance examination to study engineering. Along the years spent in lecture rooms at the University, I got the conviction that geological engineering was definitively what I wanted to do, but I also got the absolute certainty that Kim is the love of my life.

Freshly graduated, I was ready to start this PhD, entering the active life. At the same time, Kim and I were moving in together. I had never had to regret those decisions.

As I was moving forward with this project, going on the field to acquire data, spending time in the lab and in front of the computer processing data sets, traveling around the world to present

the results, Kim and I were moving forward with our lives. We got married on a beautiful day of May 2012, a day which will remain in our heart forever. Last August, we bought a magnificient house where I am sure we will be happy.

During all these years, Kim was the foundation of my life, the person I could always trust, the person always ready to hear my complaints, to give me advice and to encourage me. I will never be able to thank her enough and tell her how much I lover her.

I am also grateful to my parents and all my family for their immeasurable support during all these years.

I would also like to thank Frédéric for giving me the opportunity to carry out this project. Through his course of "Applied Geophysics", he gave me the taste for research, for doing something new and exciting. He spent so much time preparing the proposal with me in order to get the FNRS Research Fellow grant. From the beginning to the end, he has always been curious to discover my results, encouraging me to go further, acknowledging what had been accomplished.

Fred and I are working together for more than for years now. I can say that he has been more than a supervisor and a colleague to me. He started by being a mentor, he is now a friend.

This work would not have been possible without the help of all my colleagues - as well as students - of the Applied Geophysics and Hydrogeology units, particularly Tanguy, David, Jean, Gaël and Moubarak. We spent beautiful and sometimes horrible days (or nights) on the field, collecting data and monitoring processes. I guess that nobody in these units ignores where Hermalle-sous-Argenteau is!

I would also like to thank Alain Dassargues and Serge Brouyère for their advices when the time to build hydrogeological models had come and the other members of the jury for their interest in this work.

Thanks to Sam for teaching me how to use HydroGeoSphere, I may say that I have joined the community now. I am also thankful to Emilie, Gaël and Elsy for their careful proofreading.

In addition to discovering beautiful cities such as San Francisco, Leicester or Madrid to attend conferences, I had the chance to spend three great months in the Silicone Valley in California. These months spent at Stanford University are unforgettable. I greatly appreciate how Jef Caers welcomed me in his department and encouraged me to develop new things, even if I was firstly there to learn. He has always been available to answer quickly to my questions.

The stay at Stanford was the most productive time of my PhD. Everything is so different over there, I hope we will have the opportunity to go back.

I am also grateful to the FNRS for its support for 4 years as a FNRS research fellow and to the University of Liege and the Fondation Roi Baudouin for their financial support in the fulfillment of this project.

I finish by thanking David, Jean, Sam and Pierre for keeping my motivation high during all these years, through our team building activities during lunch time.

Contents

Chapter 1

Introduction

The general objective of this work is to contribute to a better description and quantification of subsurface heterogeneity for hydrogeological models in complex geological formations: alluvial aquifers. We propose to integrate shallow geophysical data and models with traditional geological data (generally borehole logs) and hydrogeological data (hydraulic heads) within a common geostatistical framework: multiple-point geostatistics.

Alluvial plains constitute essential geological bodies for environmental studies such as groundwater resources, urban or contaminated sites issues or low-enthalpy geothermal energy resources. Although hidden, the heterogeneity of these bodies governs flow and transport phenomena.

Alluvial aquifers constitute important water resources for industry and populations in Belgium and worlwide. As an example, about 2×10^6 m^3 are extracted annually in the alluvial gravel aquifer of the Meuse River, representing 5% of the total groundwater extraction in Wallonia (SPW-DGO3 2013). This is a relatively small proportion since groundwater is easily accessible also in other contexts (limestone aquifers) in Belgium. In other countries, alluvial groundwater resources are more important as they constitute the major water resource such as in Australia where water extracted in alluvial aquifers represents about 60% of the total extraction (Geosciences Australia 2013).

Numerous water catchment facilities are located in alluvial plains. Their sustainable exploitation and their protection requires to know as precisely as possible the hydrogeological context. As an example, in Wallonia it is necessary to delimit protection zones around these facilities. In complex deposits, a better description of the geology will allow a better definition

of vulnerable zones.

Given their favorable geographical location along rivers, alluvial plains are also areas with high population and industrial density. History shows that these areas were the first to be industrialized. This is especially true for Wallonia and the area of Liege which was additionally an important center of the coal and steel industry. Consequently, a lot of polluted area are located in alluvial plains. In 2007, about 3 millions of potentially polluted sites were listed in the European Union (European Environment Agency 2010). The analysis is the same for Wallonia, since the SPAQUE listed 6000 brownfields and garbage dumps (CEEW 2007). Among them more than 200 have a high risk at the moment. In order to plan adequate remediation actions, it is mandatory to have a good knowledge of these area (of preferential flowpaths as an example) to reduce the risk for groundwater resources and rivers and to restore the sites in a sustainable fashion.

The European Union committed to develop renewable energy to reduce greenhouse gas emissions (20% in 2020). Within this context, the production of energy through low and moderate temperature geothermal resources is expected to grow strongly worldwide in the future. For instance, in 2010, geothermal heat pumps accounted for 47.2% of thermal energy use and 68.3% of total installed capacity in the world (Lund 2010). Geothermal energy resources therefore constitute an essential field of research and development in the diversification of energy resources to hinder global warming. The advantage of low and very-low enthalpy systems are, first, that they are much more available than deep and high temperature geothermal systems, and second, that their exploitation involves relatively low costs of implementation. Very low energy systems exhibit underground fluid temperature ranging from 5 to $30°C$ (Allen and Milenic 2003). They may be used for cooling or heating of industrial, public or private buildings). Such systems are more easily accessible, particularly in alluvial aquifer and coastal area. In this context, the characterization of the heterogeneity of the hydrogeological and thermal properties is crucial for an efficient exploitation of these resources.

Within this context, new techniques of exploration and monitoring are needed. Indeed, few tests are available to derive the parameters responsible for heat flow and transport in the subsurface (such as the thermal response test) and new methodologies must be developed, including thermal tracing experiments. In parallel, the spatial monitoring of geothermal systems is still

challenging, main data being limited to boreholes. Geophysical methods are well suited to tackle this problem. Electrical resistivity is sensitive to temperature variations and this parameter may be used to monitor geothermal systems and follow heat tracing experiment. However, its reliability has to be proven. In this work, we will propose some developments to show that electrical resistivity tomography could be a very useful tool for such purposes.

The choice of working within a geostatistical framework is driven by the growing need to model uncertainty in Earth Sciences (Caers 2011). Geostatistics open the road to stochastic simulations, i.e. the creation of a set of equiprobable models, all fitting the same data. Indeed, in geosciences, the solution to a given problem is generally non-unique. Several models may explain the same data sets. Working with stochastic simulations will allow us to explore the posterior distribution of models. Geostatistics also offer the possibility to integrate data sets with varying resolution and spatial distribution.

Geostatistical approaches were first developed to infer parameters between boreholes where information is accurate. Indeed, direct wellbore observations are the only way to get an exact insight on subsurface materials; however, the number of boreholes is always limited both financially and physically. The most used geostatistical methods are based on two-point correlation, described by the variogram or covariance of the studied parameter: kriging and co-kriging for estimation techniques and sequential Gaussian simulations or sequential indicator simulations for simulations techniques. These methods are very useful to describe smoothly heterogeneous medium but inadequate when facing multimodal distributions, with interconnected and possibly curvilinear structures such as those of alluvial plains (Gouw 2008).

To overcome those limitations, Guardiano and Srivastava (1993) introduce the concept of multiple-point geostatistics to replace the variogram within an extended simulation framework. The aim of multiple-point statistics is to consider at the same time all the directions in the space, whereas the variogram only considers the points two by two. However, inferring multiple-point statistics from borehole observations is impossible due to the limited amount and the sparsity of direct observations. For this purpose, Guardiano and Srivastava (1993) proposed to extract the statistical parameters needed for simulations from a training image. The role of the training image is to depict the conceptual geological patterns and expected topological relationships between geological bodies. During simulations, the neighborhood of the currently

simulated point is identified. Then, the training image is scanned to find replicates of this neighborhood and infer conditional probability to find one facies or another. The algorithm of Guardiano and Srivastava (1993) was not extensively used due its high computational demand: the training image was scanned for every simulated point. It is only with the development of the SNESIM algorithm by Strebelle (2000) that multiple-point statistics became a useful and applicable technique in geosciences. Rather used in the petroleum industry, recent research works have shown the interest of using multiple-point statistics in environmental studies and fluvial settings (Feyen and Caers 2006, Huysmans and Dassargues 2009).

Geostatistics thus aim to fill the gap between direct observation points using relations inferred from the data themselves or from a training image. The role of geophysics is somehow similar. Given the limited number of observations and the poor spatial resolution of direct measurements, geophysical methods may provide indirect but very important information between boreholes. Geophysical measurements often constitute indirect insights on the deposits because they are rarely related to the parameter of interest. For example, if one wants to study the hydraulic conductivity of the deposits, there is not any method which is able to propose directly this parameter. Some methods could inform about a parameter which is supposedly correlated to the parameter of interest.

The construction of training images is one of the most critical and important step of multiple-point statistics. If the geological context is generally known (e.g. alluvial aquifer), there remains in most cases considerable uncertainty on the characteristics of facies elements and on their relationships. However, few studies have investigated the uncertainty related to the choice of a training image. Similarly, almost nothing has been done so far to verify that training images and geophysical data are consistent. Yet, the latter provides spatially distributed information on subsurface petrophysical properties, even if only indirect and imperfect. These two issues will be considered in this work.

There exist several methods sensitive to various geophysical parameters. Seismic methods for example are sensitive to the velocity of seismic waves in the subsurface. This parameter can be related to strength parameter and may be useful in geotechnics. Some tentatives also relates the seismic velocity to porosity and hydraulic conductivity (e.g. Cassiani et al. 1998). Similarly, ground-penetrating radar is sensitive to the velocity of propagation of electromagnetic

waves in the subsurface and to its attenuation, which depends on the dielectric constant of the medium and its electrical conductivity. These parameters might then be related to porosity and hydraulic conductivity (e.g. Gloaguen et al. 2001). However, the most common techniques to study water reservoirs are electrical methods. Indeed, electrical resistivity is sensitive to the lithology (for example the presence of clay) and the porosity which makes them appropriate to study alluvial aquifers (e.g. Dassargues 1997, Bowling et al. 2005, 2007).

Whatever the method used to characterize hydrogeological parameters, a petrophysical relationship is needed to link the geophysical parameter to the desired parameter. Most petrophysical relationships are empirical and site-specific. It means that they must be recalibrated for each specific study. Some relationships are physically based, but they make assumptions to reduce the complexity of the relationship. Generally, the aim is to link directly the parameter of interest to the measured geophysical parameter in a deterministic way even if uncertainty about petrophysics exists and is sometimes included in the process (e.g. Irving and Singha 2010).

Multiple-point statistics offer a probabilistic framework to use secondary data (or soft data) such as geophysical models as a constraint to model the parameter of interest. A petrophysical relationship is not required. It is replaced by a probability distribution. This interesting characteristic enables to take into account the uncertainty related to geophysical models. Indeed, geophysical models are most often obtained through inversion of the data set. This inverse problem is generally ill-posed and its solution non-unique. A common way to solve the problem is then to regularize it with additional constraints. Consequently, the resolution of geophysical methods is far from being perfect and the recovered geophysical parameter may be different from the true parameter. Considering also the noise on the data, geophysical techniques are rarely informative enough to discriminate unequivocally between multiple facies or lithologies. The probabilistic approach proposed in this work takes this uncertainty into account. The probability distribution is still site-specific, but it proposes an alternative to deterministic approaches.

In the petroleum industry, reservoirs are quite deep and difficult to explore. The most adapted geophysical technique in this case is seismic reflection. Seismic reflection is a wave-based geophysical method. Its resolution, linked to the wave length, is relatively high considering the depth of the reservoir. It is able to detect litological layers, faults and folds in the reservoir. Seismic attributes, such as seismic amplitude, are thus used as soft data to constrain geostatistical

models of the reservoir. In environmental sciences and hydrogeology, we are mostly interested in the near-surface part of Earth. Applying methods like seismic reflection is very difficult in such a context. In this work, we will focus on the use of electrical resistivity tomography (ERT) to image alluvial deposits. ERT is a potential-based geophysical method. The measurement procedure implies that large volume of subsurface are integrated. This phenomenon and the inversion process required to obtain models of electrical resistivity affect the resolution. At its relative scale, ERT will provide less sharp information about the subsurface. The application of multiple-point statistics conditioned by near-surface geophysics in a hydrogeological framework to characterize complex heterogeneity is a prospect that very few studies have explored (Trainor 2010).

However, the information brought by geophysical models may be improved. Since the solution of the inverse problem is non-unique, it is important to select among the possible solutions the one which is the most geologically plausible (Blakely 1995). The standard method consists in the addition of a smoothness constraint (Constable et al. 1987). This may be far from the reality and other constraints were and must be developed. An interesting topic of research is to integrate prior information into the inverse problem. This information may come from geology, hydrogeology or other geophysical methods. Constraining the inversion to impose what we know about the model will generally improve greatly the results, making geophysics more informative.

Geostatistical techniques offer a well-designed framework to integrate various types of data inside a unique model; the integration of dynamical data however remains challenging. Dynamical data sets require to run a forward simulator to simulate the considered process. In the case of hydraulic heads for example, it is necessary to run a groundwater flow model to calculate the response of a given model to the specified conditions of flow. This constitutes also an inverse problem and many techniques are available to solve it, generally iterative (e.g. pilot-point method, Markov chain Monte Carlo, gradual deformation, etc.). All the methods require to define a prior model to constrain the inverse solution. Within the context of this work, the probability perturbation method (PPM) will be used to integrate dynamical data (Caers and Hoffman 2006). The PPM algorithm will use multiple-point statistics simulations as a prior model. This will ensure that every available data (geological and geophysical) used to build models will also be integrated in the inversion process necessary to calibrate hydraulic heads.

The specificity of the PPM when combined with MPS is to invert for the geometry of the model, i.e. the relative position of geological bodies present in the training image is modified in order to explain dynamical data.

Finally, the whole methodology will propose an integrating technique, based on multiple-point geostatistics to create models of the subsurface, constrained by geological data (borehole data and training image), geophysical data (ERT inversions used as a base to derive probability maps) and hydrogeological data (inverse modeling using PPM). The common theme all along the thesis will be the site of Hermalle-sous-Argenteau which was used to test the different techniques and was also the base to build synthetic case studies. This site lies in the alluvial plain of the Meuse River and the thickness of alluvial deposits at this position is about 10 m.

Chapter 2 of the thesis is devoted to the incorporation of prior information into the ERT inverse problem. The mathematical framework is presented and a state-of-the-art review analyzes the available techniques. Three techniques that should be applicable in a large range of contexts are selected and compared in different field cases to highlight their advantages and drawbacks: the reference model inversion, the structural inversion and the regularized geostatistical inversion. This will prove that the integration of independent information improves, sometimes drastically, the results. However, it will also highlight that the best inversion method is site-specific and the role of the interpreter will remain preponderant.

In chapter 3, the multiple-point statistics algorithm is presented. Then, available data in the alluvial plain of the Meuse River is analyzed to try to build training images representative of alluvial deposits. A methodology is proposed to verify the consistency between those training images and available geophysical data. Finally, the role of some parameters intervening in the SNESIM algorithm will be investigated.

Chapter 4 is dedicated to the integration of dynamical data in the geostatistical model through the probability perturbation method. The PPM algorithm is presented and tested on a synthetic benchmark. This will highlight the most influencing parameters such as the role of the training image and soft data. Moreover, the methodology to integrate geological, geophysical and hydrogeological data is illustrated in the case of a pumping experiment on the site of Hermalle-sous-Argenteau.

Chapter 5 illustrates how electrical resistivity can be applied within the context of temper-

ature monitoring. First, general considerations are made about petrophysical relationships and assumptions. Then two field cases are presented. The first one uses surface array to monitor temperatures during a heat injection and storage experiment. The second uses cross-borehole ERT to follow a heat tracing experiment on the site of Hermalle-sous-Argenteau. The method proves its ability and reliability to monitor qualitatively and quantitatively temperature, even if more tests are needed in the future to fully understand the complex relationship between bulk electrical resistivity and temperature.

The last chapter of the thesis sums up the important points that can be learned from the different experiments and opens new research directions that could be followed in the future.

Chapter 2

Incorporation of prior information in the ERT inverse problem

Note. The research material of this chapter is partially published in two peer-reviewed articles published in international journals and was presented in International conferences:

Martin R., Kemna A., **Hermans T.**, Nguyen F., Vandenbohede A. and Lebbe L. 2010. Using geostatistical constraints in electrical imaging for improved reservoir characterization. AGU Fall Meeting, December 13-17, San Francisco, California.

Hermans T., Caterina D., Roland M., Kemna A., Robert T. and Nguyen F. 2011. How to incorporate prior information in geophysical inverse problems: deterministic and geostatistical approaches. EarthDoc, Extended Abstract Near Surface Geosciences 2011, D07, September 12-14, Leicester, United Kingdom.

Hermans T., Vandenbohede A., Lebbe L., Martin R., Kemna A., Beaujean J. and Nguyen F. 2012. Imaging artificial salt water infiltration using electrical resistivity tomography constrained by geostatistical data. Journal of hydrology, 438-439, 168-180, doi: 10.1016/j.hydrol.2012.03.021.

Hermans T., Caterina D. and Nguyen F. 2014. Case studies of incorporation of prior information in electrical resistivity tomography: comparison of different approaches. Near surface geophysics, in press.[1]

[1]Hermans T. and Caterina D. are co-first authors of the paper.

Most geophysical inverse problems are ill-posed. The non-linearity of the forward problem and the limited number of data against the number of parameters are causes for the non-uniqueness of the solution (see e.g., Menke 1984, Aster et al. 2005). A common way to solve inverse problems is to add regularization to a least-square problem (e.g. Tikhonov and Arsenin 1977).

To regularize inverse problems in applied geophysics, smoothness constraint regularization (Constable et al. 1987) is a standard technique, especially in electric and electromagnetic methods (de Groot-Hedlin and Constable 1990). However, in many cases, such constraint is not consistent with the geology or prior knowledge of the study site (e.g. Blaschek et al. 2008, Robert et al. 2011, Hermans et al. 2012a). For example, when the subsurface resistivities do not vary in a smooth manner, one may use other regularization operators such as the L1-norm or robust model constraint (Farquharson and Oldenburg 1998, Loke et al. 2003).

The solution of the inverse problem is non-unique, many models may explain the same data set. One should thus reduce the amount of mathematical solutions to more geologically (or hydrogeologically, depending of the main aim of the study) plausible models by incorporating all available prior information in the inversion process (e.g. Blakely 1995, Wijns et al. 2003).

Despite the fact that several methods exist to incorporate prior information in inverse problems, most of the inversions in practical field cases remain standard. Though, in most cases, prior information from borehole and logging data or from another geophysical method is available. In this chapter, we will focus on the electrical resistivity tomography method (ERT). First, the important theoretical concepts are reviewed (section 2.1). In section 2.2, we will analyze a non-exhaustive list of available methodologies to incorporate prior information. Sections 2.3 to 2.5 present three methods that were used in this work: respectively the reference model inversion, the structural inversion and the regularized geostatistical inversions. All methods are applied within the context of least-square inversion problems. At the end of the chapter (section 2.6), we consider the incorporation of prior information on the site of Hermalle-sous-Argenteau. This site is located in the alluvial plain of the Meuse River. That section is important because the results will be further integrated into geostatistical models of the alluvial aquifer in chapters 3 and 4. Finally, the different case studies enable us to draw guidelines and conclusions concerning the use of prior information into the ERT inverse problem (section 2.7).

2.1 Inversion of electrical resistivity data

2.1.1 Principles of the method

Electrical resistivity tomography (ERT) is a geophysical method aiming to map the distribution of bulk electrical resistivity in the subsurface. Bulk electrical resistivity is influenced by many soil and rock properties: nature, porosity, tortuosity, cementation, saturation, pore fluid, temperature, salinity, etc. Consequently, the method can be applied in many contexts to study variations of the given properties. This is also a drawback of the method, because resistivity distributions are difficult to interpret without additional information (prior knowledge) on the investigated zone.

ERT is a potential-based method, i.e. it is based on the measure of the electrical potential in the subsurface. It implies that relatively large volume of subsurface are integrated. Potential-based methods are generally opposed to wave-based methods (seismic, GPR) which result from the propagation of waves in the subsurface. Acquiring ERT data requires to inject a known current in the subsurface through two injection electrodes and to measure the resulting potential difference between two measuring electrodes.

The distribution of potentials in the ground when a current is injected is described by the Amper-Maxwell equation coupled with Ohm's law, yielding to the Poisson's equation for quasi static-field (e.g. Telford et al. 1990)

$$\nabla.(\sigma\nabla\phi) - \nabla.\overrightarrow{J_s} = 0 \tag{2.1}$$

where $\overrightarrow{J_s}$ is the current density due to a source of current in $[A/m^2]$, σ is the electrical conductivity of the subsurface in $[S/m]$, i.e. the inverse of the electrical resistivity ρ in $[Ohm.m]$ and ϕ is the electrical potential in $[V]$.

For an homogeneous half space (i.e. for surface data), equation 2.1 can be solved analytically. Given an injected current I in $[A]$, the value of the electrical potential at a distance r in $[m]$ of the source is

$$\phi = \frac{\rho I}{2\pi r}. \tag{2.2}$$

Equation 2.2 is correct for one injection electrode. Using the principle of superposition of

potentials, the potential difference for a classic quadrupole of measurement can be written as

$$\Delta\phi = \frac{\rho I}{2\pi}\left(\frac{1}{r_A - r_M} - \frac{1}{r_A - r_N} - \frac{1}{r_B - r_M} - \frac{1}{r_B - r_N}\right) = \frac{\rho I}{K} \tag{2.3}$$

where K is called the geometrical factor in $[m]$, r_X is the position of electrode X, A and B being the injection electrodes and M and N being the measuring electrodes.

In the general case of a non-homogeneous half-space, the true resistivity ρ cannot be deduced with a single measurement, it is replaced in equation 2.3 by the apparent resistivity ρ_a. When acquiring ERT data, one measures the potential difference, which is dependent of the current injected. Inversion softwares generally use ρ_a or the resistance R in $[Ohm]$

$$R = \frac{\Delta\phi}{I} = \frac{\rho_a}{K} \tag{2.4}$$

as input data. In ERT, data points are collected with various positions of both injecting and measuring electrodes. For heterogeneous media, equation 2.1 does not have an analytical solution. A numerical solution is sought through finite difference or finite-element methods (Sasaki 1994).

2.1.2 Formulation of the inverse problem

Let us assume that a data set of N points was collected on the field, it is a set of N measured resistances each corresponding to a given position of the quadrupole of measurement. Hereafter, we will call it the data $\mathbf{d}$. From $\mathbf{d}$, we want to deduce a model of M resistivity values $\mathbf{m}$, M being the number of elements of the discretized grid used to calculate the numerical solution. The forward formulation of this problem can be written as

$$\mathbf{d} = f(\mathbf{m}) \tag{2.5}$$

where f is the forward operator of the problem, i.e. the resolution of the Poisson's equation (2.1) for the set of quadrupoles of measurements. The forward operator consists in the calculation of data $\mathbf{d}$ for a distribution of model parameters $\mathbf{m}$. Resistivities of the model and values of resistance may split on a wide range of values, encompassing several orders of magnitude. Generally, data and model parameters are transformed to take their logarithm. Therefore, data

and model are expressed as

$$d_i = \ln(R_i) \tag{2.6}$$

$$m_j = \ln(\sigma_j). \tag{2.7}$$

In ERT, the problem is an inverse one, since the aim is to find a model $\mathbf{m}$ explaining the observed data $\mathbf{d}$. In this chapter, we will stay in the general framework of the regularized least-square inverse problem. The inversion is done through an iterative minimization of the objective function

$$\psi(\mathbf{m}) = \psi_d(\mathbf{m}) + \lambda\psi_m(\mathbf{m}) \tag{2.8}$$

where the first term on the right-hand side of equation 2.8 expresses the data misfit, the second term expresses the model functional with some assumed characteristic of the model and λ, the regularization parameter, balances these two terms. The second term in equation 2.8 is needed because the problem is ill-posed. Inverting only with a data misfit criterion would lead to noisy and implausible results. The second term stabilizes the inversion process, in the sense that the sought model has to verify some determined properties (Tikhonov and Arsenin 1977).

True data sets are polluted by noise (LaBrecque et al. 1996a). Assuming a vector $\mathbf{e} = (e_1, e_2, \cdots, e_N)^T$ containing the error associated to each data point, equation 2.5 becomes

$$\mathbf{d}^{meas} = \mathbf{d} + \mathbf{e}. \tag{2.9}$$

The data misfit is generally calculated on the basis of a L_p norm

$$\psi_d = ||\mathbf{d} - f(\mathbf{m})||^p = \sum_{i=1}^{N} (d_i - f_i(\mathbf{m}))^p \tag{2.10}$$

and its value at the end of the process depends on the noise or error level. In practice, L_1 or L_2 are used. If we note the standard deviation for each data point ϵ_i, considering uncorrelated Gaussian noise with zero mean, we can transform equation 2.10 into an error-weighted data misfit for the L_2 norm

$$\psi_d = \sum_{i=1}^{N} \left(\frac{d_i - f_i(\mathbf{m})}{\epsilon_i} \right)^2 = \| \mathbf{W}_d \left(\mathbf{d} - f(\mathbf{m}) \right) \|^2 \tag{2.11}$$

where $\mathbf{W}_d$ is the data weighting matrix. $\mathbf{W}_d$ is a diagonal matrix whose elements are the inverse of the error estimation $\mathbf{W}_d = diag(\frac{1}{\epsilon_1}, \frac{1}{\epsilon_2}, \cdots, \frac{1}{\epsilon_N})$.

Actually, the standard deviation ϵ_i are directly estimated from an error estimation (e_i), since we have

$$\epsilon_i = \Delta \ln R_i \cong \frac{\Delta R_i}{R_i} = \frac{e_i}{R_i}. \tag{2.12}$$

An error model can be estimated using the reciprocal error (LaBrecque et al. 1996a, Slater et al. 2000). Reciprocal measurements correspond to measurements where current and potential electrodes are switched. According to the reciprocity theorem (Parasnis 1988), the resistance should be equal in both case. This enables to estimate the error $|e_{N/R,i}|$ on the data

$$|e_{N/R,i}| = R_{N,i} - R_{R,i} \tag{2.13}$$

where R_N and R_R are respectively the normal and reciprocal resistance. The error can be used to weight individually the corresponding data. Alternatively, the set of data error can be used to derive an error model for the data set. As an example, Slater et al. (2000) propose to model the error using a linear model of the mean resistance, enveloping all data points

$$|e| = a + bR \tag{2.14}$$

where a represents the minimum absolute error and b defines the relative increase of the error with the mean resistance R.

The root mean square error (RMS) of the error-weighted data misfit (equation 2.11) is given by

$$\epsilon_{RMS} = \sqrt{\frac{\psi_d(\mathbf{m})}{N}}. \tag{2.15}$$

The resistivity problem is nonlinear and the minimization of the global objective function is done in an iterative process. The iteration process is stopped when an acceptable level of data misfit ψ_d is reached. From the statistical theory, data should be inverted according to their noise level and ψ_d should thus be equal to the number of data N, which corresponds to an RMS error $\epsilon_{RMS} = 1$. All inversions in this work were done with this criterion.

Equation 2.8 showed the general form of the inverse problem, with the second term of the right-hand side being a model functional, defining some characteristics of the model. The choice

of this model functional will shape the characteristics of the inverted model. The most commonly used approach in the ERT inverse problem is to use Occam's approach to obtain the smoothest model fitting the data. $\psi_m(\mathbf{m})$ is then defined as the first (or higher) order spatial derivative of the model (Constable et al. 1987)

$$\psi_m(\mathbf{m}) = \int\int \|\nabla \mathbf{m}\|^2 dxdz \cong \|\mathbf{W}_m \mathbf{m}\|^2 \tag{2.16}$$

where $\mathbf{W}_m$ is a matrix evaluating the first order roughness of $\mathbf{m}$. We will see in sections 2.3 to 2.5 that prior information can be added by modifying this operator or this term of the equation.

Finally, the general form of the inverse problem (equation 2.8) can be expressed, according to the defined operators, as

$$\psi(\mathbf{m}) = \|\mathbf{W}_d \left(\mathbf{d} - f(\mathbf{m})\right)\|^2 + \lambda \|\mathbf{W}_m \mathbf{m}\|^2 \tag{2.17}$$

where λ, also called the damping factor or the regularization parameter, balances data and model misfits.

2.1.3 Inversion algorithm

The solution of the inverse problem is based on the minimization of the objective function of equation 2.17 (Kemna 2000). The problem is solved using an iterative Gauss-Newton scheme. The iteration process starts with a model $\mathbf{m}_0$, it is a first guess, generally taken equal to the mean apparent resistivity of the data. The minimization of equation 2.17 provides, at the q^{th} iteration, a model update $\Delta \mathbf{m}_q$

$$\mathbf{B}_q \Delta \mathbf{m}_q = \mathbf{b}_q \tag{2.18}$$

with

$$\mathbf{B}_q = \mathbf{J}_q^T \mathbf{W}_d^T \mathbf{W}_d \mathbf{J}_q + \lambda \mathbf{W}_m^T \mathbf{W}_m \tag{2.19}$$

and

$$\mathbf{b}_q = \mathbf{J}_q^T \mathbf{W}_d^T \mathbf{W}_d \left(\mathbf{d} - f(\mathbf{m})\right) - \lambda \mathbf{W}_m^T \mathbf{W}_m (m_q - m_{q-1}) \tag{2.20}$$

where $\mathbf{J}_q$ is the Jacobian at iteration q and ^{T} denotes the transpose operator. The code CRTomo (Kemna 2000) was used for all ERT inversions made in this work. At each iteration step, λ is

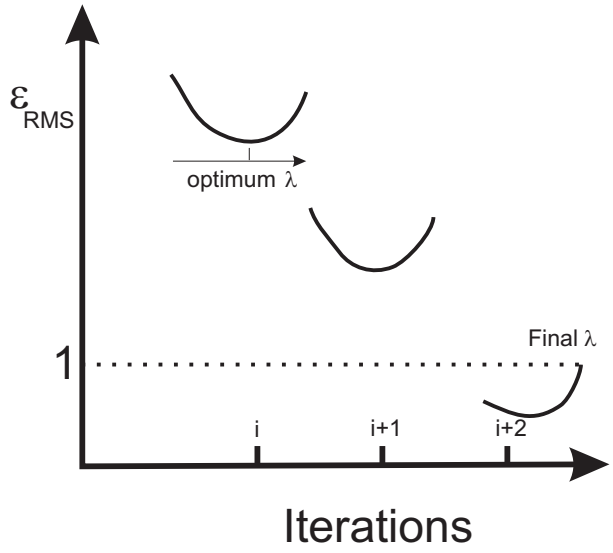

Figure 2.1: Optimization of λ in the iterative scheme to satisfy the stopping criterion.

optimized via a line search to obtain the minimum data misfit. However, when the solution has converged, i.e when $\epsilon_{RMS} < 1$, λ is maximized in order to find the unique solution satisfying the data misfit criterion ($\epsilon_{RMS} = 1$) (figure 2.1).

2.1.4 Image appraisal

Assessing the quality of an ERT image and the reconstruction of electrical resistivity is a major issue when interpreting imaging results (Caterina et al. 2013). In the following, we use the data error-weighted cumulative sensitivity as an image appraisal tool (e.g. Cassiani et al. 1998, Nguyen et al. 2009, Henderson et al. 2010). As defined in Kemna (2000), the coverage or cumulative sensitivity (hereafter we will refer to it simply as the sensitivity) $\mathbf{S}$ is given by

$$\mathbf{S} = diag\left\{\mathbf{J}^T\mathbf{W}_d^T\mathbf{W}_d\mathbf{J}\right\} \tag{2.21}$$

which depends on both data weighting and model parameters through the Jacobian matrix. A high sensitivity value signifies that a change of this parameter is going to influence the predicted data strongly, whereas a low value denotes less or no influence of this parameter on the predicted data. Obviously, a poorly covered region is unlikely to be well resolved and thus, the sensitivity may give some crude indication for how well the model parameter is represented by the data set. However, it must be emphasized, that high sensitivity does not necessary imply high resolution but rather represents a favoring factor. Caterina et al. (2013) showed that from a practical

point of view, the use of sensitivity or resolution matrices does not make such a difference if only the diagonal elements of the resolution matrix are considered. The main difference appears at the sides of the model for surface arrays, which are sensitive but not resolved.

The sensitivity as image appraisal tool can be used to define a cut-off value below which the results cannot be interpreted (e.g. Robert et al. 2011). This may define a weighting or filtering scheme for the interpretation. The biggest difficulty, however, remains to define this value (Caterina et al. 2013).

2.2 Prior information in ERT

Prior information is defined as every piece of information which can be collected on a site independently of the considered ERT data set. For example, it may consist in geological or geotechnical maps, borehole or geophysical logs, data from another geophysical method, like GPR (Ground Penetrating Radar) or seismic, or from previous ERT sections on the same site.

Not every type of information is suited for direct incorporation in the inversion process. As an example, a geological map is qualitative and cannot give any accurate information. similarly, a seismic reflection section may have a completely different scale of investigation than ERT. However, such information may be interesting in the interpretation process to explain the resistivity distribution near the surface. In contrast, high resolution GPR sections may be too informative for a large ERT section, with much more details that could be resolved by ERT.

Generally, useful prior information will consist in additional detailed information at a scale relevant for the ERT section, i.e. at a scale close to the resolution of the ERT section. Many methodologies are possible to incorporate such information. In the literature, many examples illustrate combination of techniques and/or data to improve the solution of inverse problems. To our knowledge, there are few studies which compare different methodologies based on case studies.

The first step towards the incorporation of prior information may be called the **cooperative interpretation**. It is not a method by itself, because it does not need a particular inversion scheme. The aim is to use different techniques with variable resolution to improve the quality of interpretation. For example, Garambois et al. (2002) used seismic and ground-penetrating radar (GPR) data to identify more precisely than with one single method the water table depth

and its lateral fluctuation. As another example, Bowling et al. (2005) used in combination ERT and GPR to delineate alluvial aquifer heterogeneities. GPR gives an insight on the structure of the aquifer, whereas ERT is used to qualitatively relates resistivity variations to existing facies. These two simple examples (many other could be taken as well) enhance the fact that different geophysical methods may be complementary and that combining them should yield better results.

The latest example may be used to understand the idea behind **structural inversion**. Indeed, one of the major drawback of the standard smoothness constraint method is that it tends to reduce contrasts. A transition between two zones with a high resistivity contrast will appear as a smooth transition. One possibility is to use a L1-norm instead of a L2-norm for the model constraint, which will lead to sharper contrasts all over the section (Farquharson and Oldenburg 1998, Loke et al. 2003). However, if there is some prior knowledge on the structure of the subsurface thanks to GPR or seismic refraction data for example, it can be used directly in the ERT inversion. The idea was first developed by Kaipio et al. (1999), for electrical impedance tomography of the human head. The methodology consists in building the regularization operator using a function describing the structure of the studied domain. If a known limit exists, the regularization operator is modified to reduce the penalty for changes across this boundary. They show with synthetic examples that if boundaries are known a priori, parameter value estimation in the different bodies is improved. According to these authors, when bad prior information is incorporated in the inversion process, the solution is still as good as the smoothness constraint solution. This conclusion depends on how bad is the prior information as we will see with examples later. The premise is that if you incorporate known limits, the results will be improved everywhere, not only around the limits.

Saunders et al. (2005) applied this methodology to constrain ERT inversion with seismic data. They used the second derivative of the curvature, i.e. the ratio of seismic velocity at a location over the mean seismic velocity in the model, to impose the structure in their inverse problem. This method assumes that the curvature is similar for seismic velocities and electrical resistivities and needs to know the seismic velocity everywhere in the section.

The method presented by Kaipio et al. (1999) still authorizes some smoothing across the boundaries, even if reduced. Some authors proposed to carry on **disconnected inversion**

(Günther and Rücker 2006). In disconnected inversion, the inversion domain is divided in a given number of zones represented by their boundaries; the zones are not linked through the regularization operator during inversion. It generally yields very sharp contrasts in the inverted models, but it reduces the role of the data themselves, especially if there is some uncertainty on the position of the limits.

As examples, Doetsch et al. (2012) used GPR-defined structures to build irregular grids for ERT inversion within the context of an alluvial aquifer. No smoothness constraint across the boundaries is imposed during the inversion process. In addition, the effect of the structure is amplified by a heterogeneous starting model following the supposed structure. The results of inversion follow the imposed structure and they allow seeing more details in the resistivity distribution inside the zones. Following the work of Nguyen et al. (2005), Elwaseif and Slater (2010) used the watershed algorithm to detect boundaries from a smoothness constrained solution and then used them to provide a disconnected solution. They applied this technique to detect cavities whose position is not known a priori. So, in this case, it is not really some prior information but a two-step inversion, because the limits come from ERT results themselves.

The example of Saunders et al. (2005) is a typical example where **structural joint inversion** could be used. When two or more geophysical methods may result in co-located models of different geophysical properties, the structural joint inversion consists in inverting simultaneously both data types, including information of one data set to the other(s) through a cross-gradient method (Gallardo and Meju 2003). The postulate of this method is that the structure of the different geophysical properties is similar. It would assume, for example, that electrical resistivity and seismic velocity have the same structure in the example by Saunders et al. (2005). This is not always the case. For example, S-wave in seismic are insensitive to the presence of water whereas it is a major factor affecting the electrical resistivity. Of course, this method requires to have extensive data sets for each method.

For example, this technique was applied by Linde et al. (2006) to invert jointly electric resistance and traveltime GPR data; by Hu et al. (2009) to combine electromagnetic and seismic inversion or by Doetsch et al. (2010b) to invert seismic, GPR and electric resistance data. In most examples, the best improvement is observed for methods sensitive to bulk properties (e.g. ERT), thanks to the information brought by methods sensitive to the structure (e.g. GPR and

seismic).

Bouchedda et al. (2012) developed another structural joint inversion scheme for crosshole ERT and GPR travel time data. A Canny edge detection algorithm is used to extract structural information. ERT structural information is then added to GPR inversion and vice versa.

A more and very common way to include prior information is to incorporate so called **prior or reference models** (Oldenburg and Li 1994). This is a common feature available in most inversion algorithms (e.g. Pidlisecky et al. 2007). Most of the time, the use of the reference model is limited to a homogeneous model, with resistivity value equal to the mean apparent resistivity of the data. However, the method can be used as well to define more complex prior models with multiple layers or zones. One of the drawback of the method is that it requires to define values of resistivity in addition to the structure. The structural inversion and the reference model can obviously be combined (e.g. Doetsch et al. 2012).

The importance of the reference model is highlighted in the method of the determination of the depth of investigation index (DOI) (Oldenburg and Li 1999, Caterina et al. 2013). A comparison of inversions with different reference model is used to derive to which depth ERT results are reliable. This clearly shows that the reference model has some important influence on the inverted model.

In addition to prior model, prior knowledge can also be introduced in the form of inequality to reduce the range of variation of parameters, ensuring that the parameter will remain in a defined interval (e.g. Cardarelli and Fischanger 2006) or in the form of trends in the physical property like an increase of resistivity with depth (e.g. Lelièvre et al. 2009).

The method of **layered inversion** is also a possible way to include easily prior information such as the depth of the layer. However, it requires an alternative way to formulate the inverse problem. In this method, the number of elements is reduced to bigger homogeneous elements whose parameter value is constant. The depth of the nodes becomes an unknown of the problem. This enables to include *a priori* depth values in the inversion. One of the advantage of this method is to enable some uncertainty about the depth of the layers since there is not a specific grid to be built according to structural information. The major drawback is the choice of the number of layers to invert for, since this parameter influence highly the results of inversion. Auken and Christiansen (2004) used this methodology to produce 2D resistivity section

based on laterally constrained 1D model. This technique was also applied for the inversion of magnetotelluric data by Smith et al. (1999) and de Groot-Hedlin and Constable (2004).

Except for the later, the previous techniques of integration of prior information mainly rely on modifications of the smoothness constraint inversion scheme, either by additional constraining terms or by a more complicated or more detailed calculation of the regularization operator. An alternative way is to use an *a priori* model covariance matrix to regularize the problem.

This methodology can be applied to calculate the most likely estimates through **geostatistical inversion** (Yeh et al. 2002, 2006), but the model covariance matrix may also be included in a least-square scheme to regularize the ill-posed inverse problem (Hermans et al. 2012a, Linde et al. 2006). In these two examples, the a priori covariance matrix acts as a soft constraint, since a damping factor (i.e. λ) is used to balance between data misfit and model structure.

The theoretical concept to use statistical information within geophysical inverse solutions by utilizing *a priori* model covariance matrices is based on the work of Tarantola and Valette (1982), who showed the application and estimation of a Gaussian covariance model to invert 1D synthetic gravity data. Pilkington and Todoeschuk (1991) used well log data to apply this concept within 1D magnetotelluric and DC resistivity inversions. Maurer et al. (1998) used a general model utilizing the von Kármán autocovariance function to regularize large-scale geophysical inverse problems, namely to invert 2D cross-borehole seismic data. They also showed the similarity between the so-called stochastic regularization operator, the damping and the smooth-model regularization operator. Yang and LaBrecque (1998) parameterized covariance functions, which are well known geostatistical tools frequently used within cokriging of geostatistical reservoir modeling (see for instance Journel and Huijbregts 1978 and Isaaks and Srivastava 1989), to use as *a priori* covariance within 3D ERT inverse solutions.

Chasseriau and Chouteau (2003) demonstrated the benefits of using *a priori* information in the form of a covariance matrix whose parameters were derived from experimental semivariogram data and used it as regularization operator within reconstruction of large-scale 3D density models. They used the methodology in synthetic benchmark studies and applied the same procedure to field data (scale of several kilometers). More than 3000 gravity measurements were used for horizontal variography, and two boreholes provided vertical information for separate covariogram function calculation. Linde et al. (2006), extending the work of Maurer et al. (1998), included

variogram information to achieve geostatistical regularization for ERT and GPR joint inversion. They exploited linear equidistant grids and utilized a 3D fast Fourier transform for their covariance matrix computation. They demonstrated that this type of regularization preserves spatial statistics of the joint ERT and GPR images in comparison to classical smooth-model solutions. Yet, their method is only applicable if the grid parameterization is uniform in each spatial direction and thus not applicable for more general model problem geometries.

Johnson et al. (2007) explored an inversion method to fit high-resolution GPR cross-borehole data and honor experimental variograms simultaneously. They explicitly incorporated a variogram operator in the inversion process (the a priori model characteristic is the variogram itself). In this way, they obtained a model fitting both data and statistical parameters. The approach requires calculating the experimental variogram sensitivities in order to modify the model parameters (dielectric permittivities in the case of GPR) during the inversion to preserve the spatial statistics. The question of balancing between variogram and data is addressed through additional user-defined criteria. With their method, it is always possible to find a solution reproducing the variograms corresponding to any field (even non-stationary) as long as it also honors the data. They applied this technique to cross-borehole GPR traveltime data and given variograms well constrained in the vertical direction, thanks to available logging data. There remained uncertainty on the horizontal range because of relatively low horizontal sampling.

In the next sections, we will describe the mathematical formulation and illustrate the application of three different methods to incorporate prior information: the inversion with a reference model, the structural inversion and the regularized geostatistical inversion. All models were implemented in the code CRTomo (Kemna 2000). They are respectively described in sections 2.3, 2.4 and 2.5. In each section, we will show two examples of relatively well known site for which prior knowledge is available: the Ghent site and the Westhoek site. Finally, the different methods will be applied on the site of Hermalle-sous-Argenteau (section 2.6).

2.3 The inversion with reference model

2.3.1 Mathematical formulation

The incorporation of prior information in the ERT inverse problem through the addition of a reference model is well known and documented (Oldenburg and Li 1994). When a reference

model $\mathbf{m}_{ref}$ is used, the starting model $\mathbf{m}_0$ is chosen equal to the reference model. However, the role of the reference model is not limited to be an initial guess, the reference model is explicitly incorporated in the objective function (equation 2.17). The easiest way to do it is to simply add the reference model in the equation

$$\psi(\mathbf{m}) = \|\mathbf{W}_d\left(\mathbf{d} - f(\mathbf{m})\right)\|^2 + \lambda\|\mathbf{W}_m\left(\mathbf{m} - \mathbf{m}_{ref}\right)\|^2. \tag{2.22}$$

However, equation 2.22 is similar to equation 2.17 if the reference model is homogeneous, because its derivative is equal to 0.

Generally, another formulation is preferred to increase the role of the reference model. Its aim is to control the weight that is given to the reference model. It is done through an additional term

$$\psi(\mathbf{m}) = \|\mathbf{W}_d\left(\mathbf{d} - f(\mathbf{m})\right)\|^2 + \lambda\left(\|\mathbf{W}_m\left(\mathbf{m} - \mathbf{m}_{ref}\right)\|^2 + \alpha\|\mathbf{m} - \mathbf{m}_{ref}\|^2\right) \tag{2.23}$$

where α is called the closeness factor. Its role is to weight the importance of the reference model during the inversion process. This factor is chosen arbitrarily, knowing that a relatively high value will lead to an inverted model closer to $\mathbf{m}_{ref}$ and that a relatively low value will have almost no influence on the inversion results, i.e. the solution will be very close to the smoothness constrained solution, since the regularization operator $\mathbf{W}_m$ remains similar. The latter formulation (equation 2.23) is used in this work.

It is important to note that the presence of the closeness factor will inherently introduce some subjectivity in the inversion process. It may be difficult to assess the quality or the relevance of the available prior information to choose adequately its value.

2.3.2 Application on Ghent site

The first site on which the method was tested is the Ghent site. It is located on the campus De Sterre of Ghent University. The distribution of resistivity is horizontally layered, and the site is known to be almost homogeneous laterally. ERT data were collected as a background reference for a shallow heat injection and storage experiment (Vandenbohede et al. 2011, Hermans et al. 2012b) to assess the ability of ERT to image temperature changes (see section 5.3).

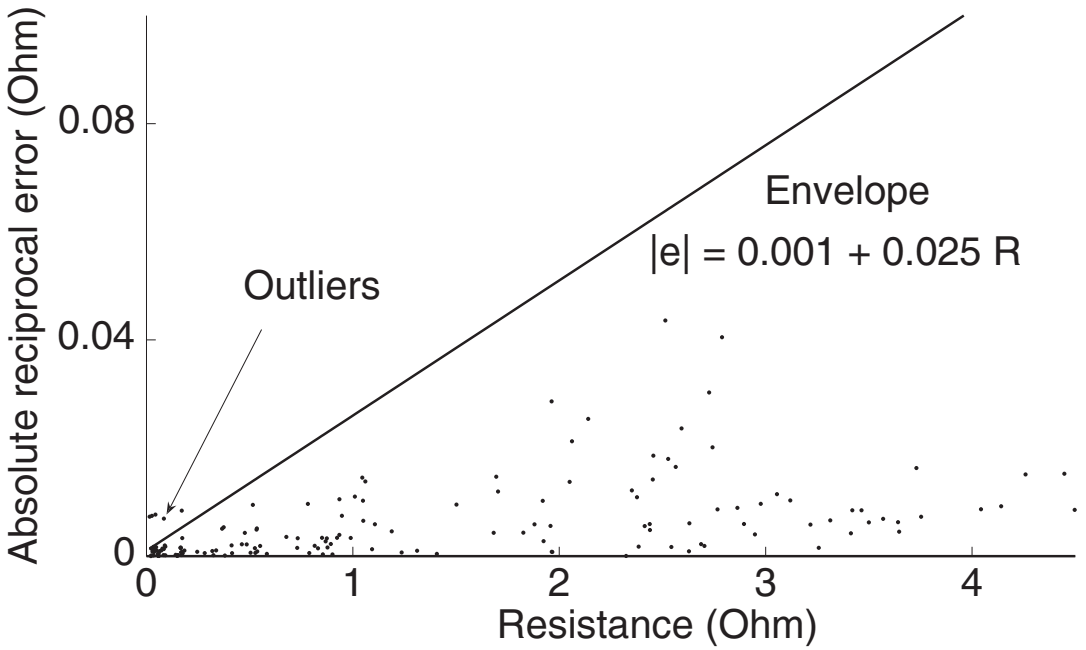

Figure 2.2: The error at Ghent site was assessed using a subset of 200 reciprocal measurements. We used the conservative approach of Slater et al. (2000) to derive an envelop curve whose equation is $e = 0.025R + 0.001$.

The data were collected with 62 electrodes separated by 0.75 m using a Wenner-Schlumberger configuration with n spacing limited to 6 and a up to the maximum possible value of 12. The error was assessed using reciprocal measurements and a linear error model (equation 2.14) with an absolute value $b = 0.001$ Ohm and a relative error $a = 2.5$ % was considered (figure 2.2). This error estimation was used to weight the data during inversion through the matrix $\mathbf{W}_d$ (equation 2.11). It is important to note that this approach is conservative. Indeed, the error is overestimated for the majority of data points. This will prevent artifacts in the inverted section.

EM conductivity logs (figure 2.3) measured with EM39 of Geonics Ltd (McNeill 1986) and laboratory measurements enable to describe the layers in terms of resistivity. Unsaturated sands (0 to -2 m) have a resistivity between 100 and 300 $Ohm.m$ depending on the saturation, saturated sands (-2 m to -4.4 m) have a resistivity around 30 $Ohm.m$ (mean value) and the clay layer (below -4.4 m) has a resistivity about 10 $Ohm.m$. For the saturated sands, a progressive decrease in resistivity is observed, certainly due to the vertical integration length (about 1 m) of the device compared to the thickness of the layer. Sharp contrasts are thus not

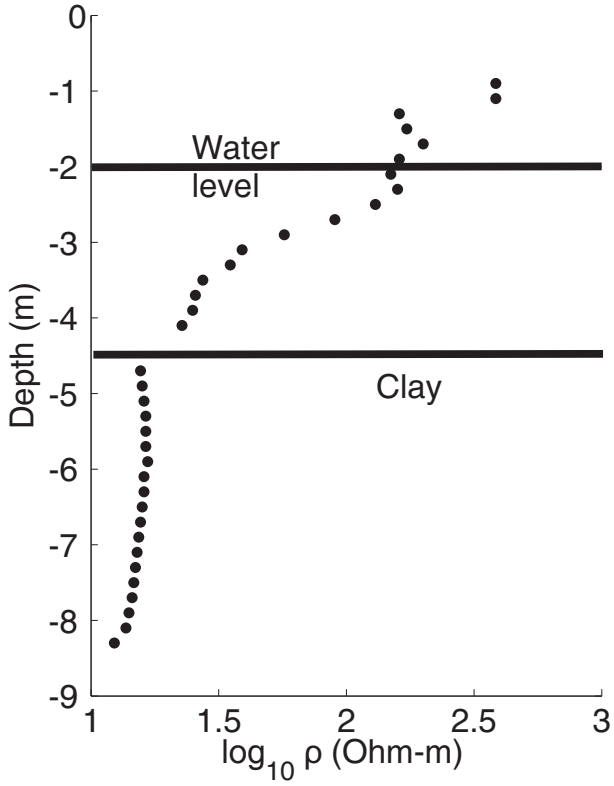

Figure 2.3: The EM conductivity log at Ghent site shows the decrease in resistivity with depth, first in the saturated zone and then in the clay formation.

clearly visible on the EM conductivity log (figure 2.3).

The EM log was used to build a three-layer reference model whose resistivities are equal to 200 $Ohm.m$ from the surface down to -2 m, 30 $Ohm.m$ between -2 and -4.4 m and 10 $Ohm.m$ below -4.4 m.

For comparison, an inversion with the smoothness constraint was done, as a reference to standard procedures (figure 2.4A). As expected from the prior knowledge of the site, the structures are horizontal, with a trend of decreasing resistivity from the surface to depth. As expected too, the limits between layers are not well defined due to the smoothness constraint and the saturated layer appears as a transition zone. When the defined reference model is added to the smoothness constraint, with a closeness factor $\alpha = 0.05$ (figure 2.4B), the solution barely differs from the smoothness constrained solution. A small variation can be observed on the bottom part of the models on the right side of the section (abscissa around 40 m and depth below 4 m) where the inverted model displays resistivity values closer to $\mathbf{m}_{ref}$. As the difference with the smoothness constrained solution is small, the factor α was increased to 0.5 (factor 10) (figure 2.4C). Doing

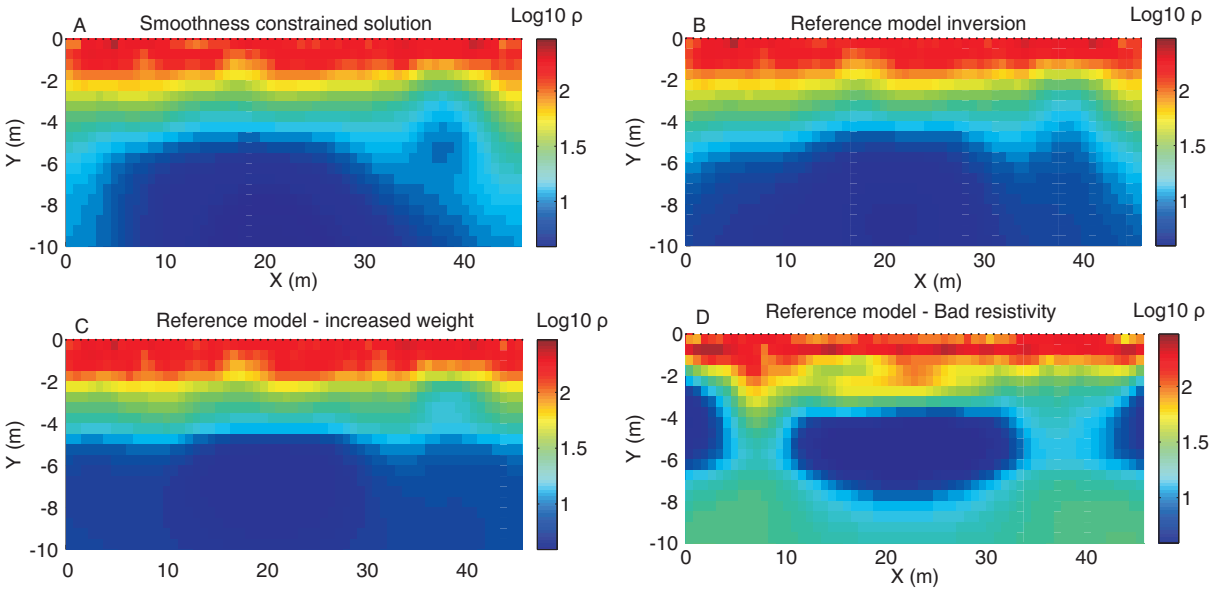

Figure 2.4: Inversions with reference model for Ghent site. A) The smoothness constraint inversion already shows a layered model with decreasing resistivity from the surface to depth, B) adding a reference model does not change significantly the results except if, C) the closeness factor is increased. D) Bad values of resistivity lead the inversion to an implausible solution.

so, the role of the reference model appears clearly, with horizontal limits better defined than previously. However, lateral variations are still visible, showing that the data contains some information on small lateral heterogeneity.

Increasing the closeness factor is not without consequences and should be always done carefully. Let us imagine that our EM log is bad due to disturbance of the signal because the site is located near a building and that a three-layer reference model is imposed: 100 $Ohm.m$ for the first meter, 10 $Ohm.m$ between -1 and -6.5 m and finally 30 $Ohm.m$ below. The closeness factor is maintained to 0.5 (figure 2.4D). This solution appears to be implausible. Thanks to information brought by the data, the unsaturated layer is imaged, but with strong lateral variations. The saturated layer is not imaged as an horizontal homogeneous medium. The clay layer appears to be divided in three lenses.

This phenomenon illustrates that imposing resistivity values is not straightforward. If for some reasons, the imposed values differ significantly from the true structure, the solution is degraded. It is important to note that the criterion of convergence ($\epsilon_{RMS} = 1$) was fulfilled for all inversions, so all the models explain the data to the same level. This is thus a crude illustration of the non-unicity of the solution in the ERT inverse problem and a demonstration of the need to look for more geologically plausible models.

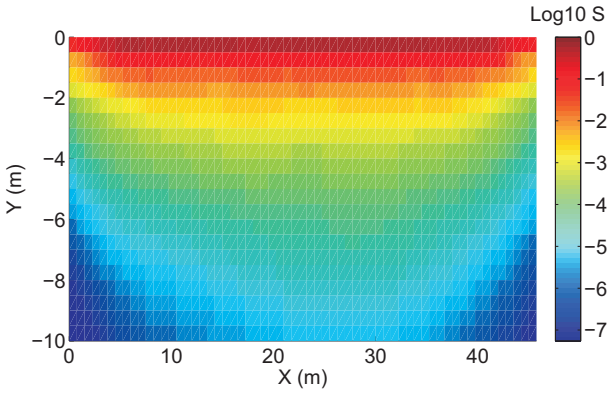

Figure 2.5: The cumulative sensitivity for the Ghent site shows the traditional decrease with depth for surface data.

These three examples already show how prior information will affect the solution. To better understand, it is necessary to have a look at the spatial distribution of cumulative sensitivity (equation 2.21, figure 2.5). For surface data, the patterns of sensitivity have a clear trend, with the lowest values at depth and on the sides of the section. It signifies that changes of model parameters with low sensitivity will less affect the data and consequently the data misfit. The minimization of the objective function (equation 2.23) for these parameters is thus linked to the model misfit, which will be minimum if the model is equal to $\mathbf{m}_{ref}$. This observation explains why the only change in figure 2.4B appears in a zone of low sensitivity, why it is the clay which is the most affected by the increase of the closeness factor (figure 2.4C) and why the worse part of figure 2.4D is also in low sensitivity zones.

2.3.3 Application on Westhoek site

The second site on which the method was tested is the Flemish Nature Reserve "The Westhoek". In this reserve, two artificial sea inlets were made in the fore dunes in 2004. Sea water has thereby access to dune slacks. However, a fresh water lens is present in the dune aquifer, which is for instance exploited for production of drinking water. Geophysical measurements were carried out to assess the evolution of sea water within the fresh water aquifer.

The deposits of the dune area consist mainly of sand about 30 m thick. However, interconnecting clay lenses form a semi-permeable layer under the infiltration ponds (Lebbe 1978). This layer hinders the vertical flow of sea water leading to enhanced horizontal flow at a depth around -5 $mTAW$ (0 $mTAW$ equals 2.36 m below mean sea level). Two different studies

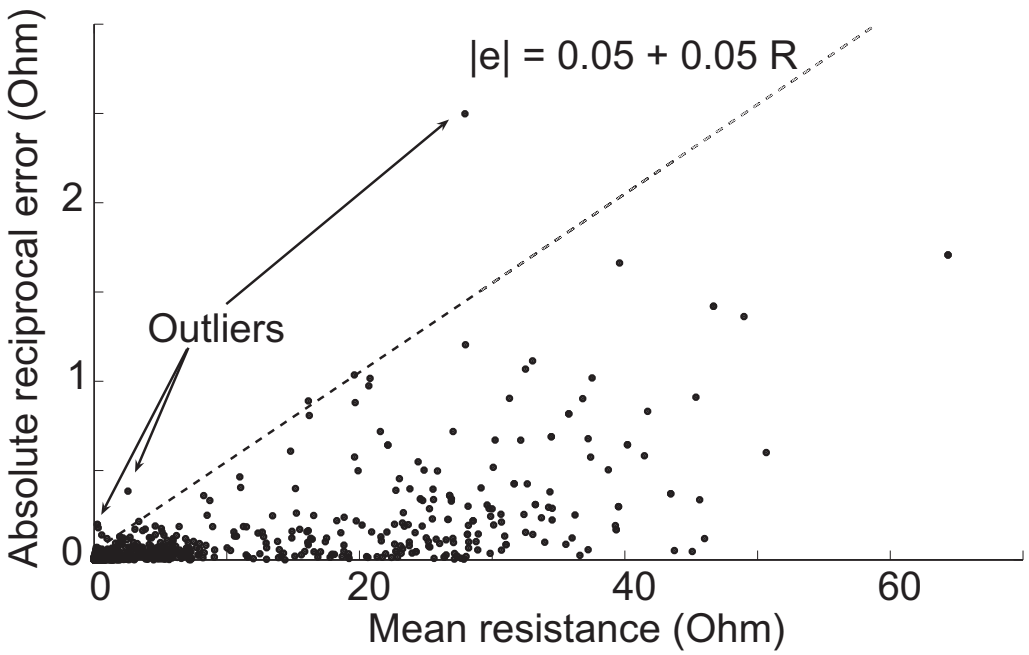

Figure 2.6: The error at Westhoek site was assessed using reciprocal measurements for almost all data points. We used individual error estimates to weight the data, except for a few points for which reciprocal was missing. For them, the envelop curve $e = 0.05 + 0.05R$ was used.

(Vandenbohede et al. 2008; Hermans et al. 2012a) investigated this lateral flow of sea water.

For the collection of ERT data, we used 72 electrodes with a spacing of 3 m and a dipole-dipole array with $n \leq 6$ and $a \leq 8$. Individual reciprocal error estimates were used to weight the data during inversion, the global noise level was about 5% (figure 2.6). This approach is less conservative than using a common error model but it was required to avoid oversmoothing in the computed section. The reason is that the common model is driven by a few points and impose a noise level even if a majority of data points have a small reciprocal error.

EM conductivity logs were made on the site (Hermans 2010). An example is given in figure 2.7, it shows the evolution of the distribution of electrical resistivity with time, with an increase of conductivity at the time where the lateral flow of sea water reaches the well.

Again, we used the smoothness constrained solution as a reference for comparison (figure 2.8A). The solutions will also be compared in the well P12 (figure 2.9). This solution clearly detects a zone of very low resistivity values corresponding to the infiltrated sea water. However, due to the smoothness constraint, the intrusion is spread on the whole thickness of the aquifer.

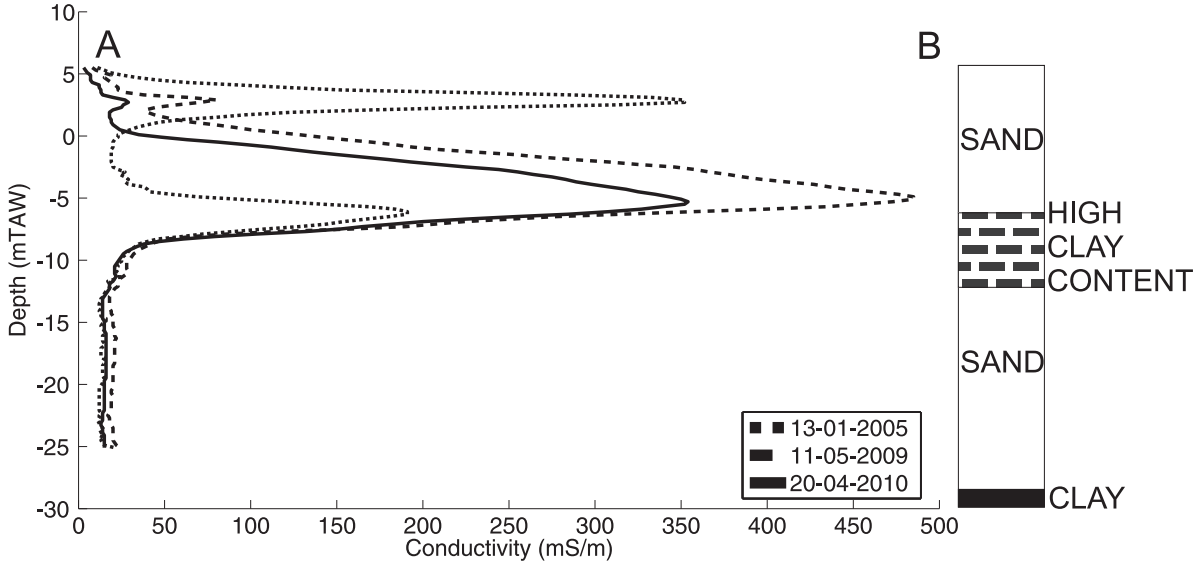

Figure 2.7: A typical conductivity log in the Westhoek area, with a high conductivity above the position of the clay layer, due to the lateral flow of sea water.

Given our previous results (section 2.3.2), we know that most effects of the reference model will influence the zone of low sensitivity. We chose a homogeneous reference model with a value different to the mean apparent resistivity and took the value of 100 $Ohm.m$ corresponding to sands saturated with fresh water at the bottom part of the aquifer. This yields the solution of figure 2.8B ($\alpha = 0.05$), with an intrusion limited in depth. We see in P12 that the solution tends to the imposed value at the bottom part of the model, but that the position and value of the maximum are not much better resolved. In contrast, if the closeness factor is increased to 2 (figure 2.8C), the position of the maximum is correct and the transition fresh/salt water is sharper as observed. However, the intrusion is quite thin everywhere in the section, whereas we know from other EM conductivity logs (Hermans 2010) that it is thicker in P18.

We also tried a more complex reference model, based on the definition of three layers: unsaturated sands from the surface down to 4 $mTAW$ with a resistivity value of 1000 $Ohm.m$, 5 $Ohm.m$ down to -6 to -8 $mTAW$ according to the position on the profile corresponding to sea water and finally 100 $Ohm.m$ below. With a low closeness factor (0.05), the more complex reference model does not yield results far from the homogeneous one (figure 2.8D). When α is increased to 2 (figure 2.8E), the mismatch in P12 becomes very good (figure 2.9). The same could be observed in P18. We may think that this solution is clearly the best possible with available information. However, looking at the distribution of resistivity on the left side of the

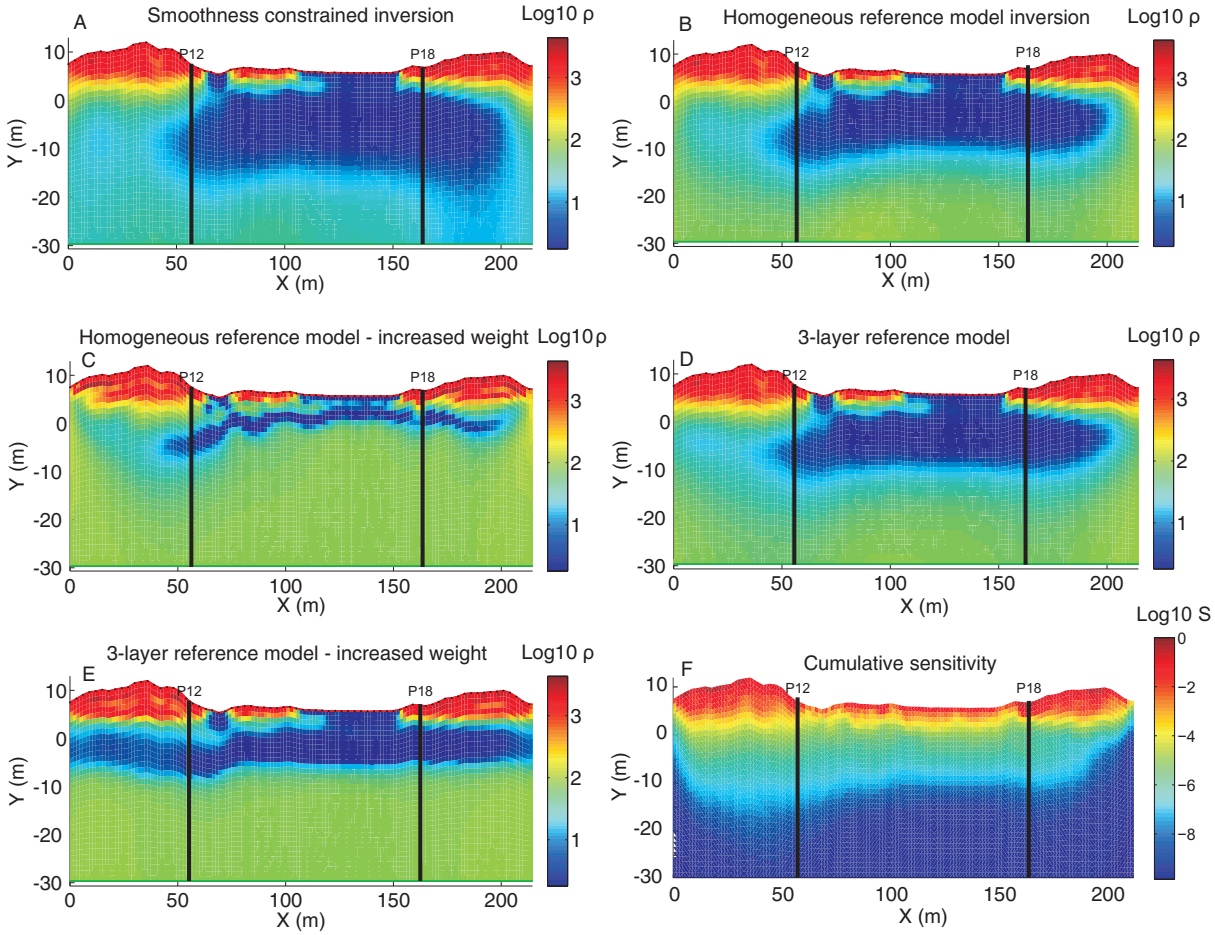

Figure 2.8: Inversions with a reference model for the Westhoek site. A) The smoothness constraint solution images the sea water intrusion, but smooths it on the whole thickness of the model. B) A simple homogeneous reference model enables to reduce the thickness of infiltrated water to a more plausible state. C) An increase of the closeness factor reduces too much this thickness. D) A three-layer reference model does not give any additional information, unless if E) the closeness factor is increased. F) The cumulative sensitivity distribution presents the typical behavior for surface ERT data.

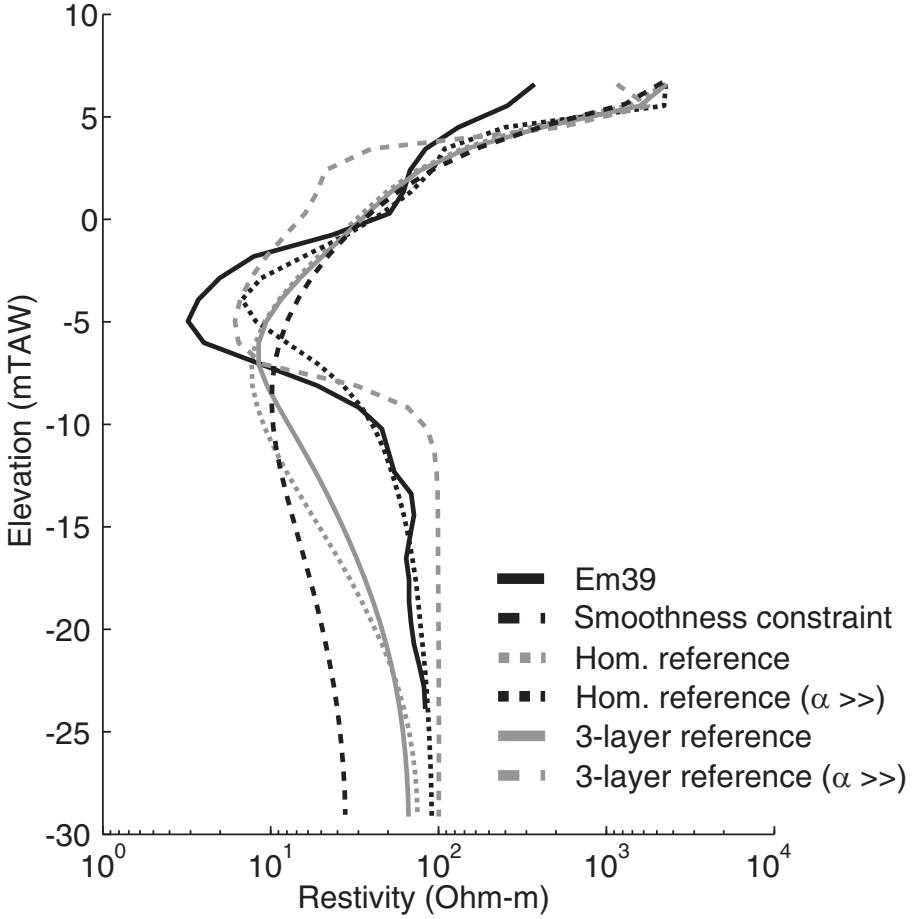

Figure 2.9: Comparison of the solution in the well P12. All inversions with a reference model bring some improvement compared to the smoothness constrained solution.

section, we see that sea water is found until the boarder of the model, which was not observed on any other profiles. We can wonder if this is not an effect of the reference model only.

This example teaches us important lessons. First, it confirms the role of the reference model regarding the low sensitivity zones (figure 2.8F). It clearly appears that the first effects are observable in zones of low sensitivity and that an increase of the closeness factor extends the effect of the reference model toward more sensitive zones. Second, we see that when using complex reference model, we are able to explain closely observed data. Nevertheless, we have to keep in mind that this data is also the one that was used to derive the reference model, so there is no proof that the inverted model is good everywhere. In this case, the fact that sea water is present at the left side of the model is most likely an effect illustrating this issue.

2.4 The structural inversion

2.4.1 Mathematical formulation

To understand how we will integrate structural information into the ERT inversion, we have first to describe with more details the calculation of the regularization operator $\mathbf{W}_m$. From equations 2.18 to 2.20, it appears that during the inversion process only the term $\mathbf{W}_m^T\mathbf{W}_m$ is needed. This smoothness constraint operator is built on the calculation of the gradient in two directions: horizontal and vertical. This can be written as

$$\mathbf{W}_m^T\mathbf{W}_m = \beta_x\mathbf{W}_x^T\mathbf{W}_x + \beta_z\mathbf{W}_z^T\mathbf{W}_z \tag{2.24}$$

where $\mathbf{W}_x$ and $\mathbf{W}_z$ are respectively the horizontal and vertical first-order difference matrix. The parameters β_x and β_z are scalar smoothness factors in horizontal and vertical direction respectively, they are used to weight differently the vertical and horizontal gradient for the whole section in case of macroscopic anisotropy (Kemna 2000). Note that the choice of an anisotropy ratio $\frac{\beta_x}{\beta_z}$ different from 1, i.e. the isotropic case, should be driven by prior information. We may say that the easiest way to introduce prior information would be to modify the anisotropy ratio.

The formulation for the first-order difference matrix is

$$\mathbf{W}_i = \begin{pmatrix} -1 & 1 & 0 & \cdots & 0 \\ 0 & -1 & 1 & \cdots & 0 \\ 0 & 0 & -1 & \cdots & 0 \\ \vdots & \vdots & \vdots & \ddots & \vdots \\ 0 & 0 & 0 & \cdots & 0 \end{pmatrix} \tag{2.25}$$

where the position of 1 and -1 depends on the numbering of model parameters and the considered direction.

The formulation of the inverse problem for the structural inversion is exactly the same as for the smoothness constraint inversion. We use the same objective function (equation 2.17). Prior information is included directly by a modification of the regularization operator $\mathbf{W}_m$, such as in Kaipio et al. (1999).

The idea is the following: at a given point located near a known boundary, we want to reduce the penalty for rapid changes across this boundary, in order to allow for sharp contrasts. This can be done by reducing the weight given to this specific gradient in the regularization operator. In $\mathbf{W}_x$ (equation 2.25), each line correspond to a specific horizontal gradient between two elements, the same can be said for vertical gradient in $\mathbf{W}_z$. A simple way to weight gradient would be to multiply the corresponding line by the desired weight, corresponding to the penalty we want to give to the boundary between the two elements.

The ratio $\frac{\beta_x}{\beta_z}$ for a given boundary will control the sharpness of the structure. The bigger the ratio (for an horizontal limit), the more the inversion tends to a disconnected inversion (e.g. Doetsch et al. 2012). When the ratio is closed to 1, the limit will be less pronounced, a value of 1 corresponding to no existing boundary.

In our implementation, we decided to modify these weights through the smoothness factors in horizontal and vertical directions. β_x and β_z were defined as scalar values in equation 2.24. Here, we have to transform them into vectors and to provide a value for each existing limit between two elements in the inversion grid. If a known horizontal boundary corresponds to the limit, we have to reduce the value of β_z. If the boundary is vertical, we have to reduce β_x. One interesting feature of this implementation is that it enables to define structures within the grid,

but also enables the definition of various zones of variable anisotropy ratio. If the structure to impose is not horizontal or vertical, the inversion grid has to be adapted (Doetsch et al. 2012).

It is important to note that the addition of a structure affects only the model of resistivity, by reducing smoothing between adjacent model parameters. Electrical current flows are not directly influenced by the limit, i.e. imposing a boundary will not prevent any current flow across it.

2.4.2 Application on Ghent site

In Ghent, the expected subsurface is composed of three horizontal layers. The limit between unsaturated and saturated zone lies at $-2\ m$ and the limit between saturated sand and clay lies at $-4.4\ m$. We thus added horizontal boundaries in our regularization operator at those positions. In addition, as the saturated sand layer is relatively thin and appears as a transition from high to low resistivity in the smoothness constrained solution (figure 2.10A), we decided to allow more vertical smoothing in this zone, using an anisotropy ratio of 0.1 between the two limits.

We tested three different anisotropy ratio $\frac{\beta_x}{\beta_z}$ for the two limits: 10, 100 and 1000 (respectively figure 2.10B, C and D). We observe a transition from the smoothness constraint solution towards a well-defined three-layer model when the boundaries become sharper. Already with a low anisotropy ratio, the inversion process is helped to draw a more horizontal clay limit. When the ratio increased, the limits are sharper and the middle layer is resolved as a unit and not as a transition any more.

For the Ghent site, the structure is slightly more efficient than the reference model to impose horizontal limits (figure 2.4). Even with a high closeness factor, some variations appear in the transitions and the saturated sand layer remains rather a transition between unsaturated zone and clay. One major advantage of the structural constraint over the inversion with a reference model is that it does not impose any resistivity values. As it is the parameter we are inverting for, this lets the data estimate resistivity variations alone.

Given that resistivity values are not imposed, we can expect that a bad position of a boundary will less affect the inversion than a bad resistivity value. This is what is observed in figure 2.11 where only one limit was imposed at $-3.2\ m$ depth ($\frac{\beta_x}{\beta_z} = 1000$). If the position of the limit

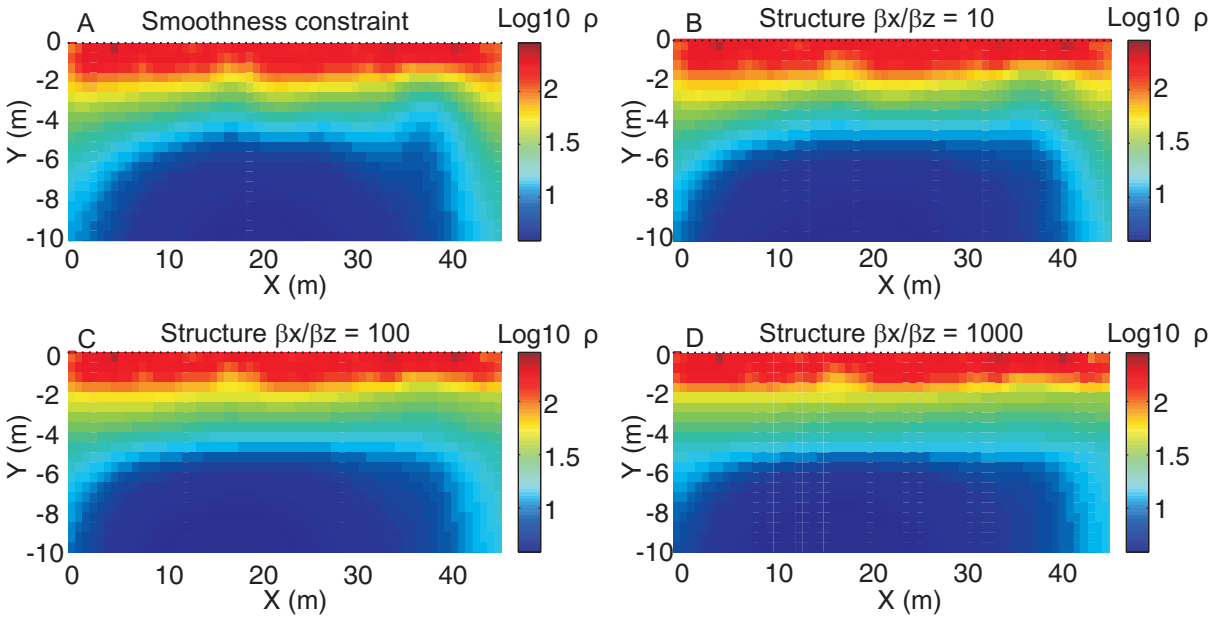

Figure 2.10: Inversions with structural constraints for Ghent site. A) The smoothness constraint inversion already show a layered model with decreasing resistivity from the surface to depth. Adding structural constraints at the position of the known boundaries, with successively B) $\frac{\beta_x}{\beta_z} = 10$, C) $\frac{\beta_x}{\beta_z} = 100$ and D) $\frac{\beta_x}{\beta_z} = 1000$, yields a more layered model with better defined limits.

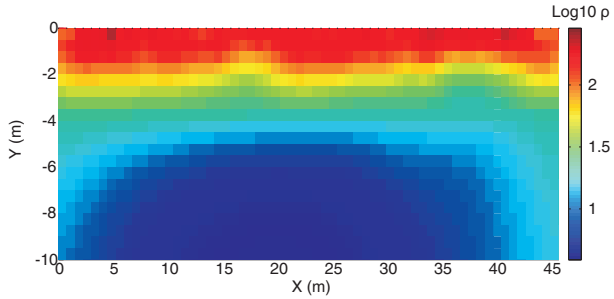

Figure 2.11: The inversion with a bad structural constraint located at $-3.2\ m$ is close to the smoothness constrained solution.

was not known, it would be very difficult to say where it was imposed. The solution is certainly not worse than the smoothness constrained solution. The data, in this case, are sufficiently informative to locate the clay at $-4.4\ m$ depth. However, without correct prior information, the clay is not extended towards the side of the section. Similarly, the saturated layer is imaged as a transition zone.

In contrast with a reference model whose effects were mainly apparent in zone of low sensitivity, the imposition of a structure may already be significant in zone of relative high sensitivity, as observed here for the limit unsaturated/saturated zones which lies at $-2\ m$ only, if it is coherent with the true resistivity structure.

2.4.3 Application on Westhoek site

The structural aspects of the Westhoek site influence the distribution of the salt water intrusion. Clearly, the role of clay lenses is crucial. They hinder the downward flow of sea water to favor its lateral extent.

GPR as well as seismic refraction data were acquired on the site to try to identify clearly the structure of the clay. Unfortunately, sea water being very conductive, electromagnetic wave are intensively attenuated and the depth of investigation of classical antennae (50 to 200 MHz) is not sufficient to reach the sand-clay limit. Concerning seismic refraction, the velocity contrast between sand and clay is not sufficient to be imaged clearly by a seismic refraction survey.

Therefore, we relied on the few borehole logs and EM conductivity logs before intrusion (figure 2.7, Hermans 2010) to delineate the top and the bottom of the clay layer and assumed a smooth transition between adjacent boreholes to infer the structure.

We have seen in section 2.3 that, for the Westhoek site, the use of homogeneous reference with a small closeness factor was really needed to obtain a reliable solution, imaging the sea water infiltrated in the aquifer and stopped by the clay layer. This solution is thus taken as the reference for comparison (figure 2.12A). First results, with only structural information gave very poor results, showing very few improvements compared to the smoothness constraint solution. We decided to try to use the structural constraint in addition to the homogeneous reference model with $\frac{\beta_x}{\beta_z} = 1000$. When the structure is added at the top of the clay, i.e. at the positions where sea water is hindered, visual results (figure 2.12B) are very close to figure 2.12A. However, when we look at results in P12 (figure 2.13), we see that a "double maximum" shape appears in the middle of the low resistive zone. This is not what is observed with EM conductivity logs and completely unexpected from a hydrogeological point of view, this is obviously related to the imposition of the structure.

The problem, here, is that we are imposing a structure based on the knowledge of the facies in the area. Clay lenses have a lower resistivity than sands and this approach would be correct, at least in its concept, without any sea water intrusion. The infiltrated sea water completely changes the context in the area. Clay acts as a barrier for vertical flow. In consequence, sea water, imaged as a low resistive body, is lying on the clay. This is a situation where two low resistive bodies are superimposed. The facies-based structure is not coherent with the electrical

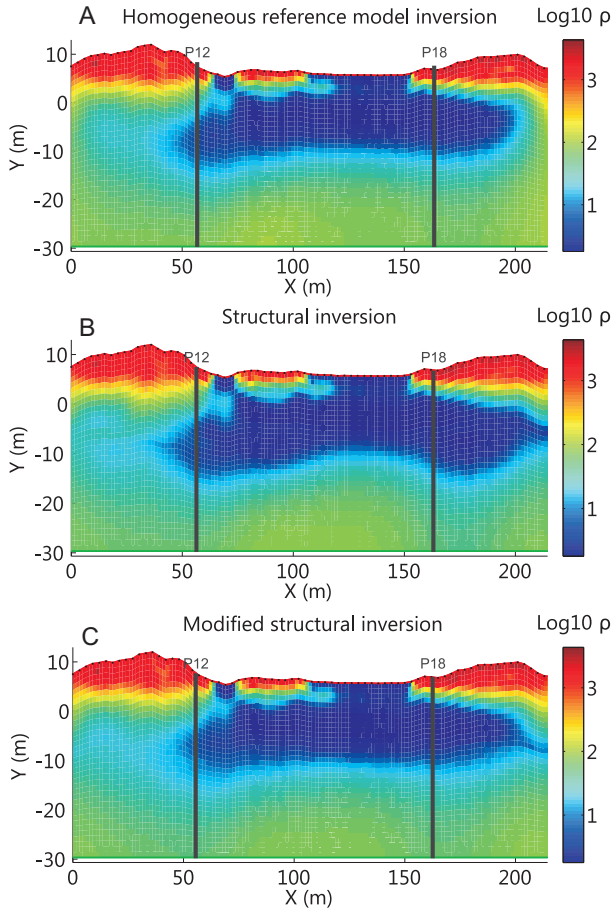

Figure 2.12: Inversions with structural constraints for Westhoek site. A) The homogeneous reference inversion was already an improvement compared to the smoothness constrained solution B) Adding a structural constraint at the supposed position of the top of the clay does not improve the solution. C) Positioning the structure at the bottom of the clay gives slightly more plausible results.

resistivity-based structure, and adding the structure at this position is not correct.

When the structure is added at the bottom of the clay (figure 2.12C), this facies-based structure is coherent with the expected resistivity structure. The "double maximum" is avoided. However, it does not really improve the results compared to the case without structure. Current flows preferentially in low resistive zones, the sensitivity drops sharply below the sea water intrusion (figure 2.8F). The reference model starts to play an important role at this depth, which corresponds to the depth of imposition of the structure. The addition of a structural constraint is thus not very efficient.

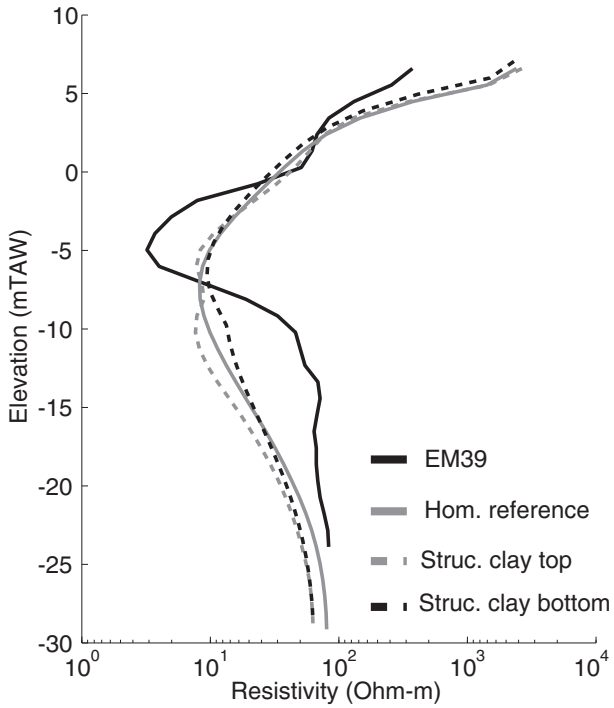

Figure 2.13: Comparison of the solution in the well P12. The solution with the structure of the clay gives a curious "double maximum" shape to the log which disappears when the structure is at the bottom of the clay.

2.5 The regularized geostatistical inversion

2.5.1 Mathematical formulation

When using the smoothness constraint operator, one makes the assumption that the solution of the problem will be the smoothest possible solution that explains the data. Therefore, this operator has a great influence everywhere in the section. Both the reference model inversion and the structural constraint keep this smoothing operator and use the same algorithm for inversion. The reference model adds an additional closeness term whereas the structural inversion modifies it locally. This produces changes in the inverted section either in low sensitivity zones or at the position of boundaries and can lead to significant improvements in the solution.

In the regularized geostatistical inversion, we replace the regularization operator ($\mathbf{W}_m$) by a model of covariance model parameter derived from an experimental variogram. The approach is similar to the work by Chasseriau and Chouteau (2003) for gravity data.

The idea behind the use of an experimental variogram is to base the inversion process on a regularization operator coming from hard data, i.e. data measured on the field by any relevant

method. Information about a parameter at one position is relevant to give a better estimate at another point if the distance between these two parameters is inferior to the correlation length or range of the variogram. This is typical spatial information that can be used to regularized a tomographic inversion.

In geostatistics, spatial parameters are considered as realization of random variables where one often has to assume stationarity in order to estimate these parameters. This hypothesis assumes that univariate and bivariate (and higher order) statistics of a variable Z are independent from the location x (Isaaks and Srivastava 1989). For a stationary process, the covariance function $C(h)$ and the variogram $\gamma(h)$, h being the lag, are known to be equivalent through

$$C(h) = C(0) - \gamma(h) \tag{2.26}$$

where $C(0)$ is the variance of the variable. It is not possible to demonstrate the stationarity of a field, since we only have access to one realization of the random function at any sampling location. This assumption is thus a decision of the operator.

The variogram can be estimated experimentally as

$$\gamma(h) = \frac{1}{2N(h)} \sum_{i=1}^{N(h)} [Z(x_i) - Z(x_i + h)]^2 \tag{2.27}$$

where $N(h)$ is the number of pairs separated by a distance $h \pm \Delta h$. The experimental variogram must then be modeled in order to have access to its value for each possible value of h. Several models exist and share two characteristic parameters: the range or correlation length a and the sill $C(0)$ (the value of the variogram at a distance equal to the range, it should be equal to the variance).

The most common models (equations 2.28) are the spherical, the exponential and the Gaussian models. The nugget effect model C_0 represents small scale variations and is often combined with other types of models.

$$\begin{array}{lll} \text{Spherical} & \gamma(h) = \begin{cases} C\left[1.5\frac{h}{a} - 0.5\left(\frac{h}{a}\right)^3\right] \; if \; h < a \\ C \; if \; h \geq a \end{cases} \\ \text{Exponential} & \gamma(h) = C\left[1 - e^{-3\left(\frac{h}{a}\right)}\right] \\ \text{Gaussian} & \gamma(h) = C\left[1 - e^{-3\left(\frac{h}{a}\right)^2}\right] \\ \text{Nugget Effect} & \gamma(h) = \begin{cases} 0 \; if \; h = 0 \\ C_0 \; if \; h > 0 \end{cases} \end{array} . \tag{2.28}$$

For geophysics, horizontal and vertical parameters are often considered as principal directions to estimate the variogram parameters. When the vertical a_v and horizontal a_h ranges are known, it is possible to calculate the range in a particular direction θ (θ being the angle between the line linking the two points and the horizontal) assuming that the principal ranges are ellipsoid axes

$$a(\theta) = \frac{a_h a_v}{(a_h^2 \sin^2\theta + a_v^2 \cos^2\theta)^{\frac{1}{2}}}. \tag{2.29}$$

For a couple of parameters, the value of the covariance can be calculated with equation 2.26, where the value of the variogram for the distance between the considered parameters is used using a fitted model (equations 2.28) with the range calculated with equation 2.29.

If the model has M parameters, the model covariance matrix C_m is a $M \times M$ matrix, where the element $C_{(m_i,m_j)}$ represents the covariance between parameters i and j. For elements far from each other, the value of the covariance tends to zero and the parameters are not correlated.

For the regularized geostatistical inversion, equation 2.17 becomes

$$\psi(\mathbf{m}) = \|\mathbf{W}_d\left(\mathbf{d} - f(\mathbf{m})\right)\|^2 + \lambda\|\mathbf{C}_m^{-0.5}\left(\mathbf{m} - \mathbf{m}_0\right)\|^2. \tag{2.30}$$

where $\mathbf{m}_0$ is a prior model. According to Tarantola (1987), it should be equal to the mean of the probability density function and thus should be homogeneous given the assumption of stationarity. Such a model can be used for the smoothness constraint inversion (equation 2.22, but a homogeneous reference model would have all gradients equal to zero, and would be without effect in the corresponding equation. If $\mathbf{m}_0$ is taken equal to zero, it means that there is a prior with mean resistivity value equal to 1 $Ohm.m$, since we are working with logarithm of model parameters. It should be noted that during the inversion process, only the inverse $\mathbf{C}_m^{-1}$ is needed.

Its calculation requires more CPU time than for a standard inversion.

At this point, it is important to note that in our mathematical formulation of the problem, the sill value has very little importance when no nugget effect is considered. Indeed, it can be seen from equations 2.28 that the sill is only a scaling parameter multiplying the equation defined by the model of variogram and the range. If the sill is constant in vertical and horizontal directions, what should be the case for a stationary field, the sill can be considered as a common factor for each element of the model covariance matrix. After factorization, this factor would simply be a scaling factor for the regularization operator λ. Changing the sill will mainly influence the value of λ at the end of the inversion process and not the solution.

The use of regularized geostatistical inversion requires to acquire some knowledge on the spatial distribution of the modeled geophysical parameter. Here, we need to have access to data about the electrical conductivity/resistivity of the subsurface. This type of data is quite specific and is not always possible to acquire. If wells with non-metallic casing are available on the site, a way to acquire such data is to carry out an EM conductivity log. This will provide a log of apparent conductivity. However, the characteristic volume investigated by an EM conductivity log is small compared to the volume of an inversion grid in ERT. EM conductivity log apparent resistivities may often directly be used to derive the vertical variogram characteristic of a study site.

Information on the horizontal range is much more difficult to acquire. In most cases, only a few wells are available on a study site, which is not enough to draw a reliable experimental variogram. A possibility is to carry out an EM conductivity survey from the surface. However, there is no guaranty that the corresponding range will be correct at depth. Most of the time, the horizontal range will remain an unknown of the problem.

To overcome this issue, we used a methodology to estimate the value of the horizontal range. First, we calculate the isotropic smoothness constrained solution. Since the process is isotropic, no prior information is introduced in the problem. Then, we calculate the horizontal and vertical experimental variograms on the inverted section, even if the ability of tomograms to derive geostatistical parameters is limited, due to their variable resolution (Day-Lewis and Lane 2004). Indeed, the sensitivity and resolution decrease with depth, leading to more homogeneous models at depth, which influences the value of the range of the variogram. Here, we model the

two variograms (horizontal and vertical) in parallel and deduced both horizontal and vertical ranges. From them, we derive an anisotropy ratio $\frac{a_h}{a_v}$. We expect the influence of the variable resolution to be smaller for the anisotropy ratio than for the absolute value of the ranges. This anisotropy ratio is used to multiply the vertical range derived from direct measurements in order to get the horizontal range that will be used during inversion.

Using a formulation of the problem as equation 2.30, where the regularization operator λ appears explicitly, the geostatistical parameters are not imposed during the optimization process. The algorithm of inversion is run imposing the ranges as a soft constraint rather than a strong constraint. This allows for uncertainty in the determination of the ranges.

In theory, the geostatistical parameters can be defined for each cell of the model separately in the implementation. This makes little sense in practice. Nevertheless, this feature enables to define variable variogram parameters in case of non-stationarity, i.e. when at least two zones have different geostatistical parameters. In those cases, no correlation is assumed between the zones, leading to possible discontinuities in the resistivity distribution. This is not a problem when the user knows this particularity and could be avoided if non-stationary covariance matrix were used (Paciorek and Schervish 2006). This allows the combination of geostatistical inversion and "disconnected" inversion or structural constraint.

2.5.2 Application on Ghent site

On Ghent site, an EM conductivity log is available in the well located in the middle of the section (figure 2.3). A variogram was calculated and modeled using a spherical model (equation 2.28) with a sill equal to 0.05 and a vertical range a_v equal to 2.4 m (figure 2.14). The variogram was calculated on the logarithm of resistivity, since this is the parameter we invert for in ERT. The cyclicity observed in the experimental variogram may be related to the layered structure of sand and clay in the subsurface. The anisotropy ratio was calculated using an isotropic smoothness constraint inversion, giving a value of 5 (horizontal range equal to 12 m).

These values were used to calculate the covariance matrix. For a fair comparison, we also computed the anistropic smoothness constraint with an anisotropy ratio $\frac{\beta_x}{\beta_z} = 5$. We see that there is almost no difference between isotropic (figure 2.15A) and anisotropic smoothness constraint (2.15B). The upper part of the model is almost similar, a few changes appear in the

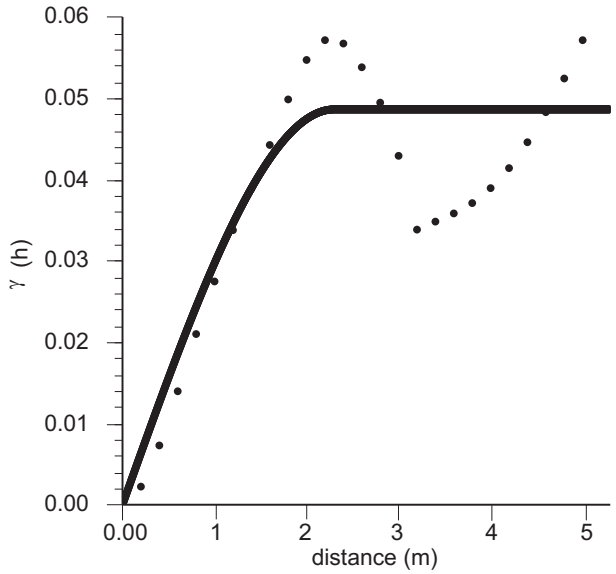

Figure 2.14: The experimental vertical variogram of the Ghent site is modeled using a spherical variogram with sill equal to 0.05 and range equal to 2.4 m.

clay zone which is slightly more extended towards the side of the section. This shows that an anisotropic smoothness constraint can be considered as the weakest form of prior information.

The geostatistical inversion (figure 2.15C) was run with a prior model equal to 10 $Ohm.m$. It displays an almost homogeneous and horizontal unsaturated zone. However, the saturated sand and the sand/clay limits are not imaged as expected, with quite strong lateral heterogeneity. It must be understood that the role of the geostatistical constraint is not to impose the thickness of the layer, but to impose a correlation length between parameters. Nothing in the constraint imposes that it represents a layered structure. In this specific case, this solution does not seem satisfactory compared to the structural inversion (figure 2.10D), but is at least as "good" as the smoothness constraint solution.

Since the uncertainty on the horizontal range is high, we tried to increase its value to 24 m. Such a high value could be justified by the fact that we know that the field is quite homogeneous laterally. It corresponds also approximately to half the length of the profile, which is considered as the highest possible value of the range that can be reliably assessed for a site. Doing so (figure 2.15D), the features of figure 2.15C are still apparent, but are more elongated in the horizontal directions. Consequently, the solution appears more laterally layered.

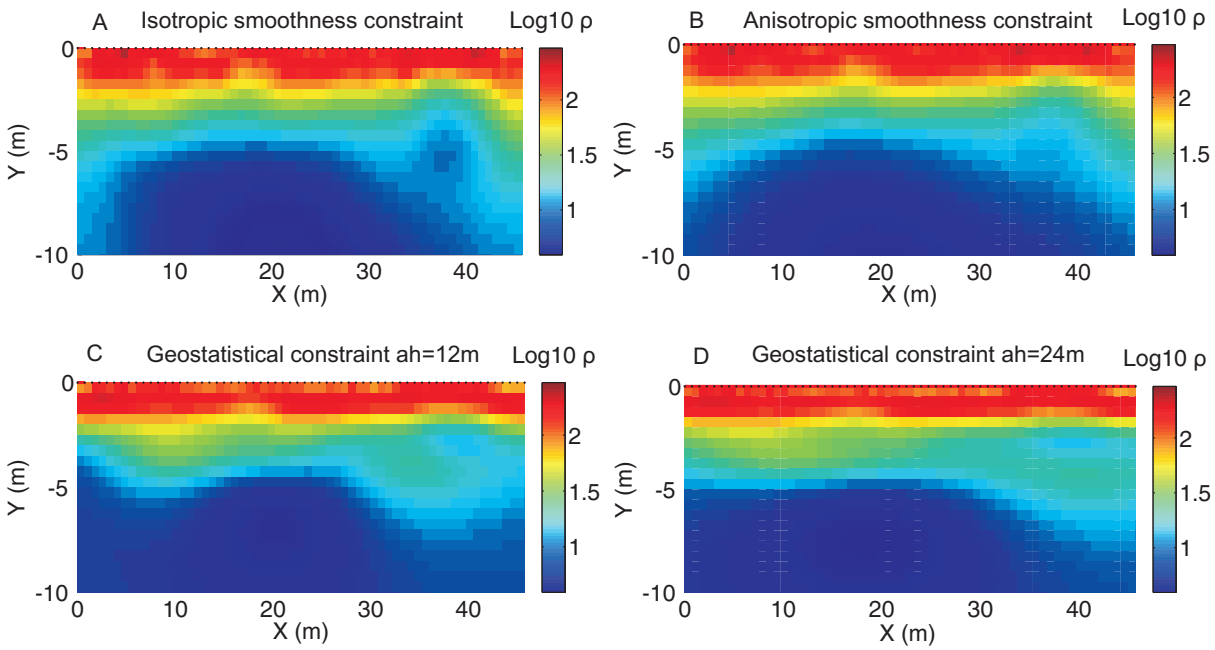

Figure 2.15: The isotropic (A) and anisotropic (B) smoothness constraint solutions are almost completely similar. The geostatistical inversion (C) fails to reproduce the layered structure of the sand/clay limit. (D) When the horizontal range is increased, the solution displays more lateral homogeneity, more in accordance with the layered structure.

2.5.3 Application on Westhoek site

In the Westhoek site, several boreholes are available to measure EM conductivity logs and to derive geostatistical parameters. A global variogram (i.e. including all boreholes) was computed and modeled using a Gaussian model with a sill value $C(0) = 0.37$ and a range $a_v = 8.4\ m$ (figure 2.16). The cyclicity observed for the experimental variogram is likely related to the expected layered structure of the clay and sea water infiltration in the subsurface. We do not expect many effects in the results neglecting this hole effect, since it is limited to less than 20% of the variance.

As for the Ghent site, an anisotropy ratio $\frac{a_h}{a_v} = 4$ was determined from an isotropic smoothness constraint solution. This ratio was used to derive the horizontal range for the Westhoek site $a_h = 33.6\ m$. Note that this anisotropy ratio was also used to calculate the smoothness constraint solution in figures 2.8. However, as for the structural constraint, we will directly compare the geostatistical solution with the smoothness constrained solution with a reference homogeneous model (figure 2.17A).

For a fair comparison, we chose the same value of 100 $Ohm.m$ for the homogeneous prior

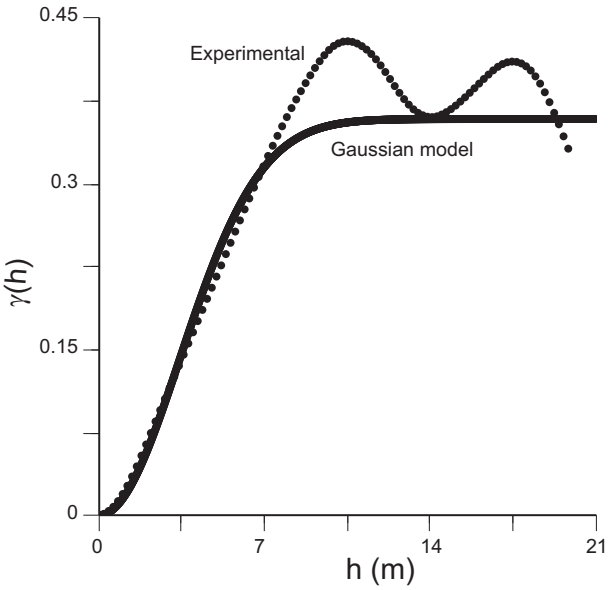

Figure 2.16: The vertical experimental variogram for the Westhoek site can be modeled using a Gaussian model with a sill value $C(0) = 0.37$ and a range $a_v = 8.4\ m$.

model in the regularized geostatistical inversion (figure 2.17B). The comparison in P12 (figure 2.18) clearly shows that imposing correlation lengths, at least in the vertical direction, clearly improves the solution. There is still an error in the position of the minimum which is imaged slightly too deep, but the amplitude is now correctly approached. In contrast with good results obtained for the reference model inversion (figure 2.8) for which the distribution observed in boreholes was extended to the whole section as a quite strong constraint, here we only impose a correlation length, i.e. the resistivity values observed in P12 are not used at all in the inversion.

The comparison of the solutions of figure 2.17A and 2.17B shows the impact of imposing a correlation length instead of smoothing, without the influence of the reference model. It clearly appears that the constraint has an effect everywhere in the section, since the thickness of the sea water intrusion is limited everywhere in the section. However, it does not act like a structural inversion, it thus enables lateral variations in the depth of the low resistive zone, as it was also observed for the Ghent site. The regularized geostatistical constraint does appear both as a conservative way to impose prior information, since it does not require too precise details on the model parameters, and as a strong constraint (just like the smoothness constraint), since it will influence the whole section.

The role of the vertical range is already illustrated with the previous example. The horizontal

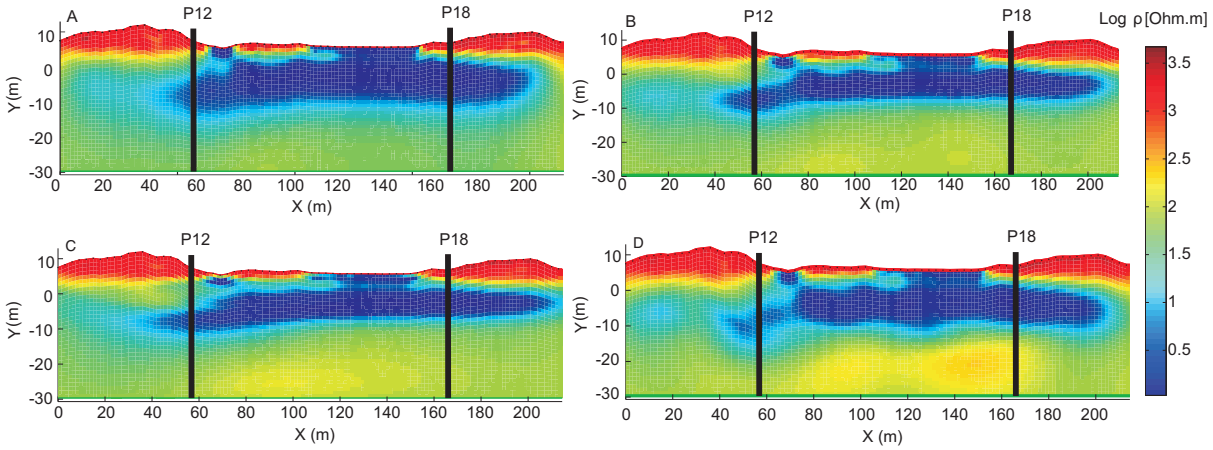

Figure 2.17: Geostatistical inversions for the Westhoek site. A) The smoothness constrained solution with reference model already improves significantly the results. B) The geostatistical inversion yields a more plausible solution with sea water stopped above the clay. C) Multiplying the horizontal range by two has a lower impact on the solution than D) multiplying the vertical range by two, which modifies strongly the sea water distribution.

range is an unknown of the problem. If we assume that the anisotropy ratio is equal to 8 instead of 4 and that we keep the same vertical range, the solution does not differ very much (figure 2.17C). The sides of the intrusion are just slightly more elongated. This is confirmed by the comparison of results in P12, where the two solutions are very close to each other. In contrary, when the vertical range is multiplied by 2 (and the horizontal range remains 33.6 m), the solution is quite different (figure 2.17D), closer to the smoothness constraint with a homogeneous reference model. As a consequence, the geostatistical inversion may be applied when the horizontal range is unknown, but it seems unrealistic to use it when the vertical range cannot be computed.

If we compute the variogram for the inverted model of figure 2.17B, we obtain a vertical range close to the one deduced from borehole data, around 9 m (figure 2.19); this observation shows the ability of the *a priori* model covariance matrix to impose the correct statistical characteristics vertically. At the opposite, the horizontal range from the experimental variogram is very large (around 70 m) compared to the prior assumption (33.6 m), which further indicates the stratified nature of the area. Again, the latter observation may be linked to the sensitivity patterns of ERT (figure 2.8F). We assume that the inversion could recover the horizontal range (which is unknown in our study case) if, for a same depth, sensitivity is laterally constant. Thus, prior information would be less important in this direction than vertically, since the sensitivity decreases with depth. This hypothesis is supported by the results obtained by modifying the horizontal and

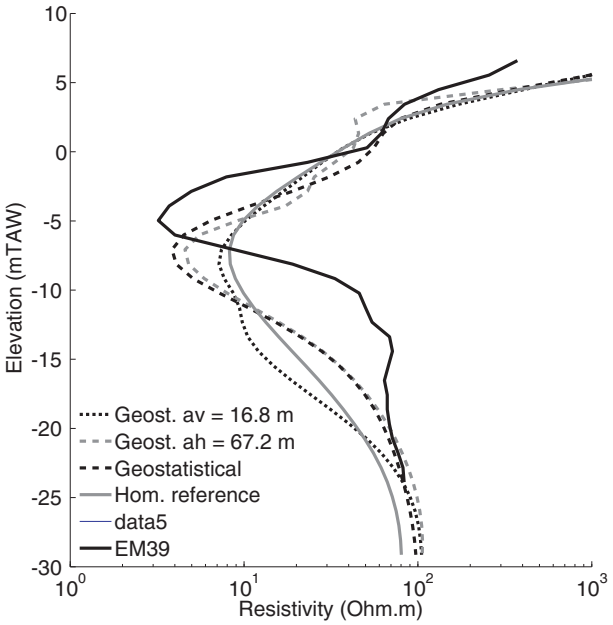

Figure 2.18: Comparison of the solution in the well P12. The geostatistical solutions with the correct vertical range are clearly the ones that fit the best the EM conductivity logs.

vertical ranges, as we see that the latter change has more impact on the solution.

The sill value is also slightly higher (around 0.5) than expected from borehole measurements (0.37, figure 2.16). A possible explanation is the high resistivity values observed close to the surface correlated with unsaturated sand of the dunes. The position of the boreholes is such that they are almost out of the zone of high resistivity, it is thus not significantly affecting the borehole data leading to a wider range of conductivity in ERT results, and consequently to higher variances.

As pointed out in the mathematical formulation, the implementation of the geostatistical inversion allows uncertainty in the imposed parameters. Through the regularization parameter λ, a balance exists between data and model misfits. If the data indicates more correlation than expected, the model is allowed to diverge from the imposed parameters. Johnson et al. (2007) also defined a degree of certainty for their variogram model. However, in our case, we have an error estimated (the true horizontal correlation length is unknown) at about 100%, which is very high.

The error in the horizontal variogram is not a critical issue. This was already observed by other authors. Indeed, Hansen et al. (2006) found in their synthetic study using sequential simulations that if longer or shorter ranges were imposed in the inversion process, the ranges

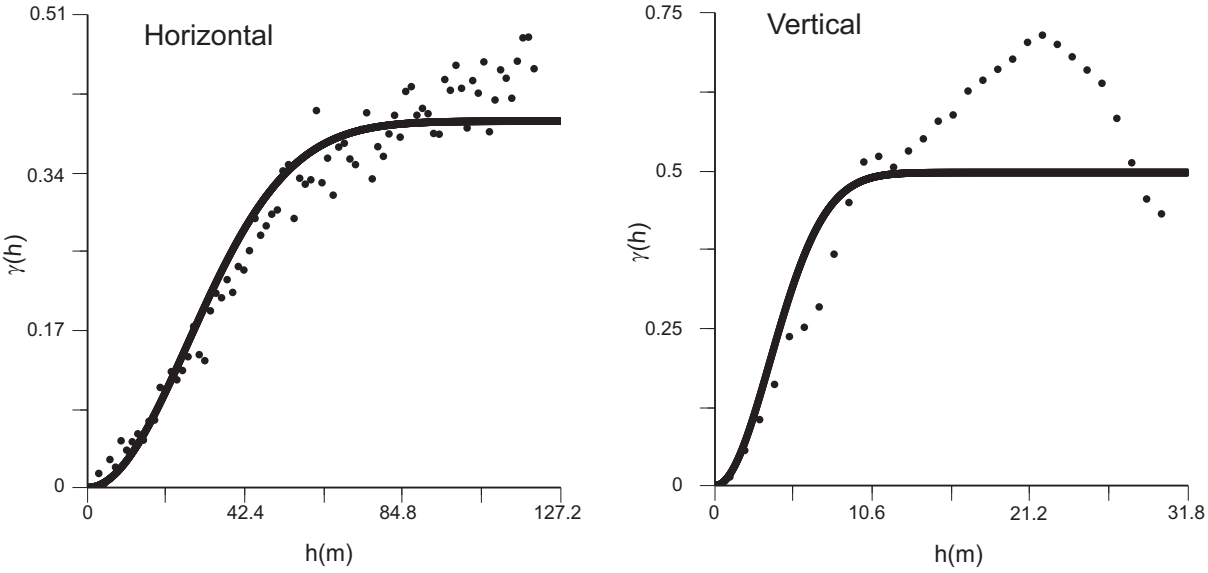

Figure 2.19: Variogram computed from the regularized geostatistical solution. The vertical range is close to the one from borehole, the horizontal range is quite different.

calculated on the solution tended to be closer to the true ones than to the imposed ones. Yeh and Liu (2000) also discussed that their geostatistical inverse method within the context of hydraulic tomography was not very sensitive to correlation lengths except for large uncertainty altering the direction of anisotropy. They relate this observation to the fact that correlation length provides an estimate of the average size of heterogeneity. Its impact diminishes when more measurements are available. We observed a similar behavior in the inversion of our field data.

A difficulty in using variogram or $\mathbf{C}_m$ formulation is to deal with the non-stationarity of the imaged field. The Westhoek study site is located at the border between the dunes and the beach where the electrical resistivity fields are different. In the dune area, there is salt water coming from former infiltration during very high tides or storm events (Vandenbohede et al. 2008). Under the beach, the salt water lens arises from the recharge of salt water on the back shore during high tides, twice a day (Lebbe 1999). These two different phenomena result in two different conductivity distributions and thus to different geostatistical parameters.

The profile shown in figure 2.17 is located within the dune area only. Another ERT profile was crossing both the dune and the beach areas (figure 2.20). The first inversion is the result using the same geostatistical parameters as for the previous case, i.e. parameters related to the dune area (figure 2.20A). These parameters underestimate the correlation lengths under the

beach area, where sea water is found on a bigger thickness. Therefore, the depth of the salt-fresh water transition is underestimated. It is found around $-5\ mTAW$, whereas Lebbe (1999) found with borehole conductivity measurements a depth of about $-10\ mTAW$.

In a second inversion (figure 2.20B), we modified the geostatistical parameters under the beach area, assuming a vertical range of 15 m and a horizontal range of 40 m, and kept the previous parameters in the dune area. The different ranges result from the different infiltration schemes on both zones. The two zones are completely disconnected, i.e. for parameters lying in different zones, the variogram is assumed to be equal to the sill value (no correlation, the covariance is equal to zero). In consequence, we observed a discontinuity where the zones are adjacent. This is an artifact of inversion resulting from the arbitrary limit between these two zones. This could be avoided if a non-stationary covariance matrix was used (Paciorek and Schervish 2006). Due to the higher correlation length used under the beach area, the solution is modified in this part of the profile and the salt-fresh water transition reaches a depth closer to the expected one. This further illustrates the role of prior information to resolve low sensitivity parts of ERT profiles. In contrary, the results for the dunes are almost exactly the same. This solution (figure 2.20B) images appropriately both zones of the profile. Only the area around the limit must not be interpreted.

2.6 Application to the site of Hermalle-sous-Argenteau

In this section, the site will first be described, then, the methodologies to incorporate prior information in the inversion of ERT will be applied. The aim of ERT in Hermalle-sous-Argenteau is to image the contrasts of resistivity that are caused by the heterogeneity of the facies in the alluvial deposits. In chapters 3 and 4, the link between electrical resistivity and the facies distribution will be investigated. This is necessary to use resistivity as a soft constraint to build geostatistical models of the aquifer with multiple-point statistics. In this section, we will focus on the improvement of ERT to better image alluvial deposits.

2.6.1 Localisation and Geology of the site

The field site of Hermalle-sous-Argenteau is a meadow located in the alluvial plain of the Meuse River, 15 km north of the city of Liege, near the Dutch-Belgian boarder (figure 2.21).

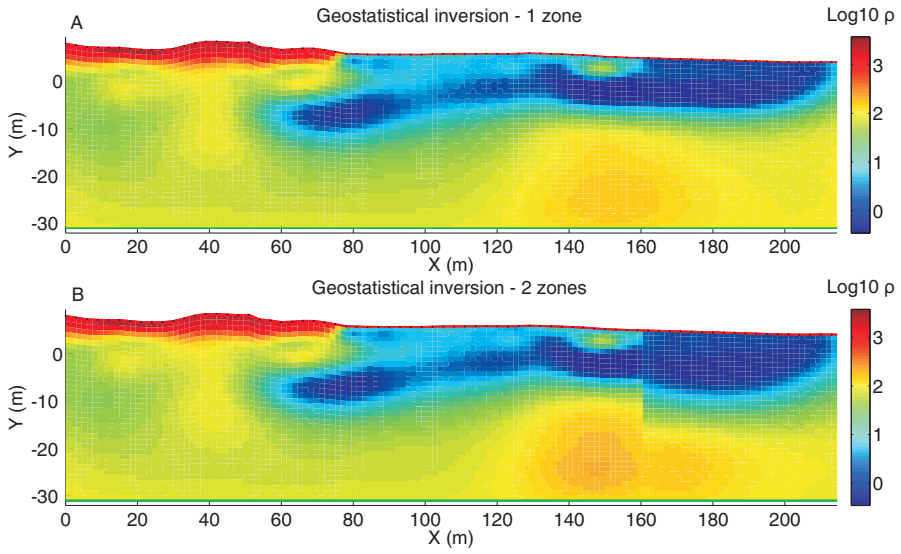

Figure 2.20: Inversions of a profile crossing both the dunes and the beach. A) The solution with the variogram parameters of the dunes underestimates the intrusion of sea water under the beach. B) With respective variogram parameters on each zone, the solution is disconnected, but the intrusion is correctly images on both zones.

This site is owned by the Walloon Region and is managed by the "Port autonome the Liege" (Autonomous Liege Harbor). The site is located between the Meuse River and the Albert Canal, about 300 m of the Meuse River and 500 m of the canal. The field site was first equipped with one well and eight piezometers to study the hydrodynamic characteristics of the alluvial aquifer (report LGIH MTP/901 1990). After the development of the Trilogiport project and the construction of a embankment to delimit the site, two of the eight piezometers were lost (figure 2.22).

Recently, in June 2012, the hydrogeology unit of the University of Liege installed 12 new piezometers upstream from the existing well. They are arranged as three control panels to perform tracer tests and study the flow and transport parameters of the alluvial aquifer (figure 2.22). Two additional piezometers were drilled in May 2013.

The bedrock of the Meuse Valley in the area of Hermalle-sous-Argenteau is composed of Visean and Houiller formations from the Paleozoic era. During the Quaternary period, the Meuse River has eroded the bedrock and has shaped alluvial deposits. More details on the general geology of the area can be found in Haddouchi (1987) and in Brouyère (2001).

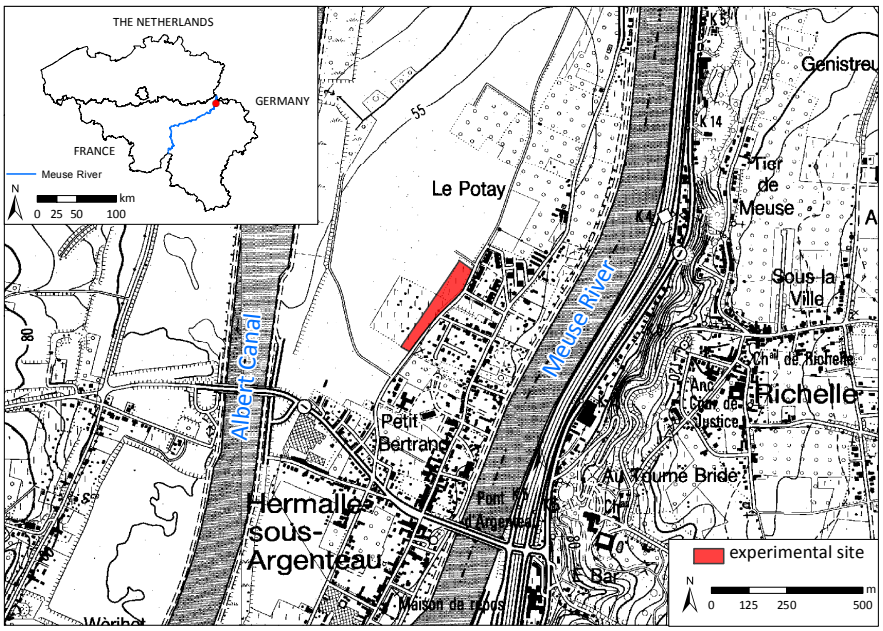

Figure 2.21: Localisation of the site of Hermalle-sous-Argenteau near the Dutch-Belgian boarder.

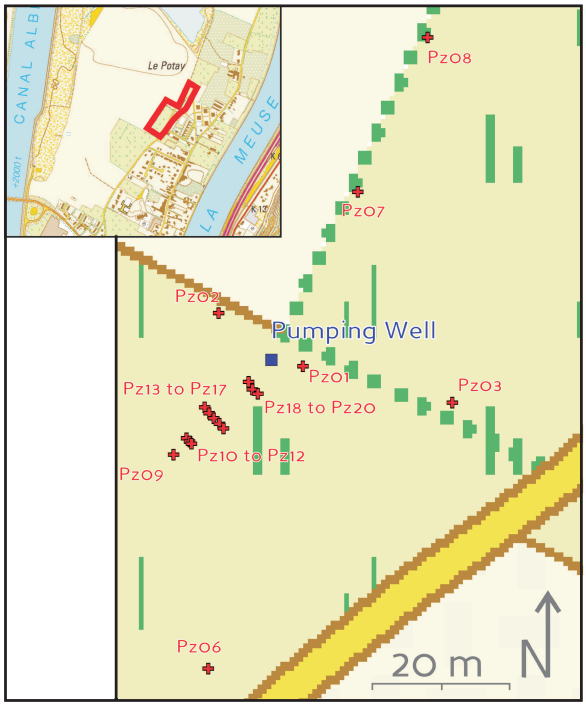

Figure 2.22: Localisation of the piezometers on the site of Hermalle-sous-Argenteau.

2.6.2 Prior knowledge available on the site

As stated in section 2.2, every piece of information concerning the geology and the hydrogeology of a specific site that may influence the distribution of geophysical parameters in the subsurface may be used as prior information and incorporated in the inversion of ERT data. In this specific case, we can distinguish mainly four types of prior information:

- borehole logs which indicate the nature of the sediments and the depth of the bedrock;
- piezometric levels which indicate the depth of the saturated zone;
- EM conductivity logs which give a local insight on the vertical electrical resistivity distribution;
- seismic refraction data sets which identify refractors, related to water table, layer transition and bedrock, but with large uncertainty and poor lateral resolution.

These four types of information may content information on the electrical resistivity distribution:

- the nature of the sediment influences its electrical resistivity, clayey and loamy sediments are less resistive than sandy and gravel sediments;
- below the water level, sediments are saturated and the resistivity is expected to decrease;
- EM conductivity logs can be used to derive a reference model or a variogram and to control the quality of inversion;
- seismic refraction models can be incorporated as structural constraints if the structure of resistivity is assumed similar to p-wave velocity structure.

All the borehole logs on the site show a similar transition between layers (table 2.1). Backfills are barely present on the site, some fragments of brick are found in the first 20 cm, but not in large quantities. The first meters are composed of brown loam, 0.5 to 4.5 m thick. Below, gravels are found in a loamy to sandy-loamy matrix. The thickness of this layer vary from 0.5 to 4 m. Above the bedrock lies a layer with millimetric to pluricentimetric alluvial gravel in a sandy matrix. For the new set of boreholes, the size of the gravels seems to increase with

Borehole	Bottom of loam (m)	Bottom of loamy gravel (m)	Bedrock depth (m)
Well	1	2	11
Pz1	0.5	3	11.5
Pz2	1	4	10
Pz3	3.5	4.5	10
Pz4	1	1.5	11
Pz5	1.5	2	9.5
Pz6	0.5	5	10
Pz7	4.5	5	9.5
Pz8	3	4	10.25
Pz9	1.3	2	10
Pz10	1.2	2.5	10
Pz11	1.2	2.3	9.9
Pz12	1.2	2	10.1
Pz13	1.4	3.2	10
Pz14	1.5	2.6	10
Pz15	1.5	2.2	9.9
Pz16	1.4	2.4	9.8
Pz17	1.4	2.4	9.8
Pz18	1.4	2.5	10
Pz19	1	2.5	9.8
Pz20	1	3	9.7
Pz21	1.2	2	> 6
Pz22	0.5	2.2	> 7

Table 2.1: Description of boreholes in Hermalle-sous-Argenteau.

depth whereas the amount of matrix decreases. The bedrock is composed of Houiller schists and lies between 9.5 and 11.5 m. Above the bedrock, there is often an altered bedrock layer mixed with gravels. However, it is important to note that it is very difficult to distinguish between the various facies of alluvial deposits.

The water level on the site is found approximately 3 m below the surface. A high precision (more than 0.5 m) cannot be obtained from ERT only given its limited precision. A small gradient is oriented from the south-west towards the north-east, in a direction almost parallel to the Meuse River.

EM conductivity logs were carried out in the oldest available piezometers with an EM39 device (McNeill 1986). This data gives an overview of the resistivity distribution on the site and can be used to deduce a vertical correlation length on the site. The design of the EM39 is such that it measures the conductivity with a vertical resolution of about 65 cm. The lateral sensitivity is low for the first 15 cm from the axis of the device. So measurements are not too much influenced by the equipment of the piezometer. The sensitivity is also quite low further than 1 m from the axis of the device. Details on the device may be found in McNeill (1986). The new piezometers (except for Pz9) being close to each other in the panels, the drilling process

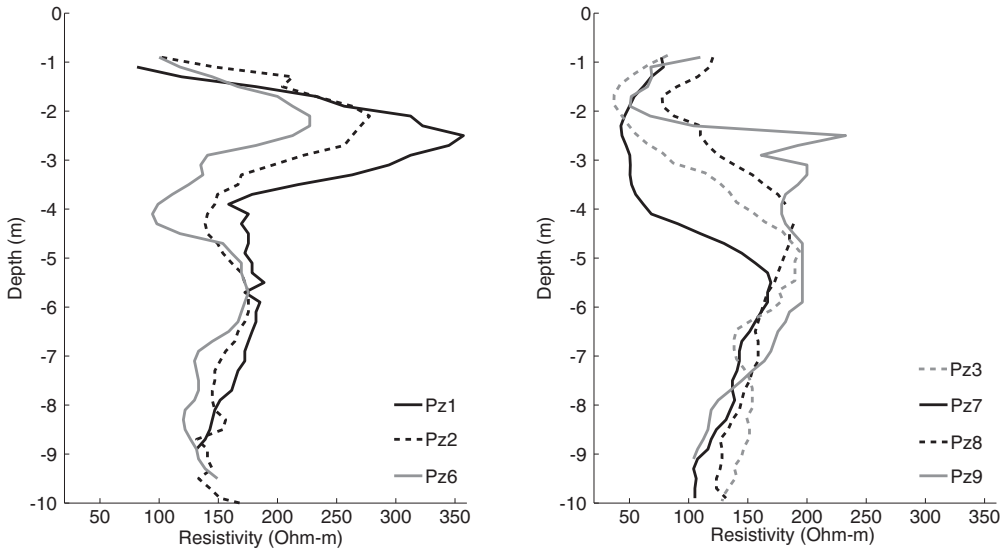

Figure 2.23: The EM conductivity logs in the boreholes show two distinct behavior according to the thickness of the loam layer.

and their equipment may influence measurements, leading to poorer data for these piezometers.

We can group EM conductivity logs in two different categories. Pz1, Pz2 and Pz6 show first an increase in resistivity up to 200 to 350 $Ohm.m$, followed by a decrease in resistivity below the water level. Note that the higher resistivities are likely dependent on the degree of saturation of the subsurface and may vary with time. The contrast between saturated and unsaturated zone is not sharp because a measurement was taken every 20 cm, which is lower than the vertical resolution of the device. In contrast, Pz3, Pz7, Pz8 and Pz9 show first value of resistivity below 100 $Ohm.m$. This is correlated with the thickness of loam at the surface, which is higher than 3 m, except for Pz9 for which we observe low resistivity value only between 1 and 2 m depth. For the saturated part of the subsurface, the distribution of resistivity vary slightly for the different boreholes, but with resistivity values ranging everywhere between 100 and 200 $Ohm.m$.

At this stage, it may be difficult to relate directly the observed resistivity with the different facies. Clearly, loamy and clayey will have a low resistive signature due to the presence of minerals with a non-negligible surface conductivity. For sandy and gravel facies, it is more difficult to discriminate because the accuracy of the description of the borehole is limited; they were drilled with a down-the-hole hammer and representative samples could not be taken. The apparent homogeneity observed in the description may be misleading. Coarse gravel facies may

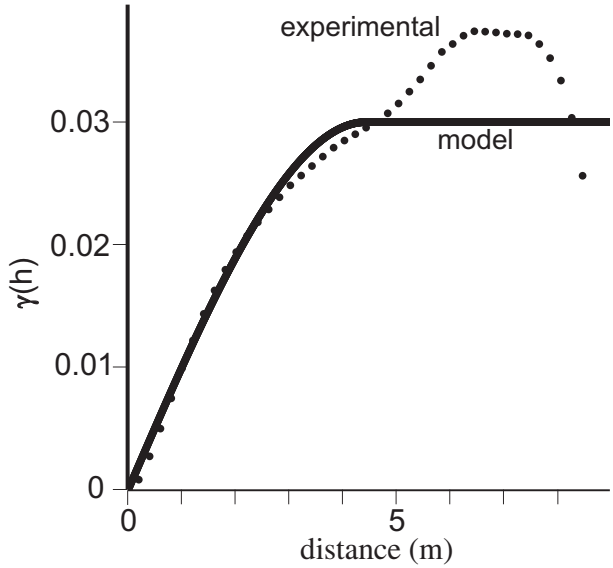

Figure 2.24: The EM conductivity logs in the boreholes were used to calculate the vertical variogram characteristic of the study site. The best fit is obtained for a spherical model with a sill equal to 0.03 and a range equal to 4.4 m.

have a higher resistivity linked to the lack of fine sediments with surface conductivity, but could also have a lower resistivity due to a higher water content. In the literature, higher resistivity values in alluvial aquifer are generally assimilated to gravel facies, with values ranging from 200 to 500 $Ohm.m$ (e.g. Bersezio et al. 2007, Doetsch et al. 2010b). A detailed comparison of resistivity values and facies is provided in chapter 4. It shows that clean gravels have a lower resistivity than sandy gravels in Hermalle-sous-Argenteau.

Based on the EM conductivity logs collected on the site of Hermalle-sous-Argenteau, a vertical variogram was computed (figure 2.24). To fit a model, we kept the sill value equal to the variance (0.03) of the logarithm of resistivities. The best fit is obtained for a spherical model with a range of 4.4 m. This is half of the maximum thickness investigated with the EM conductivity logs and thus the maximum value that could be derived using a variogram. The analysis of first ERT profiles inverted with the smoothness constrained inversion gave an anisotropy ratio of 2.5 to derive the horizontal range.

Seismic refraction surveys were carried out on the site in a systematic way. Details on the method can be found in Telford et al. (1990). Typically, three layers are detected. The first refraction occurs at the water level. In soft sediments like alluvial sediments, the seismic velocity of P-waves is generally lower than the velocity in water, so the water level is detected as the first refraction. A second refraction is observed at the position of the bedrock, i.e. between 10

and 12 m depth. Several profiles show a slightly variable position of the bedrock which is not horizontal, so the bedrock is not flat on the site.

An example of profile is given on figure 2.25. It was acquired using 24 10 Hz geophones with 3 m spacing. The first geophone was located near the well and the profile was in a SW-NE direction (figure 2.22). Three shots were done, at the beginning, the middle and the end of the profile. The first refraction is very clear and visible for each shot, it happens at about 22 ms, corresponding to a horizontal limit, the water level, slightly below 3 m depth. The first layer has a P-wave seismic velocity between 400 and 500 m/s, coherent with soft alluvial deposits (loams, sands and gravels). The second limit is more difficult to represent and more uncertainty is associated with it. However, it is not possible to explain the arrival time without a second refraction. From the interpretation of figure 2.25, the limit is found after 34 ms between 10 and 12 m depth, with a deeper interface at the end of the profile. The second layer corresponds to saturated alluvial deposits, velocities around 2100 m/s are also coherent. The bedrock appears to have a velocity of about 4000 m/s, which is quite high for schist potentially altered, but not impossible.

In addition to those data, a few 200 MHz GPR profiles are available on the site. However, given the relative high electrical conductivity of superficial loam (figure 2.23), the depth of investigation is limited and the profiles do not give interesting information for the saturated alluvial deposits. EM conductivity measurements from EM38 device are also available on the area, they provide an insight on the electrical resistivity of the near-surface layer, which is almost homogeneous.

2.6.3 Incorporation of prior information

In this section, we will analyze how we can improve the solution of ERT inversion in the case of the Hermalle site by incorporating prior information. To have some control on the results, we will compare the solutions on a profile crossing two boreholes with EM conductivity measurements, namely Pz3 which is located at 60.5 m from the beginning of the profile and Pz6, located at 112.5 m. The profile was collected using a dipole-dipole configuration with $n \leq 6$ and $a \leq 9$, using an electrode spacing of 2 m. Error was assessed using reciprocal measurements and a linear envelope model $e = 0.002 + 0.0026R$ was used.

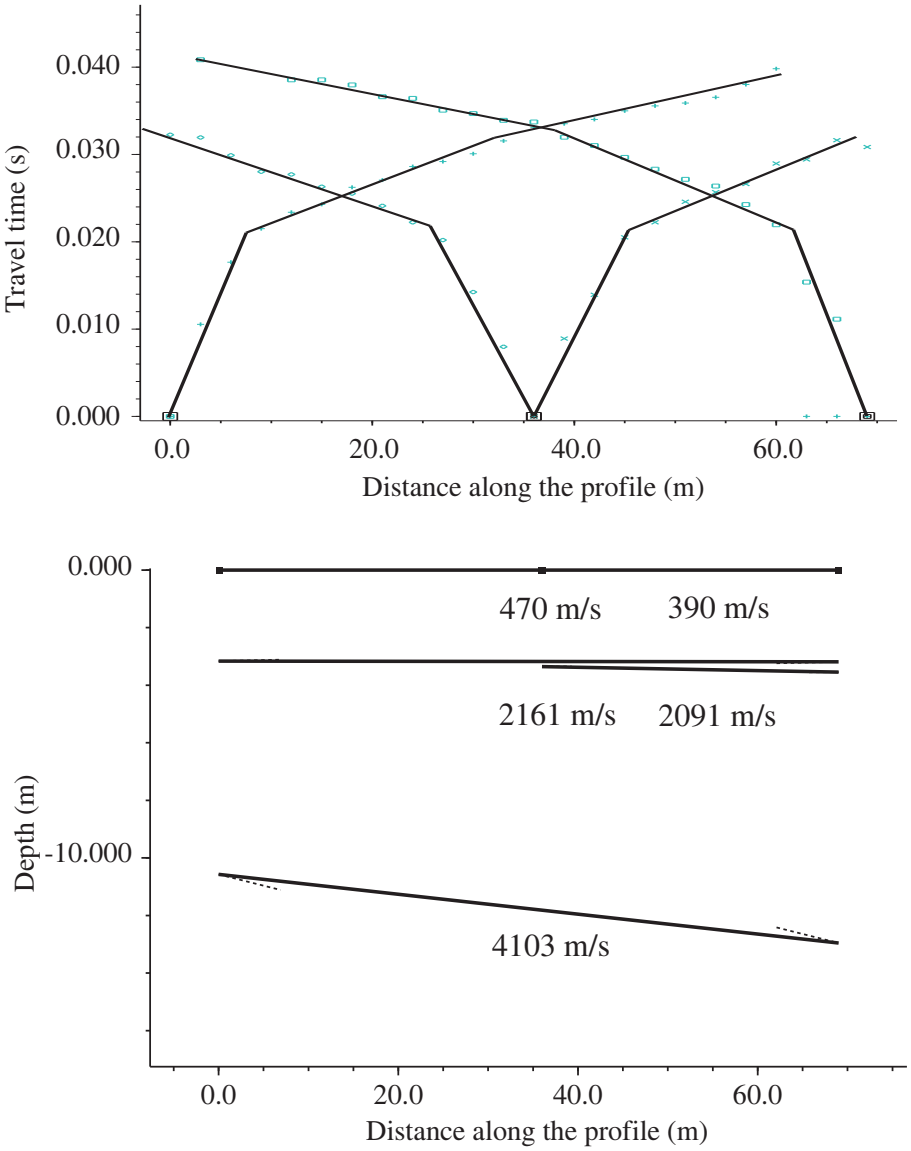

Figure 2.25: The time-distance curve for a profile of seismic refraction shows two refractions corresponding to a three-layer model.

2.6.3.1 Analysis of prior information in terms of resistivity distribution

From prior information, we can expect several features in the resistivity distribution that will be obtained after inversion. First, a layer of relatively low resistivity ($< 100\ Ohm.m$) corresponding to superficial loam deposits. Its thickness may vary from 0.5 to 4.5 m. When this layer is thin, it may not appear as clearly in the ERT section given the electrode spacing needed to reach the bedrock (1.5 to 2 m). When the thickness of loam is smaller than 3 m, an increase of resistivity should be observed in the unsaturated zone, followed by a decrease in the saturated zone where the resistivity should vary between 100 and 250 $Ohm.m$. Below 10 m depth, the bedrock should appear as a more resistive zone, given the decrease of water content in the rock compared to alluvial deposits. However, schist is altered in clay and fractures may occur in the upper part of the bedrock, making the contrast possibly less sharp than expected.

The use of a reference model whose value are not in the range of the true model, as done in Ghent (figure 2.4D), taught us that the data were able to overcome the erroneous information brought by inversion constraints where the sensitivity is sufficient. In those cases, results of inversion may indicate that a structure not coherent with prior constraint is effectively present on the site. This process may be considered as similar to the calculation of the DOI index (Oldenburg and Li 1999). We applied this methodology on the studied profile; it was inverted using the regularized geostatistical inversion, but a prior model $\mathbf{m}_0 = 1\ Ohm.m$ not coherent with expected resistivity was used (figure 2.26). Such a low value of resistivity is not encountered in such environment. We know that the inversion may be polluted by artifacts of inversion, but despite the very low resistivity imposed, a high resistive laterally homogeneous layer appears at the bottom part of the model. Without interpreting its resistivity and its precise location, this constitutes a strong indication that the bedrock is more resistive than the underlying deposits and that the electrode spacing used is sufficient to reach this depth. Indeed, if this structure is recovered after inversion, it means that it is needed to explain the data. Similarly, there is a lateral heterogeneity in alluvial deposits, with thicker loam deposits in the first part of the profile. Deposits in the bottom part of the alluvial aquifer seem to be, on average, less resistive than in the upper part. These observations must be confirmed by appropriated inversions, but they legitimate the extensions of independent prior information to the inverse ERT problem. For example, it suggests that the bedrock limit detected with seismic refraction is coherent with

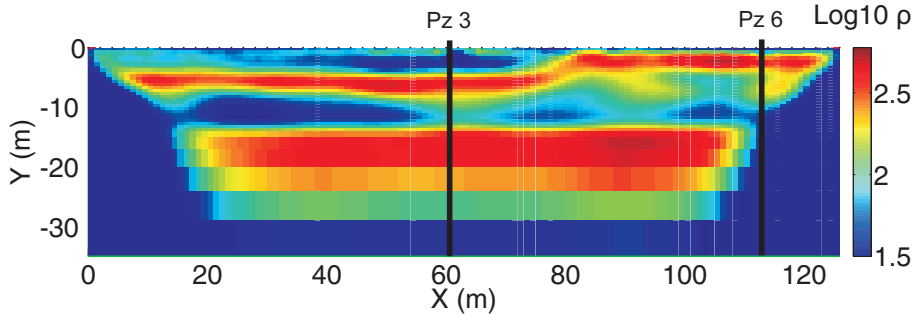

Figure 2.26: The regularized geostatistical inversion with a bad prior model highlights some structures in the resistivity distribution such as the higher resistivity of the bedrock.

a structure in the resistivity distribution.

2.6.3.2 Application of prior information on the studied profile

The site of Hermalle-sous-Argenteau is quite rich in terms of prior information and many possibilities exist to incorporate and mix the different sources of information. Many attempts were made in order to get the best possible solution. Of course, the choice of the best solution remains subjective and may partly vary from one person to another. When dealing with real field data, the misfit of the model is unknown and we have to rely on our interpretation and knowledge of the geological context to decide. Here, we will summarize our results (figure 2.27) which we believe are representative of the problem of incorporating prior information and are sufficient to decide what could be the best solution. The main argument will be the comparison with EM conductivity logs in Pz3 (figure 2.28).

The first inversion that was carried out and used as a reference is the smoothness constraint inversion (figure 2.27A). As observed in figure 2.26, the resistivity distribution is not homogeneous on the profile. As expected from boreholes, the loam layer is thicker in the northern part of the profile, leading to a low resistive body. Towards the end of the profile, the loam layer is very thin and barely appears in the solution. Below the loam, resistivity globally increases but lateral heterogeneities are clearly visible. From figure 2.28A, it appears that this constraint is not able to reproduce the shape of the vertical resistivity distribution. After the minimum which is correctly imaged, there is a progressive increase in resistivity towards a constant value of about 300 $Ohm.m$. If an anisotropy ratio of 2.5 is used, the solution (figure 2.27B) is only slightly affected and no improvement is observed.

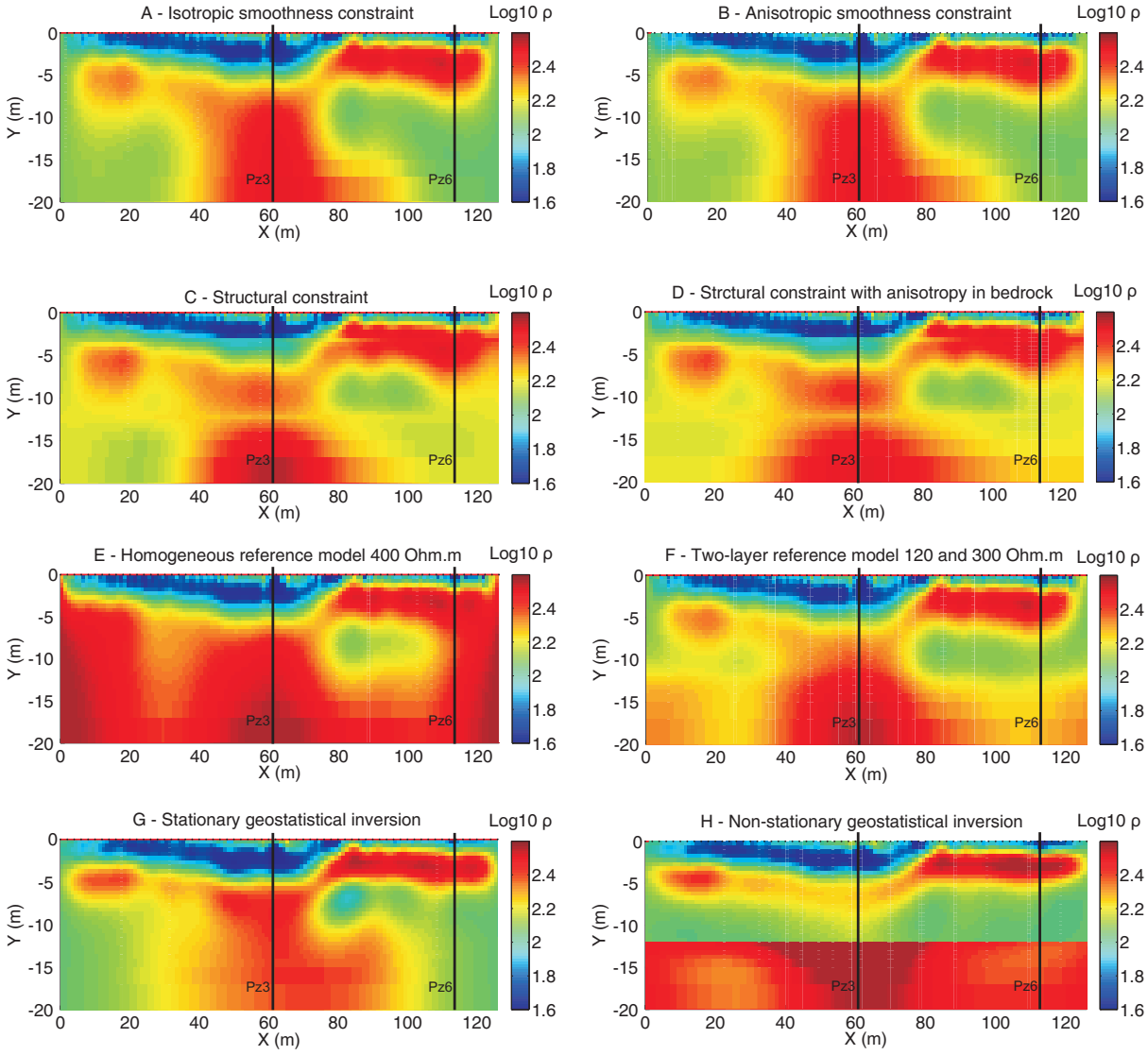

Figure 2.27: Inversions for the site of Hermalle-sous-Argenteau, comparison with EM logs are given in figure 2.28. A) The smoothness constraint inversion images roughly the expected structure. B) Adding horizontal anisotropy to the smoothness constraint has almost no effect on the results. C) Using a structural constraint at the water level and bedrock positions improves the results (detection of a maximum in resistvity) but not significantly even if D) an horizontal anisotropy is imposed in the bedrock. E) A 400 $Ohm.m$ reference model hides must of the structure. F) A two-layer reference model seems more appropriate to image the bedrock limit. G) The geostatistical inversion enables to retrieve the shape of the vertical resistivity distribution but not the values themselves. H) A non-stationary inversion disconnects the bedrock in the inversion and yields a very good vertical resistivity distribution, qualitatively and quantitatively.

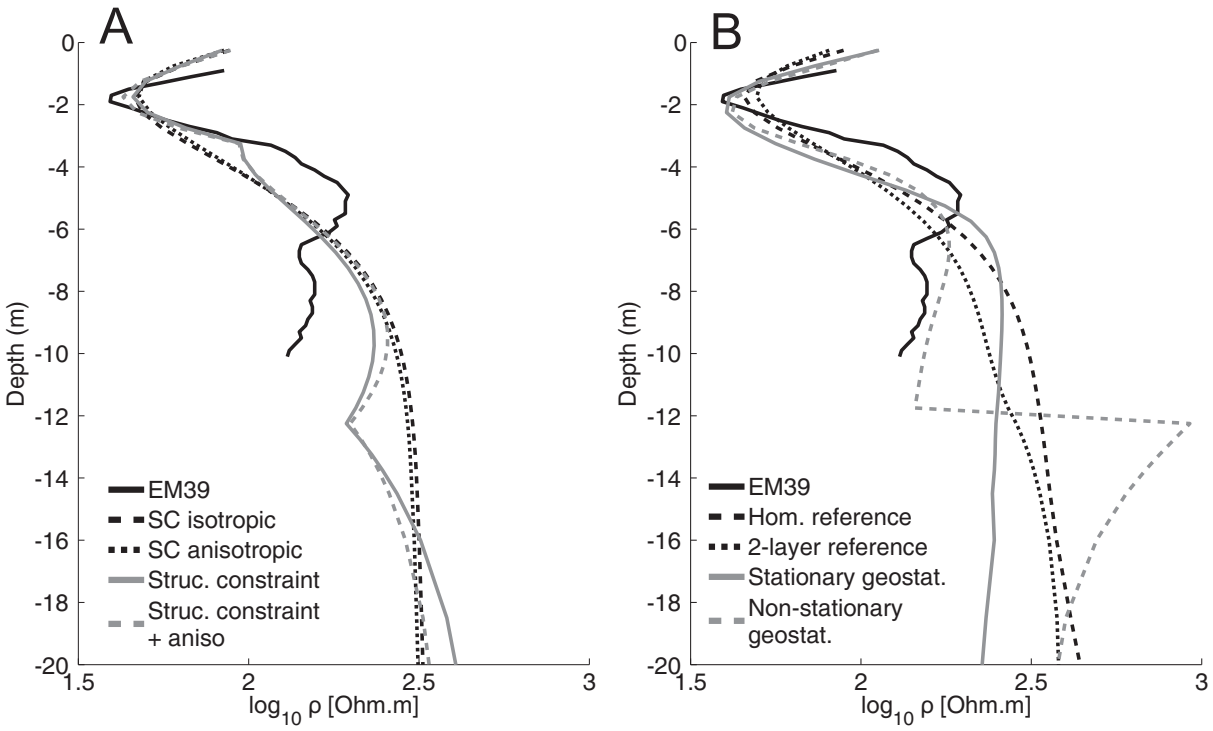

Figure 2.28: Comparison with EM conductivity log in Pz3. The non-stationary geostatistical inversion seems to be the best option in this case.

Seismic refraction and borehole data show that two "structural" limits exist on the site. Between -3 and -3.5 m is the water level, and between -12 and -10 m lies the bedrock. When those limits are incorporated in the inversion (figure 2.27C), the vertical resistivity distribution is better solved. The first improvement is that the minimum of the curve is better retrieved. However, this might be a coincidence because at Pz3, the water level corresponds approximately to the transition loam-gravel. Consequently, the limit of loam is better resolved. We see that laterally, the structural constraint has almost no effect on the results. Given the observed resistivity distribution in the first meters, such limit does not seem to exist. Deeper down the model, the resistivity distribution displays a maximum as observed in the conductivity logs. Incorporating the limit of the bedrock brings an improvement in the image, at least in the middle part. On the sides of the section, the improvement is less clear, because the aquifer anomalies are also visible in the bedrock. The structural constraint is thus not as efficient as for the Ghent site. To overcome this, an anisotropy ratio of 10 in the horizontal direction was added for the bedrock, i.e. below -12 m (figure 2.27D). This changes slightly the resistivity in the bedrock but is not sufficient to produce a laterally homogeneous layer.

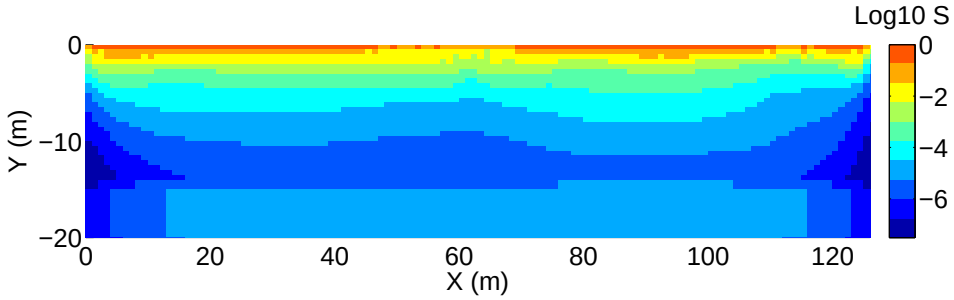

Figure 2.29: Cumulative sensitivity of the smoothness constraint solution of the reference profile in Hermalle-sous-Argenteau.

Unfortunately, there is not any prior information on the resistivity of the bedrock. So, there is no control on the solution in this part of the model and it might be difficult to build a coherent reference model. We have seen that most improvements were obtained when adding prior information in low sensitivity zone. The sensitivity pattern at Hermalle site follows the standard decrease with depth for surface arrays (figure 2.29). The apparent increase below 15 m is due to increase in grid size at depth. In consequence, in order to improve the solution, it is necessary to bring some information at depth. First, we added a reference model in the inversion. We estimated a resistivity value between 300 and 400 $Ohm.m$ for the bedrock. In figure 2.27E, the solution using a homogeneous reference model of 400 $Ohm.m$ with $\alpha = 0.05$ is presented. This constraint appears to be too strong because it hides most of the structures visible in the alluvial aquifer part of the model. We then used a two-layer reference model, with 120 $Ohm.m$ in the upper part and 300 $Ohm.m$ below -12 m (figure 2.27F). This gives a visual improvement to delimit the bedrock, but the vertical distribution of resistivity is still not well resolved.

For the regularized geostatistical solution, we first used a prior model equal to 120 $Ohm.m$ in order to improve the solution in the bottom part of the alluvial aquifer (figure 2.27G). At this stage, this solution is the one that best matches EM conductivity measurements in Pz3 (figure 2.28B). The solution has a maximum value of resistivity and then decreases slightly. However, the resistivity values expected in the alluvial deposits are greatly overestimated. If we want to use quantitatively ERT results to constrain geostatistical models, the solution must

be improved. The problem seems to be that the bedrock influences the resistivity values in the alluvial aquifer. The sensitivity would be sufficient to detect the bedrock (figure 2.26) but not sufficient to produce the expected contrast with the alluvial deposits. Since the bedrock and the alluvial aquifer are two distinct geological bodies and that the variogram parameters were derived for the alluvial aquifer only, it seems necessary to use a non-stationary geostatistical inversion. Doing so, the two zones will be disconnected during inversion (figure 2.27H). The values of the prior model were chosen equal to 120 and 300 $Ohm.m$ for the alluvial deposits and the bedrock respectively. The horizontal and vertical correlation lengths for the bedrock were 25 and 10 m respectively. Visually, the bedrock is of course well-resolved as the limit is imposed during inversion. Doing so, the vertical distribution of resistivity is very close the EM conductivity log, both on the shape and on resistivity values (figure 2.28B).

Since the bedrock is lying between -10 and -12 m, it is possible to try various depth for the limit between the two zones and to choose the one that gives the best fit with EM conductivity logs. In this case, it has little influence but the best solution for alluvial deposits is obtained with the bedrock at -10 m depth.

Comparing the solution at only one position may be too restrictive to assess which solution is the best resolved, but there are rarely more data on the field to control the solution. Here, the Pz6 is also located on the profile, but its position towards the end of the profile is such that the sensitivity (figure 2.29) is already low at small depth. The comparison of some solutions with the EM conductivity log (figure 2.30) shows that none of the solutions is able to retrieve the vertical resistivity distribution, especially the minimum observed at -4 m, likely due to the lack of sensitivity. The geostatistical solutions are still better than the smoothness constrained solution.

With this case on the site of Hermalle-sous-Argenteau, we again see that incorporating prior information will almost always provide an improvement in the calculated resistivity distribution. However, conservative ways to incorporate prior information, such as homogeneous reference model or stationary geostatistical inversion are not always sufficient to get a solution coherent with ground truth data. In that case, it may be necessary to take stronger assumptions such as the non-stationary geostatistical constraint or the more complex reference model to improve the solution. The choice becomes more subjective and the interpreter must be aware of the

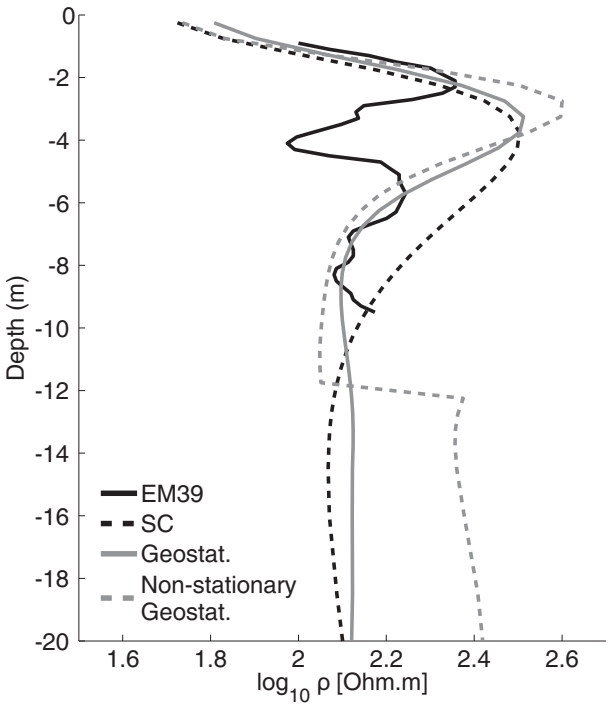

Figure 2.30: Comparison with EM conductivity log in Pz6.

assumptions he made and should always wonder if the results remain representative for the whole section or site. In this specific case, the non-stationary assumption is supported by independent field data and the improvement of the results in Pz3 can be reasonably extended to the whole section.

2.7 Guidelines and Conclusion

Results presented on the 3 experimental sites allow us to draw some guidelines about the use of *a priori* information to enhance the quality of inverted models from the smoothness constraint inversion. Each constraint has pros and cons and is more or less adapted in specific cases.

Reference model constraint. Adding a reference model in the solution is a straightforward incorporation of prior information. However, it is done through an additional weighting parameter which may be difficult to choose. With a low α value (equation 2.23), the reference model may have a relatively low impact on the solution and results may remain almost similar to the smoothness solution (Ghent site), may improve significantly the results (Westhoek site) or may be too strong (Hermalle site). With higher α values, the importance of the reference model increases and the solution begins to tend to the reference model. Low sensitivity areas are the

first to be impacted by this effect. The optimization of the closeness factor is very difficult, even with borehole data. An interesting development would be to allow α to vary according to the sensitivity. However, it would require to make its choice more objective.

Complex reference models with several layers or bodies should always be used carefully. This is somehow similar to impose both a structural constraint and the resistivity distribution of the solution. It may be too restrictive and compete with the data. The problem with this approach is that we may add too much information so that the solution obtained tends to the solution we expect *a priori*.

Consequently, the use of a reference model constraint with a large α value is well adapted only when information about the underground structure and resistivity distribution are well-known, which is rarely the case in practice. To impose sharp limits, it is safer to rely on the structural constraint.

When no information about the structure is available but well information about the resistivity distribution is present, the use of a homogeneous reference model with a small value of α is indicated. The resistivity of the reference model may be chosen according to the expected resistivity at depth where the sensitivity is low, instead of choosing the mean apparent resistivity.

In some cases, using a reference model not coherent with available prior information on the distribution of resistivity for purpose may reveal which parts of the section are most impacted by prior information and may help to highlight which resistivity structures are really coherent with the data set. This may be used as some kind of qualitative DOI.

Structural inversion. Incorporating structural information can, in some cases, significantly improve the solution. This is particularly true when the boundaries between the different underground structures are well-known and the resistivity contrast between them is well-marked (Ghent site). When the resistivity contrast is weak or the expected structure not marked in the resistivity distribution, the use of a structural constraint is not an efficient approach (Westhoek and Hermalle sites).

When dealing with structural constraint, we must moreover take care of the value of β_x and β_z (equation 2.24) that are used to weight differently the gradients along each element boundaries of the inversion grid. High ratios $\frac{\beta_x}{\beta_z}$ may lead to non-coherent coupling between the different structure units. Low ratios act as softer constraints and should be used when there is

uncertainty on the exact position of the boundary or when the expected resistivity contrast is low.

This method can be combined with various anisotropy ratio in the different layers defined by the structure, to enhance the expected homogeneity of a horizontal layer or a vertical structure.

The structural constraint is thus particularly adapted to include limits such as bedrock or water table, for which resistivity variations are often observed. It is not always the case, but including the limit will rarely degrade the quality of the solution, it will just not improve it. When the limit are not horizontal, the grid should be adapted to correspond with the structure (Doetsch et al. 2012).

In some cases, a horizontal limit exists but its precise location is not known *a priori* (water level or bedrock in the case of alluvial aquifers). In such cases, it could be interesting to develop a methodology of inversion where the location of the limit itself is inverted. The methodology could combine the method of de Groot-Hedlin and Constable (2004) to invert for models with sharp contrasts between homogeneous bodies and a classical approach to allow heterogeneities inside the defined bodies. It would allow higher contrasts in the resistivity distribution but without imposing the location where the contrasts appear.

Regularized geostatistical inversion. The geostatistical inversion may provide very consistent results and can significantly improve the solution compared to the other inversion approaches. However, it requires additional measurements to sample the resistivity distribution and compute variograms (EM conductivity logs or any other data mapping the resistivity distribution).

The method is not well adapted when a layered structure is expected, but yields results at least as good as the smoothness constraint (Ghent site). When the distribution in resistivity does not display sharp contrasts, the improvement brought by the regularized geostatistical inversion is important (Westhoek and Hermalle sites). Through the *a priori* covariance matrix, prior information will have a direct influence on all the parameters of the inverted model in a similar way as the smoothness constraint solution. This method thus has the potential to directly influence the entire image plan.

The choice of the prior model is also important and we recommend choosing it according to the expected resistivity at depth where the sensitivity is low. This choice should positively

impact the distribution of resistivity after inversion. However, the user should avoid the overinterpretation of the results where the prior has a strong effect.

It seems that the role of the horizontal range is less crucial in surface ERT than the vertical range, which may be related to the sensitivity pattern of surface ERT, exhibiting a rapid decrease with depth. The method works fine when only the vertical range is known and the horizontal range is roughly estimated.

When non-stationarity is expected in the section (Westhoek or Hermalle sites), it is possible to define different zones with different variogram parameters and prior model. It is a way to add structural information in the geostatistical regularization. As it corresponds to a disconnected inversion, such inversion should be carried out with caution because it supposes a strong assumption regarding the resistivity distribution.

In all cases, the results show that adding prior information in the inversion process led to a modification of the solution at least in zones of low sensitivity, i.e. at depth and on the sides of the section for surface arrays.

However, the choice of the best constraint to apply is highly dependent on the type and amount of information available. A reference model can always be used, but its weight in the inversion process and its complexity are challenging to address. Several attempts are necessary to deduce, if possible, the best parameter to fit borehole measurements and there is no control on other parts of the model which may lead to implausible solutions. It should then be used carefully to improve the smoothness constrained solution when there is not enough prior information to apply the other methods.

When the physical parameter (here electrical resistivity or conductivity) can be measured in several boreholes at different depths, the computation of a variogram is possible and a geostatistical constraint seems well suited. In addition to a proper prior model, this may be the method of choice to constrain the solution. However, in most cases, there will remain some uncertainty on the horizontal/vertical correlation length. The main advantage of this technique is to use borehole measurements only indirectly through the computation of a variogram. If the calculated variogram is representative of the whole site, the better correspondence observed in the boreholes is expected to be the same elsewhere in the section. When non-stationarity is expected, it is possible to deal with the problem using different variogram parameters corresponding to each

zone.

However, when lithological limits or other geophysical data sets are available and sharp contrasts expected, a structural constraint can be better suited. It enables to disconnect, more or less according to the ratio between horizontal and vertical gradients, different lithological facies and creates sharp contrasts whereas standard Occam inversion would lead to smooth transitions. It thus highlights better anomalies. This kind of constraint is often less strong than a complex reference model because it does not need to provide resistivity values before the inversion process.

When prior information is incorporated in the inversion process, the classical image appraisal tools such as the cumulative sensitivity or the resolution matrix do not show where the solution is reliable or not any more. We have seen that the solution could be highly improved with proper methods. Now, these tools indicate where the solution is mostly driven by the data or mostly driven by prior information.

Each time one includes prior information in the inverse problem, it is necessary to keep in mind that the solution is not unique and that it depends on the constraint use during inversion. It is the responsibility of the user to test different methods and to choose which solution is the most adapted to its specific case. Of course, during the interpretation step, one has to remember the assumptions he made or the constraints he used to avoid over-interpretation of the resistivity structures.

In this chapter, we have worked within the framework of regularized inversion, i.e. we are seeking a deterministic solution to the ERT inverse problem. This is opposed to geostatistical simulations and stochastic inversions which propose several equiprobable solutions to a given problem. In chapter 3, we will see how deterministic geophysical models can be included to a probabilistic framework using multiple-point statistics. Then, chapter 4 will illustrate the stochastic inversion of hydrogeological models constrained to geological, geophysical and hydrogeological data.

Chapter 3

Integration of geophysical data in multiple-point statistics

Note. The research material of this chapter is partially published in the proceedings of the 15^{th} Annual conference of the IAMG:

Hermans T., Caers J. and Nguyen F. 2013. Assessing the probability of training image-based geological scenario using geophysical data. In: Pardo-Iguzquiza E., Gaurdiola-Albert C., Heredia J., Moreno-Merino L., Dura J.J. and Vargas-Guzman J.A. Mathematics of Planeth Earth - Proceedings of the 15^{th} Annual Meeting of the IAMG, September 2 to 6, Madrid, Spain.

Acquiring geophysical data sets and building models of geophysical properties are rarely the main aims of geological studies. Geophysical data serves as relatively low-cost, easily acquired, flexible and spatially distributed indirect information to study hydrogeological reservoirs or mining and petroleum resources. This information is generally of lower resolution than direct borehole measurements and has to be linked to the main investigated parameter (for example hydraulic conductivity) through petrophysical relationships or any other way to link two physical parameters.

Geophysical models may simply help to draw the general trends and structures of geological models or may help to understand which physical processes are going on. However, the need for a better characterization of the subsurface and the development of predictive physically-based

models ask for a better integration of all available data, including geophysical data, into those geological models. For that purposes, geostatistical techniques seem very well suited.

As we have seen in chapter 2 for ERT inversion, the integration of independent and relevant information should improve the results of geological models. In the last 15 years, many efforts were made to integrate geophysical data into groundwater or environmental models. Most techniques were borrowed from the petroleum industry where the characterization of reservoir models through geophysical techniques, mainly seismic reflection, is common since the eighties.

In the next sections, we will first review some of the techniques that were adapted or developed for the integration of geophysical data within geostatistical frameworks. Then, we will focus on the method chosen within the context of this project, namely multiple-point geostatistics (MPS). In the second part of this chapter, we will focus on alluvial aquifers, and especially the Meuse River alluvial aquifer. Some geological scenarios will be created and their consistency with geophysical data will be verified through a multi-dimensional scaling approach. Finally, we will investigate how ERT inversion results may be integrated in MPS.

3.1 Integration of geophysical data within geostatistical frameworks

Geostatistical integration of geophysical data or models includes a wide range of techniques, including estimation, interpolation, classification or simulation techniques (Deutsch 2002, Kelkar et al. 2002). In this section, we illustrate some techniques of incorporation of geophysical data within geostatistical frameworks. We will not consider geostatistical inversion, i.e. inversion schemes for geophysical data with geostatistical constraints, which were discussed in chapter 2.

Most common techniques are related to two-point correlation methods, based on variograms. When data such as piezometric level or water conductivity measurements are available, generally at the position of wells, geostatistical tools may be used to calculate an estimation of the variable at each position of the model. Geostatistical techniques are interesting alternatives to deterministic methods, such as the inverse distance method. Kriging is the most common method. Given a variogram model and existing data points, the kriging equations are solved to calculate the best estimate of the parameter elsewhere in the model.

As kriging yields the best estimate of the parameter, kriging results tend to be smooth. When

a geophysical data set related to the studied properties is available on the site, the technique may be extended to take into account the secondary variable using cokriging. This secondary variable is available at locations not sampled for the primary variable. In cokriging, the estimator is still a linear combination of the primary and secondary variables. Solving the equations only requires variograms for both variables and the cross-variogram which depicts the correlation between the primary and secondary variable.

Cassiani et al. (1998) used cokriging to integrate seismic tomography and sonic log data into the estimation of hydraulic conductivity in a synthetic benchmark. They first inverted cross-borehole seismic traveltimes to recover a model of seismic slowness (inverse of seismic velocity) and use this model as secondary data to estimate hydraulic conductivity through cokriging. Vertical variograms were inferred from borehole data for both primary and secondary variables. The horizontal variogram, as it is often the case, was difficult to derive and the authors used, as an approximation, the variogram deduced from the seismic tomography. The cross-variogram was calculated using borehole data only. They showed that slowness was able to improve the estimation of hydraulic conductivity, even if the information is slightly degraded by the inversion process of geophysical data.

Gloaguen et al. (2001) carried out a surface GPR survey on an unconfined shallow sand aquifer overlying a clay layer. Two reflections occurred: one is correlated with the piezometric level, the second one is correlated with the sand-clay interface, known at the position of controlled piezometers. They used cokriging with the two-way reflection travel times as secondary variables to build a depth model for the two interfaces. Once the depth of the layers is estimated, they first derived the spatial distribution of the velocity in each layer, second the dielectric constant, third the porosity of saturated sand and fourth the hydraulic conductivity, all linked through petrophysical relationships.

Those two examples illustrate the integration of geophysical data at relatively small scale. The techniques may be used as well at larger scale. As an example, Vesnaver et al. (2006) used Landsat satellite images to improve through cokriging the lateral characterization of near-surface P-wave velocities in an on-shore seismic reflection survey for static corrections. As another example, Bélanger et al. (2010) used, similarly to Gloaguen et al. (2001), cokriging to estimate the depth to bedrock using GPR traveltimes in the study of a 12 km^2 unconfined

aquifer area. This shows that geostatistical techniques may be useful at various scales.

Estimation of hydraulic conductivity or other relevant parameters through kriging and cokriging yields a smooth distribution of the parameter over the studied area. Generally, the variability of the parameter is higher than observed in this estimation, and this variability plays an important role in processes such as groundwater flow and transport.

Instead of using estimation procedure, simulation procedures may be used. In simulations, each node of the considered area is visited following a random path. The equation of kriging or cokriging may then be used to infer the probability density distribution at a node, using variograms and cross-variograms, the primary variable at previously simulated nodes and the secondary variable. A value of the parameter is randomly chosen in the distribution and the chosen value is assigned to the simulated node. Then the process is repeated for the next nodes until the entire domain is populated. Such simulations generally render more variability in the distribution of the studied parameter (the variance is higher) and have a spatial distribution of parameters closer to the true distribution. Simulations also open the possibility to use a stochastic approach. Using a set of equiprobable realizations, the variability of the process and its uncertainty may be studied.

Rahman et al. (2008) both used estimation through cokriging and simulations (sequential Gaussian simulation (SGS)) to investigate an aquifer in Louisiania using hydraulic conductivity as primary variable and borehole resistivity logs as secondary data. As the primary and secondary variable were not colocated, they had to use a pseudo cross-variogram for cokriging and cosimulation. As expected, the use of secondary data improved the characterization of hydraulic conductivity. The results also show that the use of simulations instead of estimation can reproduce with more significance the aquifer heterogeneity and the flow-model response.

Hyndman et al. (2000) used SGS to derive a petrophysical relationship at the field scale between seismic slowness and hydraulic conductivity. First, they inverted cross-well seismic traveltimes. SGS are used to generate equally probable slowness realizations and an *a priori* relationships is used to transform the realizations into hydraulic conductivity models. Groundwater flow and transport simulations are then performed to simulate drawdowns and concentration. Then, the petrophysical relationships is perturbed through inverse modeling to improve the fit between calculated and observed data. Here, simulations are just a base for inverse modeling of

the petrophysical relationship.

Horta et al. (2013) integrated electromagnetic data under the form of apparent resistivity data to constrain the lateral and in depth distribution of ashes on a contaminated site in Portugal. A linear relationship is derived between the apparent conductivity and the thickness of ashes on the site. This relationship is then used to derive a reference map of ash thickness from geophysics. This map was used as a secondary data to produce simulations conditioned to local data (log with known ash thickness). The mean of those simulations was used as a reference image for further 3D sequential indicator simulations (SIS). The indicator variable is the presence or not of ashes. In addition, the authors used an optimization algorithm to update their simulations in order to fit their reference images of ash thickness. Running several simulations enabled to draw map of the most probable indicator (presence of ash or not) and have an idea of the probability of occurrence of ash on the site.

Bayesian statistics is also a common way to integrate geophysical data within a geostatistical framework. A review and the mathematical formalism may be found in Tarantola (1987) or in Rubin and Hubbard (2005). This technique requires a prior estimate of the probability distribution (pdf) of the primary variable $P(\mathbf{m})$. This prior estimate can be derived from the knowledge of the particular site or geologically similar sites, from expert opinions or may be obtained through an estimation technique such as kriging. This prior pdf may then be updated using any additional relevant data $\mathbf{d}$ on the site. This leads through Bayes' rule

$$P(\mathbf{m}|\mathbf{d}) = \frac{P(\mathbf{d}|\mathbf{m})P(\mathbf{m})}{P(\mathbf{d})} \tag{3.1}$$

to a posterior distribution of the primary variable given the data $P(\mathbf{m}|\mathbf{d})$, which requires the knowledge of a likelihood function $P(\mathbf{d}|\mathbf{m})$. The likelihood function is the probability to observe the data given a specific posterior distribution. The sake of the method is to consider not only an estimate of the primary variable, but the entirety of the distribution.

Ezzedine et al. (1999) used a Bayesian framework to integrate crosshole electromagnetic resistivity measurements to define the lithology (shale/sand) on the LLNL superfund site. First, they used SIS to generate lithology images based on borehole data. The prior probability is the probability of occurrence of shale in boreholes. Second, they generated a shaliness image, based on gamma-ray measurements, using sequential Gaussian simulation. From co-located borehole

measurements of shaliness and resistivity, the prior probability density function of resistivity given lithology and shaliness is defined. This prior probability is updated through Bayes' rule to take into account the lower resolution of the geophysical resistivity survey compared to borehole measurements. In the last step, the lithology image is updated through Bayes' rule, using resistivity values, since the resistivity is informative on the presence or not of shale. This likelihood function is built using post survey comparisons between lithology and resistivity.

Dubreuil-Boisclair et al. (2011) also used a Bayesian approach, namely the Bayesian multivariate sequential simulation method, to integrate GPR tomography results into hydraulic conductivity models. They used simple kriging to estimate the prior pdf of hydraulic conductivity. The likelihood function was derived from comparisons of GPR sensitive parameters (electrical conductivity and dielectric permittivity) with hydraulic conductivity in boreholes where the direct comparison is possible using a multivariate kernel density estimator. They also compared the solution with other simulation techniques such as SGS.

Bayesian approach are very popular and often used in combination with Markov chain Monte Carlo approach (McMC), which are used to sample the posterior distribution. Eidsvik et al. (2002) presents an example for hydrocarbon reservoirs. They outlined the two important steps of the procedure. First, the definition of a prior distribution with important variables (facies, porosity, density, seismic velocities) is made. The likelihood function integrates seismic reflection times, well observations and AVO attributes. It can be expressed, for example, as an objective or misfit function. Markov chain Monte Carlo simulations are used to explore the posterior probability distribution of this complex reservoir model. A first guess is drawn from the prior distribution, then the model is perturbed at some random node and new values of the variable are proposed and are kept if it is improving the model (represented by the data that should be integrated). A drawback of McMC approaches are their relatively computational cost.

Such an approach is for example used by Irving and Singha (2010) to integrate time-lapse ERT data from tracer tests to study the distribution of hydraulic conductivity to predict solute transport. In this case, the method can be seen as a joint hydrogeophysical inversion since ERT data are incorporated in terms of resistance data and not as a resistivity model. In tracer tests, there are as many data sets as time steps. To easily derive the likelihood function, the authors made an additional assumption to express the global likelihood as the product

of individual likelihood for each data set: the data sets are statistically independent. Then each individual likelihood function is calculated as a data misfit function, which requires to run a forward simulator. The Markov chain Monte Carlo procedure is a sampling technique of the posterior distribution. Here, the Metropolis sampler was used. First, a prior model of hydraulic conductivity is simulated and the tracer test is simulated. The link between hydraulic conductivity data and geophysical parameter is addressed through petrophysical relationships. If the hydrogeophysical data are well retrieved, the model is accepted, if it is not the case, it is rejected. Then 90% of the hydraulic conductivity values are kept as hard data for the next iteration. A new realization is drawn and the process starts again. To ensure that the accepted models are independent, only one model every 100 is kept as a sample of the posterior distribution. Such approach requires a lot of CPU time.

Another Monte-Carlo type approach, used by Tronicke and Holliger (2005) is called simulated annealing. This simulation technique is based on a thermodynamics principle: it assumes that there are a lot of possible initial states but those converge to a few acceptable final states. The simulation progresses with an objective function that is gradually minimized. The process starts by a random generation of a starting model. Then, the model is perturbed and if the new objective function is lower than the old one, the perturbation is accepted. If it is not the case, the perturbation is accepted with a probability P, depending on a temperature T. The lower T, the lower P. In the simulated annealing scheme, T is progressively lowered. To integrate their cross-hole GPR traveltimes data and porosity log data into a porosity model of aquifer, Tronicke and Holliger (2005) defined an objective function with 3 terms: the reproduction of the spatial statistical model (variogram), the reproduction of porosity log data and the correlation of geophysical GPR data with porosity measured in boreholes. As a perturbation, they just swapped the values at two nodes.

Dafflon et al. (2009) extended the work of Tronicke and Holliger (2005) to increase the weight of geophysical information for large-scale subsurface structures. To do so, they modified the initial algorithm. Instead of simply swapping values as a perturbation, the perturbation step consists in drawing a new random value from a conditional probability distribution. This distribution is obtained from geophysical data, considering the link to the target parameter which is derived from co-located data in boreholes. In addition, they only consider the reproduction

of the variogram for shorter lags, considering that larger lags should be driven by geophysical data. Geophysical data are now integrated in the perturbation procedure and not in the objective function calculation which simplifies the process, improves convergence and yields better results.

Engdahl et al. (2010) proposed another method to integrate geophysical data with geostatistics to build more realistic models of a heterogeneous aquifer. They used GPR to delineate individual regions or bounding surfaces (such as cross beds or erosional surfaces) to delimit sedimentological units which are then filled geostatistically using transition probability-based indicator geostatistics. The GPR bounding surfaces are treated as an indicator variable, being 1 if it is a bounding surface and 0 if not. The transition probability is the likelihood to find a given facies beside another facies at lag distance. The variogram is then replaced by a Markov chain for simulation. Here geophysical data are used as deterministic constraints for geostatistical models of the subsurface.

Oh (2013) combined seismic and electrical resistivity tomography to improve the estimation of the RQD. Instead of using the traditional Bayes' rule, he assumes the permanence of ratio (Journel 2002) to calculate the posterior probability of RQD (equations 3.12 to 3.14). The advantage of this rule is that it does not require the assumption of independence between two data sets, some redundancy is possible. The prior probability of RQD is calculated using indicator kriging from values measured at known locations. The probabilities linking RQD to seismic slowness and electrical resistivity were deduced from borehole locations where parameters are co-located by building cumulative probability distributions for the various geophysical parameter values. Using this probabilistic approach, the author provides an uncertainty analysis of its results.

Another interesting approach to integrate various geophysical data is the clustering approach. The principle of clustering approaches is to group data points or model parameters in a space of several dimensions (each dimension corresponding to a physical parameter or property) based on their distance to each other, various clustering approaches exist: crisp cluster algorithms assign each data point to a specific cluster (classification or zonation) whereas fuzzy cluster algorithms calculate how a point is close to each cluster (e.g. Holliger et al. 2008).

A key parameter in clustering approaches is the number of cluster. Paasche et al. (2006) used a fuzzy cluster analysis to integrate various hydrogeophysical parameters (crosshole GPR

and seismic, gamma-log and slug tests) in a unique model after individual inversions and test various number of clusters. Paasche and Tronicke (2007) used the same fuzzy cluster analysis technique in a cooperative 2D-inversion of GPR and seismic cross-borehole tomography. At each iteration, parameters are grouped in clusters and the new value of a parameter becomes the weighted sum of mean parameters of each cluster. Integrating the cluster analysis directly in the inversion lead to better results.

Doetsch et al. (2010b) applied a zonation cluster algorithm to classify parameters in an alluvial aquifer into 3 different lithologies. The zonation algorithm was performed on the results of joint-inversion of crosshole ERT, GPR and seismic tomography. Then, they performed a petrophysical analysis on the lithologies. This approach requires at least two different geophysical parameters everywhere in the model, which is rarely the case in field studies at higher scale.

The examples above show that there many ways to integrate geophysical data using geostatistical techniques. The chosen method generally depends on the available data and as many variants as specific case studies or applications may exist. The role of geophysical data is more or less important according to the method used. One of the main advantage of geostatistical techniques is that they generally do not require the definition of a deterministic petrophysical relationship between the geophysical parameter and the simulated parameter. However, some assumptions are sometimes needed, such as the Gaussian behavior of the variable.

Most of these examples, except clustering techniques, assume that a two-point based correlation method, such as the variogram, is sufficient to describe the heterogeneity. This is acceptable in many applications when describing smoothly heterogeneous media, but inadequate when facing multimodal distributions and curvilinear or interconnected structures, as expected in complex alluvial aquifers. This limitation was already apparent more than 20 years ago. To overcome it, Guardiano and Srivastava (1993) proposed to use multiple-point geostatistics (MPS) to model subsurface heterogeneity through simulations. In contrasts with traditional geostatistics, MPS does not require the explicit definition of a random function. Instead, it infers the multivariate distribution from a training image, which depicts the expected geological heterogeneity of the studied field. Using the training image, it is possible to analyze simultaneously the statistics in every direction, with a neighborhood approach.

In the next section, we will describe the theory of MPS and some developments that were

made in the last decade to improve the algorithms and extend the method to various cases.

3.2 Multiple-point statistics

The idea to develop multiple-point geostatistics (MPS) was first formulated by Guardiano and Srivastava (1993). However, initially, the training image (TI) had to be scanned entirely for the simulation of every node of the model. Of course, this method is computationally too expensive and hindered the development of the technique. The work of Strebelle (2000, 2002), introducing in the SNESIM algorithm the concept of the search tree to store the results of the unique scanning of the TI, made the method more attractive and its use possible. In the last decade, several developments were made to extend the possibilities of the technique. A comprehensive review can be found in Hu and Chugunova (2008).

We will here briefly summarize the basic principles of MPS for the reader unfamiliar with the matter. Section 3.3 will deal with the construction of training image-based scenarios in the alluvial deposits of the Meuse River.

3.2.1 Principle of multiple-point statistics

Let us take an attribute S which can take J possible states $\{s_j,\ j = 1, 2, \ldots, J\}$. In this work, we will consider S as a categorical variable, such as a facies or a lithology, but S can be a continuous variable (porosity or hydraulic conductivity) with its interval of variability discretized into J classes, using $J-1$ threshold values. Consider a data event d_n of size n (number of nodes or elements) and its central location $\mathbf{u}$, d_n is constituted by two sets of elements:

1. Its geometry defined by n vectors $\{\mathbf{h}_\alpha,\ \alpha = 1, 2, \ldots, n\}$.

2. The n data values taken by its n elements. $\{s(\mathbf{u} + \mathbf{h}_\alpha),\ \alpha = 1, 2, \ldots, n\}$.

In a MPS simulation, the value at the center location $\mathbf{u}$ is the unknown. A data template τ_n is constituted by the data geometry only. A subtemplate is constituted by only $n\prime < n$ vectors. The data event d_n is associated to the template τ_n.

The multiple-point statistics are the probabilities of occurrence of the data events $d_n = \{S(\mathbf{u}_\alpha) = s_{j,\alpha},\ \alpha = 1, 2, \ldots, n\}$. In other words, the probabilities that the variable S at the

nodes of the geometrical template τ_n $s(u_1), s(u_2), \ldots, s(u_n)$ are jointly in the respective states $s_{j,1}, s_{j,2}, \ldots, s_{j,n}$.

For stochastic simulations, the J possible outcomes of the random variable $S(\mathbf{u})$ are conditioned by their conditional probability distribution function (cpdf)

$$Prob\{S(\mathbf{u}) = s_j | d_n\} = f(u; j|d_n),\ j = 1, 2, \ldots, J \tag{3.2}$$

and the knowledge of the cpdf for any possible data event d_n is sufficient to generate a realization of the variable $S(\mathbf{u})$. The number of possible data events is equal to J^n. It grows rapidly with the number of categories and the number of nodes in the geometrical template.

In the SNESIM algorithm (Strebelle 2000, 2002), the cpdf are borrowed from the training image T. T is scanned to look for replicates of the data event d_n. If R replicates of d_n are found in T, the histogram of the R central values $s_T(\mathbf{u}_r),\ r = 1, 2, \ldots, R$ is used as an estimator for the cpdf (equation 3.2).

The role of the training image is very important in MPS as it will be used to infer the conditional probabilities needed for simulations. It would be impossible to infer multiple-point statistics from sampled data only. The training image does not need to represent any local and accurate data. Its role is to depict the expected patterns of geological heterogeneities. Training images for field case studies may be obtained from geological studies or outcrops, from the expertise of a geologist or derived from geophysical measurements (e.g. Huysmans and Dassargues 2009).

3.2.2 SNESIM algorithm (Strebelle 2000)

The variable S can be transformed into indicator (binary) variables

$$I(u, j) = \begin{cases} 1\ if\ S(\mathbf{u}) = s_j \\ 0\ if\ S(\mathbf{u}) \neq s_j \end{cases} \tag{3.3}$$

Similarly, the indicator variable D associated with the occurrence of the data event d_n, i.e. the n conditioning data $S(\mathbf{u}_\alpha) = s_{j,\alpha},\ \alpha = 1, 2, \ldots, n$ considered jointly can be expressed as

$$D = \begin{cases} 1 \; if \; S(\mathbf{u}_\alpha) = s_{k,\alpha}, \; \forall \alpha = 1, 2, \ldots, n \\ 0 \; if \; not \end{cases} \tag{3.4}$$

If the multiple-point statistics of $I(u, j)$ and D are available, the conditional probability can be estimated through the simple kriging equation (Journel 1993) leading to the exact expression of the conditional probability

$$Prob\{I(u, j) = 1 | D = 1\} = \frac{E\{I(u, j)D\}}{E\{D\}} = \frac{Prob\{I(u, j) = 1, D = 1\}}{Prob\{D = 1\}}. \tag{3.5}$$

The probabilities of equation 3.5 are borrowed from the training image under the assumption of stationarity.

1. The denominator $Prob\{D = 1\} = Prob\{S(\mathbf{u}_\alpha) = s_{j\alpha}, \; \alpha = 1, 2, \ldots, n\}$ is inferred by counting the number of times $c(d_n)$ this data event d_n appears in the training image, i.e. each time the same geometry with same categorical values.

2. The numerator $Prob\{I(u, j) = 1, D = 1\} = Prob\{S(\mathbf{u}) = s_j \; and \; S(\mathbf{u}_\alpha) = s_{j\alpha}, \; \alpha = 1, 2, \ldots, n\}$ is simply the number of times $c_j(d_n)$ the value of the central node is equal to s_j among the $c(d_n)$ total number of replicates of the data event.

Equation 3.5 becomes

$$Prob\{I(u, j) = 1 | D = 1\} = Prob\{S(\mathbf{u}) = s_j | d_n\} \simeq \frac{c_j(d_n)}{c(d_n)}. \tag{3.6}$$

The technique is totally dependent on the training image that is used for simulation, as all the structures of the simulation will be inferred from the structures of the training image. The role of the neighborhood is also important. If n is too small, it is not sufficient to reproduce the structure of the training image. If n is too big, the data event d_n could become too specific, so it should be always checked that a minimum of replicates are present.

Scanning the training image is the first step of the SNESIM algorithm (Strebelle 2002). Results of occurrence of the J^n possible states are stored in a search tree to easily find the needed probabilities during simulations. Generally, the number of states contained in the training image is much smaller. The tree starts at the root node of the template where the global category

histogram will be stored. Then, the tree considers the first neighboring node and splits in J branches to consider every possible facies, and the conditional category histogram given a data event. An example of search tree is given in figure 3.1 (Hu and Chugunova 2008).

From the search tree, it is possible to deduce the conditional probability distribution to the data event $d_{n\prime}$ corresponding to the subtemplate $\tau_{n\prime}$ from the conditional probability distribution to the data event d_n. Indeed, during simulations, the template will have only sparse conditioning data (at least in the beginning). So, it is necessary to identify in the search tree all nodes that are consistent with conditioning data. They are all used to infer the conditional histogram of the point to be simulated.

The SNESIM algorithm is based on the same approach as other simulation techniques, each simulated node becomes a hard data conditioning the next points to be simulated later in the sequence (Goovaerts 1997).

The SNESIM algorithm can be summed up in 6 steps (Strebelle 2000, 2002):

1. Define the geometric extent of the data events, scan the training image and store the occurrences of data events into a search tree.

2. Assign sample data (hard data) to the closest grid node. Choose a seed value to define a random path for the simulation to visit each unsampled node once.

3. At each unsampled node of location $\mathbf{u}$, look for conditioning data inside the geometric template. If there are $n\prime$ data forming the data event $d_{n\prime}$, find in the search tree the corresponding data event to estimate the cpdf of the simulated node. Here, it is possible to define a minimum number of replicates in the training image. If it is not reached, the furthest conditioning point is not considered until the number of replicates is sufficient.

4. From the cpdf read from the search tree, draw randomly a simulated value s_j for node $\mathbf{u}$. This point becomes a hard data for next nodes to be simulated.

5. Move to the next node and repeat steps 3 and 4.

6. Loop until all nodes are simulated to get one stochastic realization. Start again from step 2, with another random number to generate an alternative realization.

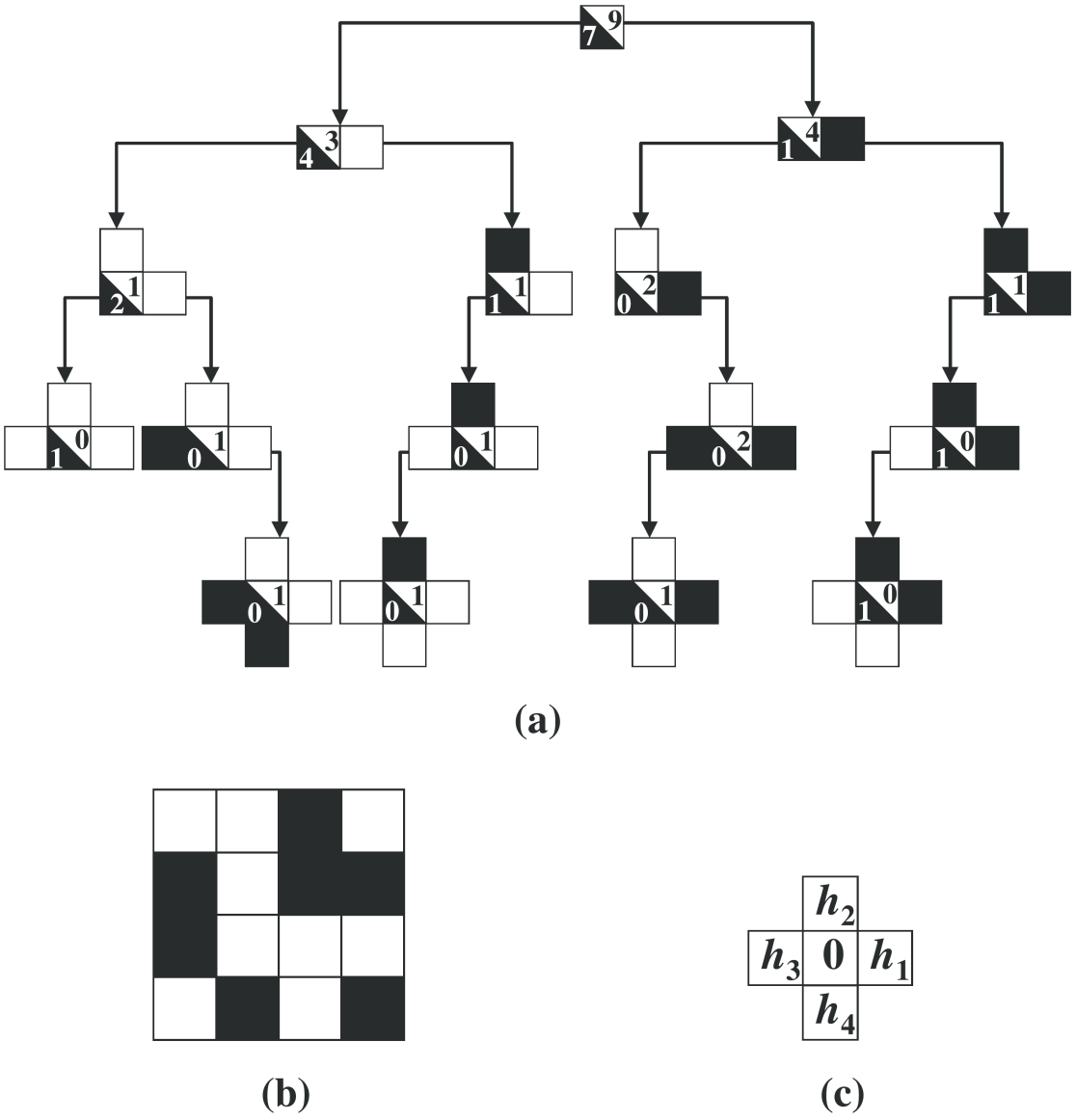

Figure 3.1: (a) Example of search tree when scanning (b) a training image (here representing a two facies model) using (c) a five points template, i.e. a central node and four neighbors. The numbers in the central node represent the occurrence of the facies given the data event $c_j(d_n)$ (after Hu and Chugunova 2008).

The algorithm as it is defined does not ensure that simulated realizations will honour any target marginal distribution $\{p_j,\ j = 1, 2, \ldots, J\}$ of the categorical variable. A first precaution is to ensure that the training image has proportions close to the target proportions. Next a servosystem was implemented (Strebelle 2000) to modify the proportions to remain close to the target proportions. If the current distribution is $\{p_j^c,\ j = 1, 2, \ldots, J\}$, the difference $p_j - p_j^c$ is added to the conditional probability inferred from the training image through a scaling parameter μ

$$Prob\prime\{S(\mathbf{u}) = s_j|d_n\} = Prob\{S(\mathbf{u}) = s_j|d_n\} + \mu \times (p_j - p_j^c). \tag{3.7}$$

If for the category s_j the proportion is overestimated, then $p_j - p_j^c < 0$, the corresponding probability is reduced.

Another possibility, when the training image and target proportions are not too different is to use Bayesian updating (Liu 2006, Hu and Chugunova 2008). Equation 3.5 can be written in the form

$$P(A|D) = \frac{P(A, D)}{P(D)} \tag{3.8}$$

where both numerator and denominator are derived from the training images. According to Bayes relation, this conditional probability can be transformed into

$$P(A|D) = \frac{P(D|A)P(A)}{P(D)} = \frac{P(D|A)P(A)}{P(D|A)P(A) + P(D|\overline{A})P(\overline{A})} \tag{3.9}$$

where $\overline{A}$ is non-A, i.e. $P(\overline{A}) = 1 - P(A)$. In this relationship, $P(A)$ from the training image can be replaced by the target proportion $P\prime(A)$. Equation 3.9 can then be expressed as:

$$P(A|D) = \frac{P\prime(A)(1 - P(A))P(A|D)}{(P\prime(A) - P(A)) + P(A)(A - P\prime(A))} \tag{3.10}$$

3.2.3 Multiple grid approach

A major drawback of scanning the training image is that the RAM and CPU demand increases rapidly with the size of the template, so the use of large template is difficult in practice. However, a large template is needed to reproduce more accurately the geometrical features

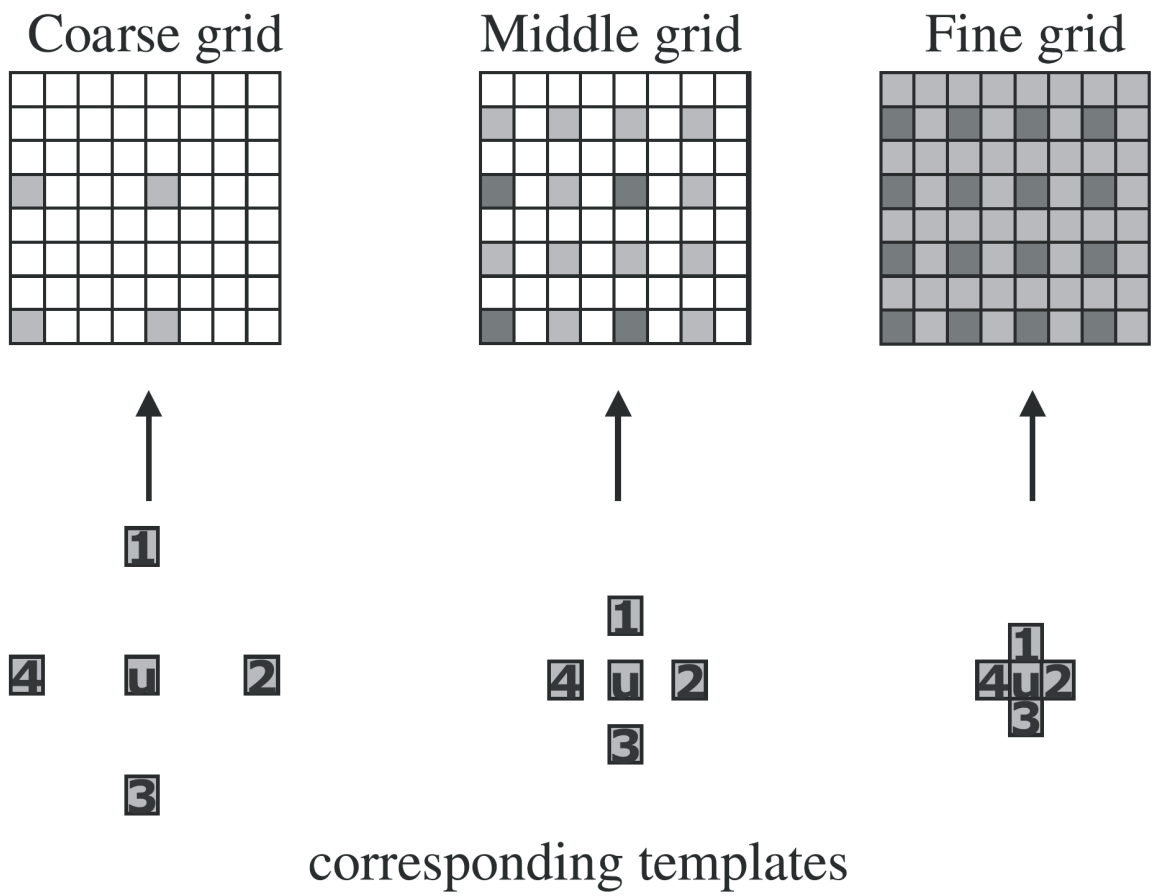

Figure 3.2: Example of the successive simulation grids and their templates considering a 3 grid approach. The larger grid enables a better reproduction of the large scale structure (after Hu and Chugunova 2008).

of the training image. Large templates also result in low reproduction of data events and non-representative statistics. In contrasts, small templates are not able to capture large scale structures in the training image.

One possibility to make a compromise between these two aspects is to use the multiple grid approach (Tran 1994). The principle is to use nested and increasingly finer grids (Strebelle 2000). If we consider G grids, the g^{th} $(1 \leq g \leq G)$ grid is constituted by each 2^{g-1}-th node of the final simulation grid $(g = 1)$ (figure 3.2). For each grid, the geometrical template $\tau_n^g = \{\mathbf{h}_\alpha^g,\ \alpha = 1, 2, \ldots, n\}$, with $\mathbf{h}_\alpha^g = 2^{g-1}\mathbf{h}_\alpha$, is rescaled to the spacing of the grid to be simulated. The larger grid captures the large scale structures of the training image, and the small grid captures the small scale structures.

The multiple grid approach requires to build a search tree for each grid. The values simulated for the grid are kept as conditioning data for the next grids. For the larger grids, sample data

are assigned to the closer node, but removed after simulation. They are only assigned for the finer grid.

Liu (2006) investigated the number of multi-grid to use for simulations. He found that large numbers of grid (more than 4 in this specific case) were not able to reproduce large scale structures better because the number of replicates in the training image becomes too small. Liu (2006) also showed that an increase of the size of the template does not always improve the reproduction of structures. Indeed, if a large template is used, the number of replicates can be too low so that some conditioning data are dropped, which is equivalent to a small template.

To improve the reproduction of patterns from the training image, Strebelle and Remy (2005) proposed a post-processing algorithm. For points which were simulated using a low number of conditioning data (clue of incompatibility with the patterns of the training image), a resimulation process is carried out.

3.2.4 Non-stationarity and spatial trends

The SNESIM algorithm assumes that the training image is stationary; it signifies that statistics are independent of the location. Using a non-stationary training image, such as a fan-delta for example, would result in realizations completely different from the training image. A possible way to overcome this and to produce non-stationary realizations is to constrain the simulation using spatial trends defining rotation angle and affinity ratios as location-dependent information (Strebelle and Zhang 2005).

In the case of channels for example, this enables to vary the direction and size of the channels according to their location on the field. Figure 3.3 shows an example of rotation and affinity according to trend regions defined using local maps.

It is also possible to define various training images on different regions or to add spatial trends, to take into account a variation of facies with depth for example.

3.2.5 Integration of secondary or soft data

Multiple-point statistics enables conditioning simulations with soft data, such as geophysical data or models. Strebelle (2000, 2002) proposes to extend the probability distribution of the variable $S(\mathbf{u})$ condition to the data event and a collocated soft data C

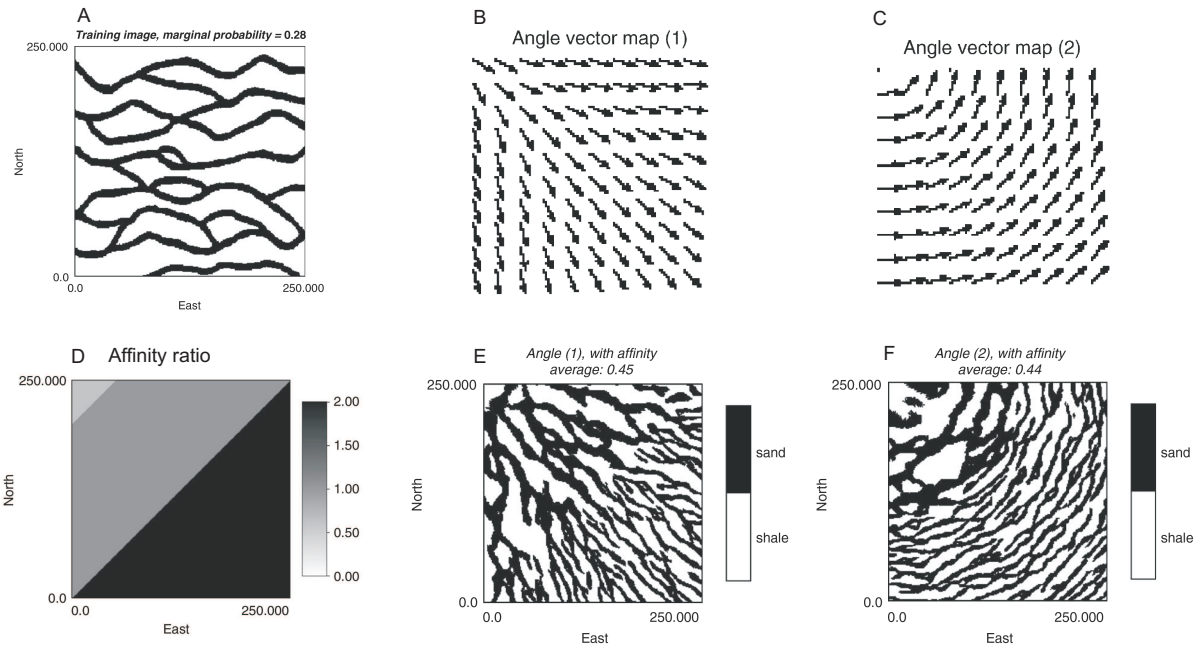

Figure 3.3: Example of rotation and affinity of (A) a channelized training image with (B) and (C) two different angle maps and (D) an affinity map. (E) and (F) show two respective realizations (modified after Liu 2006).

$$Prob\{I(u,j)=1|D=1,C\}=\frac{Prob\{I(u,j)=1,D=1,C\}}{Prob\{D=1,C\}}. \tag{3.11}$$

This approach requires to use an additional training image for the soft data, possibly by forward modeling of the initial training image. In practice, only a few-location or only the central node are used for soft data conditioning. The secondary variable is also often continuous and should be divided in a few categories (3 or 4).

If a training image of the secondary data is not available or not relevant, the analytical approximation proposed by Journel (2002) assuming the permanence of ratio to derive the so called τ model can be used. This model expresses the relation between the marginal probabilities of $A = I(u,j)$, the probabilities of A conditioned to D, the training image, and C, the soft data, and the probability of A jointly conditioned to D and C. If we set

$$a=\frac{1-P(A)}{P(A)},\ d=\frac{1-P(A|D)}{P(A|D)},\ c=\frac{1-P(A|C)}{P(A|C)}\ x=\frac{1-P(A|D,C)}{P(A|D,C)}, \tag{3.12}$$

the permanence of ratios, corresponding to a relative dependence of the contribution of D and C, expresses that

$$\frac{x}{d} \simeq \frac{c}{a} \tag{3.13}$$

and thus

$$P(A|D,C) = \frac{a}{a+dc} \tag{3.14}$$

The τ model consists in allowing some dependence between D and C by adding a exponent to the relation

$$\frac{x}{d} = \left(\frac{c}{a}\right)^{\tau}. \tag{3.15}$$

Practically, using an exponent $\tau > 1$ is equivalent to give more weight to the soft data C compared to the training image D and inversely. So the parameter τ measures the degree of redundancy between D and C with respect to A (Krishnan et al. 2005). It may be difficult to quantify the value of τ. In practice, it is almost always set to 1. In addition, the τ model can be easily extended to any additional data sets, using as many exponent τ_i as there are soft data sets (Journel 2002)

$$\frac{x}{a} = \left(\frac{c_1}{a}\right)^{\tau_1} \left(\frac{c_2}{a}\right)^{\tau_2} \cdots \left(\frac{c_n}{a}\right)^{\tau_n}. \tag{3.16}$$

As can be seen from equation 3.12, using the τ model requires to estimate $P(A|C)$, i.e. the probability to have a given facies for some value of the soft data, here the geophysical parameter. The problem is similar to find a petrophysical relationship linking two different parameter.

3.2.6 Alternative implementations

Caers (2001) proposed an alternative way to simulate with multiple-point geostatistics, using a neural network to consider all the neighbors of the template jointly. The first step consists in pattern extraction from the training image. The second step consists in pattern recognition. Here, a neural network is used to estimate the local probability model. The one-hidden-layer neural network considers all the data of the data event jointly and map the non-linear relation towards the probability using sets of parameters. These parameters are optimized using a training data set from the training image. Once trained, the network can be used to determine

the probability of facies during simulation. This is the last step of the algorithm: pattern reproduction. Here, an initial random image is constructed, i.e all nodes are assigned an initial random value, except nodes sampled with hard data. Then, each node is visited using a random path. A new facies is proposed and accepted with a probability depending on the output of the neural network. In case of soft data, the additional attribute is added to the data set of the neural network.

Zhang et al. (2006) and Wu et al. (2008) proposed an alternative to the SNESIM algorithm which works for both categorical and continuous variable, called FILTERSIM. Instead of building a search tree with possibly large template, the authors reduce the complexity of the template to a limited number of filters, reducing the RAM demand of the algorithm. All the patterns of the training image are scanned and their filtered score is stored in a database. The patterns are then classified and "similar patterns" are grouped within bins; for all bins a "prototype" representing the average pattern of the group is calculated. During simulation, the (incomplete) data event is extracted and compared with all prototypes using a distance calculation. The closest prototype is chosen and one of the patterns of this bin is selected and anchored in the simulation grid, the inner part being considered as new hard data for the next points to be simulated, the outer part being considered as soft data. So, this is not a point-by-point simulation but a pattern simulation.

Given some drawbacks of the SNESIM algorithm (high memory demand, stationarity or reproduction issues), Arpat and Caers (2007) gave up the probabilistic framework and treated the problem as a pattern reproduction problem instead of statistics reproduction problem in their SIMPAT algorithm. Consequently, the training image is used as a database of patterns, not a source to calculate cpdf and the realization is done by entire patterns. When scanning the training image, a vector with node values at the different positions is stored in a database. During simulation, the data event is extracted, with a hard data event and a previously simulated nodes event, and compared using a distance calculation to the patterns of the database. The most similar pattern, or one of them, is assigned at the position of the template and all nodes are modified, even the ones with an already simulated value, except hard data. Looking only for similar patterns, the training image does not require stationarity and the algorithm may work for continuous variable, too.

Mariethoz et al. (2010) developed another algorithm called Direct Sampling. This technique also works for both categorical and continuous variables. The technique also involves the possibility to carry out direct cosimulations. Their assumption is that sampling the cpdf does not require to compute it. In consequence, it is not needed to scan and store all data events in a search tree. What is done is to sample randomly the training image conditioned to the data event. Practically, for each simulated node, a part of the training image is scanned for n nodes with a random path and the central node of the first matching data event is assigned to the simulated node. A matching data event is a data event whose distance to the observed pattern is lower than a given threshold. To avoid large computational time, a maximum number of location in the training image are tested. If this maximum value is reached, the pattern with the lower distance is used for simulation. Soft data and secondary variable are addressed using weighted distances definition. This technique reduces the memory demand of the simulation and does not ask for a fix geometry of the data event and a multiple grid approach. CPU time is not much increased because the scanning of the training image is stopped after the first match. Meerschman et al. (2013) tested the sensitivity of the important parameters of the Direct Sampling algorithm on real TI cases, both 2D and 3D. The most influencing parameters are the acceptance threshold, the number of neighbors and the part of the training image that is scanned. Reducing the two first parameters decreases the CPU time but at the expense of the quality of the simulation.

Straubhaar et al. (2011) proposed to replace the tree structure present in the SNESIM algorithm by a list approach in their IMPALA code. The list is defined as a pair of vectors, the first being the data event and the second the occurrence of each facies in the center of the template. The list is sorted and is then used as a catalog to compute the cpdf needed during simulation. The main benefit is to reduce the RAM demand compared to the search tree. However, the algorithm based on search tree is faster, except for large training images with large templates. The use of lists allows a straightforward parallelization of the algorithm, distributing lists over several processors. Straubhaar et al. (2013) combined both methods, i.e. trees and lists, to get the benefits of both methods: low RAM demand and CPU efficiency. Practically, the lists are indexed by trees of reduced sizes. Doing so, it is not necessary to scan the whole list to find those elements compatible with the data event, just as in the tree search method

(Strebelle 2000, 2002). The parallelization of the list approach is still possible.

Renard et al. (2011) developed an algorithm based on multiple-point statistics to take into account information brought by connectivity data, obtained from tracer or well tests. They considered that two points are connected if they are part of the same geobody. They used the training image of MPS to extract data events where the specified connectivity is observed. A compatibility verification can be carried out to check that connectivity data are consistent with the training image. If two points are supposed to be connected, a replicate extracted from the training image is first anchored on the simulation grid and a specific path is extracted to connect the two points in the simulation. Then the MPS simulation is run as usual, with the path being conditioning data for next points to be simulated.

Huang et al. (2013) implemented a GPU computing scheme for the SNESIM algorithm, allowing parallel operations during the simulation of a node. The parallelization effort is made in retrieving the occurrence of the data event $c_k(d\prime_n)$.

3.2.7 Examples of application

The first successful applications of multiple-point statistics were carried out within the context of petroleum engineering (e.g. Strebelle et al. 2003, Liu et al. 2004, Maharaja and Journel 2005, Hoffman et al. 2005). Here, we will focus on applications in hydrogeology.

Feyen and Caers (2006) used multiple-point statistics to define the hydrofacies structure of a synthetic aquifer, intrafacies being built using traditional two-point correlation methods to represent the facies variability of hydraulic conductivity. The aim was to study and analyze the various sources of uncertainty for flow and transport models. The geological scenario represented by the training image, the prior proportions of facies and the orientation of channels, depicting the geometry of facies is one of the major sources of uncertainty for solute transport predictions. The second source of uncertainty lies in the hydraulic properties, i.e. the interval of variation and the variogram of hydraulic conductivity, this uncertainty has more impact for head predictions.

Huysmans and Dassargues (2009) applied multiple-point geostatistics in the Brussel sands aquifer. First, a reliable training image is built based on outcrop studies to identify sand-rich and clay-rich zones and field measurements (air permeability measurements) were carried out to study the variability of parameters of the facies. The deduced variogram was used to

simulate the intrafacies variability of the simulations. These simulations are used as input for flow and transport simulations to highlight the role of small-scale heterogeneity on the behavior of pollutants and the benefits of using MPS instead of variogram-based methods, due to the important role of clay drapes in this aquifer. Huysmans and Dassargues (2012) further highlight the role of those clay drapes during a large-scale pumping experiment revealing anisotropic drawdowns. Indeed, the direction of anisotropy was parallel to the direction of these drapes. Modeling was performed to investigate the role of these drapes, simulated with multiple-point statistics, to confirm that they may explain the large-scale behavior of the aquifer.

Michael et al. (2010) combined multiple-point statistics, variogram-based statistics, geologic process and object-based models to represent at best turbiditic reservoirs. The simulation of geologic processes produces realistic models but are difficult to constrain with actual data. They do not respect stationarity and cannot be directly used as training images. Here, they are used to extract simplified statistics about geobodies geometry (e.g. channels and lobes size) which are then used to generate object-based realizations. These realizations are used as various training images, used together to build the search tree, used in the snesim algorithm to generate conditional simulations.

Trainor (2010) studied the value of information (VOI) for spatial problems in Earth Sciences through synthetic benchmarks based on multiple-point geostatistics. The aim is to study if a new source of information will help to take the optimal action in a specific problem. Uncertainty in Earth Sciences being large, prior geologic uncertainty and data reliability have to be assessed in such a process. She focused particularly on the VOI brought by geophysical data to improve decision making and on dynamic processes.

Coz et al. (2011) used multiple-point statistics to study heterogeneities in the vadose zone along a river in Niger where the pressure exerted on groundwater recharge is increasing. Landsat images were used to build a map of current clay deposits and boreholes were dug to have insights on the vertical distribution of sediments. Horizontally, the geometry of clay bodies is very complex (oxbow lakes and abandoned channels) and the snesim algorithm was applied using actual deposit satellite images as training images. To use these 2D images to build 3D models, 3D training images superposing layers of the same 2D images were built and used to extract statistics, whereas the vertical variability was obtained by varying the vertical radius in the

search template.

Blouin et al. (2012) applied a combination of multiple-point statistics and sequential Gaussian simulations (SGS) to study aquifer heterogeneity of glacial and deltaic sediments and produce management tools for aquifer. Geological data are first associated with hydrogeological facies and a training image is built based on a first geological description of the deposits through boreholes and ground penetrating radar profiles. This methodology may not respect the stationarity of the TI and the simplification of the initial model may reduce the range of heterogeneity in the TI. The facies are simulated with MPS and the variation of hydraulic conductivity within the facies, measured on the field with slug tests, are simulated with SGS. Simulations are used as input to steady-state simulations to pick the 10 best matching hydraulic heads. Those models are then used for transport simulations of a continuous contamination source zone and the results are analyzed (mean concentration and standard deviation) to study the uncertainty related to hydrogeological models.

dell'Arciprete et al. (2012) compared multiple-point statistics with sequential indicator and transition probability simulations at different scales on an alluvial aquifer analogue calibrated on direct observations of facies. Discretized vertical facies (4 hydrofacies were recognized) maps from quarry outcrops were used as training image, with the drawback that they are not stationary and only 2D. The methods were compared based on visual inspections, probability of occurrence of facies, comparative image analysis with vertical facies maps and connectivity analysis. MPS reproduces best the shape and size of the most abundant facies, but reproduces worse than other simulation techniques less abundant facies.

Ronayne et al. (2008) used multiple-point statistics to study the alluvial fan system underlying the Lawrence Livermore National laboratory where subsurface flow and transport are driven by discrete channel deposits. They combined the geostatistical method with a stochastic hydrogeological inversion method to integrate dynamic flow data. Such a procedure will be further investigated in chapter 4.

Khodabakhsi and Jafarpour (2013) studied the uncertainty related to training images. Indeed, training images are based on assumptions and built on uncertain geologic information and may not represent the full range of heterogeneity. They propose to represent the geologic facies distribution using multiple training images. During simulations, each TI is first assessed

the same weight, those weigths are then updated according to their match with observed data through a likelihood function. In addition, they used an ensemble Kalman filter (EnKF) approach to invert flow data. EnKF results do not preserve directly the discrete nature of MPS but can be used to infer probabilities of facies distribution, subsequently used as conditioning soft data for MPS simulations. After a few updates, the weight given to the "correct" TI is almost equal to 1. The methodology does not remove the uncertainty intrinsic to each TI. If the algorithm is not able to find the optimal training image, the authors recommend to use the results to build new TIs.

The analysis of the studies above has two important outcomes.

1. The role and the uncertainty related to the training image remains a major issue in MPS. Reliable training images generally allow generating better models. However, modifications in the training image will have important impacts on the architecture of deposits. Few studies have tackled the problem of estimating the reliability of training images. Available information is not always sufficient to provide a unique training image and alternatives must be considered. Geophysical data contains relevant and spatially distributed indirect information on the heterogeneity of deposits. It aids to improve our knowledge of the prior. However, their resolution is not sufficient to image small scale structures present in the training image. In section 3.4, we will see how geophysical data may be used to verify the consistency and derive the probability of different training image-based scenarios.

2. The use of geophysical data as soft data in MPS for environmental studies is not yet well documented in the literature, especially when more than two facies are considered. In contrasts with the petroleum industry where seismic attributes are commonly used to constrain simulations, few studies have used electrical resistivity tomography, a potential-based geophysical method, as soft data. In section 3.5, we will analyze how ERT can be used to constrain MPS realization when simulating three facies models. In chapter 4, its role in the construction of hydrogeological models will be highlighted within the context of multiple training image-based scenarios.

3.3 Training-image based scenarios for the Meuse alluvial aquifer

The construction or the choice of training images is one of the most important points in multiple-point statistics. As it appears from section 3.2, the architecture of facies in the simulations will be borrowed from the training image. The training image must content the expected geological features of the simulated environment. However, the training image has also to correspond with the objective of the study and the scale of investigation. As an example, in hydrogeological studies, one would like to have the training image in relation with hydrofacies or ranges of hydraulic conductivity, but this representation would be different in the case of a small-scale study and a catchment basin study.

3.3.1 Considerations about the scale

Bayer et al. (2011) and Comunian et al. (2011) developed an interesting methodology to build a geostatistical aquifer analog model with sedimentary structures at the decimeter scale. Real geological analogs are not often used as TI in MPS. Indeed, their intrinsic non-stationarity (due to the physical nature of the processes leading to heterogeneity) produces unacceptable simulations in most cases because MPS assume a spatial repetition of the features. Another problem is the need to use 3D training images, which are difficult to derive from field analogs, to obtain 3D models. They first divide their domain into regions corresponding to large scale heterogeneity and then simulate facies heterogeneity inside the regions with 3D training images obtained from object-based simulations. However, the scale chosen to build this model is very small. They used 9 million cells of 5 cm and 23 different regions. This was required by their objective to build a very realistic analog model, but could never be applied at the scale of a site of hundred meters or more.

We work at a scale where applied geophysics techniques may bring information and be used as soft data for geostatistical simulations. More precisely, electrical resistivity tomography will be the main method used to describe the alluvial deposits. The characteristics of ERT should also be taken into account regarding the scale at which we work. In the alluvial aquifer of the Meuse River, alluvial deposits have a thickness between 5 and 15 m. Dimensioning ERT profile is always a compromise between lateral resolution and depth of investigation. The later increases with the electrode spacing if the number of electrodes is kept the same. To image the

whole thickness of the Meuse alluvial aquifer, it is required to use a spacing between adjacent electrodes of about 2 m. Consequently, it will be impossible to image small-scale structures and heterogeneity using ERT. This does not signify that the small scale heterogeneity should not be part of the training image, but that ERT will not be informative for it.

The aim of the study is to integrate hydrogeological data such as hydraulic heads. This requires to run a forward flow simulator. Using models of small-scale heterogeneity to solve flow equations at site of hundred of meters would lead to heavy models with several million of cells, leading to high computational costs. Also, the SNESIM algorithm to build such models would require high memory resources and would be time consuming. Furthermore, describing the small-scale heterogeneity of the Meuse alluvial aquifer would require direct access to the deposits and specific sedimentological study. Such outcrops or studies are lacking in the area considered in this study. For this reason, it was decided to limit the scale of the study, at each level (geophysics, geostatistics and hydrogeology), at a metric scale.

The considerations above have an implication on what we will be able to model in our deposits. As an illustration, figure 3.4 shows an outcrop in the alluvial deposits of the Meuse River in Ampsin, Belgium. The bottom part of the figure shows the corresponding interpretation in terms of facies. On the top, there is 10 cm of soil lying on an almost completely laterally homogeneous layer of loam of about 75 cm. Below, there is an alternation of clayey sand and clayey gravel about 60 cm thick. At the bottom part of the outcrop, there is some sandy gravel with clean gravel beds.

With ERT, it should be possible to detect the main variations of facies. The top soil is too thin and would be associated with the loam layer. If the resistivity contrast is sufficient, a transition would be observed between the loam layer and the clayey sand/clayey gravel layer. The lateral transitions would be imaged if a resistivity contrast exists and the lateral extent is sufficient. However, this layer is only 60 cm. Here, it is located near the surface and may be detected. However, due to the loss of resolution and sensitivity of ERT with depth, the same layer deeper down the aquifer would be more difficult to image and its resistivity signature could be different. The small intercalation of clayey gravel and the bed of clean gravel within sandy gravel have a decimetric scale and could not be detected unequivocally with ERT.

The decimetric anomalies will not be model in the training images. However, higher scale

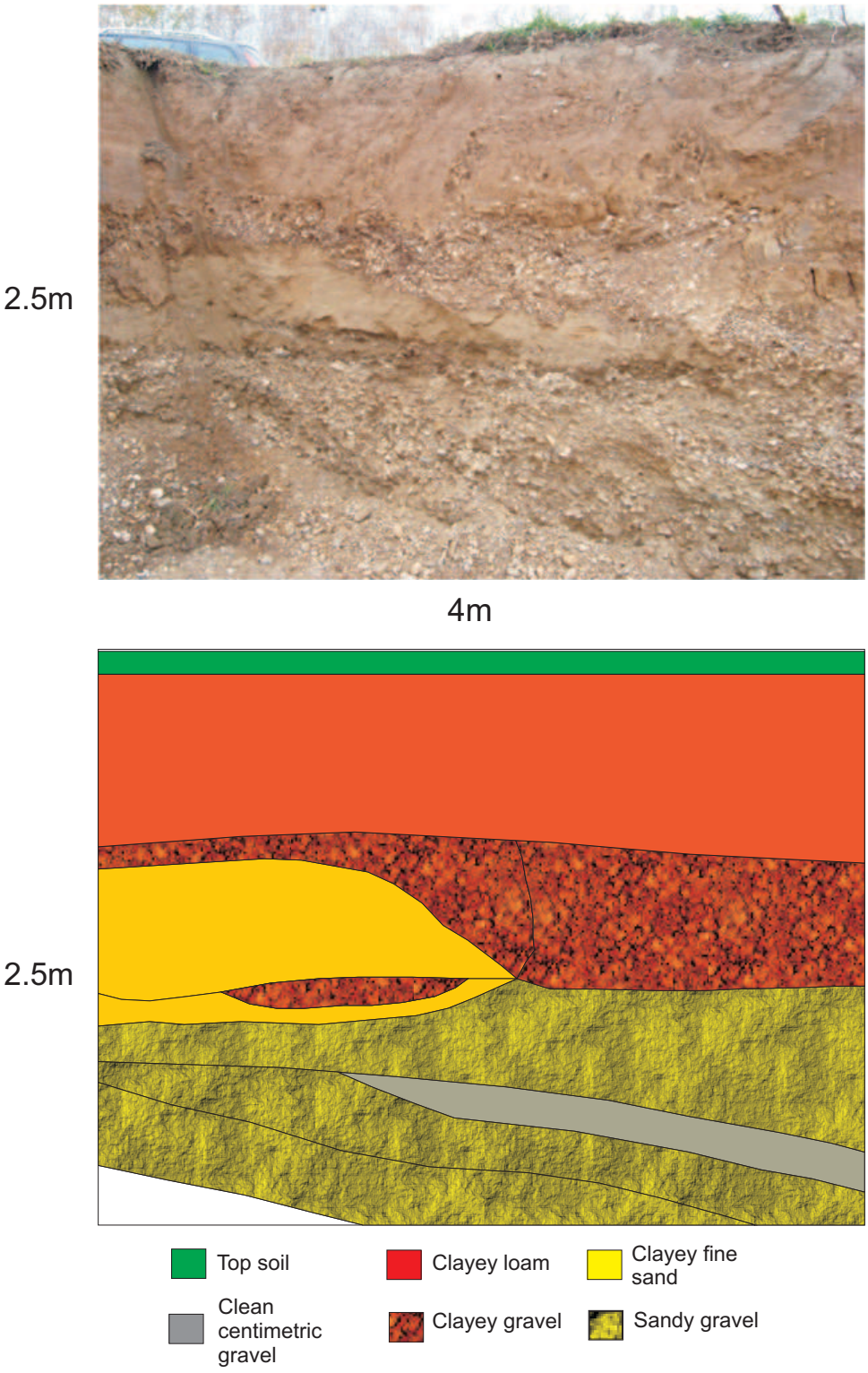

Figure 3.4: An outcrop of the upper part of alluvial deposits of the Meuse River alluvial aquifer in Ampsin and the corresponding interpretation in terms of facies.

anomalies, although not detected with ERT, could have a high influence on water flow and should be taken into account in the model. Even though imaging abilities of ERT are limited, such facies variations may be included in the training images, and subsequently into simulations.

3.3.2 Analysis of borehole data in the Meuse River alluvial aquifer

Most of the geological data sets available in the Meuse River alluvial aquifer in the area of Liege are borehole descriptions. These boreholes come from specific geological studies, geotechnical studies for civil engineer infrastructures or hydrogeological studies. Very few sedimentological studies are available to have an idea of the specific architecture of the Meuse River deposits.

Boreholes constitute very sparse data and are often not sufficient to have a comprehensive understanding of the geological environment. A first insight on the heterogeneity of alluvial deposits may be infer from the study carried out by Calembert (1968).

First, the analysis of borehole description shows that more than 20 different classes were used to describe the facies. If we consider other reports in the area, the number of description increases as the denomination may vary from one geologist to another. It is thus necessary to group some of the classes described to reduce the total number of existing categories. Indeed, for performance purposes, the number of categories in MPS should be limited to 3 to 4.

Another observation is that the proportions of the main classes (clay, loam, sand, gravel) vary along the river. In consequence, the target proportions and the proportions of facies in TI should be modified according to the specific local data. The deposits are dominated by gravel deposits, with several variants. The most abundant being gravel in sand matrix, but gravel in clay matrix are also present as well as clean gravel and pebbles. This is confirmed by other studies in the alluvial plain of the Meuse River such as the one of Monjoie (1970). Globally, in the zone studied by Calembert (1968), gravels represent about 52% of the deposits (11% for clayey gravel and 41% for sandy gravel and clean gravel). Loam, clay and sand constitute respectively 19%, 9% and 10% of the deposits. The last 10% are composed of backfills. These backfills may be constituted by many different materials and are anthropogenic.

In the study of Calembert (1968), some boreholes are more or less aligned along profiles. It enables to draw some cross-sections in the deposits. Except for sandy gravel which are more or less abundant everywhere in the deposits, it seems that adjacent boreholes do not show particular

correlation. Two adjacent boreholes are often several tenths of meters (often at least 50 m) away from each other. The architecture of the deposits is such that the set up of boreholes was not sufficient to derive clear geometrical features.

The results of Calembert (1968) are interesting because all the data were acquired within the same framework and thus some consistency is expected in the results. To derive general trends in the alluvial deposits of the Meuse River, a database of 354 boreholes description was compiled. From them, it appears that backfills are present in more than half of the cases. This can be understood by the high degree of anthropization of the studied area. In average, they represent 20% of the total length intercepted by the boreholes (from the surface to the bedrock) and are not negligible. Instead of backfills or when they are thin, a layer of loams, considered as surface loams, is encountered in 62% of the boreholes. These fluvial loams[1] represent about 15.5% of the total length. Those deposits constitute the upper part of the alluvial sediments.

The alluvial deposits of the Meuse River are often described as a three-layer system, with backfills, fluvial loams and sandy gravels. However, below the surface deposits, the sandy gravel layer displays strong lateral and vertical variations and is not homogeneous. Only 31% of the boreholes has a single unit of sandy gravel. The part of deposits composed of gravel or sandy gravel represents 36%, but it is about 56% if we except surface deposits. Sands and gravely sands represent 14% of the deposits and 22% if we except surface deposits. It is very difficult to distinguish a limit between sand and gravel because most of the time, they are both present, gravel being contained in a more or less abundant sandy matrix. The category "sand and gravel" thus represent 78% of the "non-surface deposits". Loam not present just below the surface represents only 4% of the deposits, clay and gravel in a clay matrix represent both 5% of the deposits, representing together 22% of the "non-surface" deposits.

The proportions presented here may help to guide the construction of a training image. As said previously, these proportions are only indicative of a general trend in the deposits and the results may be biased by several phenomena: the presence of backfill replacing natural deposits, some boreholes do not reach the bedrock, some surface loams should actually be classified in deep deposits, altered bedrock may be mixed with the deposits at the base of the aquifer, etc.

Our main aim in this study is oriented towards a hydrogeological application. The deposits

[1] loams are considered as the deposits with a particle size $< 63\ \mu m$, they may contain an important fraction of clayey minerals

described above may have values of hydraulic conductivity ranging several orders of magnitude, from less than 10^{-6} to more than 10^{-2} m/s. Given the description of boreholes, we decided to represent the alluvial deposits using 3 categories. They should represent the facies with low hydraulic conductivity, an intermediate facies and a facies with high hydraulic conductivity. This classification also makes sense in terms of resistivity distribution given the analogy between fluid flow and current flow. The first may be composed of deposits with fine elements (loam, clay, clayey gravel), the second may be composed of sand and sandy gravel facies, whereas the latter may be related with clean gravel or pluricentimetric to decimetric gravel. The proportions of these 3 categories may be linked to the proportions of the analyzed deposits. The first has a proportion of 22% and the sum of the two other is 78%. We estimated to 20% the proportions of clean gravel representing the third facies. The proportion of the second facies is thus 58%. Whenever possible, the proportions should be checked using site specific data and the corresponding training images should be modified accordingly.

3.3.3 Construction of training images

Few sedimentological studies have been carried out in the Meuse River to describe current alluvial deposits in Belgium. In contrast to old terrace deposits which are more easily accessible in outcrops, current deposits are difficult to observe directly. In his PhD thesis, Haddouchi (1987) tried to compile existing data and to derive geological and hydrogeological characteristics of the deposits. However, the scale of the study is not sufficiently detailed to produce reliable training images. In consequence, it was decided to base the training images on general sedimentological considerations related to traditional elements observed in fluvial systems.Considering the uncertainty related to this approach, several scenarios will be considered.

Fluvial systems are commonly divided into 4 types (e.g. Leopold and Walman 1957, Smith 1983):

- **braided systems** with numerous unstable channels and deposits dominated by gravel and sand bars;
- **meandering systems** with one channel with meanders and deposits characterized by point bars and flood plain deposits;

- **straight systems** with one straight channel and no point bar deposits, but a tendency to develop meanders;
- **anastomosed systems** with several stable channels that can be either braided, meandering or straight.

In reality, these four types are only categories in a continuum of fluvial systems. For example, between braided systems and meandering systems, many authors (e.g. Davis 1983, van den Berg 1995) recognize a transition type, called the coarse-grained meandering system, which has more coarse grained elements than traditional meandering systems. A single river may have several systems along its stream with the four types succeeding each other from upstream to downstream. At the same position, a fluvial system may also evolve with time.

Observations made in current river tend to show that the type of fluvial systems is mainly influenced by the discharge and the slope of the river (figure 3.5). The sediment load has also an influence. For example, braided systems are overloaded, i.e. they have a sediment load above the transport capacity of the stream and coarse particles are deposited (Davis 1983). To some extent, the width of the valley may also influence the fluvial type, confined valley tending to favor narrow single-thread channels compared to braided systems (Nanson and Croke 1992).

The current system of the Meuse river is highly influenced by human activities as the main stream of the river is canalized. Historic documents seem to show that before anthropogenic modifications, the Meuse river was a meandering system, with low sinuosity. However, locally, several channels were present (e.g. the current Boulevard de la Sauvenière in Liege) as it is possible in braided systems.

However, even if the current system is known, the system has largely evolved since the last glaciation. Berendsen and Stouthamer (2001) studied the Meuse river in its downstream part. The fluvial system evolved from a braided system after the end of the last glaciation period (10000 years BP) towards a meandering system or straight system in most part of its current stream.

Haddouchi (1987) stated that alluvial deposits of the Meuse river and its terraces suggest a braided system and anastomosed channels. The latter term suggesting that any kind of systems may exist in different channels. The development of braided systems being partly limited by the width of the valley, Haddouchi (1987) added that braided systems were probably present in zones

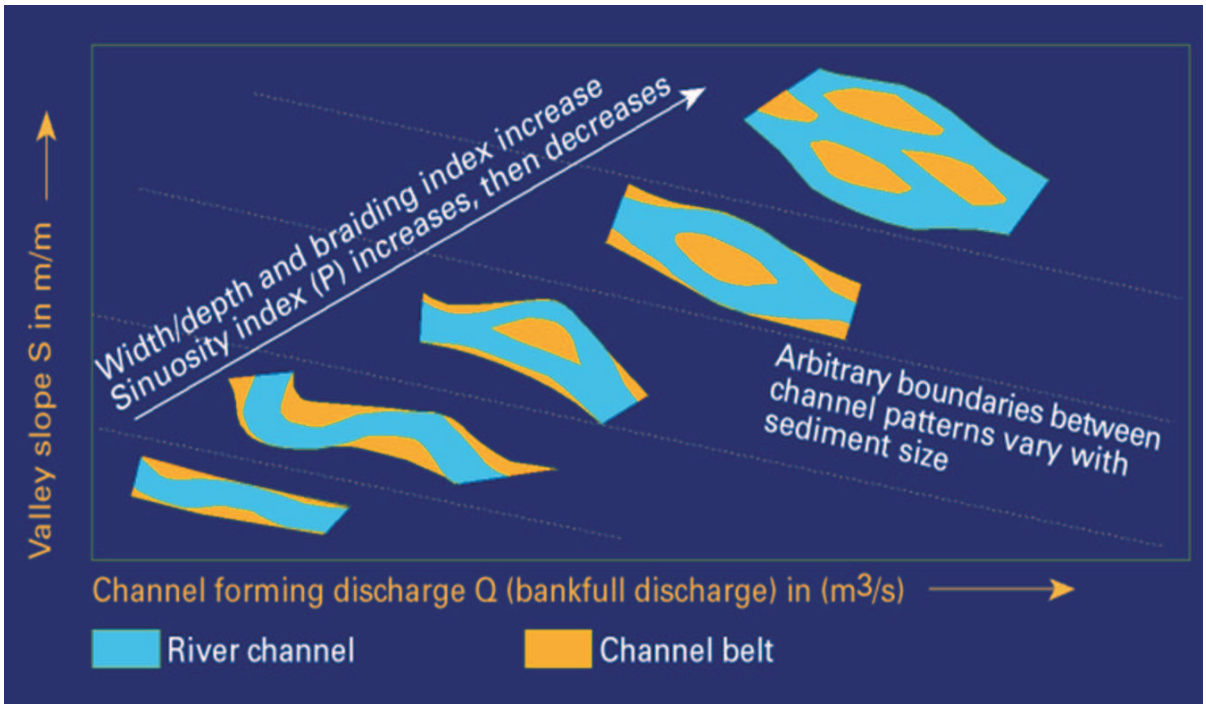

Figure 3.5: Evolution of the fluvial system with the slope of the valley and the discharge rate. Real examples show that overlaps exist between categories (Berendsen H. 2007 after Bridge 2003).

where the valley is wider. The deposits may probably display sedimentological characteristics of those deposits as well as the one of (coarse-grained) meandering systems.

In braided systems, several channels exist simultaneously and are separated by **bars** or small islands. Braided systems are overloaded and deposition occurs mainly by shifting of channels and bar aggradation. The ratio width/depth of bars can exceed 300 in some systems (Davis 1983). Generally, braided systems may have long periods of low discharge and short flooding periods during which all particles are moved. The bars are composed of sand and gravel, the coarsest particle being in the middle. Bars are often longitudinal but may also have alternative forms. These elements may be perturbed by cut and fill processes when new channels form or old channels are reoccupied (Davis 1983).

In such systems, we may expect longitudinal bars of clean coarse gravel surrounded by old channels filled with gravels in a finer matrix. Very fine sediments may be observed related to flooding events where fine sediments may have been deposited in old channels or depressions.

In meandering systems (figure 3.6), other elements are expected (Davis 1983). The load of the stream often includes coarse material that can be moved only during high discharge rate,

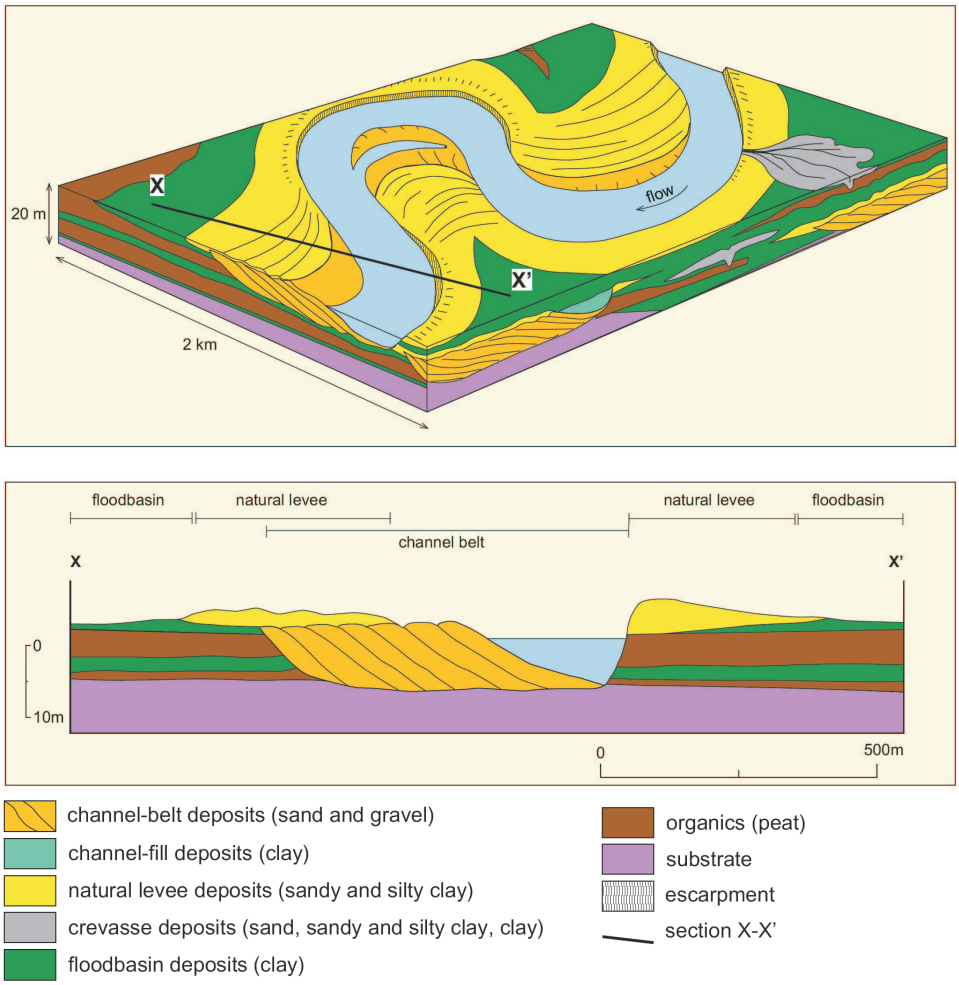

Figure 3.6: Block-diagram and cross-section of a meandering river in the Rhine-Meuse delta showing showing typical sedimentological units (after Gouw and Erkens 2007). In the area of Liege, less fine sediments and very few peat are expected.

whereas fine particles are transported downstream. These might be lenses deposited along the stream forming **channel lag deposits**. The greater accumulation environment in meandering system on the convex side of meanders is the **point bar deposit** constituted of gravel and sand. **Natural levees** are linear sediment accumulations along the stream bank with finer sediments than point bars. **Crevasse splays deposits** are localized environment where natural levees breached letting water entering the floodplain and sediment deposition occurred with a high fraction of fine sediments. **Flood basin deposits**, composed of silt and clay occupy the lowest part of the floodplain.

The sedimentological units described above may be related to the facies observed in the analysis of borehole. The high hydraulic conductivity facies may be related to the coarsest

deposits, i.e. to bars for braided systems or to channel lag deposits for meandering systems. Hereafter, we will refer to it as the "gravel" facies; it should represent about 20 % of the deposits. Conceptually, this facies should be shaped as bars or as channels. Both possibilities leading to different connectivity, both scenarios will be considered in the following.

The intermediate hydraulic conductivity unit is the most abundant in the Meuse river deposits (about 58%). It may be considered as the background facies surrounding other units. It consists of a mix of gravel and sand corresponding to point bars deposits and natural levees or the external part of bars. Hereafter, it will be denominated the "sand" facies. Being the background facies, it will not be modeled with special features but as the remaining parts between other facies.

Finally, the low hydraulic conductivity units composed of loam, clay and clayey gravel or sand represents 22% of the deposits. These deposits correspond to environments such as crevasse splays or floodplain deposits. Crevasse splays and parts of old channels may be described by objects having a lobe shape. In the alluvial deposits of the Meuse river, old floodplain deposits do not appear as continuous layers, except for the most recent surface fluvial loam. Old deposits such as floodplains may have been eroded by moving channels and could have potentially complex shapes. For simplicity, it was decided to model this facies with only one object-shape (lobe shape). It will be referred to as the "clay" facies.

This conceptualization of the deposits will lead to 3 facies training images. Figure 3.7 illustrates a field distribution of hydraulic conductivity within the Meuse River alluvial aquifer (Battle-Aguilar 2008) and shows how the proposed sedimentological bodies may be able to explain this distribution. The higher hydraulic conductivity zone could be related to a gravel channel or an elongated bar, whereas the lower conductivity zone could be linked with fine sediments in a lobe-shaped crevasse splay.

We built the training images using Tetris, the training image generator plugin of SGeMS. This plugin enables to build 3D TI with various possible object shapes and connections between different objects. Given the large uncertainty we have about the deposits, we tried to keep these training images as simple as possible to avoid adding complexity which was not supported by any data. Especially, there are very few studies about the interconnections and the size of the different objects. The distinction between channels and bars for the gravel facies will lead to

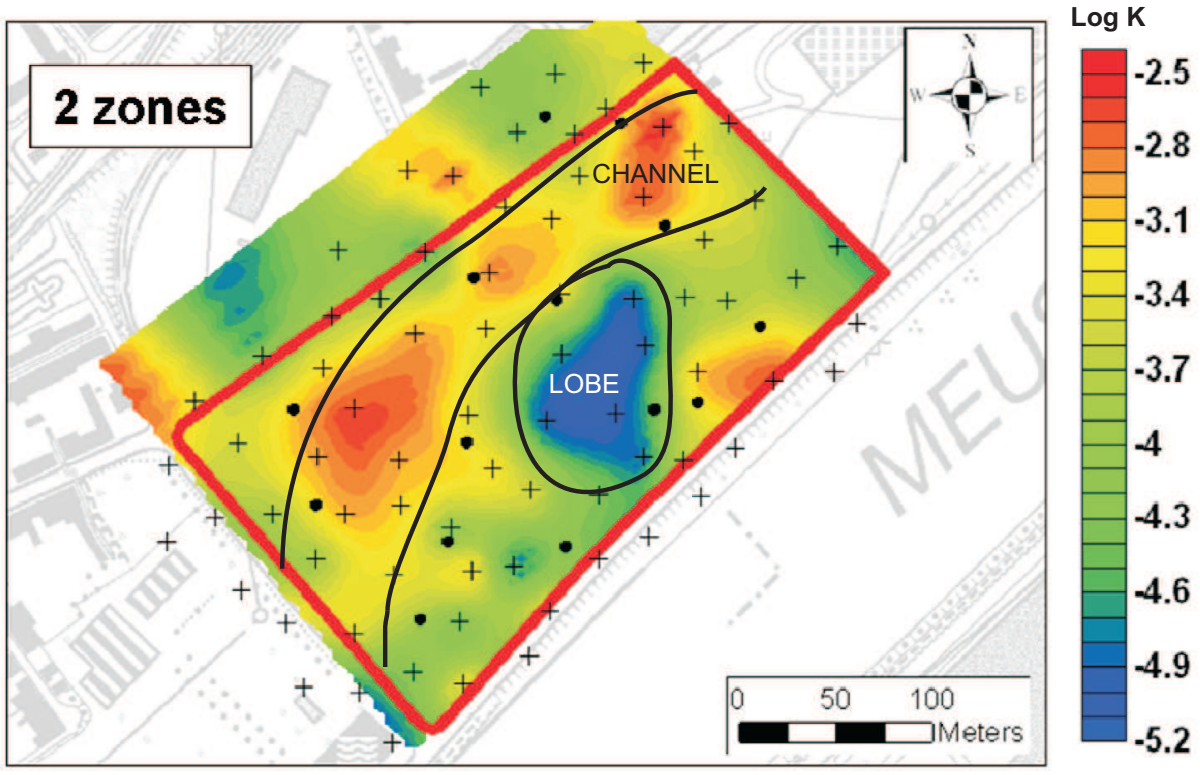

Figure 3.7: Example of the spatial distribution of the logarithm of hydraulic conductivity in the alluvial plain of the Meuse River in Flémalle, obtained using the pilot point method and a possible interpretation in terms of facies corresponding to gravel channel and clay lobe (modified after Battle-Aguilar 2008).

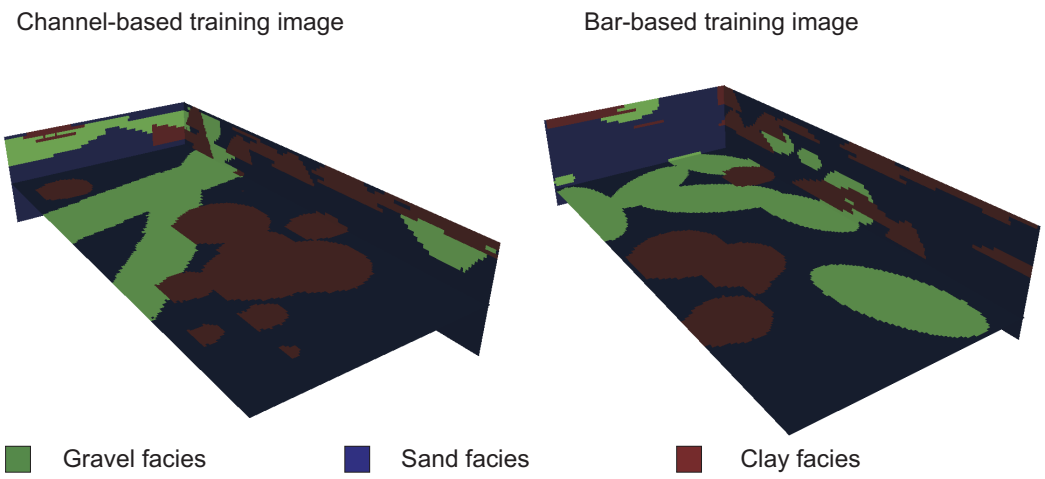

Figure 3.8: The two families of training images are characterized by a gravel facies made respectively of channels and bars.

two different families of training images (figure 3.8).

The review of available data made by Haddouchi (1987) illustrates the lack of data to derive reliable size and lateral extensions of the structural elements of the deposits. He produces a lot of cross-sections from boreholes but they are often far from each other (several tenths of meters). To overcome these limitations, he used geophysical techniques, namely vertical electrical sounding (VES) and seismic refraction. VES is sensitive to the resistivity of the deposits, however, it does not have a lateral resolution such as ERT to detect lateral variations and its vertical resolution is poor. It can only give general trends in the deposits and not detect small individual elements. Seismic refraction is suitable to detect the depth of the bedrock but alluvial deposits have mostly similar seismic velocities.

Consequently, it was not possible to draw a unique training image for the Meuse alluvial aquifer. For each category (channels or bars), several sizes of the elements (channels or bars, lobes) were considered. This introduces the uncertainty we have about the geological scenarios. In the next section, we will see a methodology to assess the consistency of training image-based geological scenarios with available geophysical data.

Category	Apparent resistivity ρ_a $(Ohm.m)$	$\log_{10} \rho_a$	Hydraulic conductivity (m/s)
1	< 100	< 2	$< 6 \times 10^{-3}$
2	$100 - 150$	$2 - 2.18$	$6 - 7 \times 10^{-3}$
3	$150 - 250$	$2.18 - 2.4$	$7 - 8 \times 10^{-3}$
4	$250 - 350$	$2.4 - 2.54$	$0.8 - 1 \times 10^{-2}$
5	> 350	> 2.54	$> 1 \times 10^{-2}$

Table 3.1: Relationship between apparent resistivity and hydraulic conductivity in the saturated gravel of the Meuse River alluvial aquifer (after Monjoie et al. 1987)

3.4 Consistency of training image-based scenarios with geophysical data

3.4.1 Extracting training images from geophysical images

Geophysical data may be used to draw the training image of specific sites. If we have a 3D cover of a geophysical parameter of some site in alluvial deposits, it would be possible to propose a classification of the geophysical parameter into categories to produce a discrete model of deposits that could be further used as a training image.

For example, Monjoie et al. (1987) proposed a classification linking apparent resistivity and hydraulic conductivity (table 3.1), based on a comparison of electrical sounding and pumping tests. These limits are based on apparent resistivity for measurements integrating large volumes of subsurface and not on the true resistivity distribution; they could thus be easily criticized. However, they almost correspond to limits visible on the histogram of the distribution of electrical resistivity observed on the field of Hermalle-sous-Argenteau (figure 3.9) where an ERT profile was carried out using a dipole-dipole array of 48 electrodes with 2 m electrode spacing (figure 3.10A).

Figure 3.10B shows the application of these limits for the specified profile in Hermalle-sous-Argenteau. It reveals the presence of different geological bodies corresponding to different values of resistivity. However, the direct application of classification on ERT images may be misleading because the resistivity structure is smoothed by the inversion process (see chapter 2). Nguyen et al. (2005) proposed to extract the limits of geological bodies using a watershed algorithm applied on the gradient image. Figure 3.10C shows the delimitation obtained after this process. A lot of individual bodies are detected due to small variations in the resistivity distribution inside bodies detected in figure 3.10B. Combining both results, figure 3.10D proposes a possible interpretation in terms of the three facies defined for the training images. Such image, possibly improved or extended using additional results, could be the starting ground to build a reliable

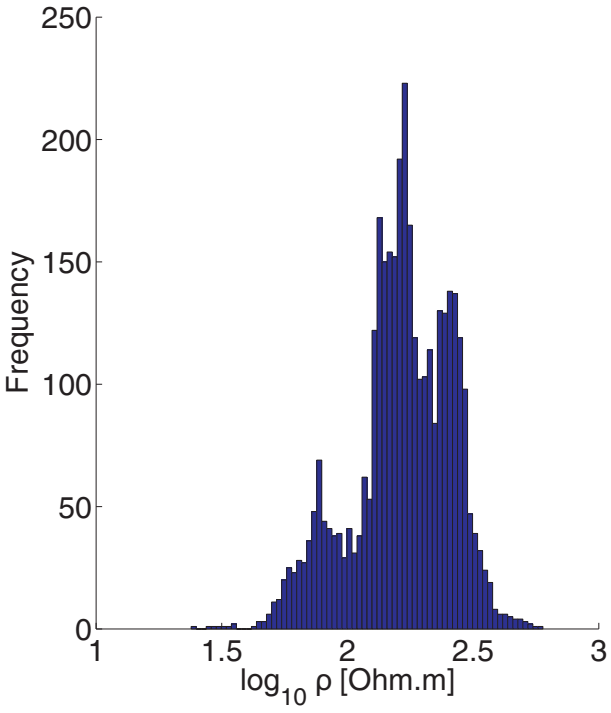

Figure 3.9: The histogram of the distribution of electrical resistivity on the site of Hermalle-sous-Argenteau shows at least three different zones characteristic of different geological bodies.

training image of the Meuse River alluvial aquifer from geophysical data.

However, using directly geophysical results to extract training images or object characteristics has two major drawbacks:

1. The aim of this study is to provide an integrated model of geological, geophysical and hydrogeological data. Similar ERT results will be further used to constrain, as soft data, MPS simulations. Using those data both for conditioning and for TI is against the principle of independence of information and does not follow the philosophy of MPS which is to use geological scenarios (not geophysical scenarios) to constrain simulations.

2. Geophysics may help to understand geological scenarios, but the resolution of ERT is not sufficient to differentiate unequivocally clay, sand and gravel facies, it only gives clues as it will be shown later. For example, small clay lenses may not be imaged because surrounded by more resistive facies and appear in the inverted section as a "sand facies". Geological interpretation may be biased by the integrating and smoothing effect of ERT.

Nevertheless, it is important to show that training images based on sedimentological considerations and geophysical data acquired on the field are consistent with each other. It could even

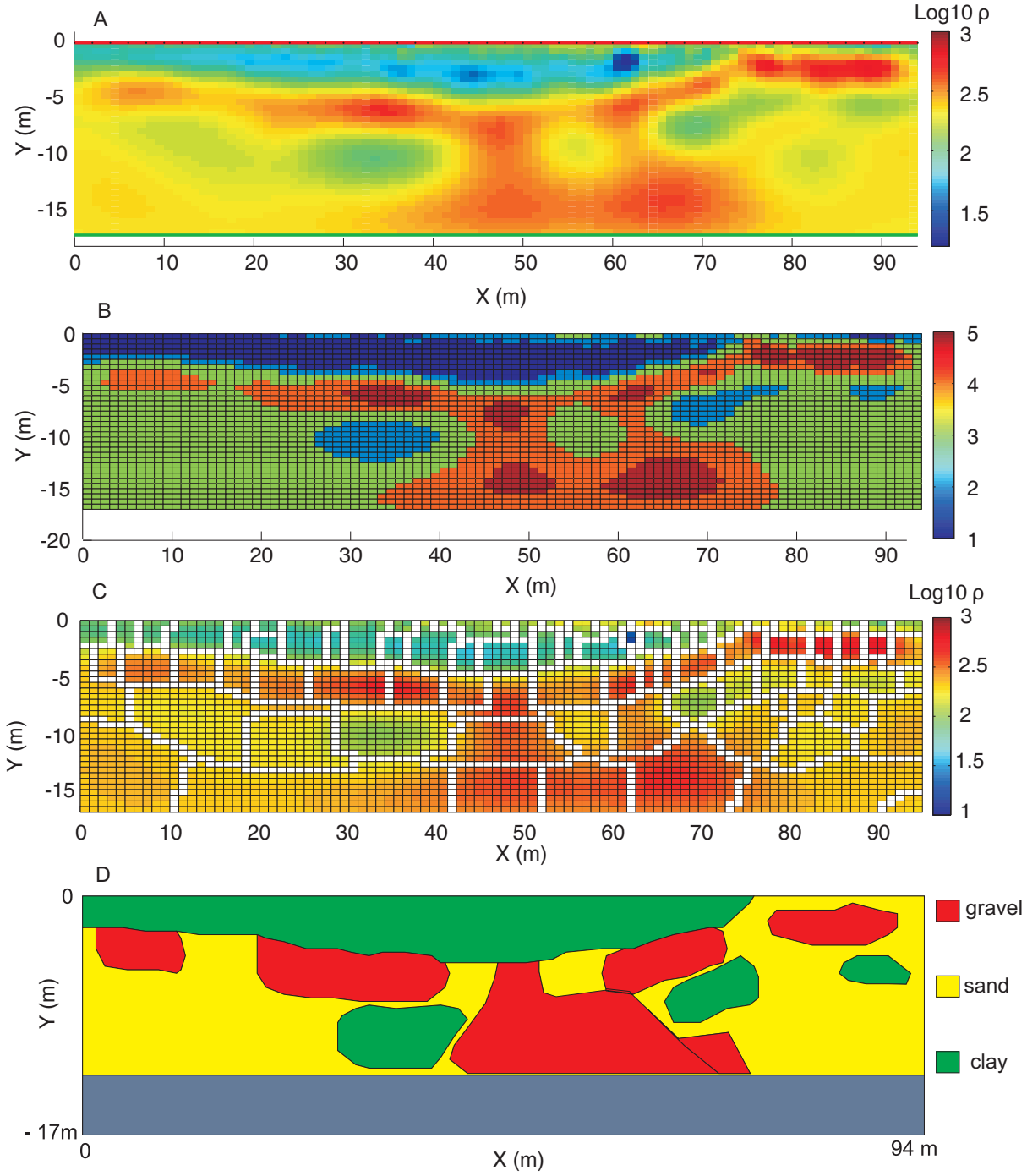

Figure 3.10: Classification of electrical resistivity into different categories. (A) The resistivity distribution shows vertical and lateral variations related to sediment heterogeneity. (B) The classification according to the values of table 3.1 enables to delimit geological bodies. (C) The application of the watershed algorithm divide the resistivity section into several pieces, limits corresponding to maximum gradients in A. (D) Combining the results of B and C yields a schematic cross-section of the deposits that could serve as a base for training image.

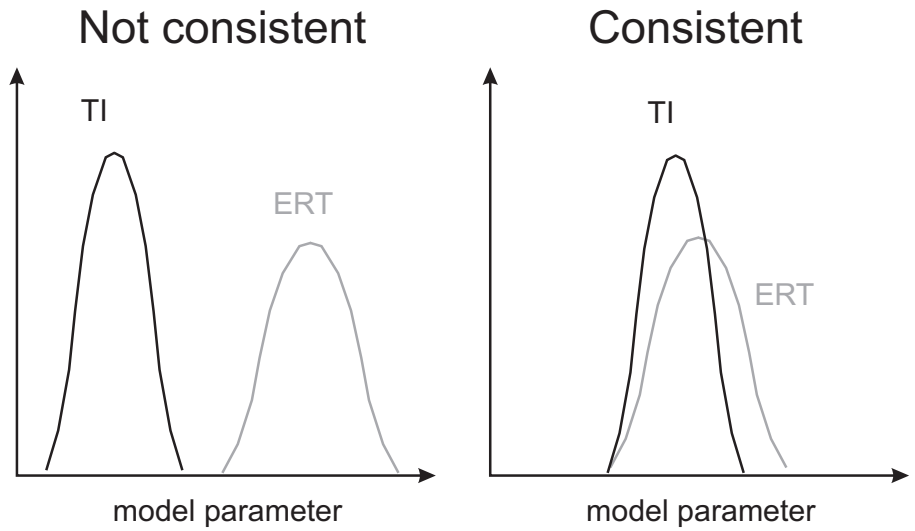

Figure 3.11: Distributions of models from TI and ERT in the case of non-consistency and consistency. Both data should share models in order to be used together in MPS simulations.

appear as mandatory since it would permit to independently validate the choice of the training image and investigate the uncertainty related to the scenarios considered in the training image.

By consistent, we mean that a model obtained by MPS simulation from a specific training image could also be recovered by a model based on geophysical data. This would validate the use of this specific geophysical data as a soft constraint for simulations. We may illustrate this using distributions (figure 3.11). If we have a distribution of model characteristics for each method (TI and ERT), both distributions should cover up each other, at least partially.

In the following section, we will develop a methodology to estimate the distribution corresponding to both types of data. This methodology will be used to verify the consistency of training images with geophysics and to try to refine the analysis of possible training image-based scenarios.

The methodology proposes to create subsurface models for each considered training image. From these models, we create synthetic geophysical data and from this synthetic data, synthetic inverted models. These models are then compared with a single inverted model obtained from a field survey, allowing for our definition of what is "consistent". To that extent, we calculate the Euclidean distance between any two inverted models as well as field data and visualize the results in a 2D or 3D space using multidimensional scaling (MDS). With this technique, it is possible to verify if field cases fall in the distribution represented by synthetic cases, and thus are consistent with them. In a second step, we present a cluster analysis on the MDS-map

to highlight which parameters are the most sensitive for the construction of TI. Based on this analysis, a probability of each geological scenario is computed through kernel smoothing of the densities in reduced projected metric space.

3.4.2 Multi-dimensional scaling approach

The aim of multidimensional scaling (MDS) si to represent measurements of similarity between pairs of objects into a low-dimensional space. In this low-dimensional space, two points close to each other will be considered as more similar than points far from each other. Representing the objects in low-dimensional space makes them more accessible and facilitate their visual inspection. For example, if we have a hundred aquifer models of several thousands of cells, it may be difficult to represent all the variability inside these models. The idea is to use an alternative parameter, that we will call the distance, to assess the similarity or difference between models. An interesting point is that the distance does not absolutely have to be calculated on the model itself, but could be calculated based on the response of the model to some stress factor: we could for example compare different models by comparing the drawdown at a well given some pumping rate.

MDS may have a lot of different applications with various levels of complexity. A simple problem used to introduce the MDS approach is to build a map of cities knowing only their distance two by two (here the distance is the length of the line linking two cities). This could be solved graphically using compasses. The relative position of the cities at the end of the process is unique, i.e. the relative position is always the same, but the final "map" may be rotated, mirrored or translated to represent the true map. This can be done for any type of distance and in any dimension. We refer to Borg and Groenen (2005) for details about the method. Here, we will only present the mathematical concepts needed to understand the method in our specific case as presented by Caers (2011) to visualize uncertainty in Earth sciences models.

We consider a number L of alternative models, a single model will be represented by the vector $\mathbf{x}_i$. Each vector $\mathbf{x}_i$ has a length N, corresponding either to the number of cells in the model or to a list of variables describing or quantifying the model. In the case of models of electrical resistivity, the vector $\mathbf{x}_i$ will contain the value of ρ for each cell of the model. We could also use a small number of variables such as the mean resistivity to describe the model.

Generally, N is quite large for Earth models, and L is often much smaller than N. The L models are collected in the matrix X such as

$$X = [\mathbf{x}_1\ \mathbf{x}_2\ \cdots\ \mathbf{x}_L]^T \text{ with size } L \times N. \tag{3.17}$$

Having L alternative models, we can build a matrix D of size $L \times L$ containing the distance between any two models. The element d_{ij} of the matrix represents the distance between x_i and x_j. If we assume that the models exist in a Cartesian space of N dimensions, each dimension being related to one grid cell in the model, we can calculate the Euclidean distance between a pair of model x_i and x_j

$$d_{ij} = \sqrt{(\mathbf{x}_i - \mathbf{x}_j)^T(\mathbf{x}_i - \mathbf{x}_j)}. \tag{3.18}$$

The distance calculation defines a metric space M. In contrast with the initial Cartesian space, M does not have orthogonal axes and origin, but only a measure of distance: we don't know exactly where the model $\mathbf{x}_i$ is, we only know how far it is to other models $\mathbf{x}_j,\ j = 1, \cdots, L$. This is similar to the problem of finding cities position from their mutual distances. It is possible to project the distance in the M space into a Cartesian grid of low dimensions using multidimensional scaling (MDS). The Euclidean distance is the easiest to use for spatial models because it compares them cell by cell. However, it is dependent on the specific location or orientation of the model. Other distances can be used to avoid this drawback or to compare spatial models based on their response to some stress factor.

The MDS procedure works in three steps (figure 3.12).

1. The distance matrix D is calculated and centered into a matrix B such that the resulting map origin is $\mathbf{0}$. This can be done by the transformation

$$b_{ij} = -\frac{1}{2}\left(d_{ij}^2 - \frac{1}{L}\sum_{k=1}^{L} d_{ik}^2 - \frac{1}{L}\sum_{l=1}^{L} d_{lj}^2 - \frac{1}{L^2}\sum_{k=1}^{L}\sum_{l=1}^{L} d_{kl}^2\right). \tag{3.19}$$

   This scalar expression can also be expressed in a matrix form. First a matrix A is constructed with elements

$$a_{ij} = -\frac{1}{2}d_{ij}^2 \tag{3.20}$$

and is centered using matrix H

$$H = I - \frac{1}{L}\mathbf{1}\mathbf{1}^T \tag{3.21}$$

with $\mathbf{1} = [1\ 1\ \cdots\ 1]^T$, $L \times 1$ and I the identity matrix such as

$$B = HAH \text{ of size } L \times L \tag{3.22}$$

In the present case, using the Euclidean distance, B can also be written as

$$B = (HX)(HX)^T. \tag{3.23}$$

2. The eigenvalue decomposition of B is calculated

$$B = V_B \Lambda_B V_B^T. \tag{3.24}$$

With, $L \ll N$ and the Euclidean distance, it can be shown that all eigenvalues are positive. Considering the expression 3.23 and 3.24 we can deduce that

$$X = V_B \Lambda_B^{1/2} \tag{3.25}$$

3. Using equation 3.25, it is possible to build a map of the models in X in any dimensions from 1 to L. We take the d largest eigenvalues such that

$$X_d = V_{B,d} \Lambda_{B,d}^{1/2} \ :\ X \xrightarrow{MDS} X_d \tag{3.26}$$

with $V_{B,d}$ containing the eigenvectors belonging to the d largest eigenvalues of the diagonal matrix $\Lambda_{B,d}$. X_d is the solution of the MDS procedure, with $X_d = [\mathbf{x}_{1,d}\ \mathbf{x}_{2,d}\ \cdots\ \mathbf{x}_{L,d}]$, and the mapped location have their centroid in the origin of the axes which are chosen as the principle axes of X. The resulting MDS map is centered at the origin of the axes. The value of the axes do not have any relevance, the axes do not have any scale or unit, only the relative position of models matters. For practical reason, the dimension of projection d is often 2, assuming that the $2D$ Euclidean distance is a good estimate of the LD Euclidean

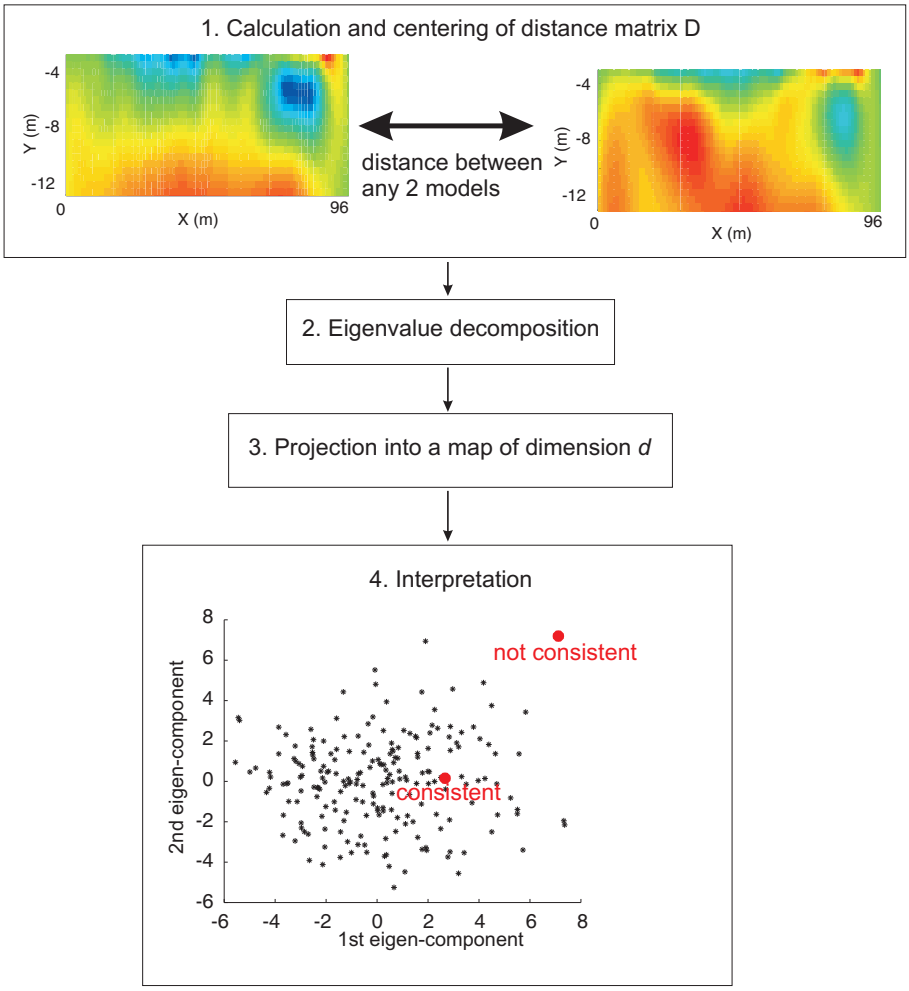

Figure 3.12: Schematic workflow of MDS.

distance between two models. The coordinates of a model in the MDS map are then

$$\mathbf{x}_{i,d=2} = (v_{1,i}\sqrt{\lambda_1}, v_{2,i}\sqrt{\lambda_2}) \tag{3.27}$$

with $v_{1,i}$ being the i^{th} entry of the first eigenvector and λ_1 the largest eigenvalue.

In this specific case, we use the MDS map to verify the consistency of field geophysical data sets with synthetic models from training image-based scenarios. We assume that the distribution of synthetic models in the MDS map is representative of the geophysical response of training image scenarios. If a field data set falls inside this distribution, the training image is consistent with available geophysical data. If it falls outside, it is not consistent.

Type of channel	Maximum width (in m)	Maximum thickness (in m)
Big	60	6
Medium	35	4.5
Small	10	3

Table 3.2: Dimensions characteristic of the channels of the training image scenarios.

3.4.3 Application to the training images of the Meuse River alluvial aquifer

In this section, the aim is to test the consistency of training image scenarios for the Meuse River aquifer with geophysical data acquired in this specific context. The geophysical data used for comparison will be ERT profiles acquired on the site of Hermalle-sous-Argenteau in 2011. We cannot directly compare training images, which are based on three categories generally represented by numbers (0, 1 and 2), and ERT data which can be represented either by field resistance data or electrical resistivity models.

Two paths could be used to compare them.

1. Transform ERT results into a three facies model as done in section 3.4.1.

2. Transform training images into resistivity models.

Given the limitations of ERT to retrieve precisely facies, the second option was chosen.

3.4.3.1 Choice of the scenarios to investigate

In section 3.3, we have seen that two families of training images were considered, with channels or with bars. These two families differ mainly at large scale as channels have a higher connectivity. Here, we will focus our analysis on 2D sections. Indeed, if 3D ERT is possible, most investigations remain 2D due to the higher cost, the more complicated logistics and the time necessary to collect 3D surveys. For 2D sections, the connectivity in 3D is much more difficult, or even impossible to capture. Actually, cross-sections of both kinds of training images look very similar. For this reason and to keep the number of scenarios to analyze sufficiently low, we will only consider one of the family and try to investigate the role of the size of geological bodies for which much uncertainty remains (section 3.3).

6 training images-based scenarios were considered for this analysis. They correspond to the combination of three different sizes of channels (table 3.2 and figure 3.13) and two different sizes of lobes (table 3.3 and figure 3.13).

Type of lobe	Length (in m)	Initial width (in m)	Maximum width (in m)	Initial thickness (in m)	Maximum thickness (in m)	Relative distance
Big	40	20	40	4	6	0.5
Small	15	5	15	2	3	0.5

Table 3.3: Dimensions characteristic of the lobes of the training image scenarios.

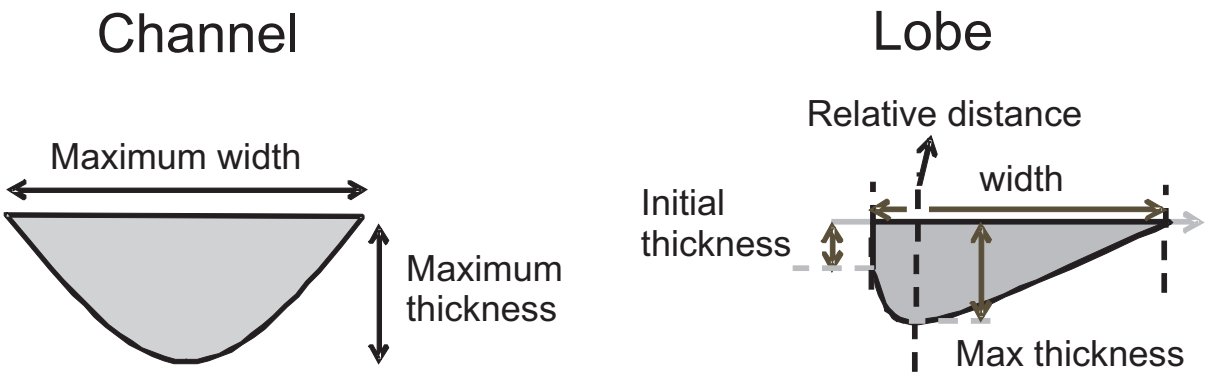

Figure 3.13: Geometrical characteristics of the simulated channels and lobes.

The proportions used for the different facies were 20% for the gravel channels, 22% for the clay lobes and 58% for the main sand facies. The size of the training images generated with Tetris was $300 \times 300 \times 18$ cells of dimension $1\ m \times 1\ m \times 0.5\ m$. In each training image, 12 different cross-sections were randomly selected to have a total of 72 synthetic models.

3.4.3.2 Simulation of synthetic ERT data sets

To be compared to ERT data, the created model must be transformed into model of electrical resistivity. To keep a simple methodology, a constant value was assigned to each category.

In most alluvial aquifers, an increase of electrical resistivity is expected with an increase of hydraulic conductivity, i.e. from clay facies towards gravel facies (Bersezio et al. 2007, Doetsch et al. 2010b). It is also what was expected *a priori* in the alluvial aquifer of the Meuse river (Monjoie et al. 1987, Haddouchi et al. 1987, Dassargues 1997, Rentier 2003).

Looking at the histogram of resistivity values obtained after inversion of field data (figure 3.9), it seems that three different distributions of resistivity appear. Values below 100 $Ohm.m$ should correspond to the clay facies, values above 200 $Ohm.m$ could be related to gravel facies, whereas the intermediate distribution, which is the most abundant is probably related to the sand facies.

From this histogram, it is possible to derive key values to assign to each facies. However, resistivity values after inversion may be affected by errors. For example, lowest and highest

Scenario	ρ clay (in $Ohm.m$)	ρ sand (in $Ohm.m$)	ρ gravel (in $Ohm.m$)
1	60	160	300
2	60	160	450
3	90	160	450

Table 3.4: Values of resistivity for each facies in the different scenarios

resistivity values may not be recovered because of the smoothing effect of inversion. To allow some uncertainty, three different scenarios were considered to transform the models (table 3.4).

In addition to the training image models which are 9 m thick, it is necessary to add cells at the bottom part of the model to represent the bedrock. The current lines may flow below the modeled depth of the aquifer. A constant value of 600 $Ohm.m$ was assigned to the bedrock.

In most cases, alluvial deposits in the plain of the Meuse River have a layer of backfill or of surface loams. These deposits do not correspond to what is drawn in the training image. To avoid the influence of such layer which may be present in the true field, we add a surface layer, 3 m thick, corresponding to the distribution of resistivity values observed for the field inverted model. Those added layers were not taken into account in the calculation of the distance between models.

Forward modeling was applied to the resulting 216 scenarios, using the same measurements configuration as the field data: a dipole-dipole configuration with 48 electrodes, 2 m spacing, $n \leq 6$ and a up to its maximum possible value. Apparent resistivity values obtained by this process were not use to calculate the distance between models. The main reason is that apparent resistivities are mostly influenced by the surface layer which is not the zone of interest in this case.

Synthetic data sets and true field data sets were then inverted using the same inversion process, using a smoothness constraint inversion scheme. Before further analysis, a visual comparison of some models may already be done. Figure 3.14 presents two synthetic models with their respective results of inversion. Gravel is not present in the first model. Even though the global proportion of this facies in the training image is 20%, it does not ensure that each sample of the training image will have the same proportions. The variability inside one training image can be high. This is something important, since we want our training image to catch most possible structures. In the inversion, the two clay structures appear, but their shape is not correctly retrieved, due to smoothing. Note the presence of high resistivity values in the bottom part of

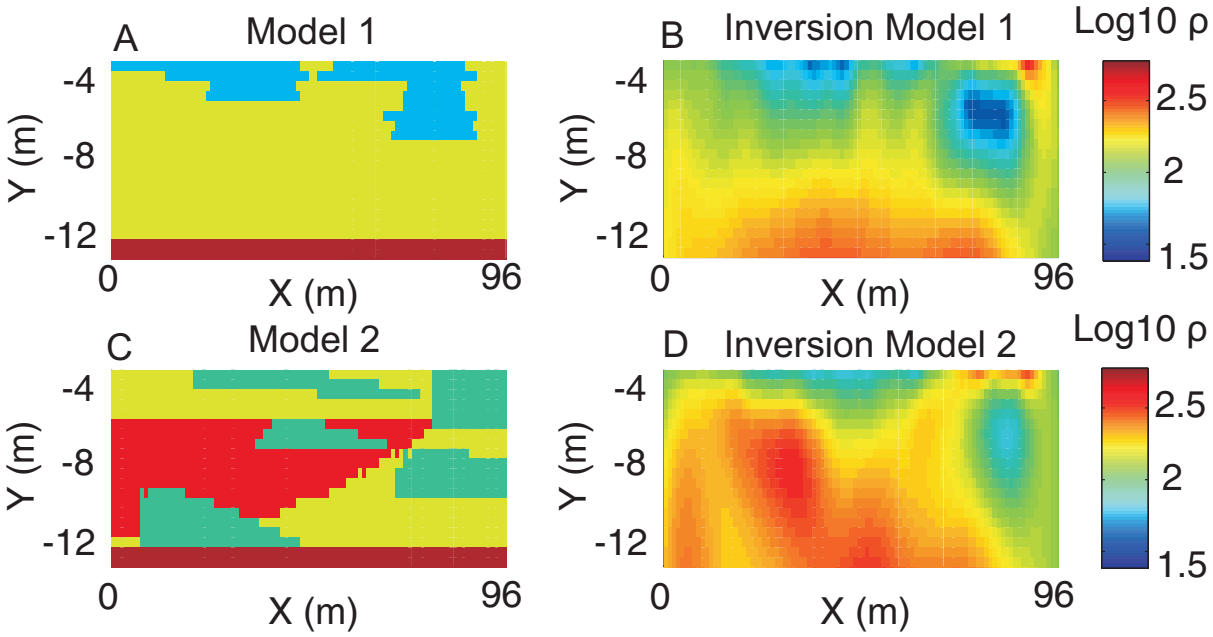

Figure 3.14: Two examples of synthetic model with their inversion. (A) The first model does not have gravel, (B) its inversion show high resistivity due to the bedrock. (C) The second model has a clay lobe at the bottom part, (D) its inversion does not image it correctly.

the inverted section, due to the presence of the resistive bedrock and in the right hand side of the upper part, due to the surface distribution. The second model has a big channel which is imaged in the inverted section. However, the small clay lobe at the bottom of the model is not very well resolved, it appears as less resistive than the gravel channel, but with a resistivity value corresponding to the sand facies. This is an effect of the limited resolution of ERT, especially at depth.

Those examples illustrate why inverted section may not be used directly as training image and why ERT is not completely informative about facies. This confirms that ERT results should be treated only as an indication of the facies. MPS frameworks with soft data under the form of probability maps offer a satisfying way to deal with this drawback. The examples also illustrate the variability of resistivity distribution that the training images may content. Especially, the second model is visually somewhat similar to the one corresponding to the true field model of figure 3.10.

3.4.3.3 MDS map

From the visual inspection of the synthetic models, we may say that training images are consistent with geophysical data collected in the alluvial plain of the Meuse River. In this section, we will try to analyze this consistency using the MDS approach more objectively. The idea of the method can be expressed as followed: if the training images are consistent with field geophysical models, the distribution of TI models in the MDS map using the methodology described in section 3.4.2 should contain the model(s) corresponding to field data. Consequently, some of the scenarios tested could be considered as coherent with data available for the alluvial deposits of the Meuse River.

In this case, training images focus on alluvial deposits. To get reliable geophysical models, we also had to consider the presence of the bed-rock and the presence of surface deposits with different characteristics. To calculate the distance between models, we first eliminate cells below $-12\ m$, corresponding to the bedrock. We also eliminate cells corresponding to surface deposits. Indeed, the cells being similar for all TI-based models, they would induce a strong similarity (small Euclidean distance) between these models which would distort the final MDS map and "exclude" models with a different distribution of surface resistivity.

Even though they are limited to the 3 first meters, the influence of surface deposits is spread deeper in the inverted sections (figure 3.14) due too smoothing. To avoid too much influence on the results, it was decided to eliminate the cells down to $-5\ m$.

The distance between synthetic models and two true field models was calculated using the Euclidean distance (equation 3.18), calculated on the logarithm of electrical resistivity. Alternative distances were also tested, using the mean value of the logarithm of resistivity in the neighborhood of the cell. The results using this distance are very similar to the ones using the resistivity value directly and would lead to similar conclusions.

To visualize the consistency of training images with ERT inversions, we first visualize the distribution of models in a 2D map (figure 3.15). The first two eigen components represent about 60% of the total variance of the distribution (the highest eigenvalues correspond to the highest contributions to the total variance). On this map, it appears that field models fall among the distribution of true field data. One of the two tested field model lies close to the middle, the other one is more towards the side of the distribution. Higher order projections are not shown

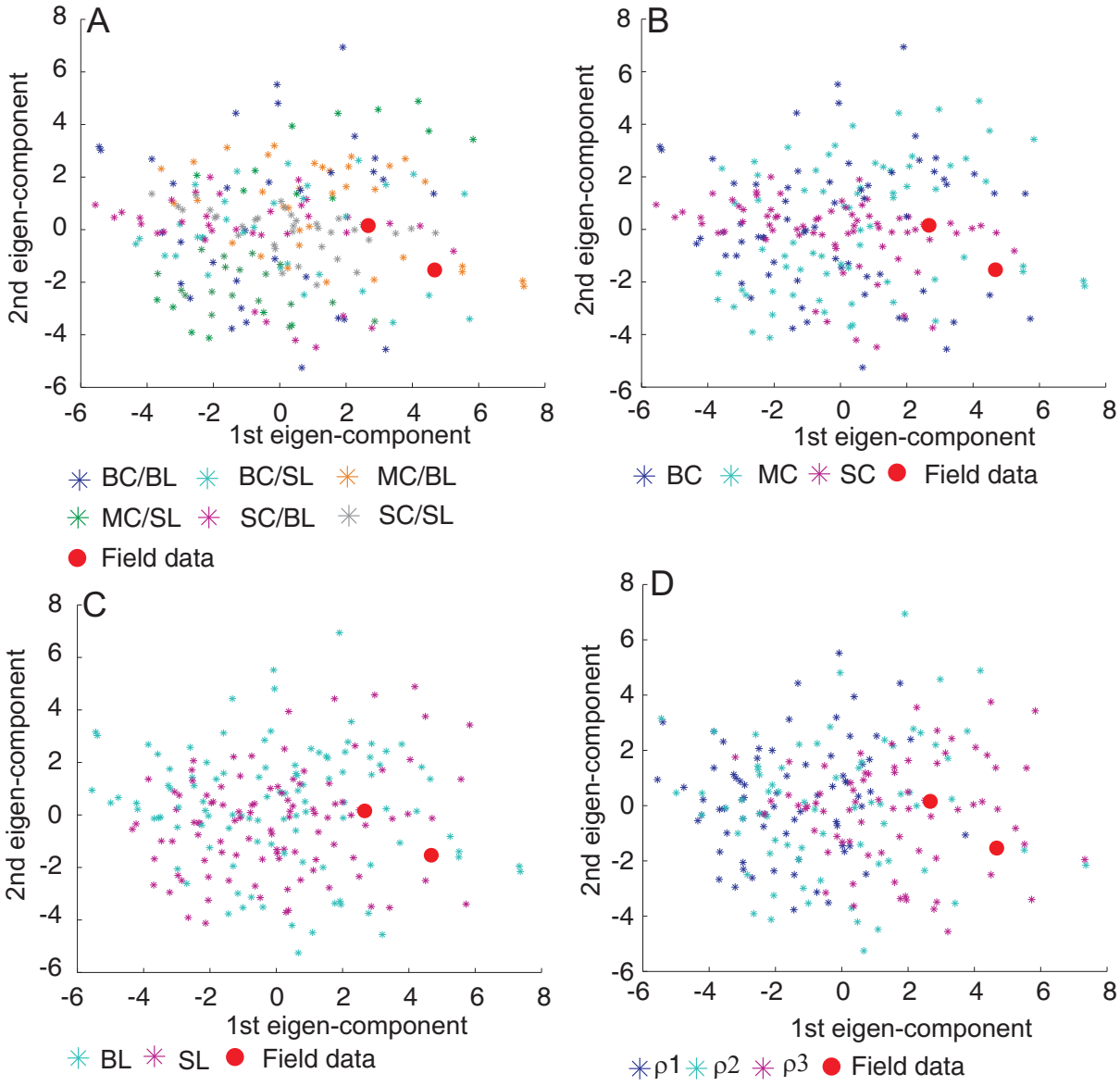

Figure 3.15: MDS mapping to verify the consistency of training image-based scenarios: field data are among the distribution of synthetic cases. (A) Analysis in terms of the six training images scenarios. (B) Analysis in terms of the size of channels. (C) Analysis in terms of the size of lobes. (D) Analysis in terms of resistivity distributions. BC = Big Channels, MC = Medium Channels, SC = Small channels, BL = Big Lobes, SL = Small Lobes.

because they are very difficult to visualize. However, the 3D projection would show that the field data lies also within synthetic models, but are located towards the border.

Figure 3.15 illustrates the limitations of the chosen distance to really discriminate the different scenarios. The different maps analyzing the different scenarios do not show clear trends in the different parameters. In figure 3.15A, we just see that three scenarios (SC/BL, SC/SL and MC/BL) are centered around the 0 of the 2^{nd} eigen-component axis and have a higher density around field models. Figure 3.15B confirms that models with small channels are aligned parallel to the 1^{st} eigen-component axis. No trend is observable concerning the size of clay lobes (figure 3.15C). The map with the analysis of resistivity distribution (figure 3.15D) shows that the third distribution produces models lying on the right side of the map, whereas the first distribution has models in the left part. Models of the second distribution are spread all over the map. Field models lying in the right part, the third distribution seems to be more probable.

This first observation on MDS maps already gives some kind of sensitivity analysis on the different parameters used to create the geological scenarios. However, this analysis is only qualitative. In the two next sections, we will try to analyze the results more precisely and we will propose a methodology to somehow quantify the uncertainty of the proposed scenarios.

3.4.3.4 Clustering approach

The first attempt to analyze more deeply what is observed in the MDS map is a clustering approach. In figure 3.15, we see that some scenarios are not present at certain locations on the map, other may be denser, but this is difficult to analyze visually.

Here, we propose to divide the MDS distribution into a given number of clusters and then to analyze the parameters inside each cluster, especially clusters containing the field models, to try to highlight some trends in the distribution. The k-means clustering approach was used in this case. This is a hard clustering approach, i.e. after the clustering is done, each model belongs to only one particular cluster. Clusters are formed iteratively in order to minimize the variability in each cluster, i.e. the sum of the squared Euclidean distance of points to the centroid of the cluster.

The results may be sensitive to the number of clusters. The choice of the number of clusters is made by the user according to his/her expertise, his/her knowledge of the problematic and

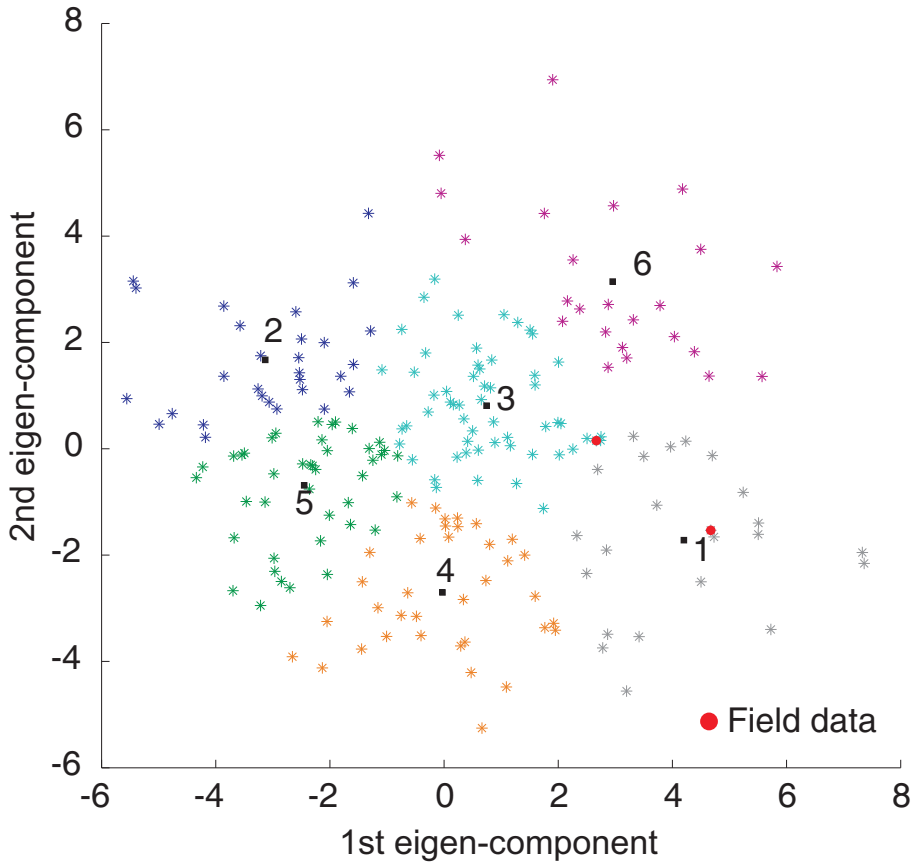

Figure 3.16: MDS map divided into 6 clusters. Field data are classified in clusters 1 and 3.

his/her understanding of the results. Here, six clusters were used since it corresponds to the number of training images used in the study. The approach was also tested with 5 clusters showing similar trends for the analysis. The results also show little influence of the starting points used as initial centroids of the cluster, which were randomly selected.

Clustering of the MDS map yields a central cluster (cluster 3) and five clusters distributed along the sides (figure 3.16). One of the field data lies in the middle of cluster 1, very close to its centroid; the other one is in cluster 3, but close to the border with cluster 1. These clusters therefore seem of higher interest to analyze the geological scenarios (figure 3.17).

The size of the channels seems to be a relatively sensitive parameter. We see that in clusters 1 and 3, small channels represent about 50% of the models whereas big channels are less than 20%. Scenarios with big channels thus seem less coherent with available geophysical data. In contrasts, small channel models are almost absent in clusters 5 and 6.

Concerning the resistivity distribution, the most probable scenario, as expected from the MDS map (figure 3.15D) is the third distribution, especially for cluster 1. In cluster 3, the three

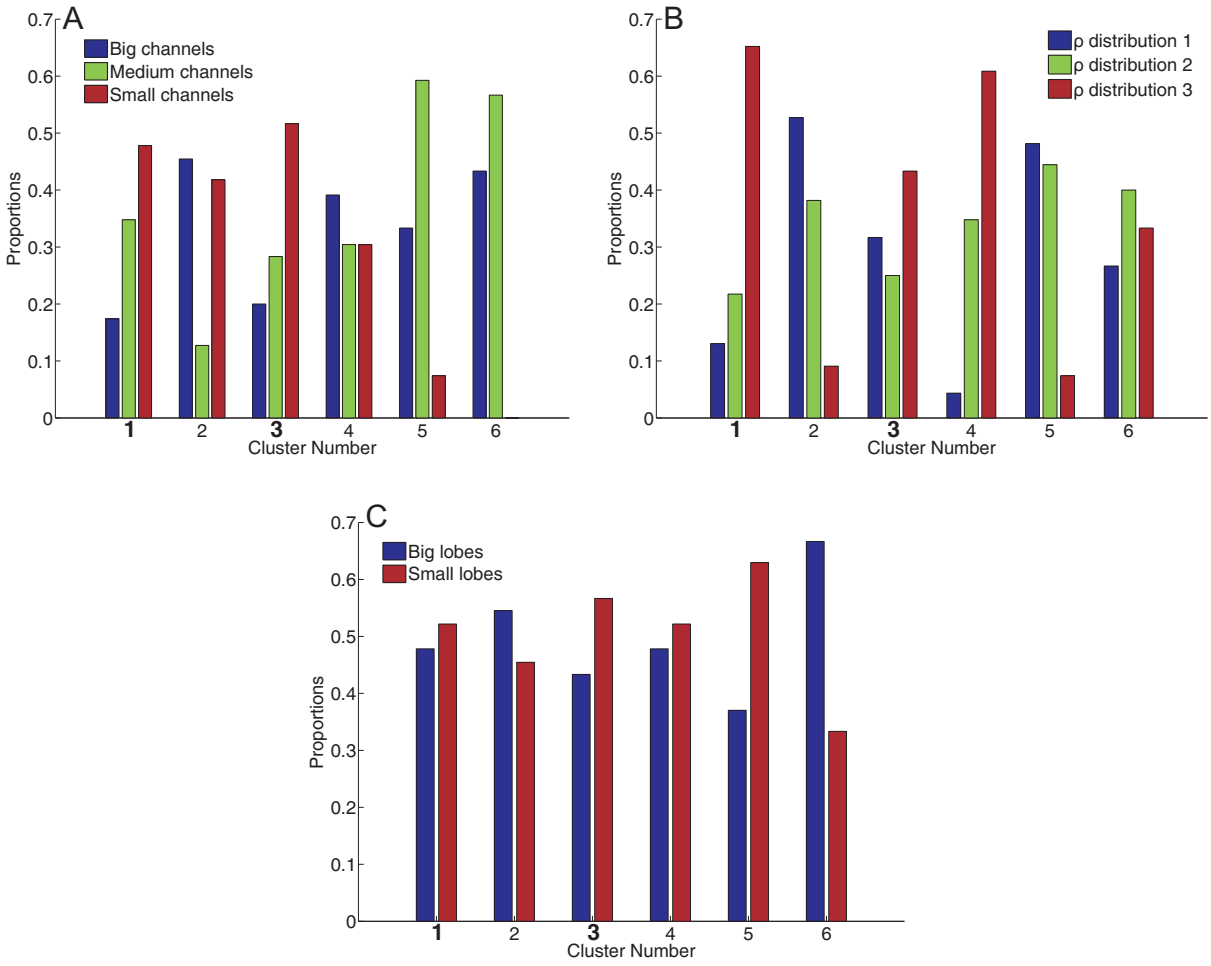

Figure 3.17: The analysis of the parameters inside clusters (see figure 3.16) shows that (A) small channels are more abundant in clusters 1 and 3, (B) the ρ distribution 3 is the most represented in clusters 1 and 3 and (C) the size of lobes is not a very sensitive parameter.

scenarios are represented.

The size of the clay lobes does not seem to be a very sensitive parameter. Except in clusters 5 and 6, the proportions of small and big lobes is quite similar, close to 50%. Thus both sizes of lobes could be consistent with geophysical data.

3.4.3.5 Probability analysis

The MDS and clustering approaches highlight that field geophysical models seem to be somehow consistent with the proposed training image-based geological scenarios. However, all the scenarios are not represented with similar proportions everywhere in the map. Some of them seem to be more likely to occur than other. The analysis shows that it would be very difficult to select only one scenario among all the proposed scenarios.

Uncertainty about the chosen training image scenario exists but is very difficult to quantify. The problem could be stated as follows: "What is the probability of a particular training image-based scenario, given the observed geophysical data?". Mathematically, this can be expressed as a conditional probability problem: $P(TI = ti_k|\mathbf{D} = \mathbf{d}_{obs})$. This probability may be very difficult to estimate. Park et al. (2013) propose to use Bayes' rule

$$P(TI = ti_k|\mathbf{D} = \mathbf{d}_{obs}) = \frac{f(\mathbf{d}_{obs}|ti_k)P(TI = ti_k)}{\sum_{k=1}^{K} f(\mathbf{d}_{obs}|ti_k)P(TI = ti_k)} \tag{3.28}$$

where the prior probability $P(TI = ti_k)$ is an input of the problem. In our case, we consider six different scenarios with equal probability, so $P(TI = ti_k) = 1/6$. It is necessary to estimate the likelihoods function $f(\mathbf{d}_{obs}|ti_k)$, i.e. the likelihood of observing a specific geophysical data $\mathbf{d}$, given a training image-based scenario ti_k. $\mathbf{d}$ may be high dimensional, here it is the number of cells in the aquifer model, but we are mostly interested in the variation of $\mathbf{d}$ with the various training images. The 2D MDS map is used to estimate the likelihood. In the MDS map, the density of points from each TI around a field model is representative of how likely this TI is for the given field model.

To estimate quantitatively the density of points around the field model, an adaptive kernel density estimation with the bivariate normal distribution function is used (Park et al. 2013)

Field data	BC/BL	BC/SL	MC/BL	MC/SL	SC/BL	SC/SL
Model 1	0.28	0.64	0.97	0.37	1.17	**2.57**
Model 2	0.09	0.90	**2.55**	0.15	0.97	1.33

Table 3.5: Ratio of the conditional probabilities to the prior probability for the 6 TI scenarios according to the two true field models. BC = Big Channels, MC = Medium Channels, SC = Small channels, BL = Big Lobes, SL = Small Lobes.

$$f(x,y) = \frac{1}{2\pi\sigma_x\sigma_y} \exp\left(-\frac{1}{2}\left[\frac{(x-\mu_x)^2}{\sigma_x^2} + \frac{(y-\mu_y)^2}{\sigma_y^2}\right]\right) \tag{3.29}$$

where x and y are the coordinates in the MDS map, μ_x and μ_y represent the mean along the axes and σ_x and σ_y are the standard deviation of the distribution.

The adaptive kernel smoothing enables to vary the bandwidth (σ_x and σ_y) of the Gaussian kernel to match the density of models across the space. Practically, this is done by using the k-means clustering results as subspaces of the MDS map to calculate the standard deviation along the axes.

Actually, the kernel is estimated for each point of the MDS map considering the specific field case as the mean value. The kernel estimation for models from similar scenarios are added up. Then the probability of each scenario can be derived by comparing the values and normalizing them to have a sum of probabilities equal to 1.

The probability of each training image-based scenario was calculated for the two field models of figures 3.15 and 3.16. It was then expressed as the ratio to the prior probability of each TI, which is equal to $1/6 = 16.67\%$ (table 3.5). A ratio superior to 1 suggests a more probable scenario whereas a ratio inferior to 1 indicates an unlikely scenario. The first model (Model 1) is the model in the third cluster. The most probable scenario is the one with small channels and small lobes. For the second model, the scenario with medium channels and big lobes is the most likely. We see that scenarios with big channels have low probabilities to occur, the same is true for the scenario with medium channels and small lobes.

The probabilities given above are based on the analysis of geophysical data only. These geophysical data are not perfect and give a smoothed vision of the reality, in 2 dimensions (actually the assumption is $2.5D$). They may be used as indicator for the choice of training image or to introduce geological uncertainty into stochastic processes. However, the two examples show that the deduced values may noticeably vary, even for a single site (here Hermalle-sous-

Argenteau). They should therefore be used as qualitative indicators and not as quantitative values to draw strong or radical conclusions about geological scenarios.

3.4.4 Conclusion

In this section, we have developed a new methodology to verify the consistency of training image-based geological scenarios with geophysical models. This constitutes an important contribution within the context of uncertainty assessment in Earth Sciences. Indeed, training images used in MPS depict the expected geological heterogeneity which remains in many cases uncertain. It is thus important to consider available geophysical information to decide which scenarios are more likely to occur. The process is summed up in figure 3.18.

1. Construction of independent training image-based scenarios with multiple facies.
2. Determination of the value(s) of the geophysical parameter for each facies.
3. Selection of 2D sections in the training images and transformation into geophysical synthetic models.
4. Forward modeling of geophysical data sets.
5. Inversion of synthetic and field geophysical data sets to generate inverted geophysical models.
6. Distance calculation between any two models.
7. MDS map calculation. If field models fall in the distribution of synthetic models, the training image is considered to be consistent with geophysical data
8. Cluster analysis and conditional probability calculation.

We applied this methodology to verify the consistency of 6 traning image-based scenarios with ERT sections in an alluvial aquifer. 12 sections were selected in each training image and three resistivity distribution were considered. The MDS map was computed using a 2D projection of Euclidean distances.

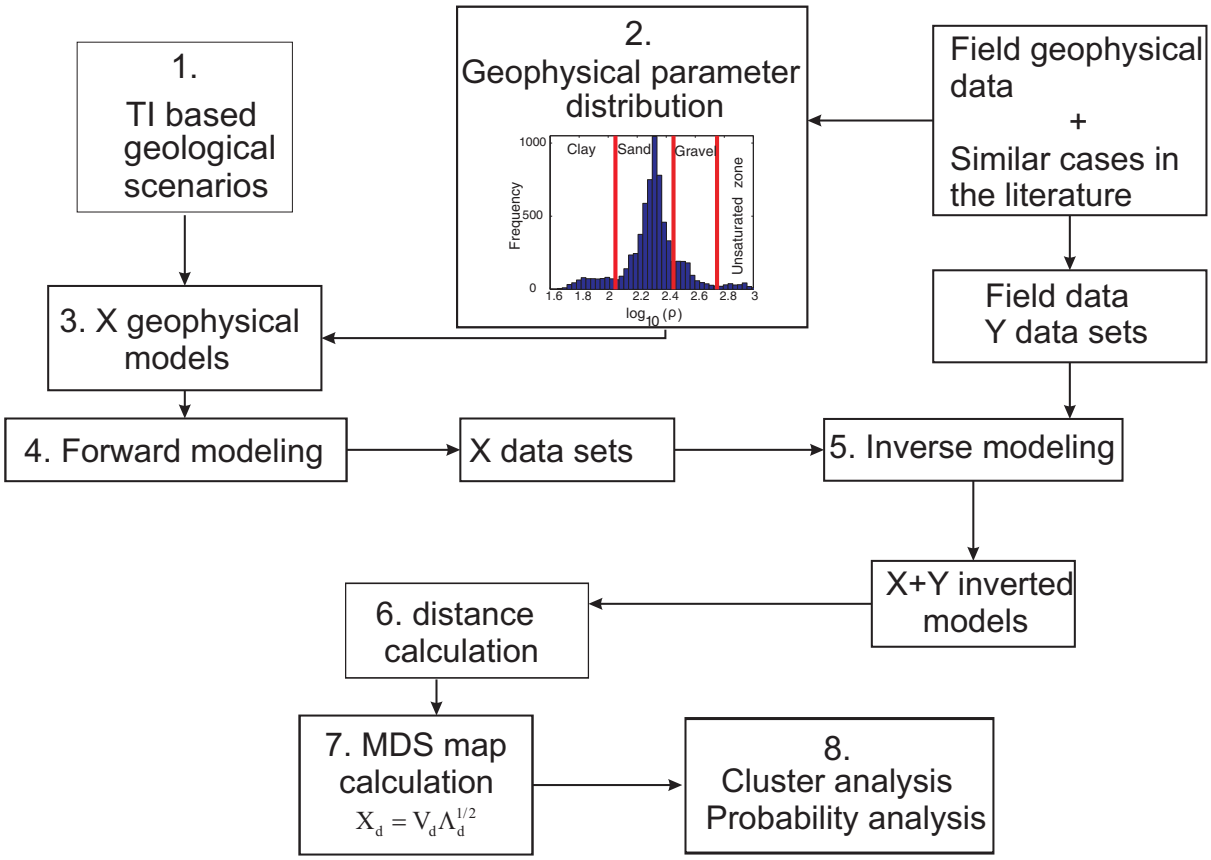

Figure 3.18: Flowchart of the methodology applied to verify the consistency of TI-based scenarios with geophysical data.

The application of the methodology shows that field models fall into the distribution of synthetic models; hence, according to our assumption, those scenarios are consistent with geophysical data. If it was not the case, one should try different scenarios to obtain consistent training images.

However, the consistency of training images with available geophysical data does not mean that those training images are perfect. Geophysical models obtained by inversion are imperfect and may have poor-resolution (see chapter 2). The methodology only indicates whether training images are coherent or not with the observed deposits and which scenarios are the most probable. This gives some highlights to select the best training image(s) to use for further simulations.

The methodology itself have some drawbacks. First, we use the Euclidean distance between models as a measure of similarity. This may influence the results as this distance is dependent on the position, whereas the training image concept is not locally dependent. Any other measure or combination of measures or geophysical attributes could be used, but all would have similar drawbacks. A solution would be to compare some response of the models. In hydrogeology, we could use the time of transfer of a solute species or the drawdown curve of a well as the base for distance calculation. This is more difficult to define for geophysical models. The results are also dependent on the dimensions used to project the models. A 2D space is often used to facilitate the visualization, but higher dimensional space may also be used to catch more variability.

To improve its portability and its efficiency, the methodology can be extended to 3D models. This may help to discriminate more complex scenarios, for example differentiate the response of channel and bar models. However, this requires 3D field geophysical models which are more time consuming and more expensive to acquire. Such models will be rarely available in the early state of a study, when this kind of methodology can be applied.

In this specific case, we can confirm that the proposed training image-based scenarios are consistent with geophysics, more particularly with ERT sections. The two sources were acquired or produced independently, they may thus be used simultaneously for multiple-point statistics simulations, using ERT data as soft conditioning data. This process will be developed in the next section.

3.5 Conditioning multiple-point statistics simulations with ERT

In the previous section, we have established a methodology to verify the consistency between training images and geophysical data. If we conclude that both are consistent, it is worth to integrate geophysical data into multiple-point statistics simulations to build models constrained by both geology and geophysics. Geological data acts at two levels. First, the training image depicts the geological heterogeneity. It proposes the architecture and topological relationships between facies as expected from our geological knowledge. It will be used to calculate the conditional probabilities used to draw randomly the facies at each node. However, the training image is not constrained to any specific location. It means that if a sufficient number of unconditional simulations are carried out, the posterior proportions of facies at each cell of the model should be equal to the prior proportions. Second, geological data in the form of borehole logs are introduced as hard data. Hard data is considered in the simulations as certain knowledge. It means that the facies from borehole logs are imposed during simulations at the nearest node. Hard data enables to constrain spatially the simulations at specific locations.

Hard data are generally sparse and limited in number at the scale of the model. Geophysical data can be used to overcome this limitation. Geophysical techniques (e.g. ERT) provide 2D or 3D models of geophysical parameters (e.g. electrical resistivity) that may be linked to the simulated parameter. In this context, the value of the geophysical parameter, which is locally dependent, is very useful to constrain spatially the geostatistical simulations. Nevertheless, geophysics gives only an indirect insight on the parameter interest, it should thus be integrated in the simulations as a secondary or soft data.

Integration of secondary data into MPS (section 3.2) may be done through a training image for the secondary data or through the τ model proposed by Journel (2002). Equations 3.12 to 3.15 explain how the joint probability $P(A|D,C)$ can be obtained from individual conditional probability from the training image $P(A|D)$ and from the soft data $P(A|C)$. So the integration of ERT data into multiple-point statistic simulations can be performed in 2 steps.

1. Calculating the probability maps $P(A|C)$ or in this case $P(A|\rho)$, i.e. the probability of having clay, sand or gravel facies given the observed electrical resistivity value.

2. Simulating facies using training images and soft data combined with the τ model.

The aim of this section is to give an overview of the integration of geophysical soft data in MPS simulations in the case of a three facies alluvial aquifer simulation. To ease the visualization of the results, we will illustrate the process with a fictious 2D example. We will analyze the role of hard data, soft data and the training image. This will help to understand the results of chapter 4 where 3D MPS simulations will be used as the prior for hydrogeological inversions.

3.5.1 Deriving probability maps from resistivity

Calculating $P(A|\rho)$ is necessary to use ERT results as soft data in MPS simulations. Literally, it signifies that if we observe an electrical resistivity ρ_{obs} somewhere, we have to transform this measures into the probability of having the different facies, namely clay, sand and gravel. This philosophy is coherent with the observation made in section 3.4. We have seen that ERT inversions are not perfect, even if they can be improved using the techniques of chapter 2. Indeed, using specific thresholds of resistivity to define facies and to extract training images (section 3.4.1) or using a petrophysical relationship between hydraulic conductivity and electrical resistivity (Dassargues 1997) would deny the equivocal character of inverted resistivity sections. A clay lens surrounded by gravel may appear with an intermediate resistivity value (figure 3.14) and would inevitably be classified as a non-clay facies or would be assigned a higher hydraulic conductivity value. Using a probability map approach, the possibility exists that higher resistivity values will be associated with the clay facies.

The obvious and direct way to build these probabilities is to use a direct comparison between inverted electrical resistivity values and facies observed in boreholes. However, this requires a sufficient amount of field data, especially direct observations, to derive a reliable relationship. From direct observations, we have a database of facies with their respective electrical resistivity, i.e. we have access to the likelihood $f(\rho|A)$, or at least to the histogram that can be used as an estimator. Using Bayes'rule, it is possible to derive $P(A|\rho)$:

$$P(A=a_i|\rho) = \frac{f(\rho|A=a_i)P(A=a_i)}{f(\rho)} = \frac{f(\rho|A=a_i)P(A=a_i)}{\sum_{j=1}^{J} f(\rho|A=a_j)P(A=a_j)} \tag{3.30}$$

where the prior distribution of the facies $P(A=a_i)$ is also deduced from direct observations. It is also possible to derive directly the relation from cumulative probability curve (e.g. Oh 2013).

Facies	Prior probability	μ	σ
Clay	0.22	2.1096	0.1515
Sand	0.58	2.1921	0.1362
Gravel	0.2	2.2715	0.1411

Table 3.6: Characteristics of the Gaussian distribution of resistivity of the three facies. The values for mean and standard deviation are given in logarithm of resistivity (base 10) expressed in $[Ohm.m]$.

Joint probability of several geophysical parameters could be computed (e.g. using the τ model) if more than one soft data type are available.

Here, we estimate equation 3.30 using the synthetic models constructed to characterize the consistency of training image scenarios (section 3.4.3). These synthetic cases provide a big database of correspondence between facies and inverted electrical conductivity, which will take into account the inversion effects on the resistivity distribution, such as low resolution and smoothing effect.

The global histogram of resistivity after inversions of the synthetic case would not reveal the three different distributions. The histograms for each category were computed and displayed on figure 3.19. They all have a Gaussian shape

$$f(x) = \frac{1}{\sigma\sqrt{2\pi}} e^{-\frac{(x-\mu)^2}{2\sigma^2}} \tag{3.31}$$

where μ is the mean of the distribution and σ is the standard deviation.

The mean of the three distributions is different, but a significant overlap can be observed. Indeed, the difference between their mean is of the same order of magnitude as their standard deviation (table 3.6). This is due to the smoothing effect of ERT inversion on the resistivity distribution: small and high values (clay facies and gravel facies) tend to be over- and underestimated by the inversion process. Almost all resistivity values can be taken by the three facies, obviously in various proportions.

Note that this histogram is the average for all depths. The near-surface cells are the best resolved by ERT. Histograms for these cells could thus be more discriminating than for deeper cells.

Using the Gaussian likelihood functions and the prior probability, it is straightforward to apply Bayes'rule using equation 3.30 to calculate the conditional probabilities (figure 3.20). For very low resistivity values, the probability to be in clay is almost equal to one. With increasing

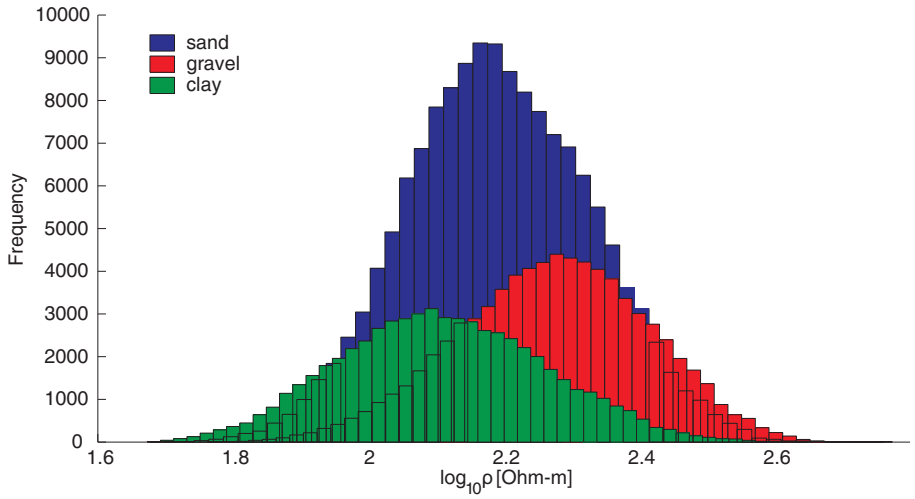

Figure 3.19: The distributions of the logarithm of resistivity of the different facies have a Gaussian behavior.

resistivities, the conditional probability of clay decreases whereas the ones of sand and later of gravel increase. Around $\log_{10}\rho = 1.95$, the probability to be in sand or in clay is the same (≈ 0.45), whereas the probability to be in gravel remains low. At $\log_{10}\rho = 2.2$, the probability to be in sand is maximum, but hardly above the prior probability (58%). Then, the probability to be in sand decreases in favor of the probability of gravel. Around $\log_{10}\rho = 2.45$, the probability to be in gravel becomes larger and tends to 1 towards $\log_{10}\rho > 3$.

The distribution of electrical resistivity is thus not very informative about the sand facies. It mostly indicates that values of resistivity below 100 $Ohm.m$ are likely related with the clay facies and that values of resistivity above 280 $Ohm.m$ should probably correspond to gravel. The use of complex resistivity could be more discriminant given its correlation with hydraulic conductivity (Kemna et al. 2012).

Using the law illustrated on figure 3.20, it is now possible to transform the electrical resistivity section into probability maps that will be used as input for subsequent MPS simulations. We use a field resistivity model and transform it in probability maps (figure 3.21). This transformations mainly shows four zones where the probability of gravel increases to at least 50% and a zone in the upper part of the model where the probability of clay is high. Elsewhere, the resistivity is intermediate and the probability of sand is close to its prior probability.

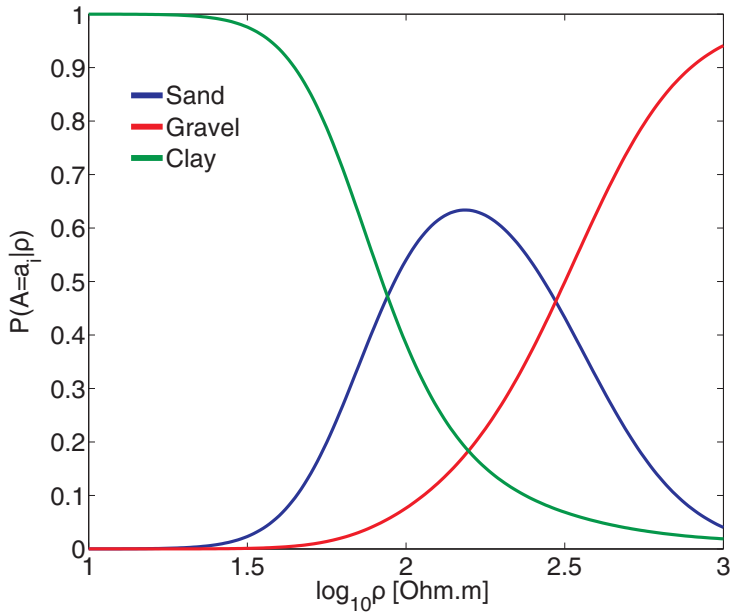

Figure 3.20: The conditional probabilities $P(A|\rho)$ show that, except for very low or very high resistivities, a given resistivity may be coherent with the presence of every facies.

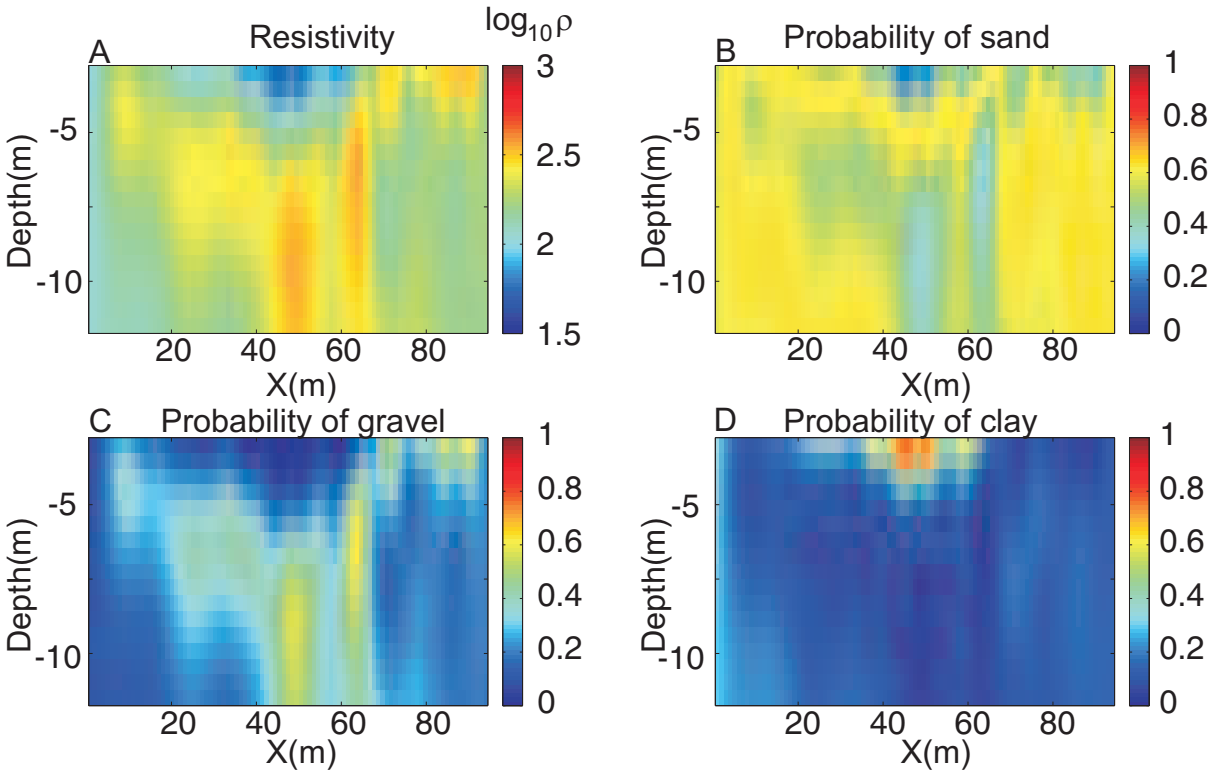

Figure 3.21: (A) The resistivity distribution can be transformed into probability maps for (B) the sand facies, (C) the gravel facies and (D) the clay facies.

3.5.2 MPS simulations

MPS simulations use training images as the main source of information to build realizations of the studied process. Structures are borrowed from the training images and reproduced in the realization. The simulations are often conditioned with borehole data, considered here as hard data that has to be preserved in every simulation.

In the petroleum industry, seismic reflection attributes are regularly used as a soft constraint for simulations. Seismic reflection is a wave geophysical method with a relatively high resolution, dictated by the wavelength. However, such method is difficult or even impossible to apply in environmental studies due to the need of high frequency source, the attenuation of the high frequency signal, the noise (seismic noise, superposition of refracted waves, surface waves, etc.), the size and configurations of most of the study sites. In such contexts, ERT has already proven its efficiency to image a lot of environmental processes. ERT is a potential geophysical method, integrating a relatively large volume of subsurface for each measurement. The resolution of ERT survey is complex to define because it depends on the experimental set-up, the inversion process and the distribution of resistivity itself. The method has not been extensively studied within the context of MPS (Trainor 2010). However, the use of tomographic images has been recently studied within the context of radar by Lochbühler et al. (2013). In this section, we explore how some parameters of MPS simulations affect the simulations and the role of ERT as a soft constraint.

The 2D simulations were carried out using the SNESIM algorithm (Strebelle 2000, 2002) implemented in SGEMS (Remy et al. 2009) described in section 3.2 with the probability maps of figure 3.21 as soft conditioning data.

Hard data was simulated, imposing facies at two different positions on the section. At location 25 m, the well log is composed of 0.5 m of clay, lying on 1.5 m of sand, 3 m of gravel and then sand down to the bottom of the aquifer. At 58 m, there is 1 m of clay, then 4.5 m of sand and finally gravel. The aquifer deposits are supposed to be 9 m thick, represented by 18 cells 0.5 m thick. The width of the simulated model is 94 m with cells 1 m wide. The training image used for simulation has a mix of big, medium and small channels and big and small lobes (figure 3.22).

For each case, we will show examples of independent realizations and posterior probability

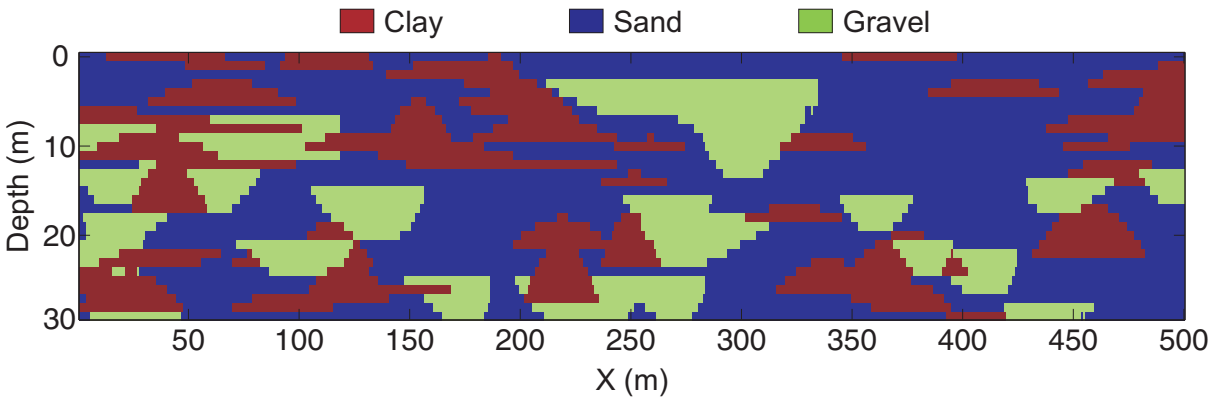

Figure 3.22: The training image used for simulations has a mix of channels and lobes of different sizes.

maps calculated on 100 simulations. A classified section will also be presented, the facies of each cell being determined according to the most probable facies of posterior probability maps.

3.5.2.1 Effect of soft data

Simulations were run with hard data only (figure 3.23), soft data only (figure 3.24) and both hard data and soft data (figure 3.25).

When only hard data is used, borehole facies are imposed in each realizations. Therefore, independent simulations of figure 3.23 have similarities around the position of boreholes. There are more differences towards the sides of the section. Geometrical features are borrowed from the training image (figure 3.22), even if the random process and the limited size of templates distort geological bodies.

The posterior distributions and the classification based on 100 realizations are dominated by the presence of hard data. Of course, posterior maps have values 1 or 0 at borehole positions and close values just around. Elsewhere, values are close to the prior probabilities of each facies. The classification process tends to locate two gravel channels, almost symmetrical, where gravels are imposed in boreholes. The shape of the channel is well marked, illustrating the role of the training image to represent sedimentological features. Surprisingly, some clay is adjacent to the boreholes in the classification. This is also an effect of the training image. This might disappear if more realizations were used for classification.

When soft data is used alone, without hard data, different realizations have more variability (figure 3.24). Facies are never imposed in the simulation, but chosen according to the training

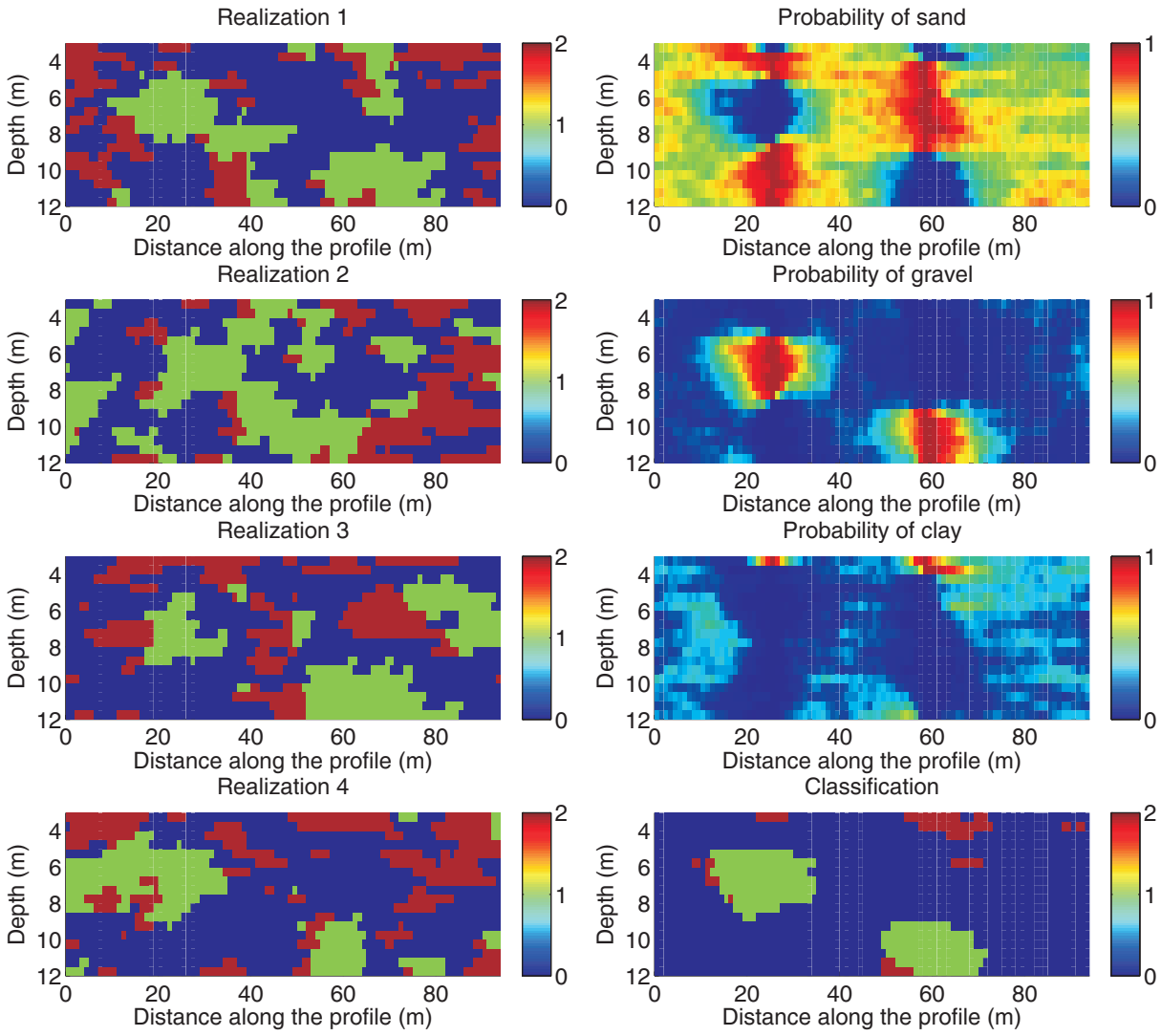

Figure 3.23: Four examples of realizations and posterior probability maps using hard data only. Posterior probability maps reflect mainly hard data ($P = 1$).

image and soft data through the τ model. Here the simulations used $\tau = 1$. During the simulation, even if the soft data probability is high, it may be tempered by the training image conditional probability and another facies may be randomly chosen. Gravel channels may thus be found everywhere in the section. Of course, with a high number of realizations, they should appear preferentially where the soft probability is high. The training image also dictates that clay lobes should be present even if clay soft probability is not very high.

This can be seen in the posterior probability maps, where gravel posterior probability is higher in the middle of the section, which is in accordance with the probability map of figure 3.21C. This is also true for other facies. The higher variability in the simulations yields a less-marked classification. Some cells are classified as gravel in the middle of the section, but their shape is more erratic than with hard data. This is a a result of the quite strong overlapping of resistivity distribution of the different facies.

In most real cases, hard data and soft data, if existing, will be used jointly (figure 3.25). In this case, the role of soft data is to improve the constraint between boreholes that may be too far from each other to reproduce correctly the deposits. Compared to figure 3.23, the use of soft data tends to produce a connection between the two gravel zones detected in boreholes, but this feature is not present in all realizations.

The posterior maps are still influenced mostly by hard data, but we see that gravel probability has increased between the two gravel zones. This is also visible in the classification where gravel channels are more extended laterally, as expected from the soft probability maps. So soft data brings an update of the probability of occurrence where hard data is lacking.

3.5.2.2 Effect of the inversion

MPS simulations took their information from three different sources: hard data, soft data and training image. Hard data is something we cannot work on, this is something which is considered as known and, to some extend, certain (actually, uncertainty and errors in the interpretation of borehole logs cannot be excluded). In contrasts, soft data, here ERT inversions, comes from a process whose solution is non-unique. We have seen in chapter 2 that incorporating prior information into the inverse problem should modify and improve the solution. If the resistivity distribution is different, this will have an influence on soft probability maps as well.

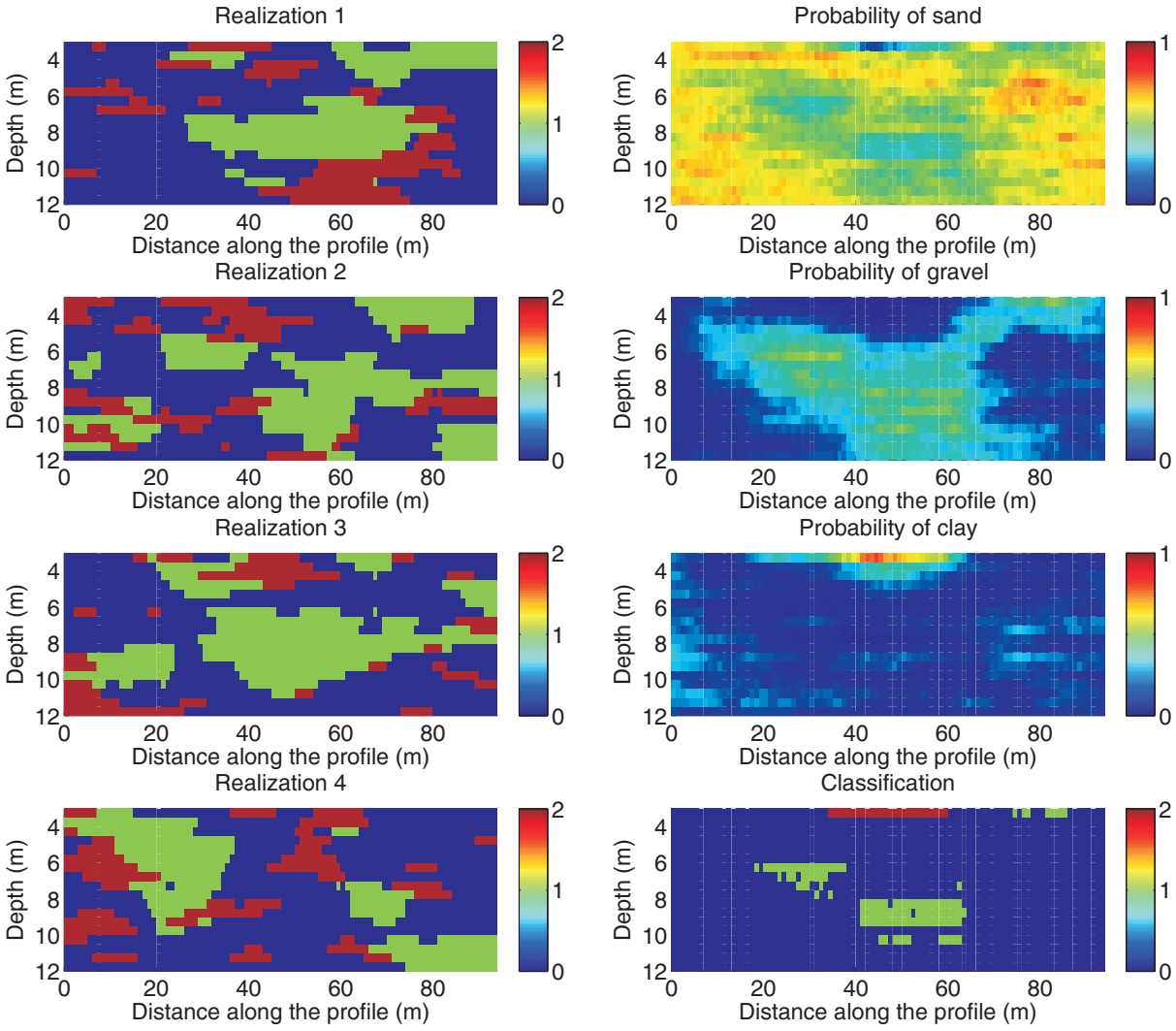

Figure 3.24: Four examples of realizations and posterior probability maps using soft data only. Posterior probability maps are close to soft data probability maps.

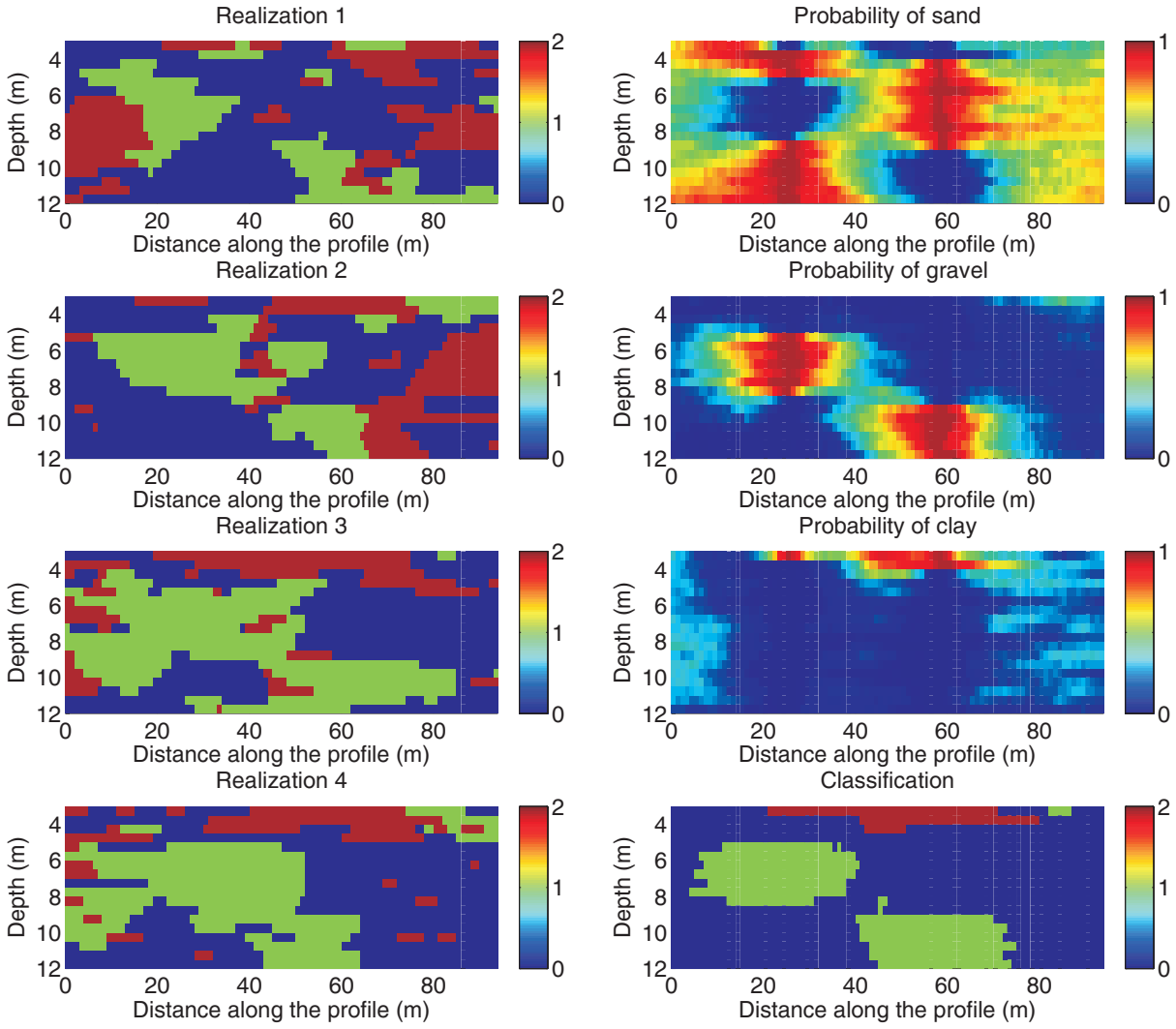

Figure 3.25: Four examples of realizations and posterior probability maps using hard and soft data. Soft data influences slightly the posterior probability maps.

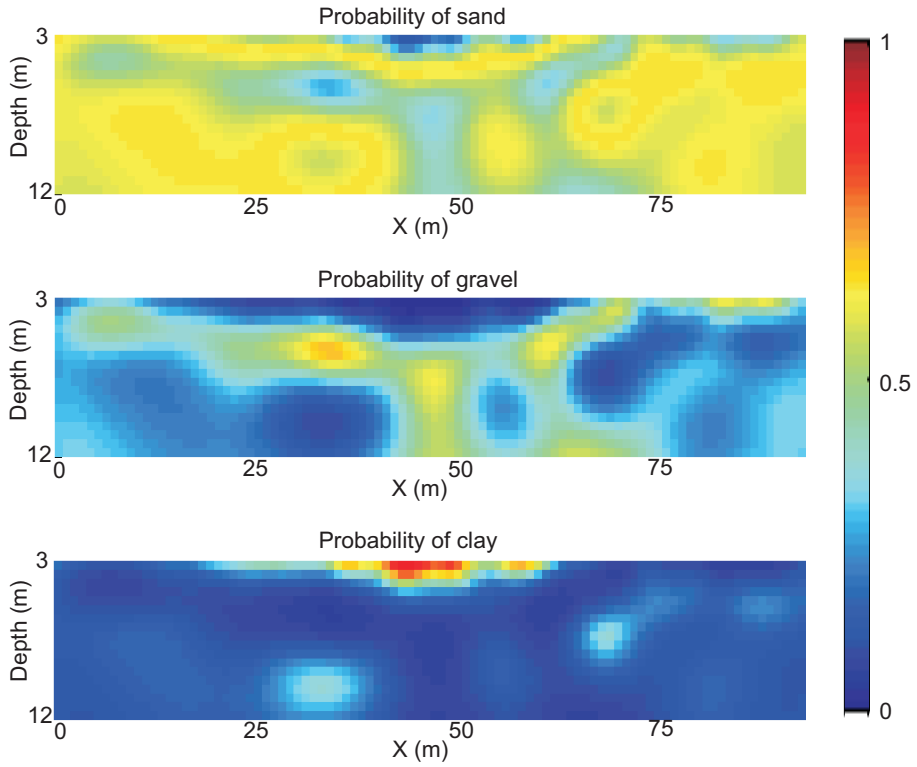

Figure 3.26: The probability maps obtained after transformation of resistivity from the geostatistical inversion are slightly different from the ones obtained with the smoothness constraint solution (figure 3.21).

Figure 3.26 represents the soft probability maps obtained after the geostatistical inversion of the field ERT data. Only the effect of the inversion is taken into account, the same conditional probability maps were used (figure 3.20). In reality, we could expect that inversions incorporating prior information would yield sharper contrasts between facies and increase the improvement brought by prior information (see chapter 4). By comparison with figure 3.21, we see that two spots of higher probability appear in the clay distribution. The shape of the high probability of gravel zone is also slightly modified.

The influence of this modification in the simulation with soft data only is not visible on single realization (figure 3.27 to compare with figure 3.24). This is expected given the relative influence of soft data, the patterns observed in the training image are still reproduced. The effect is more visible on posterior probability maps. The probability of clay is modified according to the variations observed in the corresponding soft probability map. In the classification, gravel does not appear in two different zones anymore, but there is now a link whose shape corresponds to the high probability of gravel zone (figure 3.26). The center of the gravel zone is also moved

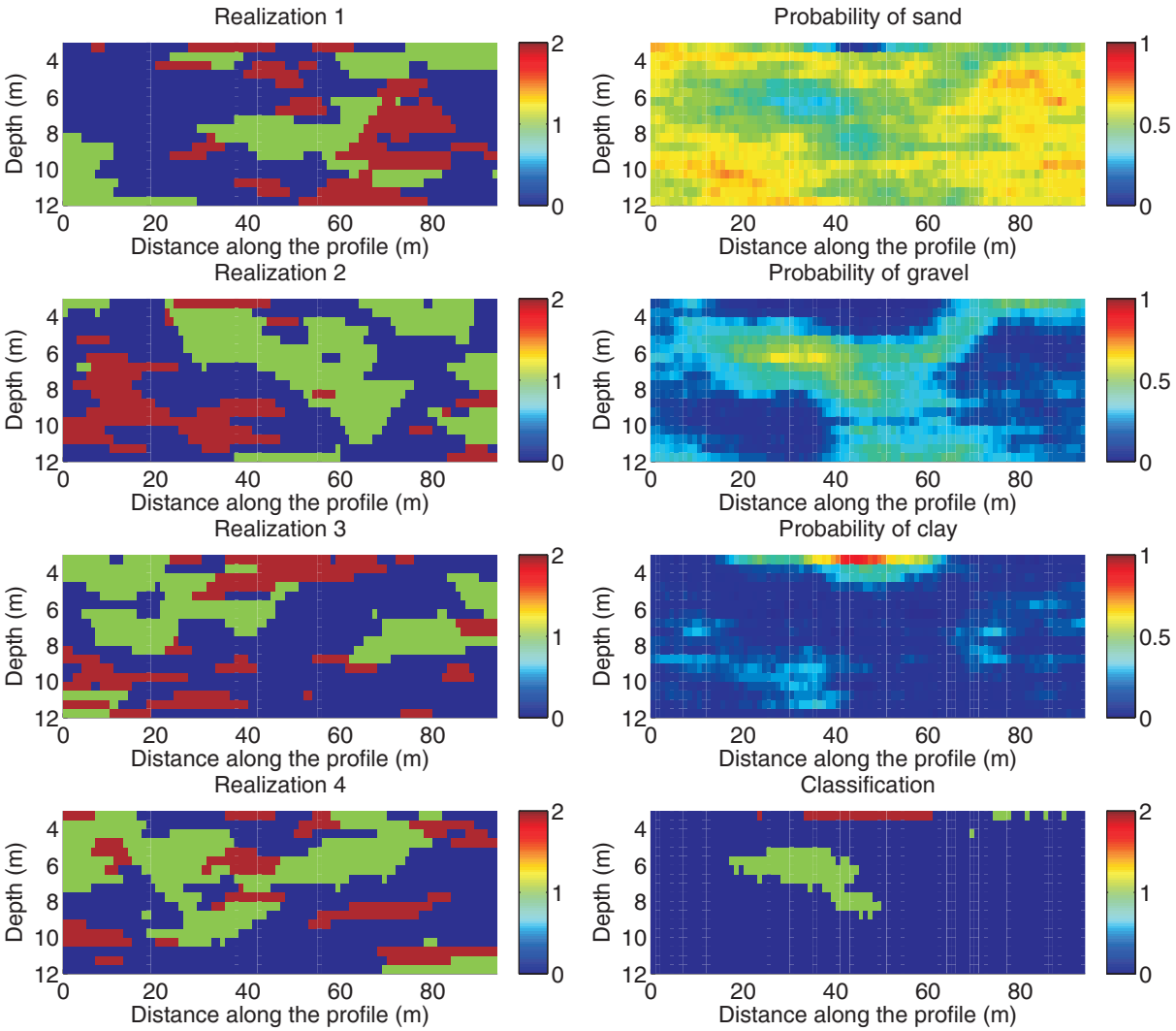

Figure 3.27: Four examples of realizations and posterior probability maps using soft data with geostatistical inversion to produce probability maps. The inversion method influences the classification.

to the left side of the section.

The inversion method can thus significantly change the results of the simulations. The choice of the inversion to produce probability maps should thus be made carefully. An inversion more consistent with the geology could also result in "more discriminating" conditional probabilities which could bring another improvement to the method.

3.5.2.3 Effect of the τ exponent

In most studies using MPS simulations, the value of τ is set to 1 (equation 3.15), assuming a relative independence of the contribution of training image and soft data to the facies probability.

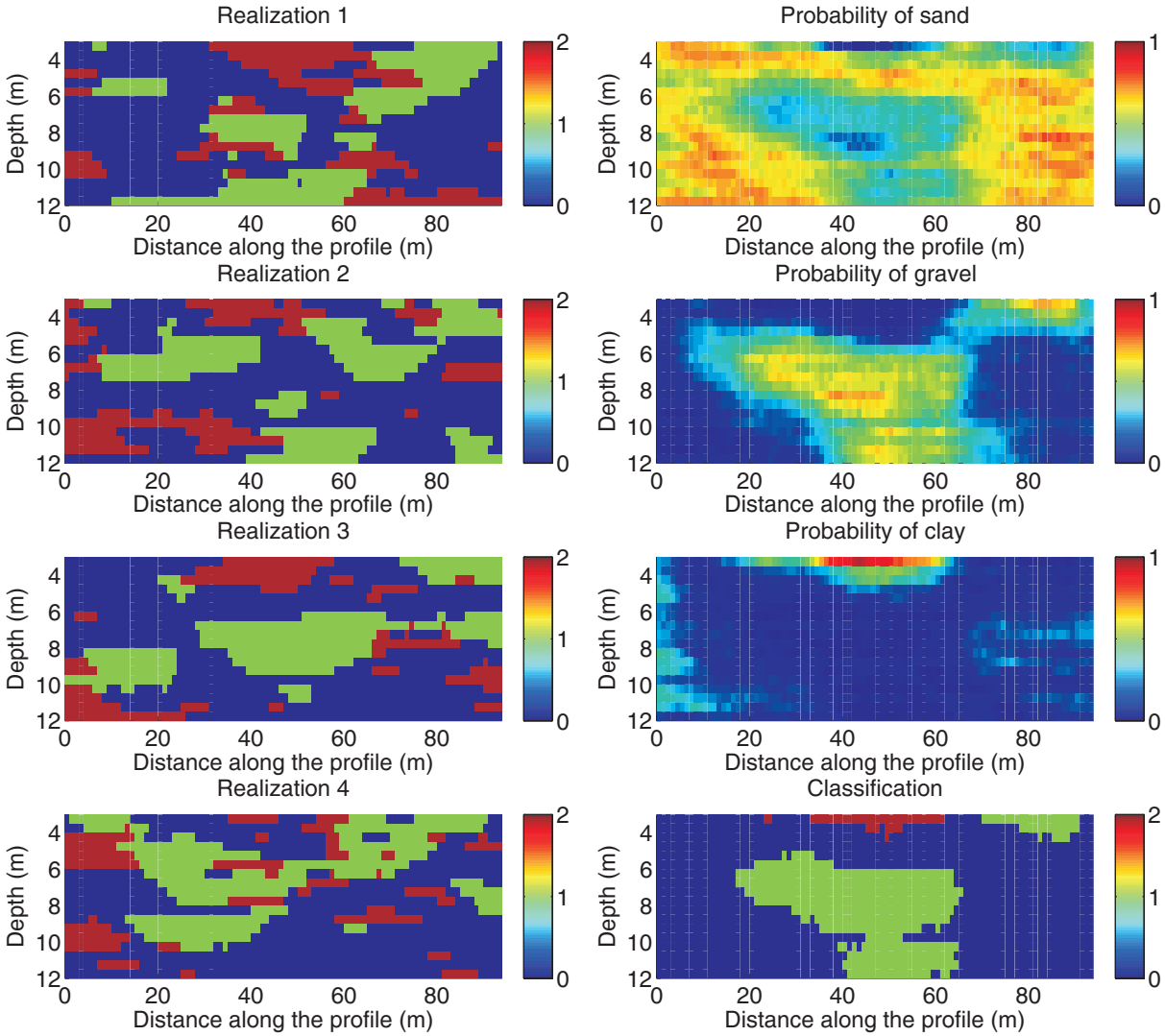

Figure 3.28: Four examples of realizations and posterior probability maps using soft data with $\tau = 2$. The simulations give more weight to soft probability maps.

In many cases, it would be very difficult to justify another value for this exponent. However, modifying τ offers a simple way to change the relative weight of training image and soft data in the conditioning process. We have seen that training images were uncertain and ERT inversion non-unique, it may be helpful in some cases to vary the default value of τ.

As an illustration, we increased its value to 2. The resulting effect (figure 3.28 to compare with figure 3.24) is that more weight is given to soft data, which becomes more important than the training image in the simulation process. However, the training image still plays an important role. Indeed, even with low soft probabilities, clay lenses still appear in individual realizations. The effect of changing τ is mostly visible on posterior probability maps. The patterns are very

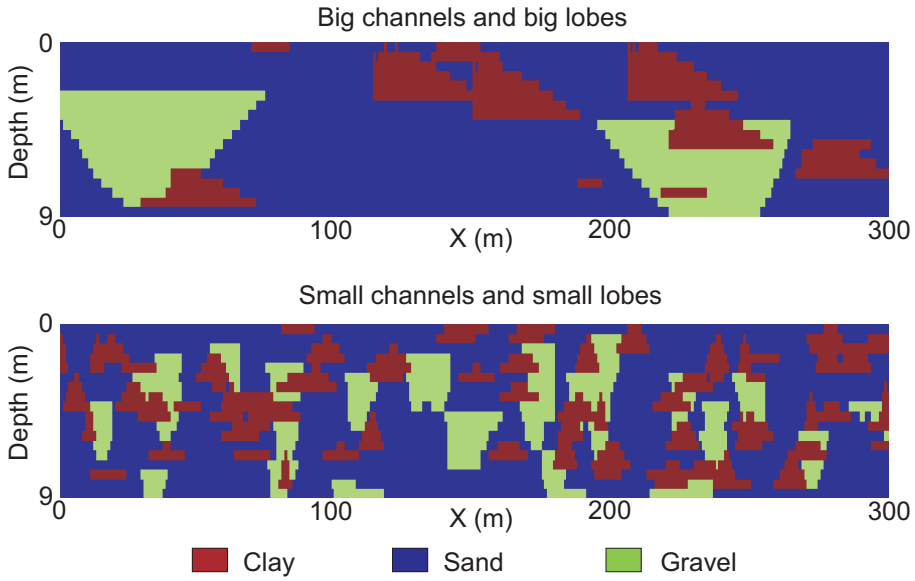

Figure 3.29: Two different training images used for simulations with big channels/big lobes and small channels/small lobes.

similar to the soft probability maps (figure 3.21). The high probability of gravel in the upper right corner is enhanced in the posterior probability and cells in this area are now classified as gravel.

Increasing τ thus leads to a classification closer to the resistivity distribution. The choice to give more or less weight to the results of geophysics is a choice of the operator and depends on the confidence he has on the results. Even if the classification is modified, it must be kept in mind that individual realizations will lead the stochastic simulation process and that the heterogeneity of the training image is still playing an important role.

3.5.2.4 Effect of the training image

The training image of figure 3.22 has channels and lobes of various sizes. To illustrate the effect of the training image on the realizations, we tested the results obtained using two different training images: one with big channels and big lobes and another one with small channels and small lobes (figure 3.29).

The importance of geometrical features contained in the training images are reflected in figures 3.30 and 3.31. The prior information on the size contained in training images is mainly visible through the size of gravel channels in individual realizations. With the first training image, big channels are reconstructed and their superposition leads to one or two large zones of

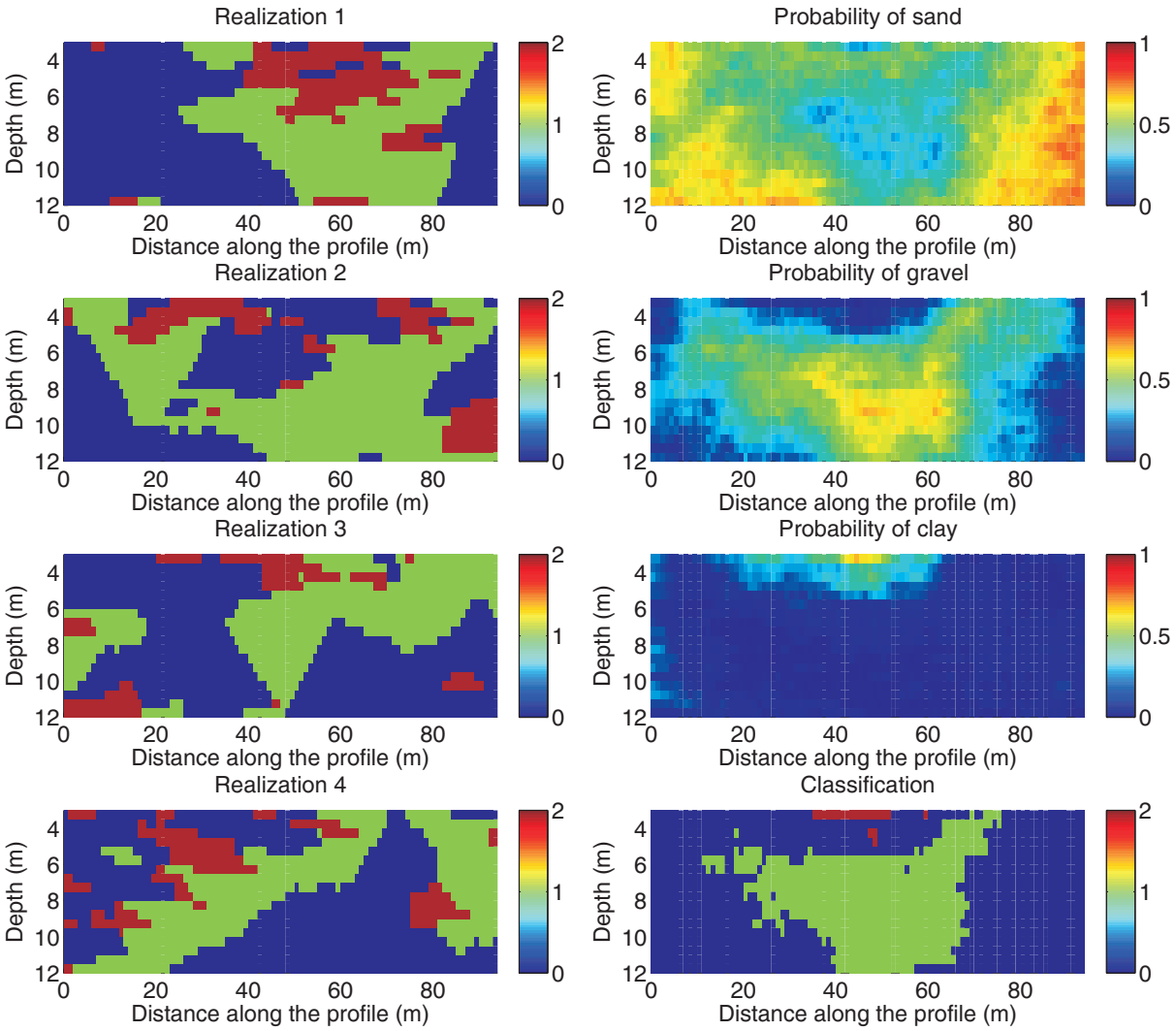

Figure 3.30: Four examples of realizations and posterior probability maps using soft data and the training image with big channels and big lobes. The posterior probabilities reflect the size of geometrical bodies.

gravel in the realizations. With the training image displaying small channels, the realizations contain smaller and less connected gravel zones.

The posterior probability maps and the classification also illustrate the difference using different training images. With big channels, almost all realizations have a large gravel channel in the middle of the section where the soft probability of gravel is high. This yields a classification with a high number of cells classified as gravel. With small channels, this effect is very limited and only the cells where the soft probability of gravel is the highest are finally classified as gravel after 100 realizations.

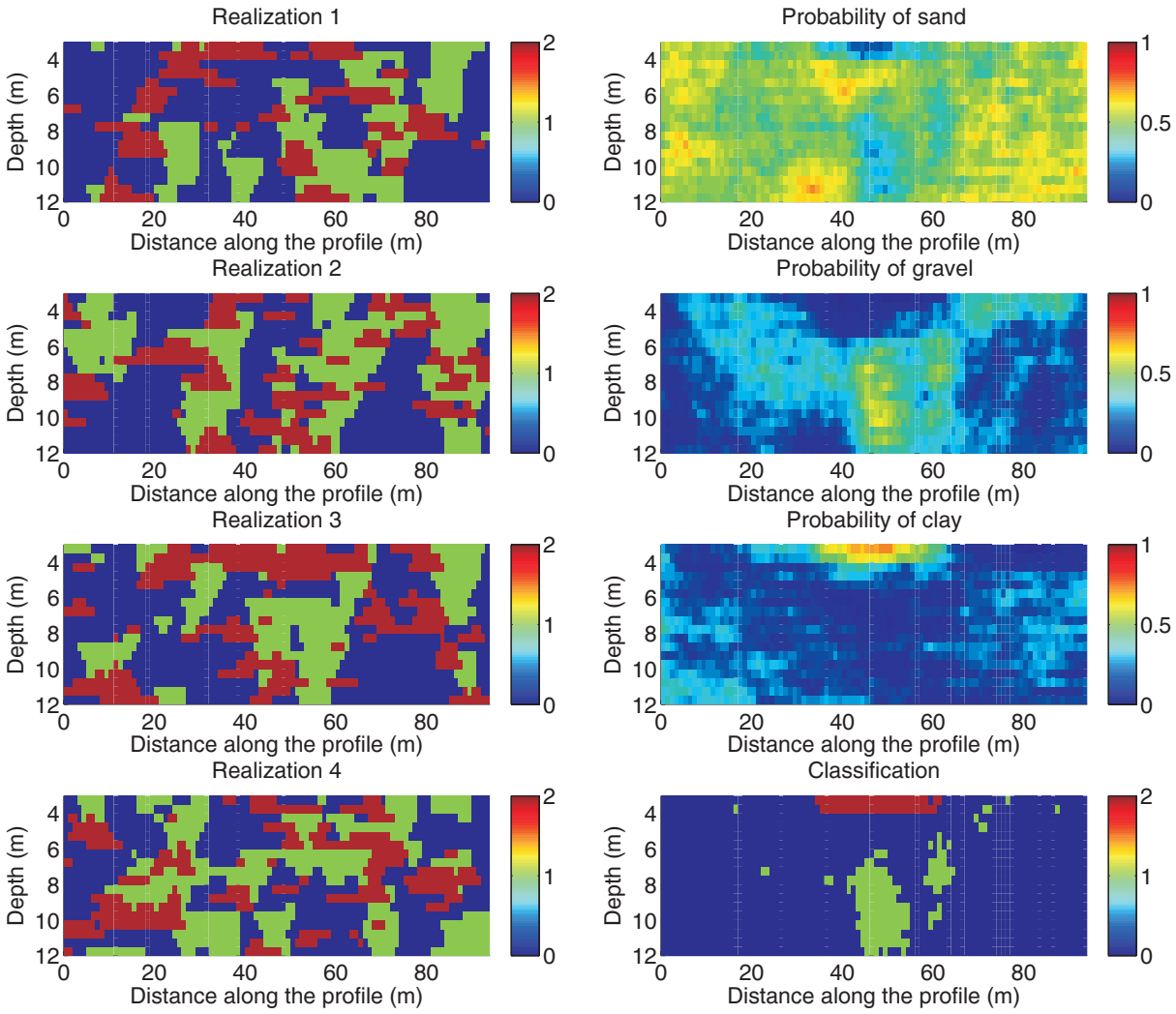

Figure 3.31: Four examples of realizations and posterior probability maps using soft data and the training image with small channels and small lobes. The posterior probabilities reflect the size of geometrical bodies.

3.5.3 Summary

The examples of the previous sections illustrate the role of ERT as soft data in MPS simulations. First, it is necessary to build probability laws linking the geophysical parameter and the facies. The comparison with direct observations is a straightforward way to derive such a relationship. It can be applied for most field studies and is generally satisfying. However, in some cases, more complex strategies may deliver better results. For example, Caers and Ma (2002) proposed a neural network approach to calculate the probability distribution. It enables to take into account the neighborhood of the considered cell. This approach was also tested in this work, but it was yielding similar results.

Alternatives exist. As an example, Lochbühler et al. (2013) propose a workflow where the probability distribution does not need to be computed. The initial training image is the base for simulations that are associated to their tomogram yielding a bivariate training image (facies and tomogram). This first part of their methodology is similar to our methodology to check the consistency of training images and geophysical data, since it also requires to choose a value of the geophysical parameter for each facies. Then, MPS simulations are created (using the direct sampling algorithm) and the forward geophysical response is calculated. The simulation is kept only if the difference with actual field data is sufficiently low. This technique is between the conditioning of MPS with tomograms and the stochastic inversion of geophysical data constrained by a training image. It would be interesting to apply the same methodology to ERT inversions. Its major drawback is the need to use a petrophysical relationship to propose tomograms of the training image, which is not necessary in an approach based on the direct comparison. However, it ensures that the models explain the geophysical data within the expected error level.

The role of soft data is clearly evidenced by the proposed examples. Geophysical data contains spatial information which helps to position the facies in the model. Indeed, the training images are independent of the location and hard data only provides very local information. The use of spatially distributed information constrains the simulation process to more geologically plausible realizations. However, it is clear from the examples that the constraint is not strong, except if the τ exponent of equation 3.15 is increased.

Within this context, the role of the inversion procedure to process ERT data is important. We have demonstrated in chapter 2 that the incorporation of prior information in the inversion yields

solutions closer to the ground truth. Consequently, these solutions contain sharper information to constrain MPS simulations.

However, surface ERT suffers from decreasing sensitivity and resolution with depth. It signifies that model parameters at the bottom of the model are less well resolved. Ideally, this should be taken into account in the probability distribution, which is likely depth-dependent. For field studies, direct observations are generally to sparse to integrate this additional complexity. Synthetic benchmarks should be carried out to see how the probability distribution evolves with depth. Then, the potential link with sensitivity and resolution should be investigated. It can be expected that the standard deviations of the probability distributions will increase with depth, together with decreasing sensitivity and resolution.

Finally, the training image is the most impacting parameter in MPS. It is thus mandatory to create training images consistent with available data to reproduce as well as possible the deposits of the studied site.

Combined together, these techniques enable to integrate geophysical data into a geostatistical framework in a process taking into account the lower resolution and non-uniqueness of geophysical models.

In the next chapter, 3D MPS simulations of alluvial aquifers constrained with ERT will be used as the basis to integrate hydrogeological data.

Chapter 4

Integration of hydrogeological data in multiple-point statistics through inverse modeling

Note. The research material of this chapter was partially presented in an International conference:

Hermans T., Scheidt C., Caers J. and Nguyen F. 2013. Probability perturbation method applied to the inversion of groundwater flow models using HydroGeoSphere. 3^{rd} International HydroGeoSphere User Conference, April 3-5, Neuchatel, Switzerland.

Hermans T., Scheidt C., Caers J. and Nguyen F. 2014. Inverting hydraulic heads in an alluvial aquifer constrained with electrical resistivity tomography data through multiple-point statistics and probability perturbation method: a case study. Geoenv 2014, July 9-11, Paris, France.

4.1 Introduction

In chapters 2, we have investigated different techniques to improve geophysical inversions. Those results were subsequently integrated to geostatistical models in chapter 3. Geophysics and geostatistics are rarely the final objective of the study. Commonly, these techniques are used to improve the knowledge and understanding ofsubsurface reservoirs, for energy, mineral

or groundwater resources.

Within the context of alluvial aquifers, we will have to integrate typical data for hydrogeological models such as piezometric levels or subsurface flows in natural or pumping conditions and tracer experiments. Such measurements are related to the primary variable of the problem (here, the facies characterized by its hydraulic properties) through a dynamical process which cannot be resolved through a direct geostatistical approach (as soft data) but requires to solve groundwater flow (and possibly transport) equations in an iterative inverse modeling approach.

There exist some similarities in the inversion of ERT data and hydrogeological data. The problem in both cases is to find the set of model parameters which will best describe the observed data. What we expect by "best" is generally quantified through an objective function to minimize. We have seen that for ERT, the objective function is a combination of data and model misfits (equation 2.17). In hydrogeology, it is commonly defined as a (weighted) least-square data misfit objective function, i.e. the sum of the square difference between observed and calculated data (Hill and Tiedeman 2007) and the model constraint is generally imposed by the conceptual understanding of the site. Finding a model with a low value of the objective function will ensure a good calibration of the model.

Particular to hydrogeological inversion is the possibility to divide the period of observation for which data are available in several intervals. It is then possible to calibrate the model with a given time period and to validate the results with the other periods. The quality of the calibration is important for model results and predictions (Hill and Tiedeman 2007).

In geophysics, the data are generally acquired with a geometry ensuring a sufficient coverage of the model to process to an automatic inversion. In hydrogeology, the observations are often very limited compared to high number of model parameters. Looking simultaneously to the optimum value of each parameter is a very challenging task and the dimensionality of the problem makes it difficult to solve.

This problem is commonly simplified by parameterisation, i.e. the definition of a limited number of parameter (hydraulic properties) within the model space. This reduces the number of unknowns in the inverse procedure drastically (Carrera et al. 2005). The calibration can be done manually using trials and errors (Anderson and Woessner 1992) but this technique is subjective and may be tedious. Nowadays, automatic inversion techniques are increasingly used.

A common inversion technique in hydrogeology is the zonation. It is inherited from the trials and errors technique. The model space is simply divided into different zones of homogeneous parameter. This is a deterministic approach where the zones are defined according to geological formations or geological knowledge of the field. Then, the value of the parameters inside each zone can be optimized automatically to minimize the objective function (e.g. Carrera and Neuman 1986a, 1986b). A major disadvantage of the method is the need to increase the number of zones to achieve a sufficient calibration due to the heterogenity that may appear inside geological units. A second disadvantage is the uncertainty related to the zonation.

Another method commonly used for inverse modeling in hydrogeology is the pilot point method (de Marsily et al. 1984, LaVenue et al. 1995, Doherty et al. 2003). This is a non-linear bayesian technique of inversion and optimization. The pilot points are model parameters that are designated as the unknowns of the problem. The values at these points are chosen during the inversion and they are used to solve the kriging equations to determine the model parameters at the other positions in the model. The values of the model parameters at the pilot points are optimized to minimize the objective function. The method requires the definition of prior knowledge about the geostatistical distribution of the parameters (for example the definition of the variogram). However, this technique does not aim to sample the posterior distribution of the model and is generally applied in a deterministic way. Indeed, the hydrogeological inverse problem is also ill-posed and many different solutions may explain the data as well.

Sampling the posterior distribution in complex non-linear problems cannot be done analytically such as in linear inverse problems (Tarantola 1987). It requires to apply stochastic or sampling techniques such as Monte Carlo methods (Robert and Casella 2004). The aim is then to produce a set of models explaining the data in order to assess the variability of the posterior distribution. These techniques require the definition of a prior, which constrains spatially the distribution of the models.

Within the context of this study, we already have geostatistical facies models integrating geological and geophysical data to constrain the spatial distribution of facies (prior). It is logical to choose a stochastic approach based on these realizations to solve the inverse problem. The technique used will not determine a single solution, but a set of possible solutions. Two approaches can be easily used to integrate additional hydrogeological data.

1. Each realization of the geostatistical approach, i.e. MPS simulation, can be considered as one possible zonation of geological features. Then, an optimization algorithm, such as PEST (Doherty 2004) can be applied to find the best parameter values inside each zone to fit the observed data. Such approach was used by Rentier (2003) which defined a zonation based on co-kriged hydraulic conductivities (continuous variable) classified using threshold values (discrete variables), each realization resulting in a different zonation. The drawback of this method is that the optimum value of the parameters of a facies may vary from one realization to another.

2. Each realization of the geostatistical approach, i.e. MPS simulation, can be considered as the starting model of a "geometrical" optimization. The methods cited above all aim to optimize the value of the parameters. Here, the idea would be to optimize the geometry of geological features in order to get the minimum objective function. The value of the parameters are fixed, only the geometry is modified, but respecting hard and soft data in the geostatistical approach. This technique, first developed for history matching with MPS in the petroleum industry is called the "probability perturbation method" or PPM (Caers 2003, Caers and Hoffman 2006, Li and Caers 2008). The disadvantage of the method is the need to fix *a priori* the value of the parameter.

For the coherence with our global approach in integrating different type of data within the same geostatistical framework, we choose the second approach which ensures that geological and geophysical data will still be involved in the hydrogeological inversion process. Ronayne et al. (2008) applied PPM with for hydrogeological data only within the context of an alluvial fan aquifer system. Their aim was to find models matching an aquifer pumping test. The combined use of MPS and PPM enabled them to explain apparent anomalous drawdown curve, related to the geometry of conductive channels.

In the next sections, the PPM method will be described. Then, a synthetic benchmark will illustrate the global integration process and will show that the choice of the hydraulic parameter values can be investigated in a separate step. Finally, the methodology will be applied on the field site of Hermalle-sous-Argenteau.

4.2 The Probability Perturbation Method

The method was first developed for history matching in the petroleum industry, proposing an inversion technique combining MPS and dynamical data. The comprehensive theory of the probability perturbation method (PPM) was published in Caers and Hoffman (2006). Here, we will recall the important concepts to understand the method. The PPM is a stochastic inversion method used in a Bayesian context, i.e. that aims at sampling solutions from the posterior density distribution of the model parameter $\mathbf{m}$ given some informative data $\mathbf{d}$

$$f(\mathbf{m}|\mathbf{d}) = \frac{f(\mathbf{d}|\mathbf{m})f(\mathbf{m})}{f(\mathbf{d})} \tag{4.1}$$

where $f(\mathbf{m})$ is the prior distribution of the model describing the spatial dependency between model parameters (here facies values). Within the context of this work, this prior distribution is expressed by the training image used to generate the MPS realizations. $f(\mathbf{d}|\mathbf{m})$ is the likelihood density depicting the relation between the observed data and any particular model. It accounts for modeling and measurement errors. Data and models are related through a forward operator

$$\mathbf{d} = g(\mathbf{m}) \tag{4.2}$$

and the density $f(\mathbf{d})$ is dependent on the prior distribution of model and the forward operator.

In this case, we present the method for categorical variables but the method can also be used for continuous variables (Caers 2007) and could be extended to various inversion problems.

4.2.1 Sampling the distributions

Let us consider a binary variable described by an indicator random function model,

$$I(\mathbf{u}) = \begin{cases} 1 \text{ if the event occurs at } \mathbf{u} \\ 0 \text{ if not} \end{cases} \tag{4.3}$$

where "event" is the presence of a given facies for example. The model parameters of the inverse problem is represented by a vector of indicator variables, one at each position of the grid:

$$m = \{I(\mathbf{u}_1), I(\mathbf{u}_2), \cdots, I(\mathbf{u}_N)\}. \tag{4.4}$$

The prior distribution $f(\mathbf{m})$ is then simply the joint distribution of all indicator random variables at all grid node locations. To sample this prior distribution, the PPM uses sequential simulation to generate realizations of $\mathbf{m}$ (SNESIM algorithm in this case). Since the simulation of a node is conditioned to all previously simulated nodes (equations 3.6 and 3.11), it ensures that the expected statistics, as well as hard and/or soft data are observed. Two realizations only differ by the random seed used to generate the simulations. This random seed determines the path to visit the nodes of the grid and the numbers used to draw a value from conditional density functions.

To generate samples from the posterior distribution, the same sequential decomposition is applied. There is an additional data $\mathbf{d} = g(\mathbf{m})$ which is more difficult to manage due to the non-linearity of its relation with $\mathbf{m}$. The problem can be expressed similarly as a conditional probability $Prob\{I(u) = 1|D, C, d\}$. If we introduce $A = \{I(u) = 1\}$ and $B = \mathbf{d}$, we have $Prob\{A|B, C, D\}$ where A represents the presence or not of a facies, B is the hydrogeological data, C the soft geophysical data and D the training image.

Equations 3.12 to 3.16 describe how it is possible to decompose the joint conditional probability into "pre-posterior" distribution $P(A|B)$, $P(A|C)$ and $P(A|D)$ using the τ model (Journel 2002). $P(A|D)$ is calculated from the training image and hard data and $P(A|C)$ are the probability maps from geophysical data. In the following, we took all the τ exponents equal to 1. The only remaining unknown to proceed to sequential simulation is the pre-posterior $P(A|B)$. This cannot be directly calculated because it results from a complex non-linear relationship between the model parameters and the data. The PPM uses an iterative calibration process to determine this probability.

4.2.2 Iterative calibration

The inversion process starts with a realization $i_{CD}^{(s)}$ (subscript CD signifies that the realization is conditioned to C and D) drawn with the random seed s conditioned to hard data, soft data and respecting the training image using sequential simulation. To estimate $P(A|B)$ at all grid nodes, a stochastic search is performed in order to match the data B.

Actually, a probability $P(A|B)$ is assumed and a new realization is drawn, combining $P(A|B)$, $P(A|C)$ and $P(A|D)$ to calculate the joint distribution $P(A|B, C, D)$ with the se-

quential simulation algorithm. Of course, it is difficult to directly derive the correct $P(A|B)$ at all nodes of the model. The technique that is used is a perturbation parameterization of all probabilities $P(A|B)$ using a single parameter as follows

$$P(A|B) = (1 - r_B) \times i_{CD}^{(s)}(\mathbf{u}) + r_B P(A), \tag{4.5}$$

where r_B is a parameter between $[0, 1]$ and is independent of the position in the grid. Now, it is possible to compute $P(A|B, C, D)$ using the initial realization $i_{CD}^{(s)}$ and a given value of r_B. The problem is now an optimization problem of the single parameter r_B. The general workflow (figure 4.1) of the algorithm is (Caers and Hoffman 2006):

1. Choose an initial random seed s
2. Generate the initial realization $i_{CD}^{(s)}$ conditioned to hard data, soft data and the training image using the random seed s
3. Iterate (outer loop) until the data B is matched (run flow simulation and check objective function)
   (a) Choose another random seed $s\prime$
   (b) Choose a value of r_B to calculate $P(A|B)$ with equation 4.5, and generate a new realization $i_{r_B}^{(s\prime)}$.
   (c) Optimize the value of r_B to minimize the misfit between observed and calculated data using a single parameter optimization technique (inner loop).
   (d) Generate the final realization $i_{r_B^{opt}}^{s\prime}$ of this iteration using optimum r_B and use it for the next iteration and go back to 3.

The parameterization only depends on the value of the single parameter r_B. The way it works can be understood by the three possible cases.

1. If $r_B = 0$, then $P(A|B) = i_{CD}^{(s)}$. $i_{CD}^{(s)}$ is an indicator, its value is either 1 or 0, so any realization built with this value of $P(A|B)$ will be equal to $i_{CD}^{(s)}$, whatever the value of the random seed. This case corresponds to "no perturbation" of the current realization.

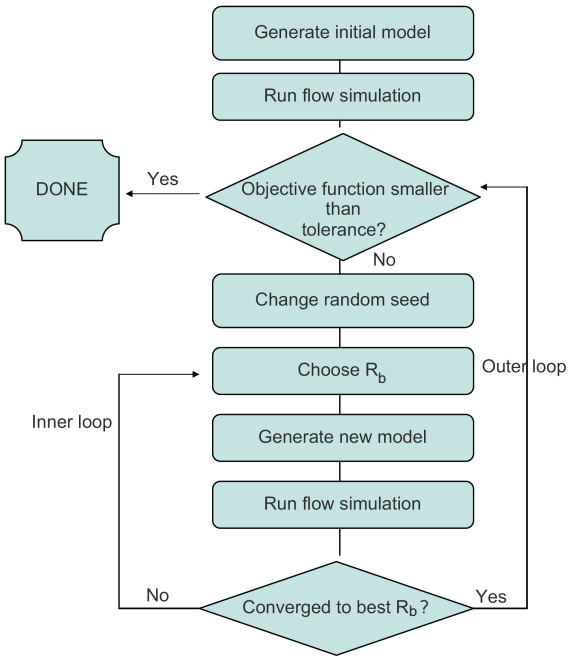

Figure 4.1: Typical flowchart of the PPM method (modified after Li and Caers 2008).

2. If $r_B = 1$, then $P(A|B) = P(A)$, i.e. the prior probability of the facies. Using this in the τ model gives $P(A|B, C, D) = P(A|C, D)$. The perturbation is equivalent to draw a new equiprobable realization with an alternative random seed $s\prime$. This case corresponds to the "maximum perturbation" within the prior model constraints and soft data.

3. If $0 < r_B < 1$, the perturbation will generate a new realization $i_{r_B}^{(s\prime)}$ between the initial realization $i_{CD}^{(s)}$ and another equiprobable realization $i_{CD}^{(s\prime)}$.

The value of the parameter r_B is optimized at each iteration for a given random seed and several iterations are necessary to reach a sufficient level of mismatch for the dynamical data. The algorithm can thus be divided in two loops: an *outer loop* where the random seed is modified and an *inner loop* to optimize r_B. In this implementation, the Brent optimization method (e.g. Press et al. 1992) is used to optimize r_B and its initial value is set to 0.5. To limit the CPU time of the algorithm, a maximum of five values of r_B are tested to find the optimum value. If at the end of an iteration, the objective function has not decreased, the algorithm continues at the next iteration with a new random seed.

4.2.3 Multi-category PPM and regional PPM

The PPM can be extended easily to multiple category variables as it is the case in this work (Caers and Hoffman 2006, Li and Caers 2008). A set of J indicators are created for the MPS algorithm (equation 3.3) and equation 4.5 is generalized in J equations

$$P(A_j|B) = (1 - r_B) \times i_{CD}^{(s)}(\mathbf{u}, s_j) + r_B P(A_j),\ j = 1, \cdots, J \tag{4.6}$$

where $P(A_j)$ is the proportion of the corresponding category. This equation is such that there is not any closure problem since

$$\sum_{j=1}^{J} P(A_j|B) = 1. \tag{4.7}$$

With the single parameter r_B, the method is a global perturbation method, i.e. the parameter r_B being constant for all cells of the model, the perturbation of the probability $P(A|B, C, D)$ has a similar form everywhere in the model. To improve the efficiency of the method for large and complex models, Hoffman and Caers (2005) proposed an extension of the method to a multiple parameter or regional PPM. The whole domain is divided into regions and a perturbation parameter is assigned to each region.

4.3 Synthetic benchmark

The methodology to integrate dynamical data into MPS constrained by geophysical data will be first illustrated using a synthetic benchmark. The final objective is to have models of the subsurface integrating geological data, geophysical data (here ERT) and hydrogeological data (here piezometric level). The first one is integrated through hard data conditioning and through the choice of the training image (topological relationships between facies). The second one is integrated as soft data with a probability map for each facies. The latter one is integrated through PPM.

After the detailed presentation of the synthetic benchmark, the results of the integration will be presented, focusing on the contribution of geophysical data to improve the models. Then, an analysis will be performed to highlight the effects of the values of hydraulic conductivity chosen to run PPM. The uncertainty about the training image will also be investigated.

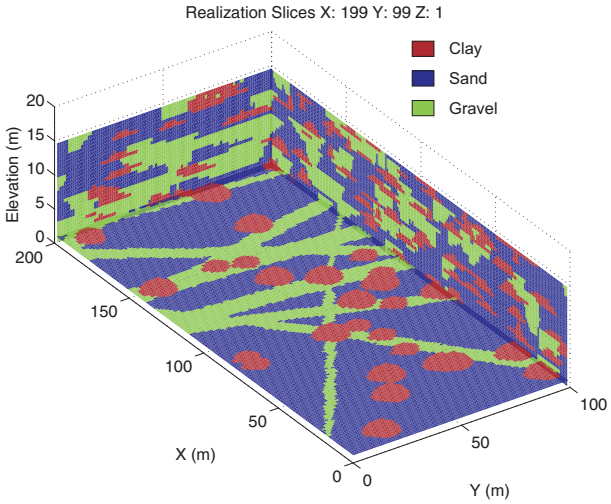

Figure 4.2: Training image used to build the synthetic model with small gravel channels and small clay lobes.

4.3.1 Presentation of the case

The synthetic benchmark represents an alluvial aquifer and is inspired by results described in chapter 3.

The true model is an unconditional realization of the SNESIM algorithm on a 3D grid of 136×24 cells (total of 189312 cells) of size $1\ m \times 1\ m \times 0.5\ m$. The length of the model (136) is chosen to correspond to an ERT profile of 64 electrodes spaced every 2 m with 5 additional meters at the sides of the profile. The width of the model corresponds approximately to the available space at Hermalle-sous-Argenteau. The thickness (12 m) is close to the expected thickness of alluvial deposits.

The only spatial constraint is the training image. The training image corresponds to the "small channels and small lobes", i.e. the training image with the highest probabilities of chapter 3. It has three facies: gravel, sand and clay with respective proportions 20 %, 58 % and 22 % (figure 4.2). To limit the time and memory demand of the algorithm, the size of the training image was limited to a grid of $200 \times 100 \times 30$ cells. With such configuration, the SNESIM algorithm may have some difficulties to reproduce large scale features of the training image, especially the continuity between channels.

The realization considered as the true model is displayed on figure 4.3. The reproduction of the features is satisfactory. As expected, the structures of the training images are not totally reproduced, the realization is slightly more erratic. The effect will be the same for realizations

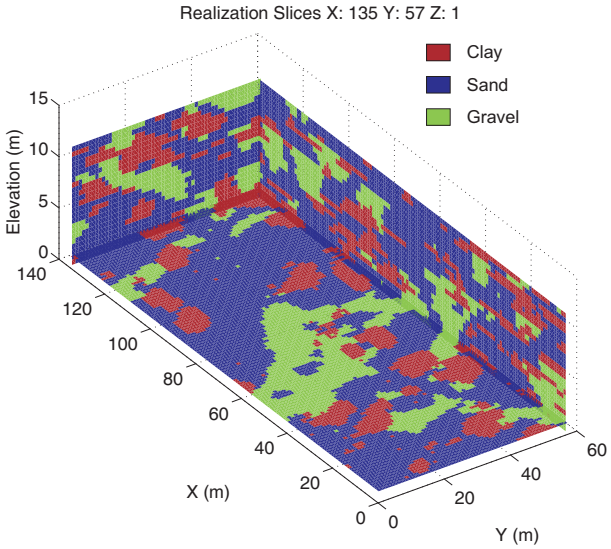

Figure 4.3: The true model of the synthetic case is characterized by small channels and small lobes like the training image.

during the integration process. In consequence, parameters related to the SNESIM algorithm will not have strong effects on the results.

This true facies model was transformed into an electrical resistivity model using the third resistivity distribution presented in chapter 3. From this model, 13 parallel ERT profiles were modelled to simulate the acquisition of ERT data sets. Random noise was added to the data with a maximum absolute error equal to 10^{-4} Ohm and a maximum relative error of 0.5 %. This level of noise was determined from reciprocal measurements made on the site of Hermalle-sous-Argenteau.

The 13 ERT profiles were inverted independently and combined to obtain a 3D model of resistivity. We used the standard smoothness constraint inversion to invert the data, with the addition of a structural constraint (ratio $\beta_x/\beta_z = 1000$) at the expected position of the bedrock (12 m depth) (see chapter 2). The data were inverted using the error model $|e| = 0.0001+0.005R$ to account for the noise on the data, the resulting sections are thus assumed to be free of artifacts.

The 3D ERT model was then transformed into facies probability maps. The methodology of section 3.5 was used. Since the third distribution of resistivity was used, we kept the 72 synthetic models of chapter 3 corresponding to this case to derive the relation between resistivity and facies, analyzing the sections cell by cell. The distributions are also Gaussian. The parameters are described in table 4.1. Electrical resistivity is slightly more discriminating than in chapter 3 because only one resistivity distribution was selected.

Facies	Prior probability	μ	σ
Clay	0.22	2.1776	0.1323
Sand	0.58	2.2293	0.1229
Gravel	0.2	2.3298	0.1197

Table 4.1: Characteristics of the Gaussian distribution of resistivity of the three facies for the synthetic benchmark. The values for mean and standard deviation are given in logarithm of resistivity (base 10) expressed in $[Ohm.m]$.

The resulting probability maps for gravel and clay are presented in figure 4.4. A similar map could be obtained for sand by combination. Higher probabilities of gravel are related to channel zones and high probability of clay are related to lobes. The three maps can be used as soft data in the SNESIM algorithm.

From the true field model (figure 4.3), 9 boreholes were simulated extracting facies information (hard data) for the simulations. The boreholes are distributed in a systematic manner, with a central borehole at position (68 m, 29 m), a first row of 4 boreholes at respective position (P5: 53 m, 20 m), (P6: 53 m, 38 m), (P7: 83 m, 20 m) and (P8: 83 m, 38 m); finally a second row of 4 boreholes at respective position (P1: 38 m, 29 m), (P2: 98 m, 29 m), (P3: 68 m, 12 m) and (P4: 68 m, 46 m).

The same set of boreholes was used to simulate hydrogeological data. It is composed of the drawdowns observed in the 9 piezometers corresponding to a pumping test at the rate of 100 m^3/h in the central well. This test was simulated using HydroGeoSphere (Therrien et al. 2010), in steady state. For simplicity, the boundary conditions were an imposed hydraulic heads of 12 m everywhere and the initial state (without pumping) is thus a constant hydraulic head in the model (no natural flow).

For flow simulation, it is necessary to give a hydraulic conductivity to each facies. We have three facies, one with a relative high hydraulic conductivity (gravel channel), one with a relative low hydraulic conductivity (clay lobe), and one intermediate. We imposed no horizontal anisotropy for each facies (same conductivity in x and y directions) and a ratio of 10 between horizontal and vertical conductivity. The hydraulic conductivity values used to simulate the pumping data are presented in table 4.2.

Those pumping conditions result in drawdowns in the different piezometers presented in table 4.3. In homogeneous conditions, the piezometers equidistant from the well should have a similar hydraulic head during pumping. Differences are related to the distribution of hydraulic

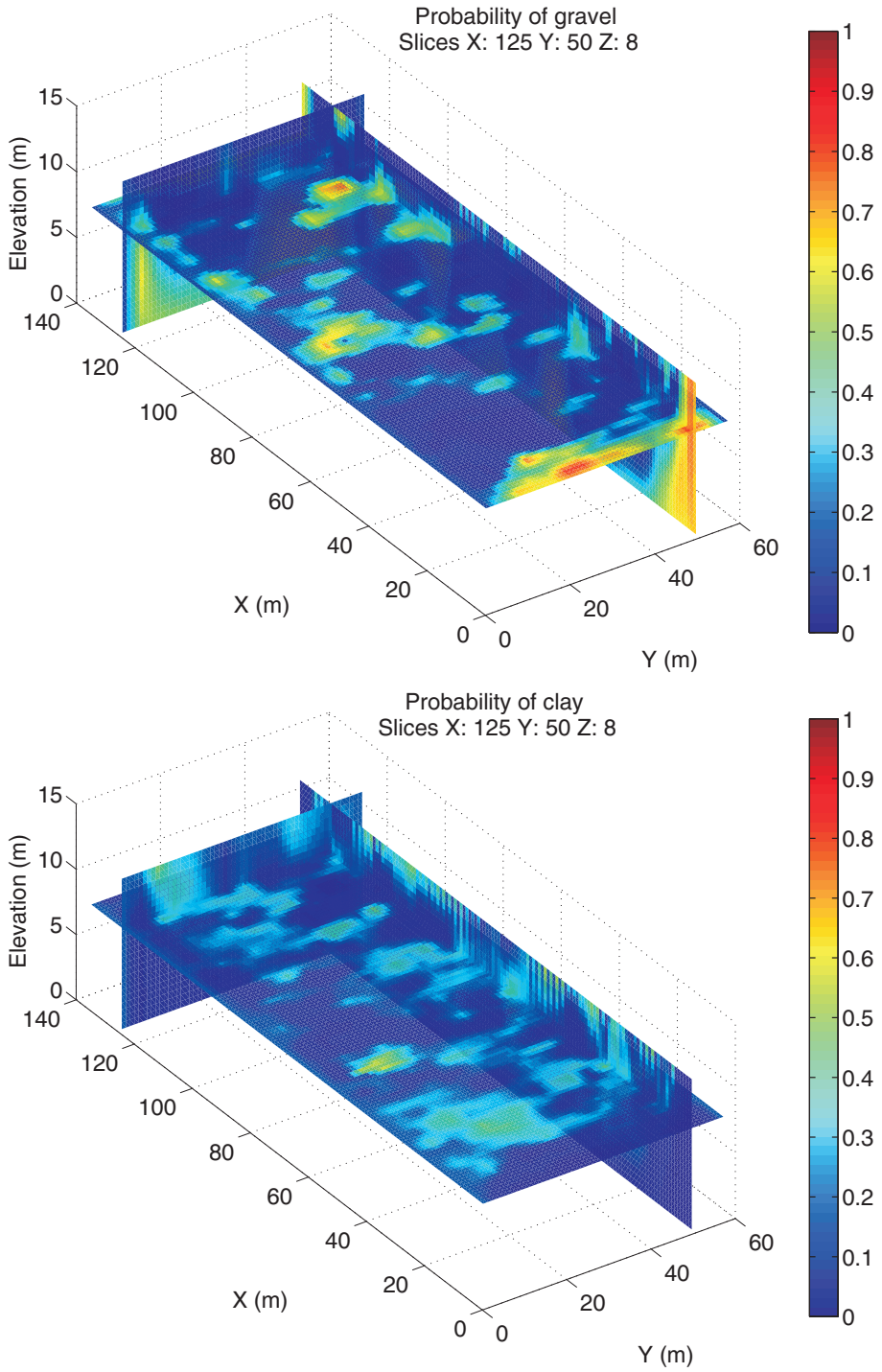

Figure 4.4: The facies probability maps derived from ERT for gravel (top) and clay (bottom) are related to the presence of gravel channels and clay lobes in the true model.

Facies	K_h (m/s)	K_v (m/s)
Clay	$5\ 10^{-6}$	$5\ 10^{-7}$
Sand	$5\ 10^{-4}$	$5\ 10^{-5}$
Gravel	10^{-2}	10^{-3}

Table 4.2: Hydraulic properties of the facies for the simulation of pumping data.

Piezometer	ΔH (m)
P1	0.077
P2	0.052
P3	0.131
P4	0.191
P5	0.180
P6	0.183
P7	0.136
P8	0.278
Well	0.816

Table 4.3: Drawdowns resulting from the simulated pumping test.

conductivity linked to the facies. For example, the drawdown is 50 % higher in P8 compared to P6 even though they are at the same distance from the well.

4.3.2 Analysis of the results

The PPM algorithm was applied to get 50 realizations for different cases. The objective function was defined as the sum of the square difference between calculated and observed data

$$\Phi(h) = \sum_{i=1}^{N} (h_i^{obs} - h_i^{calc})^2 \tag{4.8}$$

where N is the number of hydrogeological observations. The stopping criterion for the outer loop (figure 4.1) was then defined as a weighted objective function

$$\Phi_w(h) = \sqrt{\frac{\Phi(h)}{N}} < 0.025. \tag{4.9}$$

To limit the computational time, the maximum number of iterations of the outer loop was set to 10 and the number of value of r_B tested in the inner loop was limited to 5. PPM is designed to perturb the model in order to converge, as rapidly as possible, towards a solution. Using $r_B = 1$ would correspond to the rejection sampler, for which the model is rejected if the stopping criterion is not met at the first iteration and accepted if it is. This technique may find a solution but with a lot of iterations.

We compare the various cases based on 4 different criteria:

1. The mean value over 50 realizations of the weighted objective function $\Phi_w(h)$ at the end of the process (convergence or 10 iterations).

2. The number of realizations for which the final stopping criterion was reached (convergence).

Case	TI	Soft data	K_{sand}	K_{gravel}	K_{clay}	Mean $\Phi_w(h)$	$\Phi_w(h) < 0.025$	Classif.
Case 1	SC/SL	Yes	5×10^{-4}	10^{-2}	5×10^{-6}	0.028	18	48.24
Case 2	SC/SL	No	5×10^{-4}	10^{-2}	5×10^{-6}	0.060	0	17.27

Table 4.4: Results of the synthetic cases. The hydraulic conductivities are expressed in m/s and the classification in %; SC=small channels, MC=medium chanels, SB=small bars, BB=big bars, SL=small lobes, BL=big lobes.

3. The posterior probability maps computed from the results of the 50 realizations.

4. The percentage of gravel cells of the true model correctly classified as gravel on the basis of the posterior probability maps.

The two first criteria are used to verify if the algorithm is able to converge to a satisfactory solution. The third criterion is used to analyze spatially the results and the last criterion is an estimate of the performance of the method. We choose to analyze the classification of gravel because it is the most influencing facies for groundwater flow. The global performance (based on the three facies) would be biased by the fact that all facies are not equiprobable. Indeed, a method that would classify all cells as sand would have a classification performance of 58% (proportion of sand) even if it is not able to locate gravel bodies. This last criterion can only be used for synthetic benchmarks for which the true distribution is known.

The first test which was performed was the analyzis of the improvement brought by geophysical data. The results are summed up in table 4.4. The PPM algorithm was run two times, with (Case 1) and without (Case 2) soft data, all other parameters being the same. The training image was the "correct" training image of figure 4.2 and the hydrogeological parameters were supposed to be known for each facies (table 4.2). The difference between the two cases is simply the use of the probability maps of figure 4.4.

With hard data only, i.e. the facies extracted from the boreholes are imposed for each realization, the mean objective function at the end of the process is 0.06, this corresponds approximately to an average difference of level of 6 cm between measured and calculated levels. There is not any model which fulfils the convergence criteria among the 50 realizations. The best model has a final objective function of 0.033. The inversion process fails to converge to a sufficient level. The number of iterations should be increased to ensure the convergence of the method, which would increase the computation time.

With soft data, the mean objective function for 50 realizations is 0.028 just above the specified

limit of 0.025. It signifies that at the end of the inversion process, most of the realizations have an objective function close to the expected values. Among them, 18 models are really "history matched", i.e. their final objective function verifies equation 4.9.

The corresponding posterior probability maps are presented on figure 4.5 for gravel. In both cases, the presence of gravel in wells is highlighted by very high probabilities around wells and probabilities equal to 1 at the position of the well itself. However, differences appear. Without soft data, the highest probability of gravel looks like an almost circular zone around the well. It illustrates that the SNESIM algorithm, driven by the training image will preferentially impose gravel next to gravel occurrence, since gravel is found inside continuous channels. With soft data, this effect is less marked. For example a low probability zone appears in the area ($X = 45\ m$, $Y = 30\ m$). This corresponds to a zone of low probability of gravel (and higher for clay) from soft data in figure 4.4. High posterior probability of gravel also appears in the area where wells are not present: ($X = 0\ m$) and ($X = 120\ m$, $Y = 45\ m$). Here, it corresponds to a zone of high probability in figure 4.4.

The posterior probability of gravel with soft data is also characterized by sharper contrasts in the distribution. Globally, probabilities are closer to 0 (dark blue) or 1 (red) and less often in between. Remember that the prior probability of gravel is 20%.

The classification resulting from the posterior probability maps shows that ERT aids to locate more accurately gravel channels. Without soft data, only 17.27% of the gravel cells are correctly identified after 50 realizations. With soft data, the performance increases up to 48.24%. This is a strong improvement which illustrates the ability of ERT to characterize spatially the deposits. The classification of gravel suffers partially from the low prior proportion of gravel (20%) compared to the sand facies. It explains that only half the gravel cells are identified.

With this analysis, we understand the results for the mean objective function and the number of history matched models. Using soft data in the SNESIM algorithm results in initial models where gravel channels are, in average, more accurately located. Those models are more appropriate to explain the observed hydraulic heads which gives smaller objective function. When the model is perturbed, soft data is still taken into account and this behavior is kept during the whole PPM process. Without soft data, initial models with correctly located gravel channels are, in proportions, less abundant and the same is true during perturbation. This explains why

Case	TI	Soft data	K_{sand}	K_{gravel}	K_{clay}	Mean $\Phi_w(h)$	$\Phi_w(h) < 0.025$	Classif.
Case 1	SC/SL	Yes	5×10^{-4}	10^{-2}	5×10^{-6}	0.028	18	48.24
Case 2	SC/SL	No	5×10^{-4}	10^{-2}	5×10^{-6}	0.060	0	17.27
Case 3	SC/SL	Yes	5×10^{-4}	10^{-3}	5×10^{-6}	0.937	0	48
Case 4	SC/SL	Yes	5×10^{-4}	10^{-2}	5×10^{-7}	0.028	13	48.67
Case 5	SC/SL	Yes	5×10^{-5}	10^{-2}	5×10^{-6}	0.067	0	48.18
Case 6	SC/SL	Yes	5×10^{-4}	5×10^{-2}	5×10^{-6}	0.112	0	34.1
Case 7	SC/SL	Yes	5×10^{-4}	10^{-2}	5×10^{-5}	0.026	28	47.49
Case 8	SC/SL	Yes	10^{-3}	10^{-2}	5×10^{-6}	0.027	14	44.24

Table 4.5: Results of the synthetic cases. The hydraulic conductivities are expressed in m/s and the classification in %; SC=small channels, MC=medium chanels, SB=small bars, BB=big bars, SL=small lobes, BL=big lobes.

the convergence is speeded up using ERT as soft data. Among all the possible models that could be drawn using SNESIM, soft data helps to choose the ones that have a higher probability to explain the observed hydraulic heads.

4.3.3 Sensitivity to hydraulic properties

The main disadvantage of the PPM algorithm is to explore only the geometrical uncertainty of models. It is necessary to estimate the hydraulic conductivity of the different facies separately. This can be done through an estimation from field measurements (pumping tests) or from knowledge of the different facies or using trials and error or optimization during calibration.

Here, we know the hydraulic properties that were used to simulate the data (table 4.2). However, it would not be the case in field conditions. We provide a short sensitivity analysis to highlight the role of the hydraulic properties of the different facies by increasing and decreasing the value of hydraulic conductivity (Cases 3 to 8). The results are summed up in table 4.5

Cases 3 and 6 correspond respectively to a decrease and an increase in the hydraulic conductivity of the gravel facies. With a decrease of one order of magnitude, the mean objective function after 10 iterations is more than 30 times higher than with the "true" value. Even if the gravel facies represent only about 20% of the cells, it influences greatly groundwater flow and the drawdonws observed during pumping. Reducing the hydraulic conductivity of gravel results in increased drawdowns and it becomes impossible to fit the targeted objective function. When the hydraulic conductivity is increased, the opposite effect is observed: drawdowns are reduced and it is also impossible to fit the data sufficiently. For this case, the classification performance also decreases down to 34.1%.

Case 4 corresponds to the reduction of the hydraulic conductivity of the clay facies from

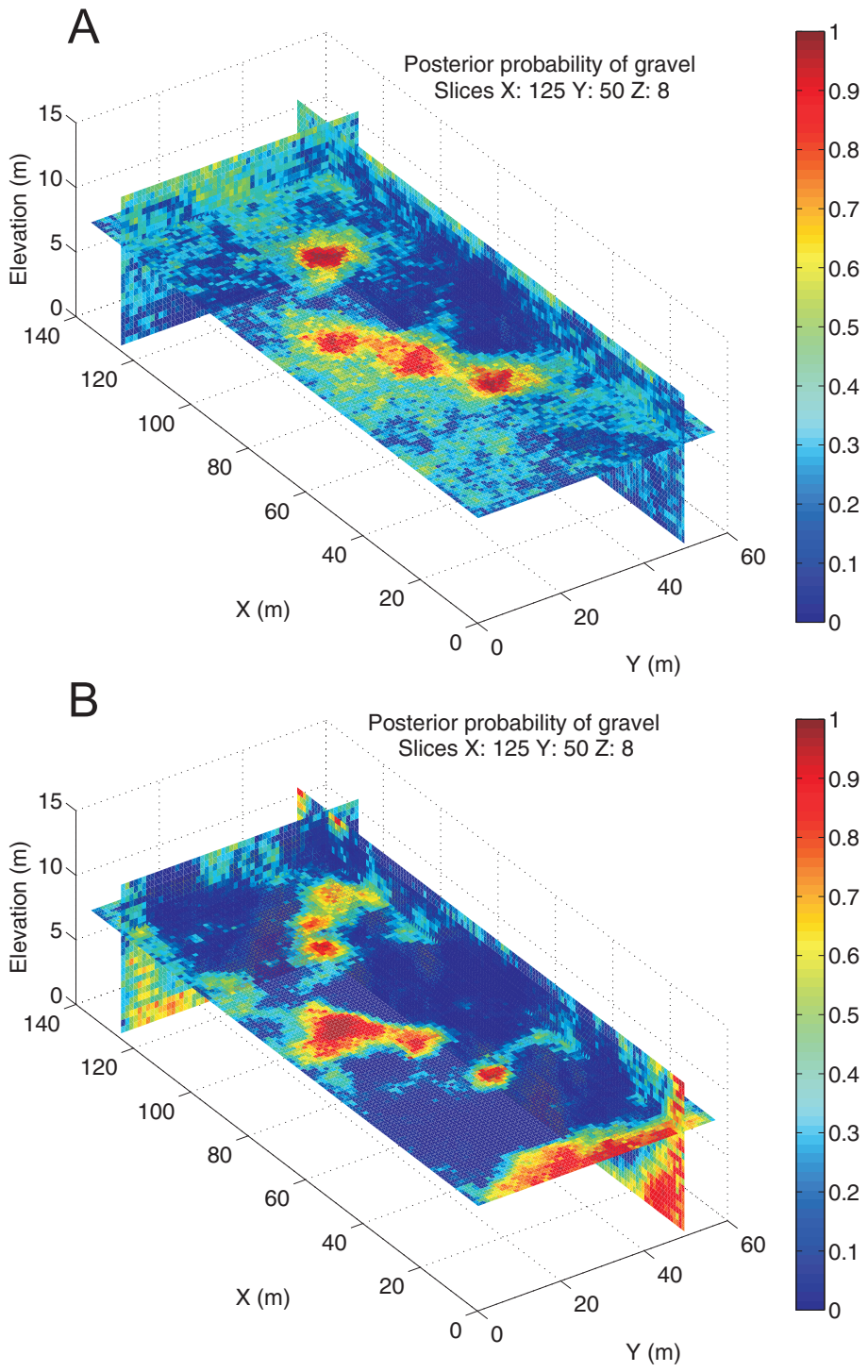

Figure 4.5: The posterior probability maps for gravel without (A) and with (B) soft data show some differences. With soft data, the presence or absence of gravel is modeled with less variability. In both cases, gravel in wells is highlighted by posterior probability equal to 1.

5×10^{-6} to 5×10^{-7} m/s. This has little influence on the results since the mean objective function is similar to the reference case and 13 models are history matched. This is understood since this facies is relatively not permeable compared to other facies. In the reference case, this facies already acts as a barrier to groundwater flow and this phenomenon is not more emphasized in this case. When the hydraulic conductivity of clay is increased up to 5×10^{-5} m/s (Case 7), the mean objective function is smaller than for the reference case (0.026), but not significantly and 28 models are history matched which is slightly better. Changing the hydraulic conductivity of clay with one order of magnitude does not seem to impact strongly the solution. This is not a sensitive parameter.

Cases 5 and 8 correspond respectively to a decrease and an increase in hydraulic conductivity of sand (table 4.5). In case 5, the mean objective function is less favorable (0.067). Less permeable sands result in globally higher drawdowns and it is impossible to explain the observed data. It is interesting to note that this level is similar to case 2 where no soft data was used. The reason for "failure" is nevertheless different. Here, the reason is clearly an inadequate choice of parameter whereas in case 2 the explanation is related to the geometrical architecture of the different facies. This illustrates the importance of both aspects in hydrogeological inversions: bad calibration may be related to an inconsistent parameter or an inadequate geometry of the deposits.

In case 8, the hydraulic conductivity of sand is doubled. Its value is still one order of magnitude below the value of gravel. It seems that flow is still driven by gravel channels, since there is no clear effect: the mean objective function reaches a similar level (0.027) with 14 history matched models.

The posterior probability maps of those cases help to understand how PPM and MPS are working (figure 4.6). Indeed, cases 3 and 4 have completely different final objective functions and case 3 does not yield any history matched model in contrast with case 4. Nevertheless, the posterior probability maps for gravel look very similar. The same zones where the posterior probability of gravel is high can be observed as in figure 4.5B, even if local differences are present. This highlights the geometrical character of MPS and PPM. An initial model is built with MPS and perturbed through PPM, but the perturbation concerns the relative position of facies elements as expected in the training image. In both cases 3 and 4, the training image and the soft

data are similar, the proposed realizations are thus similar. For case 3, bad hydraulic properties are imposed, it prevents the PPM algorithm to converge to the targeted objective function. Nevertheless, the minimization of the objective function produces solutions (figure 4.6) quite similar to what is obtained with the correctly estimated hydraulic parameters. The classification performance confirms this observation since the level is equivalent to the one of case 1, with about 48%.

To obtain reliable stochastic realizations of calibrated models, it is thus necessary to consider both effects. Consistent hydraulic parameters should be estimated either by trial and errors or using an optimization technique. In this case, the most important parameter is the hydraulic conductivity of gravel. In this section, we have shown that the objective function is, as expected, clearly influenced by this parameter and can be used to derive the optimal values to use in PPM. Then, all PPM realizations are run with the same hydraulic properties. It results in a set of history matched models all calibrated with the same properties.

This approach has a strong difference with the one proposed by Rentier (2003). In her approach, two realizations differ both in the zonation (or geometry) and in the hydraulic properties since an optimization technique was used to find the best parameters for calibrating each realization. Here, two realizations only differ in the geometry. Geometries which are not able to explain hydraulic heads are rejected.

4.3.4 Sensitivity to the training image

In chapter 3, we have seen that the role of the training image was crucial in multiple-point statistics. Its major influence is to constrain the geometry and topological relationships between facies. We have also seen that several training images could be consistent with geophysical data and it may be necessary to consider several training image-based scenarios, possibly with different probabilities estimated with our multi-dimensional scaling approach.

In this section, we investigate the role of the training image in the calibration of hydrogeological models using PPM. In addition to the training image corresponding to the true model (small channels and small lobes), 7 different training images were considered. They correspond to the combination of 2 sizes of clay lobes (small and big) with 2 different sizes of channels (small and medium) or 2 different sizes of bars (small and big). There are thus 14 new cases: cases

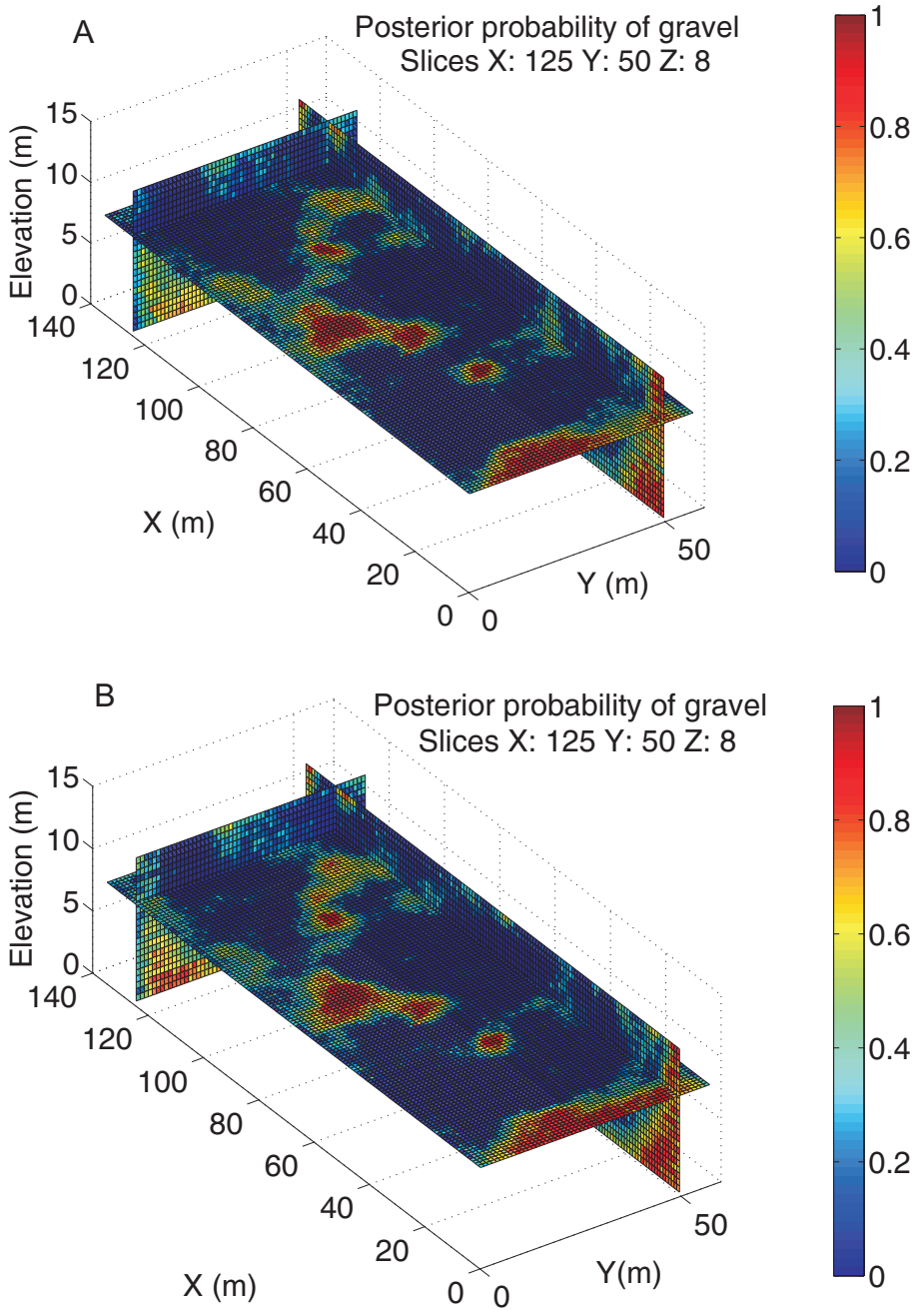

Figure 4.6: The posterior probability maps for gravel for cases 3 (A) and 4 (B) look very similar even if the final objective function is completely different. In contrasts with case 3, case 4 yields history matched results.

Type of bar	Length max (in m)	Width max (in m)	Thickness max (in m)
Big	35	16	5
Small	20	6	3

Table 4.6: Dimensions characteristic of the bars of the training image scenarios.

9 to 15 use hard data and soft data from ERT, cases 16 to 22 use only hard data from wells. The size of channels are the same as investigated in chapter 3 (see tables 3.2 and 3.3). The bars were simulated using ellipsoid, their dimensions are presented in table 4.6. The difference between bars and channels is visible in realizations (figure 4.7): training image with channels (figure 4.7B) tends to produce gravel zones crossing the whole simulation grid, whereas it is not always the case for bars (it is possible if several bars are aggregated). The results are summed up in table 4.7.

If we look at the value of the mean objective function, we see that there are some disparities between the cases when only hard data is used: the mean objective function varies between 0.038 and 0.077. Surprisingly, some alternative training images perform better than the "true" one. All the training images with bars have a mean objective function smaller than 0.06. This is also the case for the training image with medium channels and small lobes (case 17). For some of the cases, the PPM algorithm yields history matched models for which equation 4.9 is verified. This was not the case with the actual training image. However, the number of calibrated models remain small compared to the 50 realizations, so it may be a coincidence. Similarly, cases with medium channels and big bars have a better classification performance (21 to 24%) than the reference case (case 2). This observation illustrates that the uncertainty related to the training image is very important. It could be expected that the choice of the training image would be reflected in the mean objective function, as it was the case for the value of hydraulic conductivity. Apparently, it is not the case, even if realizations from two training images may be quite different (figure 4.7). So the choice of the best training image cannot be done *a posteriori* according to the mean objective function. Alternative training images performing at least as well as the actual training image, the uncertainty or the choice of the training image must be done previously and independently, as it was proposed in section 3.4.

Then, the analysis of table 4.7 confirms the results of section 4.3.2 concerning the role of soft data. Indeed, for every training image, except the one with small bars and small lobes (cases 12 and 19), the final objective function is smaller for the case with soft data compared to the case

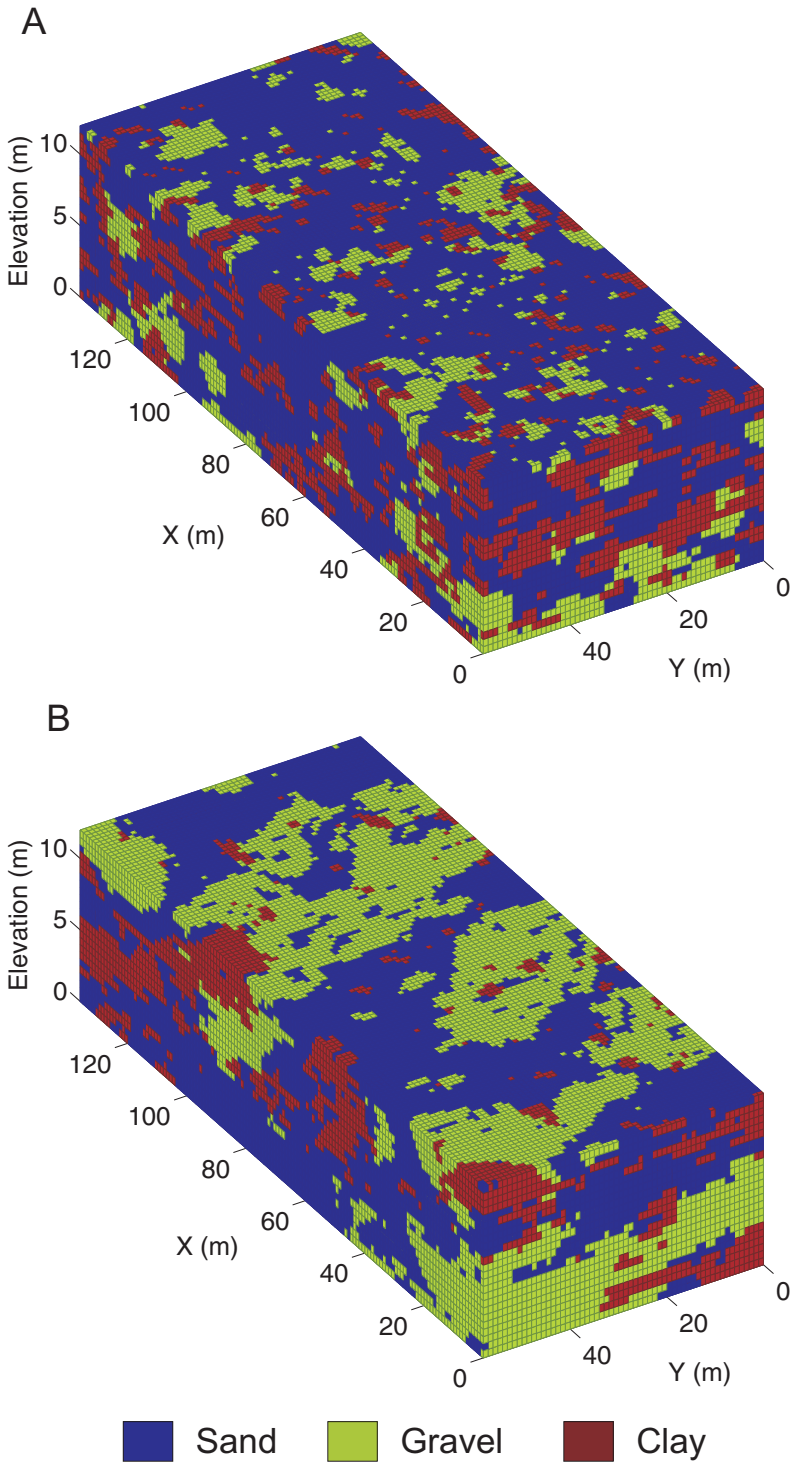

Figure 4.7: A realization using the training image "small bars and small lobes" (A) is quite different from a realization using the training image "medium channels and big lobes".

Case	TI	Soft data	K_{sand}	K_{gravel}	K_{clay}	Mean $\Phi_w(h)$	$\Phi_w(h) < 0.025$	Classif.
Case 1	SC/SL	Yes	5×10^{-4}	10^{-2}	5×10^{-6}	0.028	18	48.24
Case 2	SC/SL	No	5×10^{-4}	10^{-2}	5×10^{-6}	0.060	0	17.27
Case 9	SC/BL	Yes	5×10^{-4}	10^{-2}	5×10^{-6}	0.028	11	31.52
Case 10	MC/SL	Yes	5×10^{-4}	10^{-2}	5×10^{-6}	0.027	17	40.36
Case 11	MC/BL	Yes	5×10^{-4}	10^{-2}	5×10^{-6}	0.027	18	37.78
Case 12	SB/SL	Yes	5×10^{-4}	10^{-2}	5×10^{-6}	0.038	2	33.36
Case 13	SB/BL	Yes	5×10^{-4}	10^{-2}	5×10^{-6}	0.328	8	34.42
Case 14	BB/SL	Yes	5×10^{-4}	10^{-2}	5×10^{-6}	0.032	10	36.66
Case 15	BB/BL	Yes	5×10^{-4}	10^{-2}	5×10^{-6}	0.032	7	39.85
Case 16	SC/BL	No	5×10^{-4}	10^{-2}	5×10^{-6}	0.071	4	10.14
Case 17	MC/SL	No	5×10^{-4}	10^{-2}	5×10^{-6}	0.047	2	23.74
Case 18	MC/BL	No	5×10^{-4}	10^{-2}	5×10^{-6}	0.078	2	23.85
Case 19	SB/SL	No	5×10^{-4}	10^{-2}	5×10^{-6}	0.038	0	11.22
Case 20	SB/BL	No	5×10^{-4}	10^{-2}	5×10^{-6}	0.052	1	10.74
Case 21	BB/SL	No	5×10^{-4}	10^{-2}	5×10^{-6}	0.057	0	21.18
Case 22	BB/BL	No	5×10^{-4}	10^{-2}	5×10^{-6}	0.045	0	21.05

Table 4.7: Results of the synthetic cases. The hydraulic conductivities are expressed in m/s and the classification in %; SC=small channels, MC=medium chanels, SB=small bars, BB=big bars, SL=small lobes, BL=big lobes.

without it. For all cases, the level of correct classification is also higher using geophysical data to constrain simulations. It signifies that soft data is able in each case to improve the calibration process in PPM. When we look at the interval of variations of the mean objective function, we see that its size is reduced compared to the case without soft data. Here, it fluctuates between 0.027 and 0.038. If we eliminate the worst case (maximum value), it even becomes 0.027 to 0.033 which is relatively small. From these results, it seems that soft data tends to smooth the variations in the objective function between the various cases. The information brought by ERT seems to "correct" the differences in topological relationships of the training image in posterior probability maps. The facies are still of different shapes and sizes in the realizations, but soft data, through the τ model, improves their location which subsequently improves the calibration of the hydrogeological model. The tiny differences in the mean objective function do not enable to really sort the training images according to their performance. The number of history matched models (equation 4.9) shows that three training images perform as well to integrate hydraulic heads data: small channels and small lobes which is the actual one, medium channels with small or big lobes obtain similar criteria.

Only the classification criterion is able to discriminate the actual training image from the other cases. The classification performance of alternative training image is at maximum 40%, which is significantly lower than the performance of the actual training image (48%). Unfortunately, this criterion is not available for field cases.

The performance of the models with the training image "small bars and small lobes" is not improved with the use of soft data. This may indicate that this training image is not consistent with the ERT survey simulated on the true model. In this training image, the length of bars is relatively limited (table 4.6). Even if several bars may be adjacent, this topology is relatively different from channels which are crossing the whole area. These characteristics are mirrored in the distribution of resistivity. For big bars, the ratio of the length of the bar to the width of the model is higher, which makes this topology closer to a "channel case".

Figures 4.8 and 4.9 present the posterior probability of gravel for cases 18 and 19 and cases 11 and 12 respectively. They correspond to the same training image (medium channels/big lobes and small bars/small lobes) but for realization without and with soft data. Those figures are also to compare with figure 4.5 for the reference case (small channels and small lobes).

Without soft data (figure 4.8), the posterior probability maps are slightly different. Compared to figure 4.5A, there are less zones of "intermediate" probability for the small bars and small lobes case. The role of the training image is well illustrated by the relatively continuous zone of high probability of gravel crossing three wells. With medium channels, whose size is not negligible compared to the dimensions of the simulation grid, the high probability zone encompasses the three wells, and seems to be one big zone of high probability. During the simulation, most of the realizations have a common channel at this position. In this posterior probability map, there are also little constrained zones (intermediate probability), but they look more structured and less random than in figure 4.5A. The training image with small bars has smaller elements, the three wells appear as more dissociated in the posterior probability.

For the cases with soft data, the differences between the three cases are somewhat reduced. The general trends of the reference case are also visible with other training images, which is related to the use of ERT as soft constraint. This was not the case without soft data. As an example, the zone of intermediate probability (X=50 to 60 m, Y=0 to 20 m) has disappeared since it corresponds to a zone of very low probability of gravel in figure 4.4A. P1 ($X = 38$ m, $Y = 29$) and P5 ($X = 53$ m, $Y = 20$) also appear as more disconnected when soft data is used. This confirms the analysis made on the basis of the mean objective function and the number of history matched models: the use of soft data smooths the results of PPM in terms of posterior probabilities.

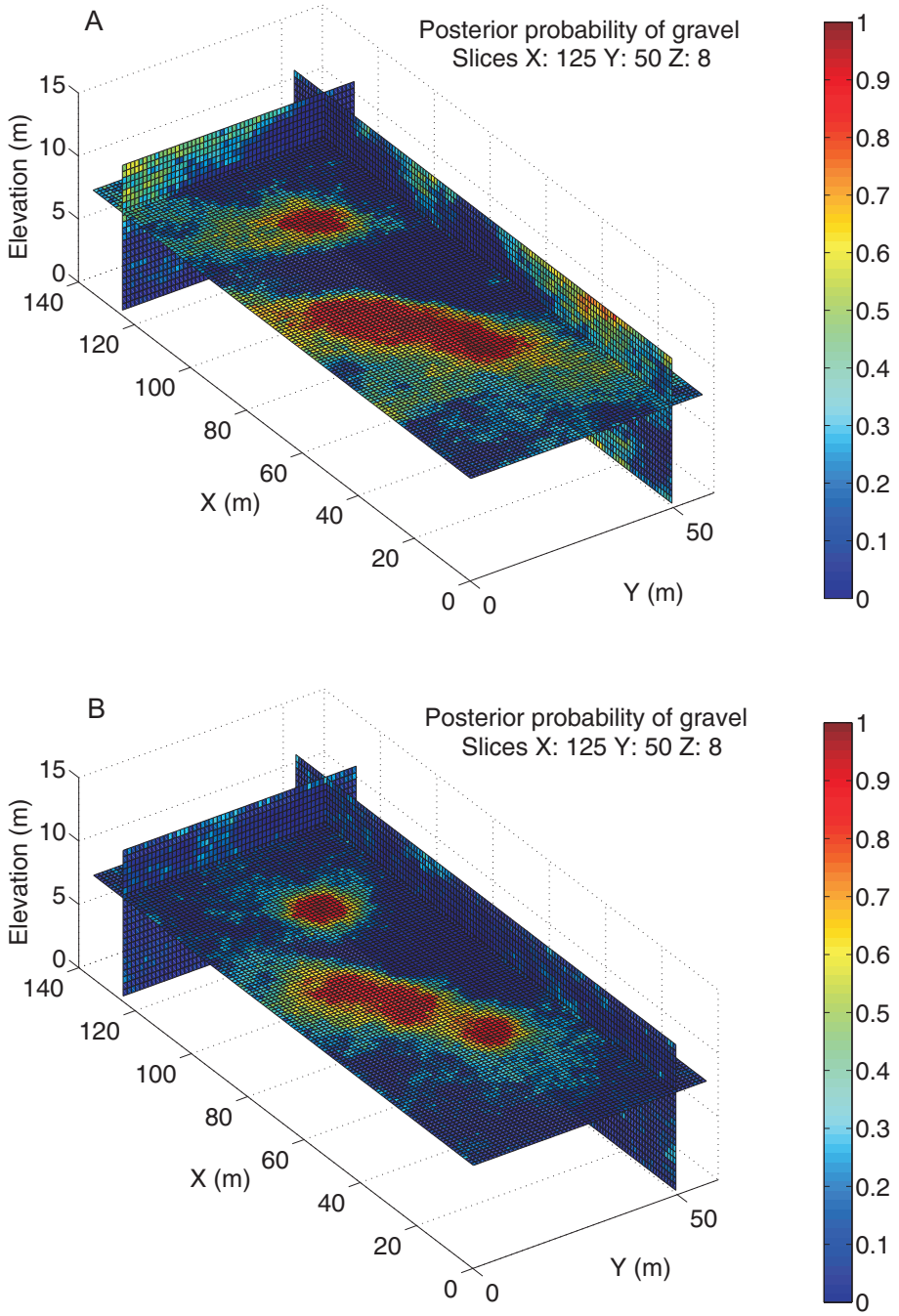

Figure 4.8: The posterior probability maps for gravel for cases 18 (A) and 19 (B) are slightly different due to the objects used in the training image and their size. The training image with medium channels produces more continuous structure in the posterior probability map.

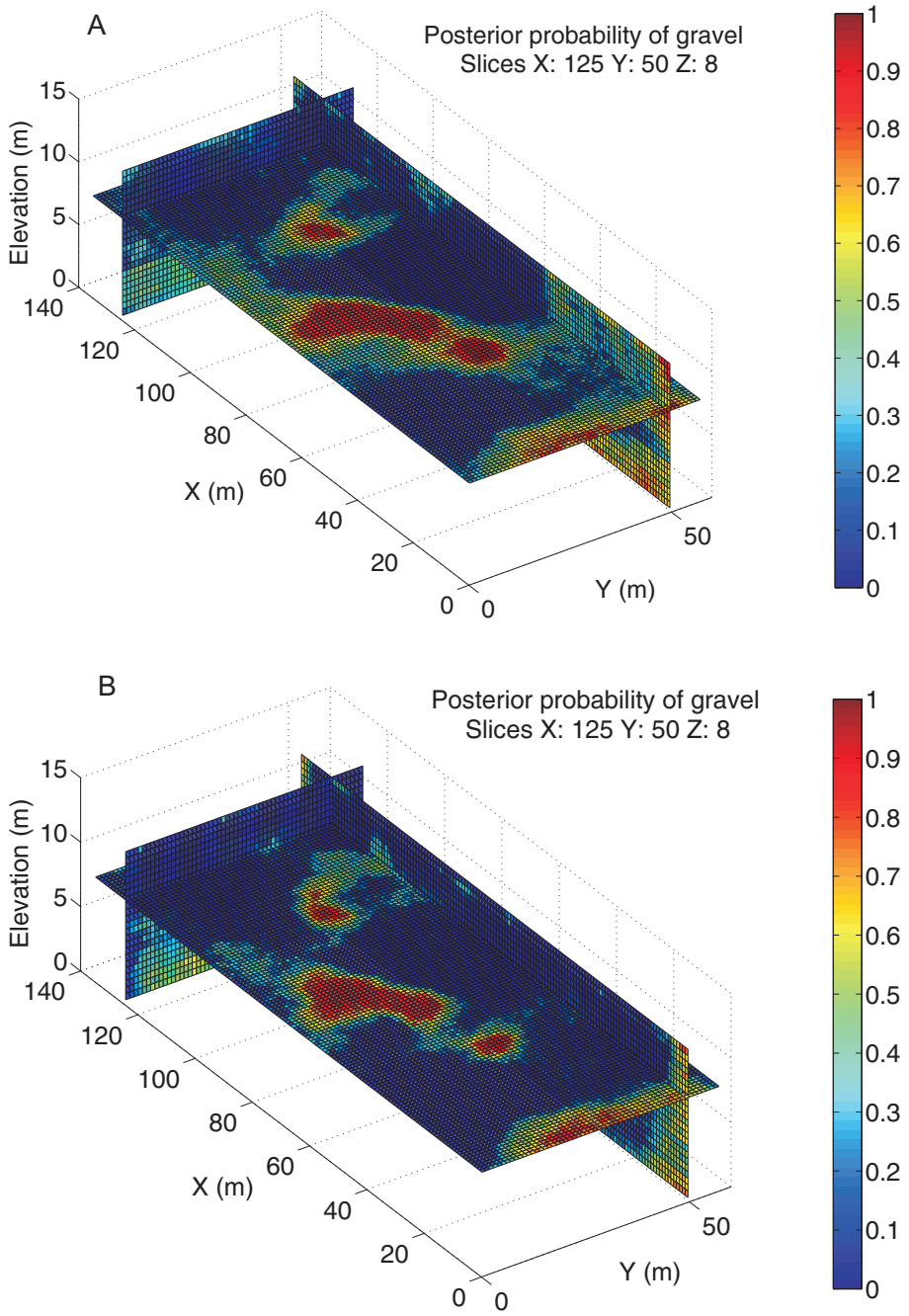

Figure 4.9: The posterior probability maps for gravel for cases 11 (A) and 12 (B) are slightly different due to the objects used in the training image and their size, but the use of soft data reduces the differences compared to figure 4.8.

4.3.5 Summary of the synthetic benchmark

In section 4.3, we have presented a synthetic case with several variants. This synthetic benchmark helps us to understand important features of the methodology we are trying to build.

1. As stated previously in section 3.4, the choice of the training image is a major source of uncertainty. In controlled conditions (we know the true model and the original training image), alternative conceptual models have performed as well as the initial one, producing similar history matched models in terms of level of the objective function. The choice of the training image is thus crucial as it may lead to calibrated models but with wrong assumptions on the geology. Hydraulic heads only are not sufficient to discriminate between different training images (or at least all of them). The choice must thus be done *a priori*. However, the addition of tracing experiments data in the calibration process may help to discriminate various cases by highlighting preferential flow paths (see chapter 5).

2. Soft data acts as an accelerator of convergence. Indeed, the final objective function is always smaller and the classification of gravel improved with soft data. During the stochastic process, this additional constraint helps to produce models more able to explain hydrogeological data, as it contains, through facies probabilities, the link between hydraulic conductivities and electrical resistivity. This process also narrows the results of PPM by giving sharper distributions of the posterior probabilities. Soft data helps to eliminate realizations that are not compatible with ERT, and thus tends to reduce the uncertainty of the prior and the variability of the posterior distribution.

3. Ensuring a common constraint for all cases, soft data tends to smooth the differences in the posterior probability maps of the various cases. All the criteria used for comparison (mean objective function, number of history matched models, posterior probability maps and classification) are more alike when soft data is used. Individual realizations are still different for the various cases, but the global results are filtered through this additional constraint.

4. Only a criterion based on the classification of cells according to posterior probability maps is able to unequivocally identify the best training image to use for the construction of

models. However, such criterion cannot be used for field cases. The uncertainty of training images will thus remain a major concern for field case studies. Therefore, it is important to characterize it with geophysics (see chapter 3).

5. The level of the mean objective function at the end of the process is heavily affected by the hydraulic properties of the facies. This sensitivity analysis shows that the most important parameter in this case is the hydraulic conductivity of gravel. It is thus necessary to estimate a value for the parameters with confidence before applying PPM. This may be done on individual realizations through a classic optimization method (e.g. Doherty 2004) or through trials and errors.

4.4 Field case : site of Hermalle-sous-Argenteau

The methodology illustrated with the synthetic benchmark will now be tested on a field site: the site of Hermalle-sous-Argenteau. This site was already presented in section 2.6 (figures 2.20 and 2.21). The site was chosen for several reasons.

1. It is located in the alluvial aquifer of the Meuse River.

2. It is easily accessible for geophysical investigations.

3. It has already been investigated previously, hydrogeological data are available and hydrogeological models have already been calibrated.

First, we will describe how geophysical data was acquired on the field and how the data were processed to provide soft probability maps for simulations. Then, we will analyze the hydrogeological model, the choice of the data to fit, the boundary conditions and the hydrogeological properties. Finally, the PPM algorithm will be run with various training images.

4.4.1 Geophysical data acquisition and soft data

With the aim to provide soft data for multiple-point geostatistics, 12 ERT profiles (figure 4.10) were carried out on the site (profile 1 is the southern profile). The first five profiles were acquired in Augustus 2012, the seven other profiles were acquired in September 2013. The

objective was to collect parallel profiles with 4 m spacing between individual profiles, in a direction parallel to the main direction of flow (orientation of the new piezometers). This is almost verified for the two data surveys individually, but an error of orientation occurred between the two surveys.

The first eleven profiles were collected with 64 electrodes spaced every two meters. Each profile is thus 126 m long. The twelfth profile is only 102 m long (52 electrodes). Its size was reduced due to logistical constraints. The position of the profiles is such that almost all piezometers and wells (except Pz4, Pz5 and Pz8) on the site are covered by one profile. This will enable us to compare directly ERT resistivity results with the facies described in borehole logs.

The same protocol was used for data acquisition of the 12 profiles. A dipole-dipole configuration, with factors $n < 7$ and $a < 9$ was used for its good lateral resolution to image heterogeneity in the deposits. It suffers from a low signal-to-noise ratio (Dahlin and Zhou 2004). However the noise level on the site of Hermalle-sous-Argenteau is acceptable. It was monitored using reciprocal measurements for 9 of the 12 profiles. The level of noise was very similar for all the profiles. Based on the reciprocal error analysis (figure 4.11), a linear error estimate (Slater et al. 2000) was used $|e| = 0.002 + 0.0026R$, where the error e and the mean measured resistance R are expressed in $[Ohm]$. This error model overestimates the error for a large majority of points, it may be considered as sufficiently conservative to avoid artifacts of inversion related to noise in the inversions. A model encompassing all the points, even the minority with a very large error would be too conservative and would smooth many resistivity contrasts. Points with very reciprocal and repeatability errors were ignored for inversion.

Even though a 3D inversion was possible, given the number of data available with 12 parallel ERT profiles, it was decided to invert each profile separately, with the $2.5D$ assumption. This was required because the methods of incorporation of prior information are not yet implemented in the code CRTomo for 3D inversion. Based on our analysis in chapter 2 about the incorporation of prior information, we followed the results of section 2.6 to select the best possible solution. This profile corresponds to profile 2 on the investigated area. The non-stationary geostatistical inversion (figure 2.27H) was the solution explaining the best the observed resistivity distribution in Pz3 (figure 2.28). This solution was computed with a vertical range for the variogram of

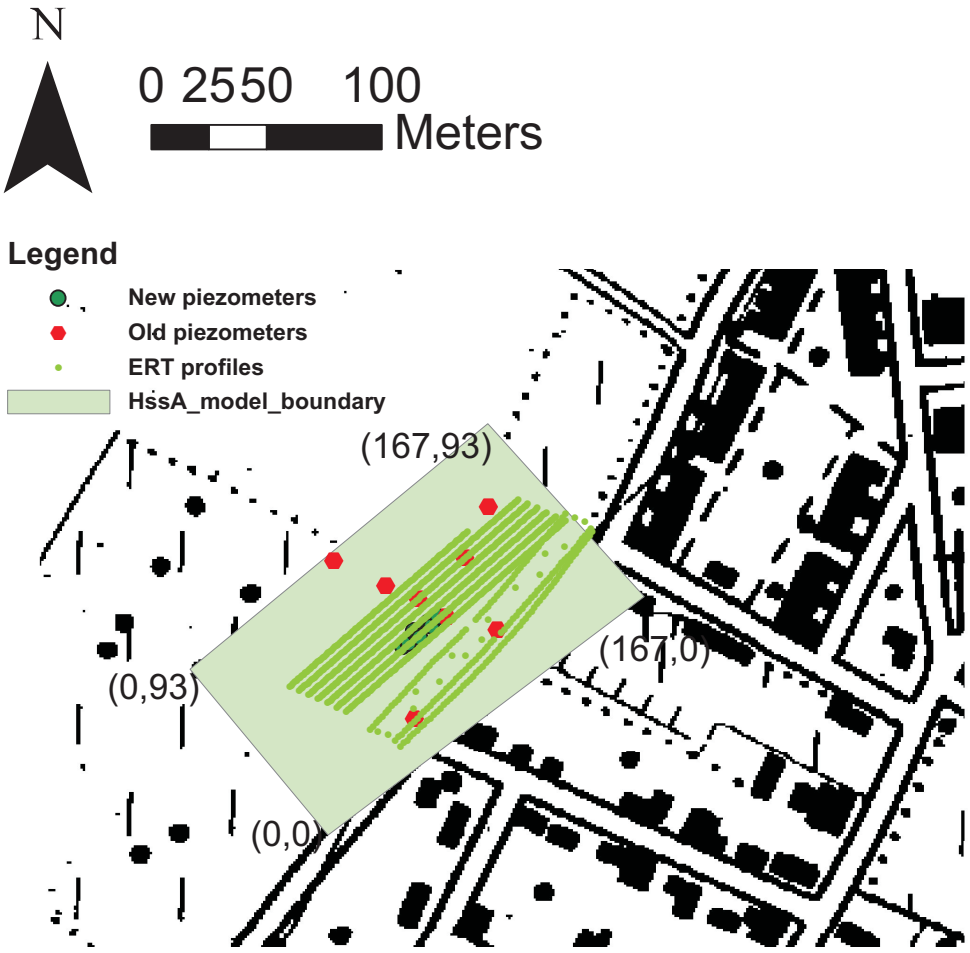

Figure 4.10: The site of Hermalle-sous-Argenteau with the relative position of the ERT profiles, of old and new piezometers and the limit of the local hydrogeological model.

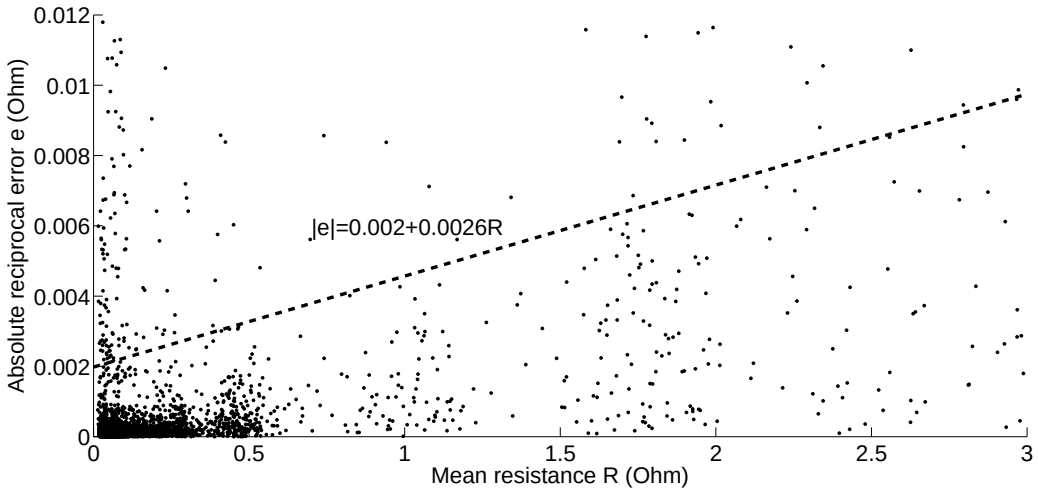

Figure 4.11: The error level on the site was assessed using reciprocal measurements. A common error model (Slater et al 2000) was used for inversion: $|e| = 0.002 + 0.0026R$.

4.4 m (figure 2.24) and an anisotropy ratio of 2.5. The non-stationarity appeared at the position of the bed-rock. Based on the depth of bedrock in the piezometers and the seismic refraction profiles available on the site, the bedrock limit was set at 10 m depth. The prior model used in inversion (equation 2.30) is also heterogeneous, with a value of 120 $Ohm.m$ in the alluvial deposits and 300 $Ohm.m$ for the bedrock.

The results of inversion validate the assumption to invert in $2.5D$. Indeed, the structure observed in the inversion results of several profiles (figure 4.12) show that the general structures are perpendicular to the direction of the profiles. On the first part of the profiles (north-eastern part of the site), the first meters have a low electrical resistivity. This zone corresponds to thick loamy and clayey deposits, which explain the low resistivity. Elsewhere, the thickness of loam is limited (about 1 m) and the electrical signature of loam is less marked. This thick loam deposits may correspond to an old channel or a crevasse splay filled with fine elements. Below the loam layer, alluvial deposits are characterized by two different electrical resistivity values corresponding to gravel and sand deposits. One is around $120 - 130$ $Ohm.m$ and the other one is characterized by electrical resistivities above 200 $Ohm.m$. The first is mainly located at the bottom part of the aquifer. The depth of the transition varies along the profile and lateral heterogeneities appear, showing that the deposits are not constituted by large blocks of homogeneous facies.

Now, the ERT results have to be transformed into soft probability maps in order to be used

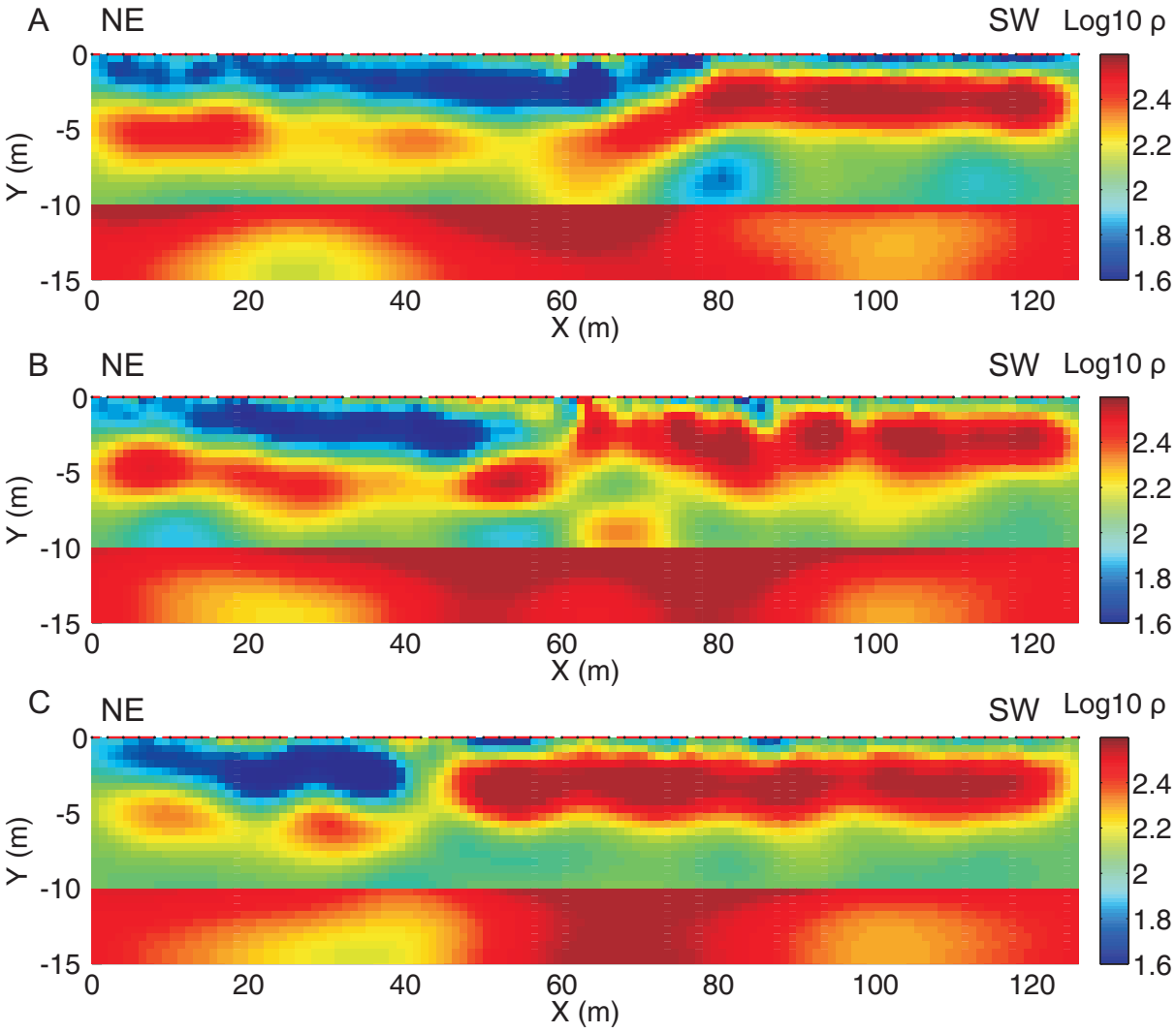

Figure 4.12: Inversion results of 3 profiles on the site of Hermalle-sous-Argenteau: (A) profile 3, (B) profile 7, (C) profile 10. The global structures are perpendicular to the profiles.

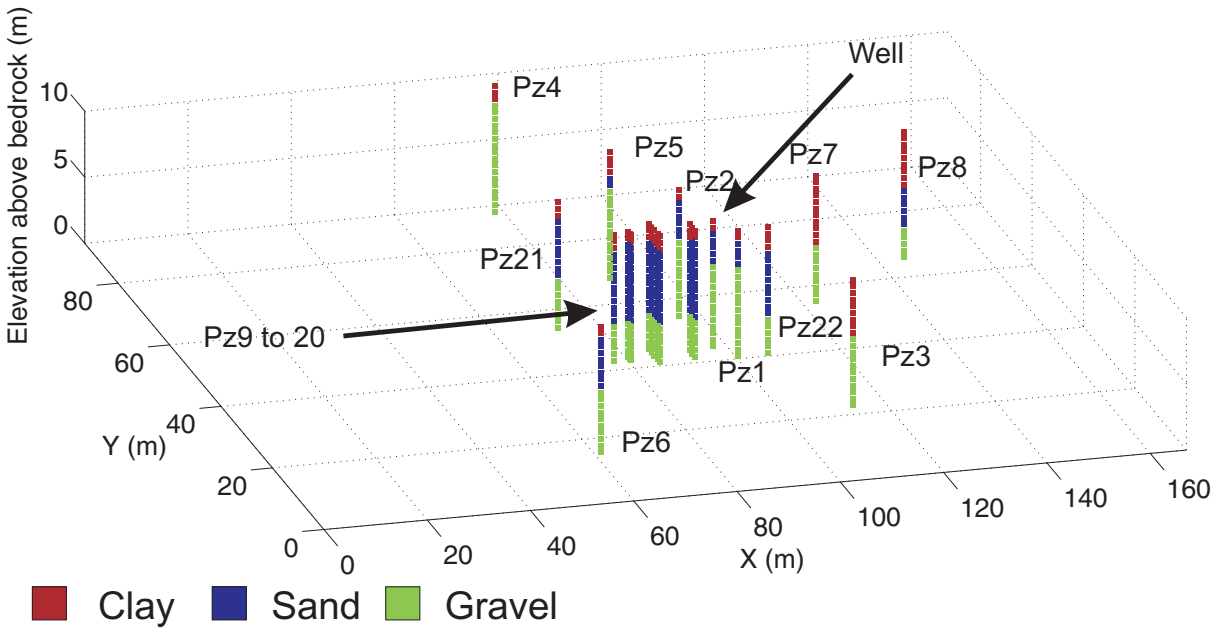

Figure 4.13: Interpretation in terms of facies of the borehole available on the site of Hermalle-sous-Argenteau.

within multiple-point statistics and PPM. For the synthetic benchmark, we used an approach based on the direct comparison between facies and inversion results for all elements of the inversion grid of ERT. For the field case, it is not possible to consider such a comprehensive data set since we do not know the facies everywhere. However, the site of Hermalle-sous-Argenteau has a quite dense set of boreholes where we have ERT profiles (see figure 4.10). It is thus possible to use the comparison of ERT and direct observation of facies at the position of the boreholes as an estimate of the resistivity distribution for each facies.

However, the determination of the facies is not straightforward. The description of the old piezometers is relatively different from the new. Based of our knowledge of the site, the limit between the sand facies (intermediate hydraulic conductivity) and the gravel facies (high hydraulic conductivity) was defined with the presence or not of large fluvial pebbles, generally associated with a less abundant matrix, making them close to "clean gravel". When loam was a major element of the deposits or of the matrix, the horizon was classified as clay facies (low hydraulic conductivity). Finally, the borehole logs were interpreted as illustrated in figure 4.13. This figure also represents the potential hard data that can be used to constrain the MPS realizations. Note that a local reference system is used (figure 4.10).

This classification is partially subjective and may be criticized. Some incoherences may ap-

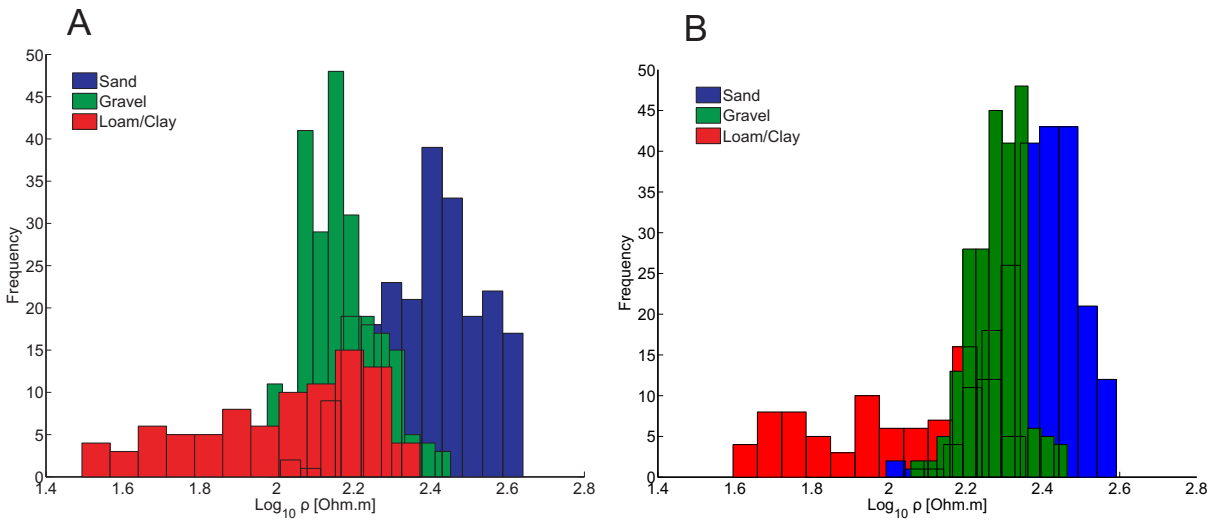

Figure 4.14: Resistivity distribution for each facies on the site of Hermalle-sous-Argenteau for (A) the geostatistical inversion and (B) the smoothness constraint inversion.

pear in the description of some of the old piezometers, particularly regarding the non-homogeneous vertical resistivity distribution observed with electromagnetic logs for homogeneously described facies (according to the description). For want of anything better, we decided to keep the old description and to consider that error in the description would only make ERT slightly less informative than it could have been with a more precise description.

From figure 4.13, it is possible to deduce the target proportion of each facies. On the site of Hermalle-sous-Argenteau, the most abundant facies is the gravel facies with 42%. The sand facies has a similar proportion (40%). The clay/loam facies is less abundant with only 18%. The latter proportion is coherent with the mean proportion observed in the alluvial deposits in the area of Liege (see chapter 3). On the contrary, the sand facies is less abundant than expected, in favor of the gravel facies. Those proportions will be used for multiple-point simulations and also for the creation of appropriate training images, i.e. the selected training images will be adapted to account for the correct proportions.

The relationship between facies and electrical resistivity is straightforward to build using the simple comparison at the position of the boreholes. Electrical resistivity logs were extracted from ERT inversion results (e.g. figure 4.12). Then for each facies, a histogram was build to illustrate the corresponding resistivity distribution (figure 4.14).

Differences appear between the geostatistical and smoothness constraint inversions (respectively figure 4.14A and B). With the smoothness constraint inversion, the facies are almost

completely superimposed, with values of logarithm of resistivity between 2.2 and 2.6. The geostatistical inversion enables to distinguish the mode of gravel and sand distributions. This is an additional argument to justify the use of this type of inversion and the use of prior information in the inversion of ERT data. This difference would obviously influence the calculation of probability maps (see section 3.5). The analysis of figure 4.14A also reveals three very important points.

1. In contrast with what is often observed, the gravel facies globally has a lower electrical resistivity (145 $Ohm.m$) than the sand facies (245 $Ohm.m$). This can be explained by the nature of the gravel facies in Hermalle-sous-Argenteau. It is composed of very large pebbles with a relatively small amount of matrix. In consequence, its porosity may be greater than the one of the sand facies resulting in a higher water content (see chapter 5 for more details on petrophysical relationships) and a smaller bulk electrical resistivity.

2. As expected, the clay facies is the only one characterized by resistivities lower than 90 $Ohm.m$. However, the clay facies is also characterized by values of resistivity in the same range as the gravel facies. This may be explained by an effect of the inversion. For boreholes located in the zone where surface loam deposits are thin (right handside of figure 4.12), the thickness of the facies is smaller than the electrode spacing. In consequence, such a thickness is difficult to image and the resulting resistivity is influenced by the underlying deposits (mainly sand). It is thus important to note that those distribution are dependent on the electrode spacing, and thus on the resolution of ERT. Using 1 m or 5 m spacing would lead to very different results.

3. The distributions resulting from the regularized geostatistical inversions are sharper and less superimposed than the one from the smoothness constraint inversion (figure 4.14). This is related to the incorporation of prior information in the inversion of ERT results which reduce the smoothing effect of the regularization compared to traditional smoothness constrained inversions. The distributions are thus also dependent on the method of inversion which is used. This highlights how prior information may increase the informative content of ERT data sets.

The mean and standard deviation of the three distributions are presented in table 4.8. Those

Facies	Prior probability	μ	σ
Clay	0.18	2.0081	0.2313
Sand	0.4	2.439	0.1364
Gravel	0.0952	2.1675	0.0952

Table 4.8: Mean and standard deviation of the distribution of resistivity of the three facies. The values for mean and standard deviation are given in logarithm of resistivity (base 10) expressed in $[Ohm.m]$.

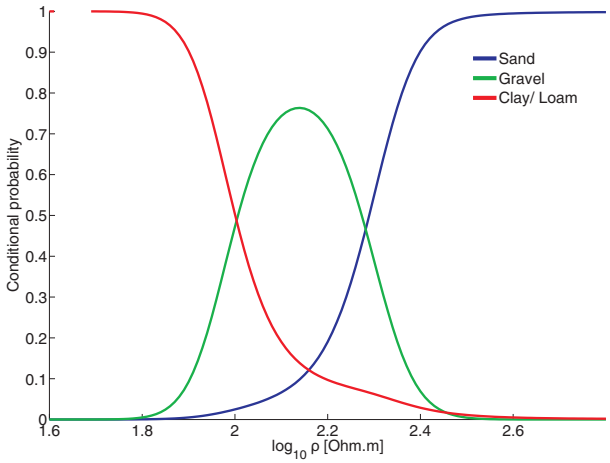

Figure 4.15: Modeled conditional probability distributions for the three facies on the site of Hermalle-sous-Argenteau based on the histogram of figure 4.14A.

distributions are estimates of the likelihood function $f(\rho|A)$, where A is one of the three facies. The conditional probabilities $P(A|\rho)$ (figure 4.15) were built using the distributions of figure 4.14.

For resistivity values $\log_{10}\rho < 1.8$, the probability to observe the clay facies is almost equal to 1. Similarly, resistivity values $\log_{10}\rho > 2.5$ correspond to a probability of sand close to 1. It signifies that ERT is quite efficient to discriminate extreme values. For very low and very high resistivities, the ERT distribution is almost deterministic, it may be used to decide if we have clay or sand. Through the τ model (equations 3.12 to 3.15), this will results in strongly constrained simulations. However, it concerns a limited number of cells.

For the range of resistivity values $1.8 \leq \log_{10}\rho \leq 2.5$ (most elements are characterized by such values), the probability of clay first decreases in favor of the probability of gravel. They have similar probabilities (just below 0.5) around $\log_{10}\rho = 2$ (100 $Ohm.m$). Then, the probability of sand starts to increase and sand becomes more probable than clay around $\log_{10}\rho = 2.15$ (140 $Ohm.m$), but at this value gravel has its higher probability (more than 70%). Further, probability of gravel decreases in favor of sand which is the most probable facies above $\log_{10}\rho = 2.3$ (200 $Ohm.m$).

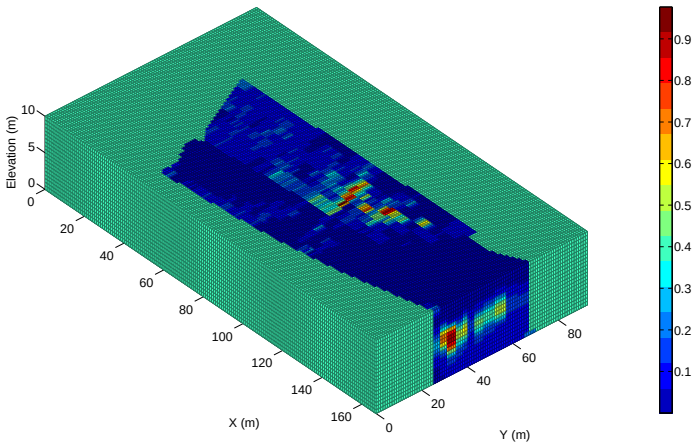

Figure 4.16: Soft probability map for the sand facies in Hermalle-sous-Argenteau.

The 12 parallel ERT profiles do not cover the entire site. Indeed, the hydrogeological model was chosen slightly more extended in order to ease the definition of boundary conditions (figure 4.10). The zone modelled for groundwater flow is a rectangle of 93 $m \times 167$ m which is more or less centered on the pumping wells and the new piezometers. The coordinates of the corners of the grid are defined on figure 4.10. The same grid is used for SNESIM simulations in SGEMS and groundwater flow in HydroGeoSphere.

The soft probabilities derived from ERT were simulated on the same grid using the nearest neighbor approach. However, to avoid an influence of those results on zones not covered by ERT, the areas outside ERT profiles were not assigned a soft probability value (actually, the soft probabilities are equal to the prior probability of the facies, which makes it non-informative). As an example, figure 4.16 shows the soft probability map of the sand facies. Zones where the probability is equal to 40% corresponds to the lack of ERT data. Jagged variations are related to the method of interpolation.

The informative character of ERT to describe the facies is illustrated on the soft probability maps of clay and gravel (figure 4.17). Zones of low resistivity values are recognized by their high clay probability. If ERT images (figure 4.12) could make think that the bottom part of the aquifer is only made of gravel, the soft probability maps show that lateral variations may occur, with higher probabilities either for sand or clay. Since gravel is the facies with intermediate resistivity values, its presence is never sure and the probability of other facies remains non-negligible. This distribution will ensure some variability in the MPS realizations.

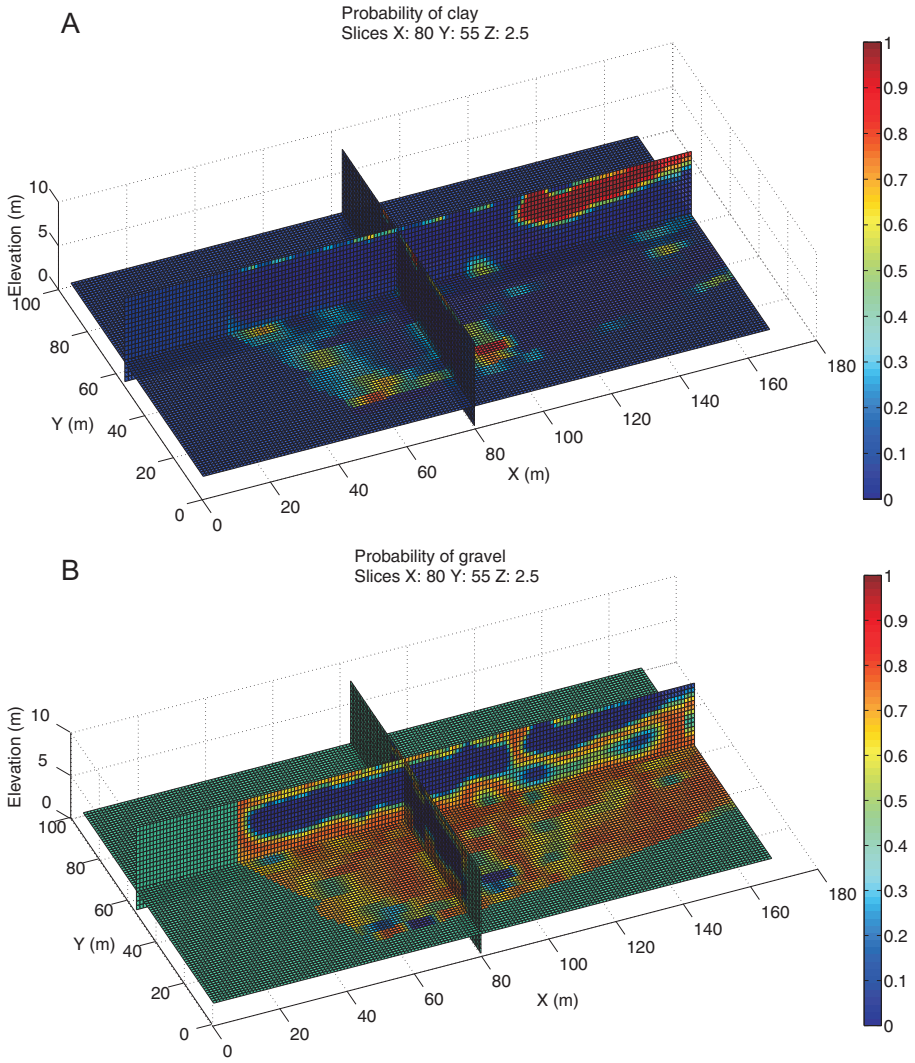

Figure 4.17: Soft probability maps for the clay facies (A) and the gravel facies (B) in Hermalle-sous-Argenteau. The structures observed in ERT are well retrieved in the probability maps, illustrating the quite sharp distributions of figures 4.14 and 4.15. The sand facies can be obtained by substraction.

4.4.2 Hydrogeological model

As explained in the beginning of this chapter, hydrogeological data are dynamical data and their incorporation in the geostatistical model through an inversion procedure (PPM) requires to solve groundwater flow equations. For this purpose, it is necessary to discuss two important points:

1. the conceptual model and the boundary conditions;
2. the choice of the hydraulic parameters used for simulation.

These two points will be discussed in the next sections. The zone which is modeled for groundwater flow corresponds to a rectangle of 93 $m \times 167$ m. The base of the model is the bedrock as it was modelled for ERT inversion. The top of the model correspond to the surface. The model is discretized with 1 m side cells in the horizontal directions and 0.5 m thick cell in the vertical direction. Since only the integration of hydraulic heads is considered, the model will be run in steady state conditions.

4.4.2.1 Conceptual model and boundary conditions

The conceptual model and the boundary conditions were barely discussed for the synthetic benchmark. They were kept very simple (constant and homogeneous boundary conditions) to avoid any influence on the analysis of the results. In the case of the site of Hermalle-sous-Argenteau, the aim is to include measured data and the conceptual model must remain as close to the reality as possible. As stated previously, the site of Hermalle-sous-Argenteau was chosen to test the methodology because it has already been used for several experiments.

Brouyère (2001) used the site to study solute transport in the subsurface. To perform solute tracer experiments, a constant pumping rate was kept at the well (52.6 m^3/h). This "pumping experiment" offers an interesting data set to test the incorporation of hydraulic heads into MPS framework. Table 4.9 sums up the data corresponding to this stress factor. Note that the hydraulic heads were "translated" to correspond to the level above the bedrock as imposed in ERT inversions.

The detailed work of Brouyère (2001) also includes the construction of regional and local flow models on the site of Hermalle-sous-Argenteau. The regional model has boundaries at the Meuse

Piezometer	Head in natural conditions (m)	Translated head (m)	Drawdown (cm)
Well	53.19	6.55	17
Pz1	53.2	6.56	15
Pz2	53.2	6.56	12
Pz3	53.19	6.55	11
Pz4	53.2	6.56	10
Pz5	53.21	6.57	11
Pz6	53.22	6.58	11
Pz7	53.19	6.55	11
Pz8	53.17	6.53	8

Table 4.9: Description of the data used to constrain the geostatistical realizations with PPM with a pumping rate of 52.6 m^3/s.

River (imposed hydraulic heads), at the boarder between alluvial plain and slopes (no flux) and 400 m north and south from the pumping well (imposed hydraulic heads). A groundwater recharge from precipitation of 9.5×10^{-9} m/s (300 $mm/year$) is considered. Infiltration from the Canal Albert is also modeled. The model is composed of two layers: clean gravel at the base of the aquifer and loamy sandy gravel in the upper part of the aquifer.

The local model is defined for better modeling of tracing experiments. The boundary conditions are imposed hydraulic heads extracted from the regional model. In this work, the local model is different, but the same approach is used to derive the boundary conditions. The procedure is divided in three steps.

1. The regional model is calibrated in natural and pumping conditions (52.6 m^3/h) using PEST (Doherty 2004)

2. The calculated hydraulic heads at the nodes of the regional model are interpolated using linear interpolation to derive a value at the nodes of the boundary of the local model.

3. Interpolated hydraulic heads are used as boundary conditions to simulate the pumping experiment on the local model of the site.

The extracted hydraulic heads globally show a decrease with increasing values of abscissa X. The main flow direction is thus parallel to the orientation of the model (figure 4.18). As highlighted in figure 4.10, the model was oriented along the main direction of flow. Those boundary conditions are themselves a strong constraint on computed flow and hydraulic heads. It is thus expected that adapted values for hydraulic conductivity should enable us to calibrate the flow model quite easily.

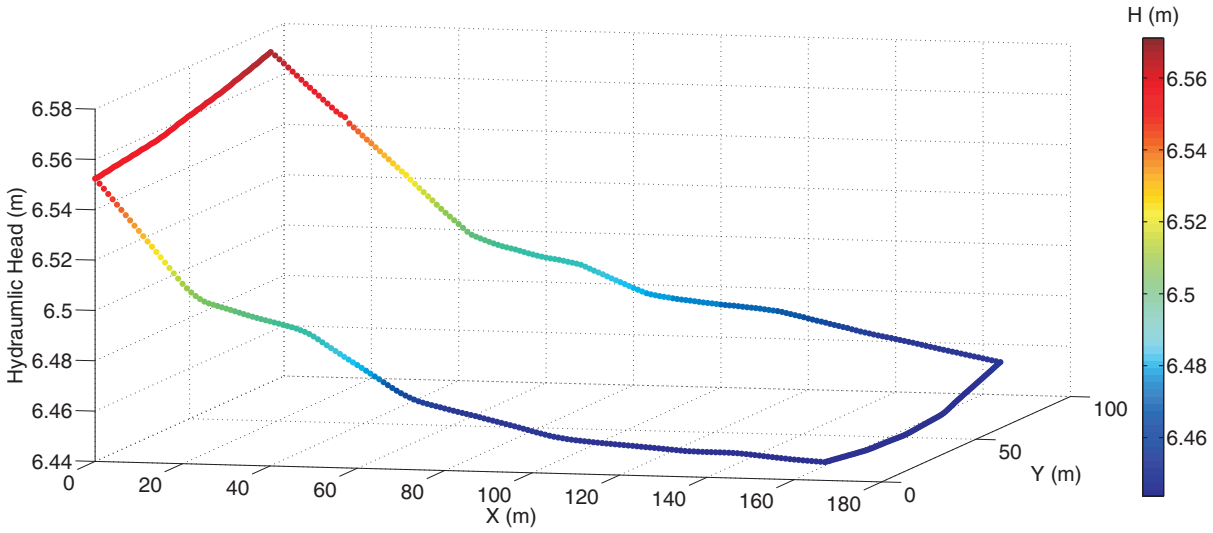

Figure 4.18: Hydraulic heads extracted from the regional flow model in pumping conditions for the site of Hermalle-sous-Argenteau.

4.4.2.2 Hydrogeological parameters

It is now clear that the PPM method aims at optimizing the geometry of the deposits by reproducing the facies architecture contained in the training image through a perturbation process. As stated previously, it requires to estimate a value for the hydrogeological parameters. In this case, working in steady state flow, the parameter to estimate is the hydraulic conductivity K. From our knowledge of alluvial deposits and the assumptions we made when choosing three facies to simulate, we should have $K_{clay} < K_{sand} < K_{gravel}$. To estimate the value of the parameters, we carried out a SNESIM simulation constrained by hard and soft data (figures 4.13 and 4.17). Then, we calculated the solution of the groundwater flow model using HydroGeoSphere for various values of the parameters (trials and error approach). The calibration of Brouyère (2001) already gives us order of magnitude for the gravel layer.

Some results of this estimation process are detailed in table 4.10. We compare the various cases using the weighted objective function (equation 4.9). The value of the clay facies is not very sensitive (cases 1 to 3), so its value was chosen intermediate at 10^{-6} m/s. Similarly to the synthetic benchmark, the most influencing parameters is the hydraulic conductivity of gravel, enhanced by its high proportion (42%). It was necessary to apply a value of 5×10^{-2} m/s to reach drawdonws of the correct order of magnitude. This value is coherent with results of Brouyère (2001). The influence of the hydraulic conductivity of the sand facies is less important than gravel. The tests show that considering a value of 10^{-4} m/s is coherent.

Case	K_{gravel} (m/s)	K_{sand} (m/s)	K_{clay} (m/s)	$\Phi_w(h)$
1	10^{-2}	10^{-4}	10^{-6}	0.1518
2	10^{-2}	10^{-4}	10^{-7}	0.1519
3	10^{-2}	10^{-4}	10^{-5}	0.1509
4	5×10^{-2}	10^{-4}	10^{-5}	0.0084
5	5×10^{-2}	10^{-4}	10^{-6}	0.0084
6	5×10^{-2}	5×10^{-4}	10^{-6}	0.0086
7	10^{-2}	5×10^{-4}	10^{-6}	0.1303

Table 4.10: Estimation of the hydraulic properties used for PPM application in Hermalle-sous-Argenteau.

4.4.3 Consistency and probability of training images

The analysis of specific data in Hermalle-sous-Argenteau (section 4.4.1) together with the initial analysis of section 3.4 enables to refine the choice of training images used as the base for subsequent simulations. Firstly, the proportion of facies is different for Hermalle-sous-Argenteau with 42% for gravel, 40% for sand and 18% for clay. This must be corrected for the actual training images. Secondly, the analysis shows that the size of clay lobes is not very sensitive. So, we decided to let the size of these lobes unconstrained, i.e. the new training images have lobes with size ranging from small to big with a uniform distribution. Thirdly, the scenarios with big channels were not very probable. Consequently, they were considered as unconsistent and discarded for the following simulations. Fourthly, the detailed analysis of geophysical results shows that the assumption on the resistivity distribution should be modified to be consistent with figure 4.14 and table 4.8.

This reduces the number of training images to 4: small channels, medium channels, small bars and big bars. All of them have similar clay lobes. The geometrical characteristics of the bodies are the same as the ones of the synthetic benchmark (section 4.3). The elements are oriented along the Y direction (supposed direction of the structure as observed on ERT profiles), but the orientation is allowed to vary slightly around this main direction. The training images built with Tetris are less structured than an image that would be given by a geologist. It allows to keep a large variety of possible geometries since the geological uncertainty about the deposits is still large. What we suppose is the presence of elongated zone of higher hydraulic conductivity and some zones of smaller hydraulic conductivity. Their relationships and connections, especially in 3D, are largely unknown. The 4 proposed training images (figure 4.19) are consistent with this interpretation.

Given the new training images and the collected geophysical data, it is necessary to verify

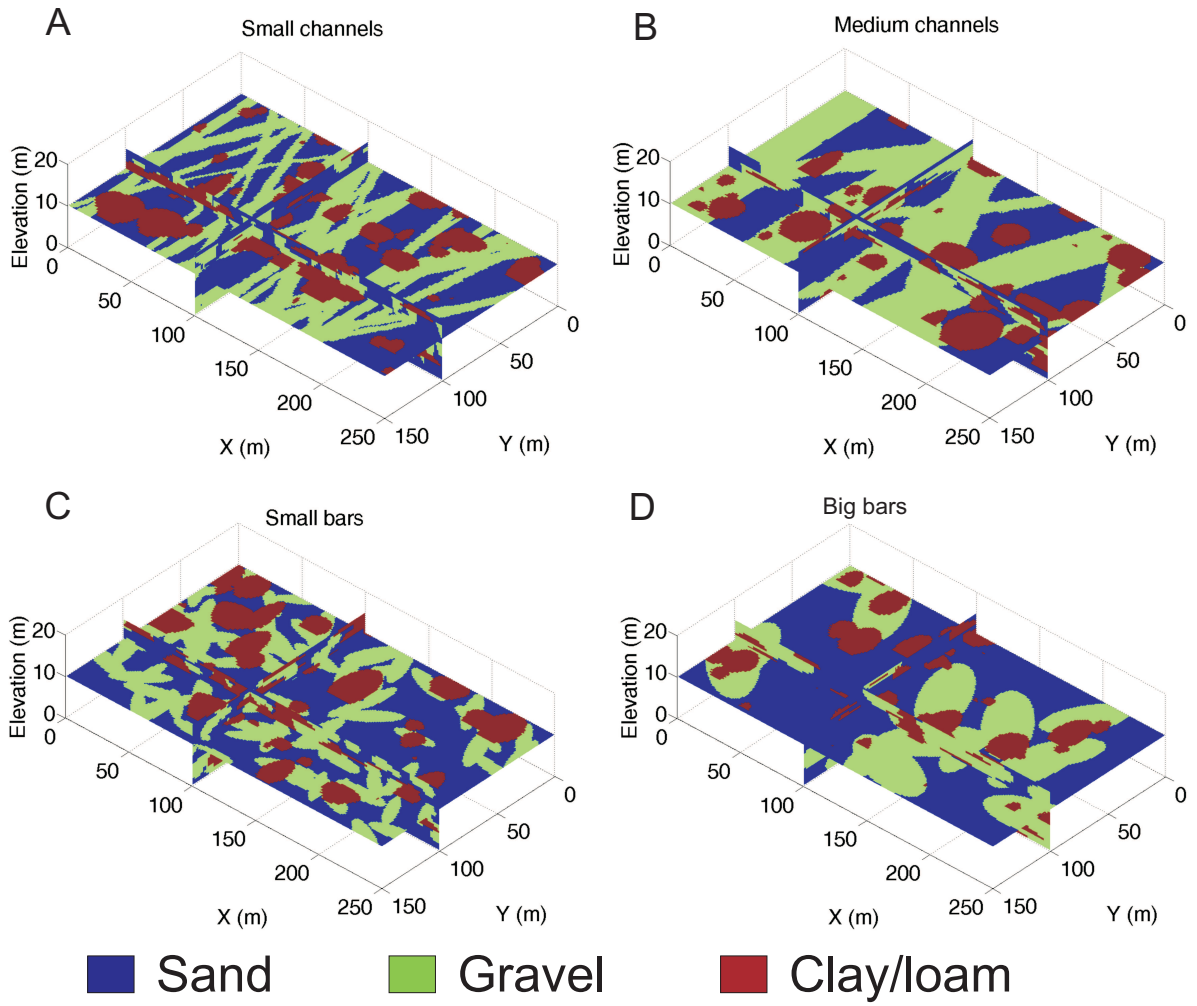

Figure 4.19: Scenarios for the training images in the case of Hermalle-sous-Argenteau.

their consistency. We applied the methodology of section 3.4 to our new set of training images. Rigorously, 3D simulations of the training images should have been performed. This would have taken into account 3D characteristics of the training image and 2D/3D artifacts in the inverted sections. To overcome the necessity to invert in 3D, we applied the methodology to 2D sections from the training images. This will enable us to verify the consistency with 11 2D sections instead of a single 3D model.

For the 4 scenarios, 24 2D sections were extracted, resulting in 96 synthetic TI-based scenarios. According to table 4.8, we transformed facies-based sections into electrical resistivity sections. The clay facies was applied a value of 100 $Ohm.m$, the gravel facies a resistivity of 140 $Ohm.m$ and the sand facies a resistivity of 240 $Ohm.m$. Electrical current flow forward modeling was applied to simulate resistance data which were inverted using the standard smoothness constraint algorithm, yielding 96 inverted electrical resistivity models. The distance between these models and each field model was calculated.

The MDS map of synthetic models is shown on figure 4.20 with the first 11 field profiles as illustration. Since the field models fall in the distribution of synthetic models, both in 2D and 3D, we can assume that the training images are consistent with available geophysical data. Based on the 2D MDS map, we calculated the probability of each training image based scenario for every field profile. To avoid the mutual influence of field data on the MDS map, the probability calculation was carried out separately for each profile (MDS map calculated with one field data at a time). The results are summed up in table 4.11.

The average probabilities, calculated as the mean of probabilities for individual profiles, show that there are few differences between the training images. However, the prior probability of each training image being 0.25, we see that training images with channels are slightly less probable than training images with bars. Looking at individual profiles, we see that differences may appear between some of the profiles even if the resistivity distribution of parallel profiles are not very different. This may be a result of the use of the Euclidean distance to calculate the distance between models. Indeed, the Euclidean distance is location dependent which may make it relatively sensitive to small variations. This should be further investigated using alternative distances. Using a large number of synthetic models to compute the MDS map aids to overcome this limitation. The MDS map should mainly be used to verify that field models lie within the

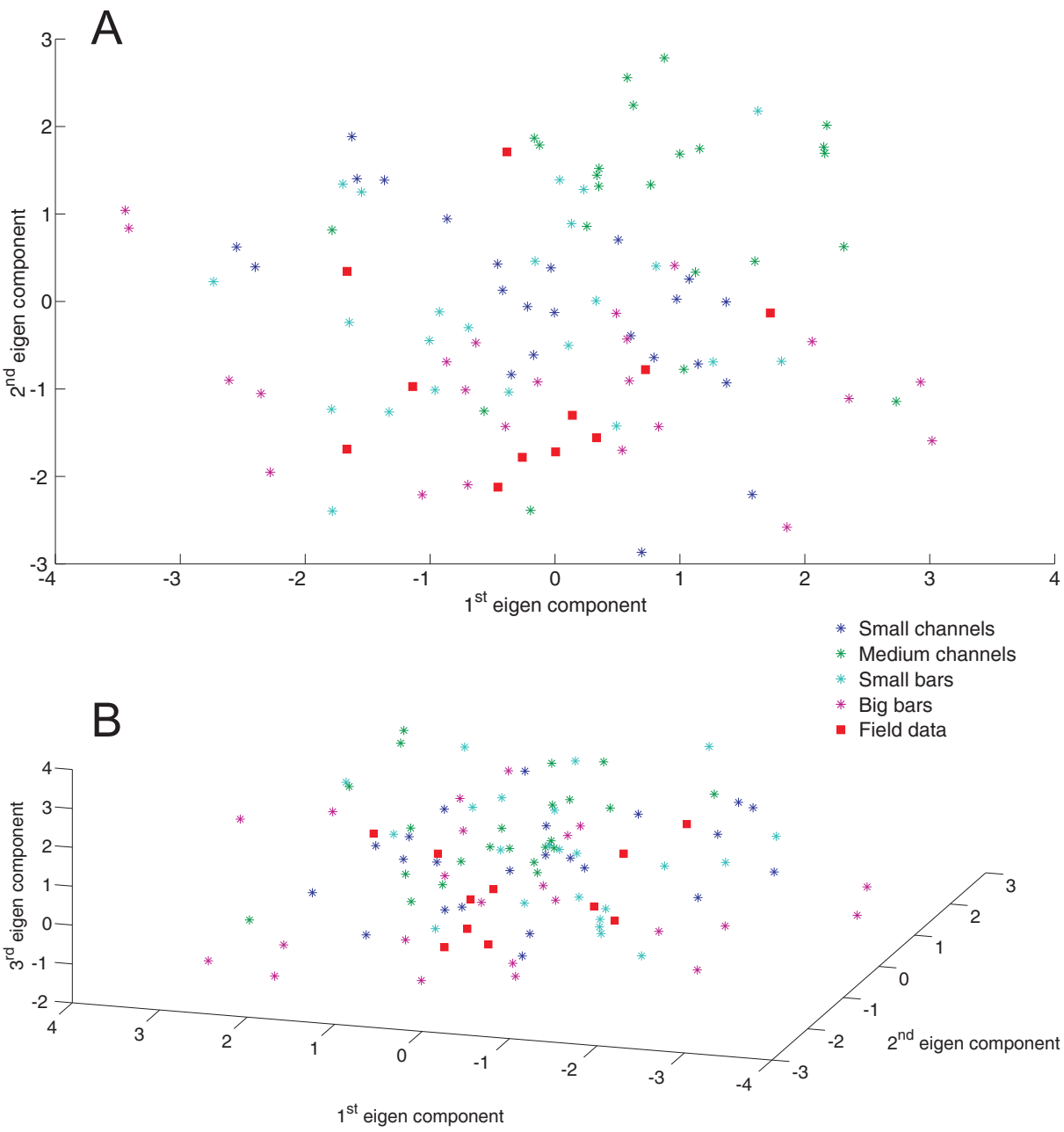

Figure 4.20: (A) 2D and (B) 3D MDS maps for the training images of Hermalle-sous-Argenteau. The field models fall in the distribution of synthetic models, so we assume that the training images are consistent with field data.

Field Profile	Small channels	Medium channels	Small bars	Big bars
1	0.17	0.59	0.24	0
2	0.38	0.2	0.33	0.09
3	0.11	0.07	0.45	0.38
4	0.12	0.16	0.2	0.52
5	0.08	0.19	0.14	0.59
6	0.02	0.05	0.39	0.54
7	0.13	0.15	0.21	0.51
8	0.19	0.11	0.26	0.44
9	0.22	0.10	0.3	0.38
10	0.39	0.07	0.29	0.25
11	0.40	0.24	0.17	0.19
Mean	0.2	0.18	0.27	0.35

Table 4.11: Probability of training image scenarios given the field models.

training image-based models, as a qualitative tool. Probability for individual are only crude indications. However, we assume that the average probabilities, here based on 11 profiles are more robust estimates of the probability of the training image.

4.4.4 PPM application

In this section, we first analyze the results of the first case scenario (small channel) when data is progressively added in the prior model. Secondly, we analyze the results for different training images.

As for the synthetic case, we limited the number of iterations to 10 and the optimization of r_B was limited to 5 attempts. We considered that a weighted objective function equal to 0.01 was representative of a calibrated model. It corresponds to a mean difference of 1 cm between observed and calculated hydraulic heads. The stopping criterion for PPM was chosen at 0.005 to ensure that the 10 iterations are run.

4.4.4.1 Integration of geophysical data

The aim of this thesis is to propose a framework to integrate data of various origin in a hydrogeological model. First, we used unconditional MPS simulations (without hard and soft data) to produce models for the probability perturbation method (figure 4.21). Then, the process was repeated with hard data (figure 4.22) and finally with hard and soft data (figure 4.23). Results are summed up in table 4.12.

The first case (table 4.12) corresponds to the integration of hydrogeological data (hydraulic heads during pumping) only. We assume that the heterogeneity is correctly depicted by the

Case	Training image	Hard Data	Soft data	Mean OF	Initial model = best model
1	SC	No	No	0.0089	0
2	SC	Yes	No	0.0079	0
3	SC	Yes	Yes	0.0094	31
4	MC	Yes	Yes	0.0127	26
5	SB	Yes	Yes	0.0096	38
6	BB	Yes	Yes	0.0132	27

Table 4.12: Summary of the results for the integration of data with PPM in Hermalle-sous-Argenteau. SC = small channels, MC = medium channels, SB = small bars, MB = medium bars

training image of figure 4.19 with small channels. We do not take into account the borehole logs and the ERT profiles. First, it must be noted that the PPM algorithm find calibrated models within the imposed number of iterations. In a few iterative steps, the algorithm is able to seek solutions with correct hydraulic heads. The final objective function is as good for this case as for cases with hard and soft data. This is partly due to the chosen boundary conditions which ensure that calculated hydraulic heads will not be very far from the true ones. However, all proposed models are not calibrated, initial models for PPM may have objective function above 0.025 which confirms that heterogeneity in the aquifer has an effect on observed hydraulic heads. The probability perturbation method is thus successfully applied to generate calibrated models.

The posterior probability of gravel (figure 4.21) calculated on 50 history matched models illustrates that hydraulic heads only are not very informative about the lithology. Indeed, it does not clearly reveal preferential flow paths in the aquifer. Most cells have a posterior probability around 42%, which corresponds to the prior probability. Near the location of the pumping well, there is a zone (X = 90 m, Y = 20 to 50 m) of higher probability of gravel (around 60%). This zone may be slightly more constrained by hydraulic heads because the drawdown in the well is the most affected by variation in hydraulic heads. Lower probability zones are also observable, but they seem almost randomly distributed and could disappear if more realizations were considered.

The results of PPM without additional constraining data confirms the non-uniqueness of the solution of the inverse problem. A wide ranges of models with the same prior geological assumptions are able to explain the observed data. Reducing the variability of the solution must be done through additional data. It could be hydrogeological data more informative on preferential flow paths existing in the aquifer as it will be seen in chapter 5, or alternative geological and geophysical data. The latter option is considered in this chapter.

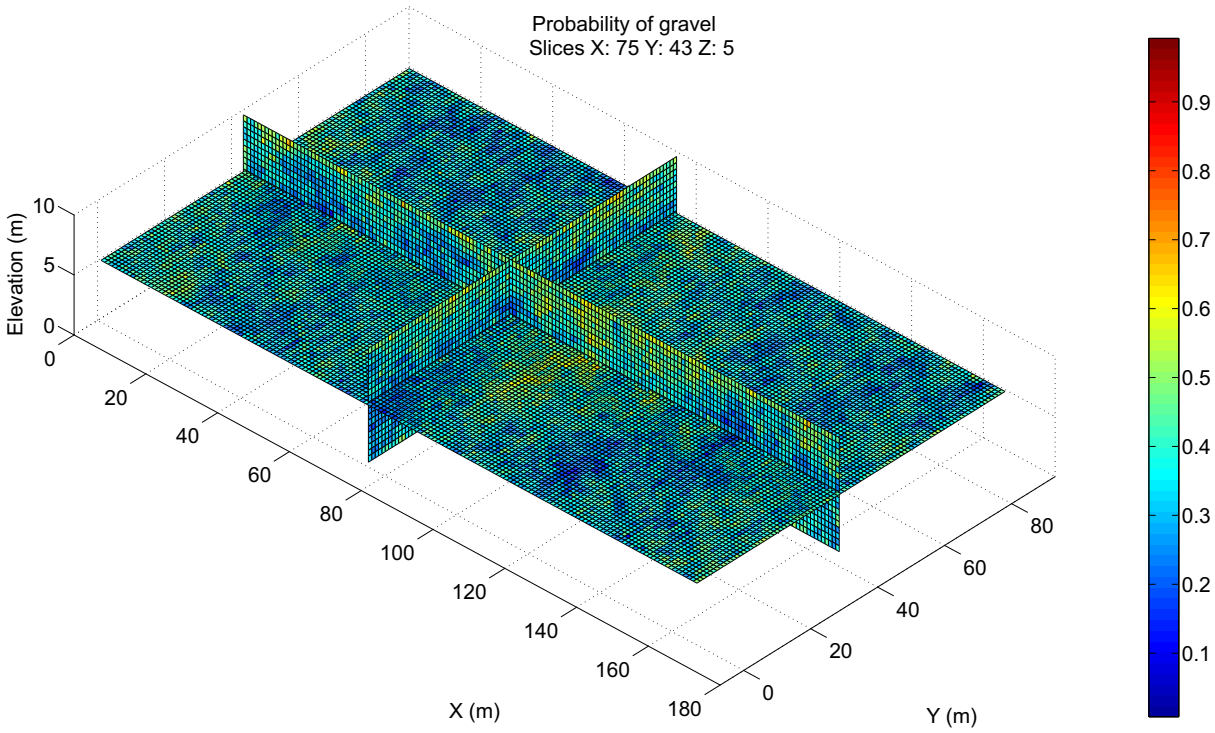

Figure 4.21: Posterior probability of gravel in the case of Hermalle-sous-Argenteau without any soft or hard data. The hydraulic head data is not very discriminant to derive the distribution of facies.

The integration of hard data in geostatistical models reduces drastically the uncertainty of the solution. It ensures posterior probability equal to 1 or 0 at the position of the wells. Given the relatively high density of direct observations in part of the model, it ensures a small uncertainty. The posterior probability map of the gravel facies (figure 4.22) clearly shows the location of wells and makes out some "channel-shaped" zones of higher probability of gravel. Outside the central zone of the model, where no borehole is present, the posterior probability is close to the case without any data.

The addition of hard data does not largely influence the final objective function, since history matched models were already obtained without any data. However, the PPM algorithm converges more quickly to a solution. Almost all starting models have a weighted objective function close to 0.01 and only a few improvements are needed for convergence.

The addition of geophysical data confirms this tendency. Indeed, in 31 cases, the initial model proposed by multiple-point statistics was already calibrated. It signifies that this additional data reduces the uncertainty related to the prior (the number of models respecting hard and soft data together with the training image becomes smaller) in such a way that it is not really necessary

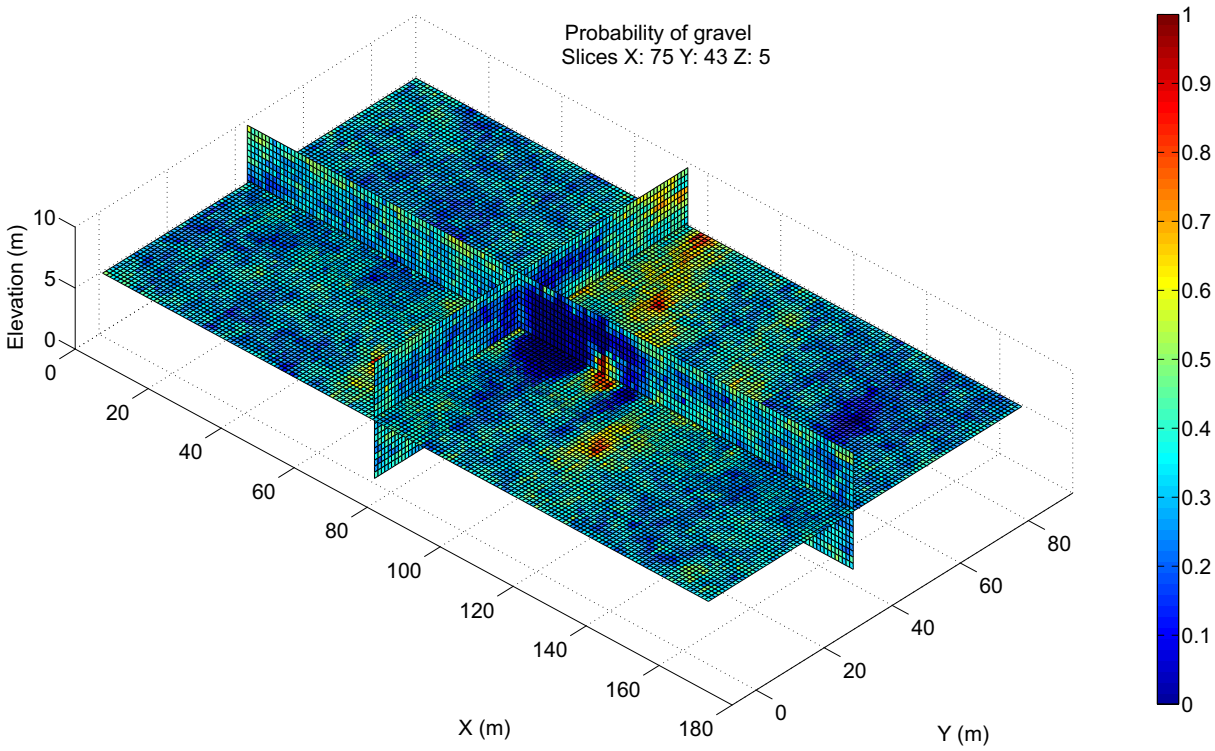

Figure 4.22: Posterior probability of gravel in the case of Hermalle-sous-Argenteau with hard data. The position of boreholes is visible where the probability are close to 1 or 0.

to perturb and optimize it to ensure calibration. The reduction of prior uncertainty is such that PPM could be avoided and replaced by a rejection sampler which could be as efficient in this specific case.

The effect of geophysical data on the posterior probability map is also noticeable (figure 4.23). At first sight, the result is almost similar to the case with hard data only, an effect of the high borehole density. However, ERT brings information around and between boreholes. For example, it confirms the low probability of gravel in the middle of the slice at $X = 75\ m$ or in the slice at $Y = 43\ m$ for $X > 100\ m$. Similarly, the "high probability zone" near Pz3 ($X \approx 100\ m$ and $Y \approx 30\ m$) is extended toward higher Y values.

It must be recalled that ERT profiles do not cover the whole hydrogeological model (figure 4.16). It explains why the southwestern part of the model is less constrained and the posterior probability similar to the one of the first case. The slightly higher mean objective function for this case compared to the case with hard data only (table 4.12) may indicate that there is some conflict between hard and soft data at some locations. There could be too much constraints on the geostatistical models. But the objective function still reaches an acceptable

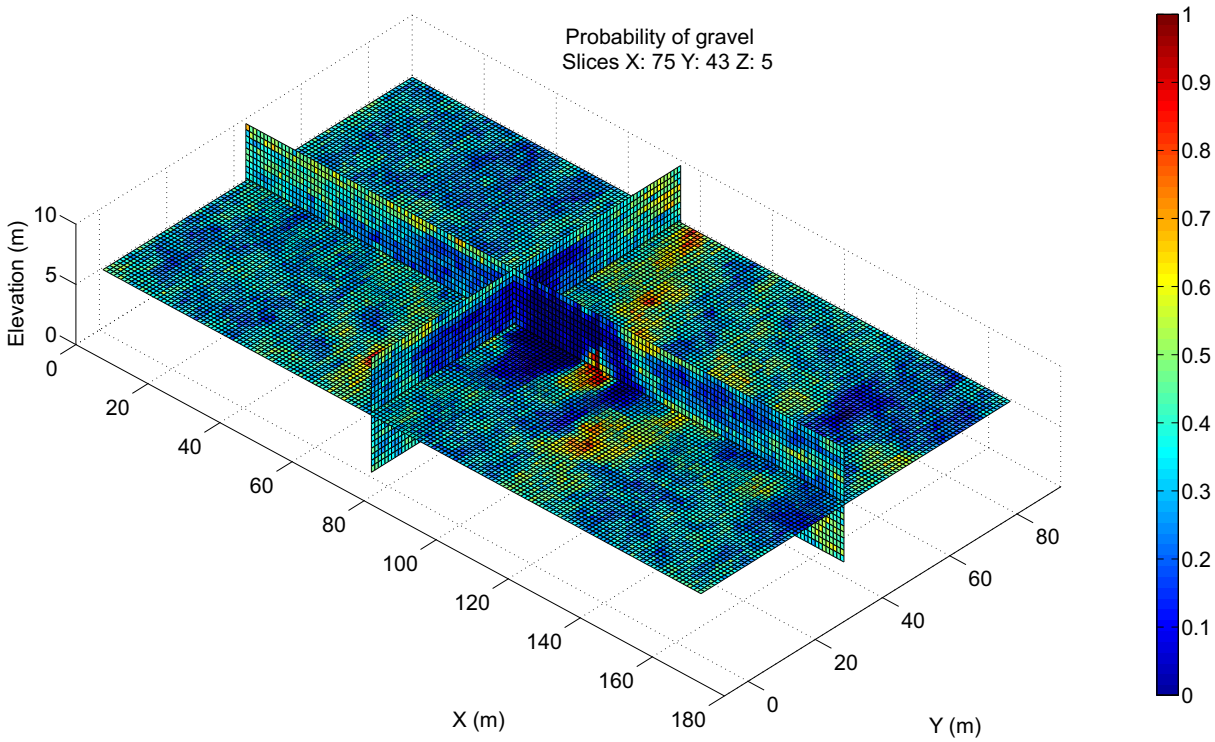

Figure 4.23: Posterior probability of gravel in the case of Hermalle-sous-Argenteau with hard and soft data. Geophysical data helps to refine the distribution by adding information around and between boreholes.

level. Of course, hard data has the priority during geostatistical simulations, but there is some uncertainty on the interpretation of borehole logs which may explain such contradiction. The situation is different from the synthetic benchmark for which the convergence was more difficult to reach.

Considering the posterior probability maps of the case with hard and soft data, a classification of the cells of the aquifer model is proposed. Each cell is assigned the lithology of the most probable facies (figure 4.24). The difference between the slice at 5 m and 2 m illustrates that the gravel facies is more abundant in the bottom part of the aquifer, a tendency visible both in borehole logs and in ERT. The large clay zone visible in the slice at $Y = 50$ m is typically an effect of the soft data, as proved by the soft data probability maps of figure 4.17. The cells classified as gravel around this clay body is a drawback of the use of ERT as soft data. Indeed, even with the geostatistical regularization, the inversion of ERT tends to smooth the transitions. In consequence, the transition between a clay and a sand body will inherently display resistivity values corresponding to high probability of gravel. This feature is not present in each individual realization, but the classification is some kind of mean based on 50 models.

This tentative classification moderates somewhat the traditional layering proposed for the alluvial deposits of the Meuse River. Generally, a three layer model is proposed, with a first layer of loam, then a sand layer and gravel at the bottom part of the aquifer. This is in accordance with the general trend observed in figure 4.24, but the results are more complex than this simple model. First, the thickness of the loam layer may vary significantly on a short distance. Secondly, the gravel facies is not limited to the bottom part of the aquifer and is likely found in significant proportions in the "sand" zone of the aquifer. The predominance of gravel in the bottom part of the aquifer is confirmed by borehole logs, geophysical data and also tracer tests (see chapter 5). However, these observations do not exclude the appearance of heterogeneity within this zone. Geophysical data reveals that clay lenses (e.g. $X = 80$ to $100\ m$ and $Y \approx 20\ m$ or $X = 50\ m$ and $Y = 40\ m$) may occur in the aquifer, even if not crossed by drilling.

The sometimes "erratic" behavior of classification could probably be reduced using more than 50 realizations to calculate the posterior probability maps.

4.4.4.2 Uncertainty of the training image

The methodology of integration of hard and soft data in multiple-point simulations was repeated for the three other training images considered for the site of Hermalle-sous-Argenteau (figure 4.19). We present the posterior probability of gravel and the proposed classification based on 50 models. The posterior probability of gravel is representative because the 4 training images differ only by the shape and size of the gravel facies.

For the medium channel case (table 4.12), the mean objective function is above the *a priori* fixed limit of 0.01. The prior model (training image, hard and soft data) for this case seems to be less efficient to propose models which explain sufficiently hydrogeological data. This could also be an effect of the optimization of hydraulic parameter which was done on a model with small channels.

The role of the training image is again clearly visible on posterior probability maps (figure 4.25). Medium channels yields an increased connectivity between gravel zones revealed by borehole logs. In consequence, the "high probability" zones visible in figure 4.23 are enhanced in figure 4.25 with values closer to 1. It thus appears that the apparent uncertainty in the posterior distribution is dependent on the choice of the training image, which is itself uncertain. This

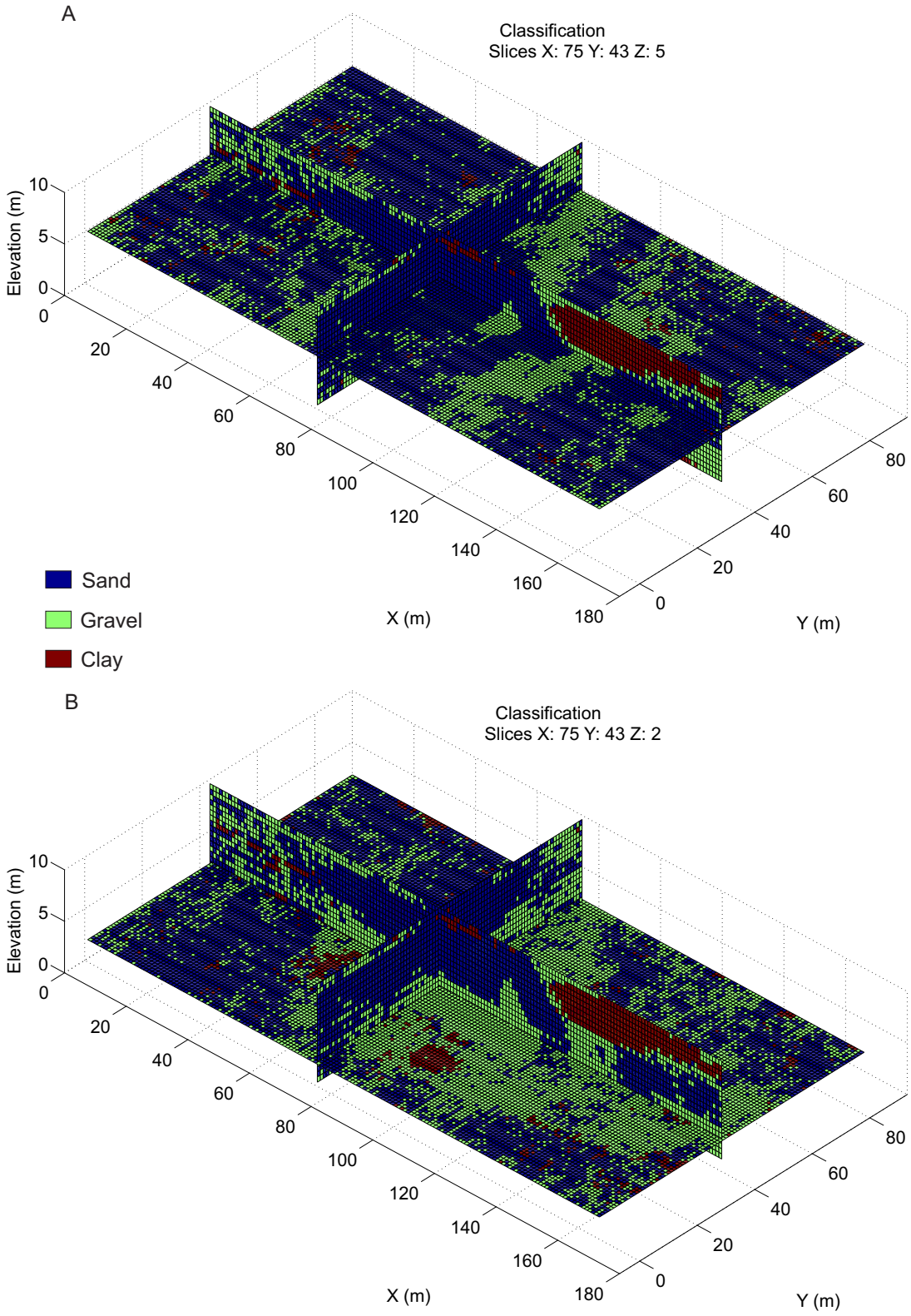

Figure 4.24: Classification of the elements according to the posterior probability at (A) 5 m and (B) 2 m above the bedrock. Characteristics of the soft probability maps clearly influences this distribution.

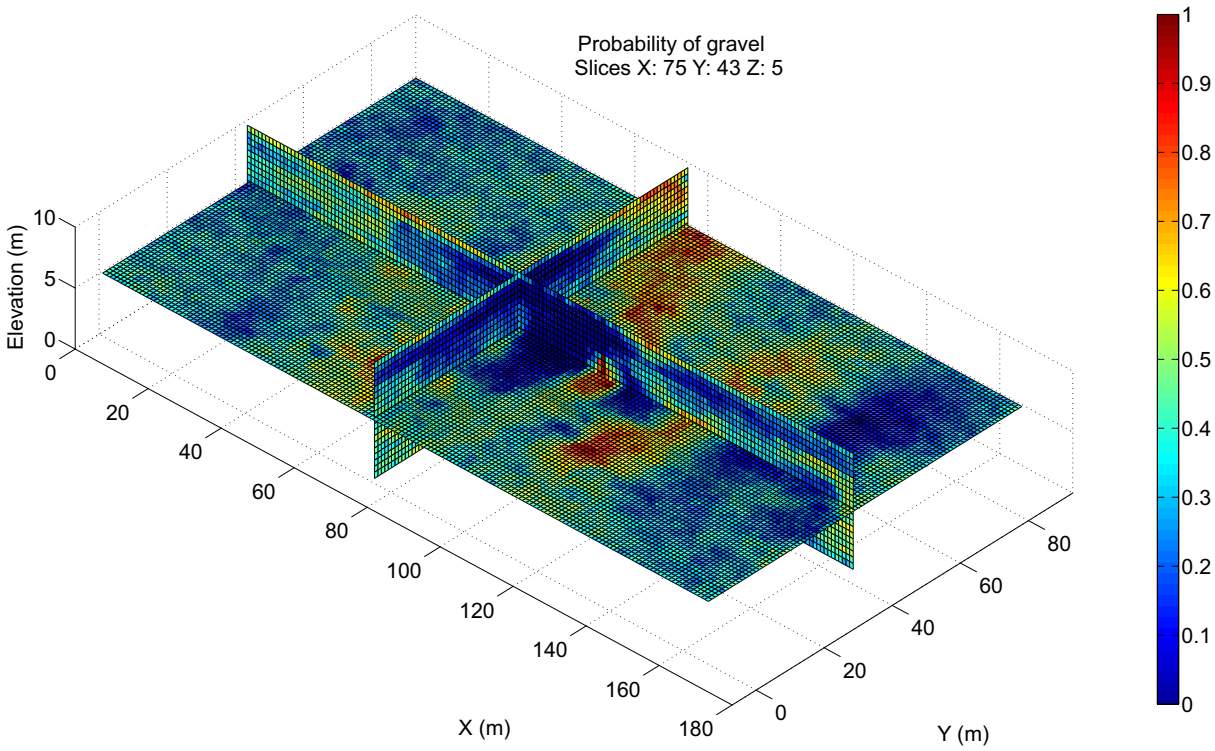

Figure 4.25: Posterior probability of gravel in the case of Hermalle-sous-Argenteau with hard and soft data and the medium channels training image. The influence of the training image is visible on the posterior probability of gravel, compared to figure 4.23.

confirms the importance to assess the uncertainty related to the training image.

The same effects are present in the classification results (figure 4.26). The gravel zones in the slice at $Z = 5\ m$ are wider than with small channels (figure 4.24). This is obviously coherent with the choice of a training image with wider channels. In the bottom part of the model (figure 4.26B), almost all heterogeneity disappears in the classification model. Due to the simulation of medium channels, almost all cells are classified as gravel, even if individual realizations present heterogeneity. The clay anomalies, detected with ERT and observable in the classification of figure 4.24 are reduced to a few cells of the model.

When the training image with small bars is used, the calibration and convergence of the PPM algorithm is similar to the case with small channels (table 4.12). It reaches the target objective function of 0.01 easily. Many starting models are even already calibrated as it was the case with small channels. The posterior probability of gravel (figure 4.27) seems to show a less strong influence of the soft probability maps. It still proposes zone of lower or higher probability of gravel, but they are less clear than with the training images with channels. This effect was

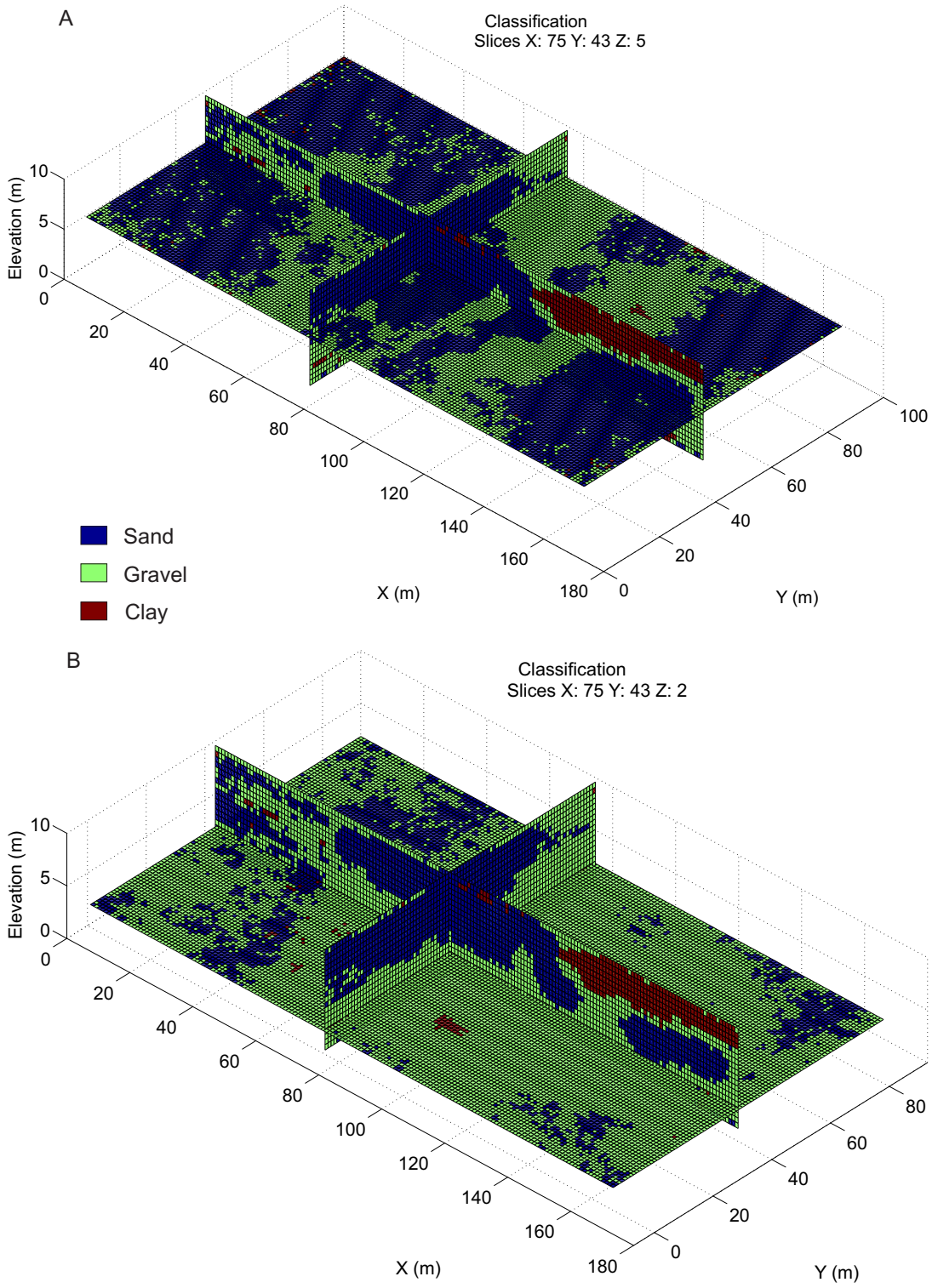

Figure 4.26: Classification of the elements according to the posterior probability at (A) 5 m and (B) 2 m above the bedrock for the training image with medium channels. The training image influences clearly the classification, gravel zones are more extended than in figure 4.24.

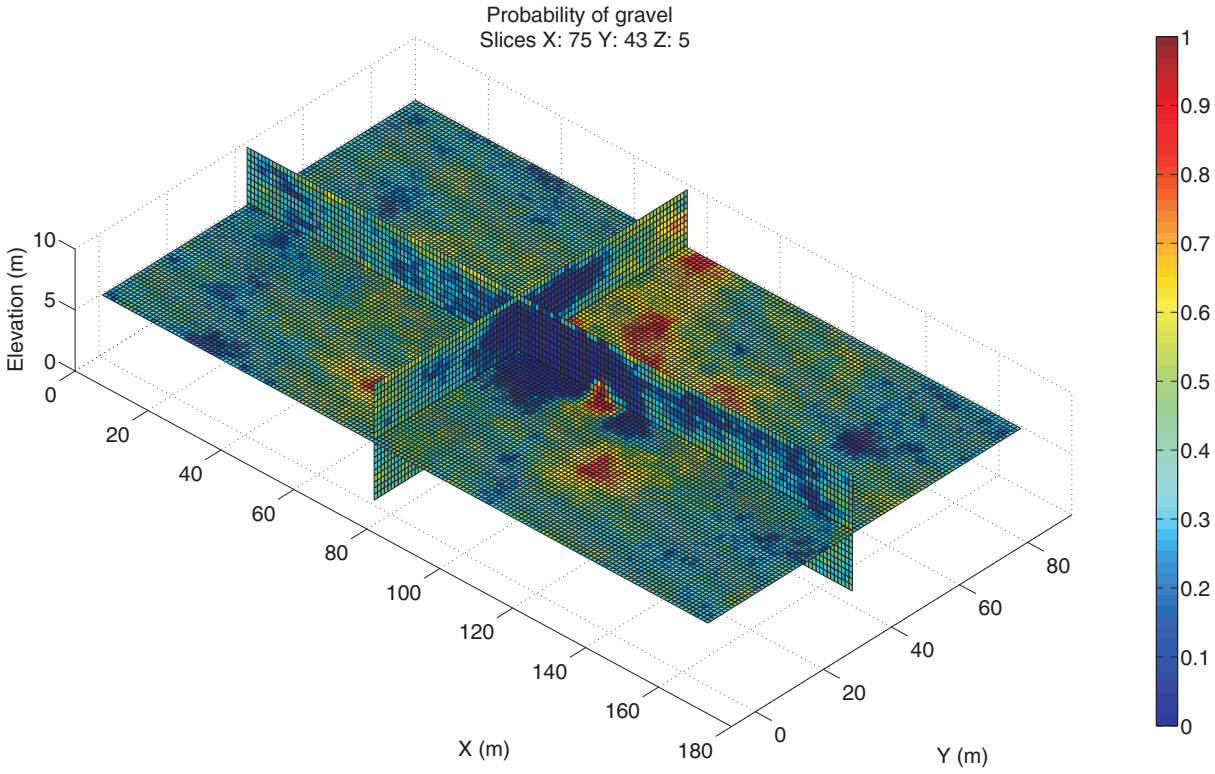

Figure 4.27: Posterior probability of gravel in the case of Hermalle-sous-Argenteau with hard and soft data and the small bars training image. The influence of the training image is visble on the posterior probability of gravel, compared to figure 4.23.

already highlighted in figures 3.30 and 3.31. Small structures allow for more heterogeneity inside individual realizations and result in less certainty in the location of the gravel facies.

This clearly appears in the classification model (figure 4.28) where the bottom of the model has less cells classified as gravel than it was the case with other training images. The clay zone present with the other training images ($X = 80$ to 100 m and $Y \approx 20$ m) disappears when small bars are used. In the upper part of the model, the clay zone is also less pronounced. It must thus be kept in mind that the posterior distribution observed is highly dependent on the choice of the training image used to generate geostatistical simulations.

Finally, the opposite effect is obtained when big bars are used in the training image. The posterior gravel probability map (figure 4.29) is quite discriminant (a lot of value either close to 0 or 1). Gravel appearances detected in boreholes or with a relative high probability with ERT tend to be connected through relatively large bars in individual realizations which is reflected in the posterior probability maps.

The classification (figure 4.30) renders a solution close to the one obtained with medium

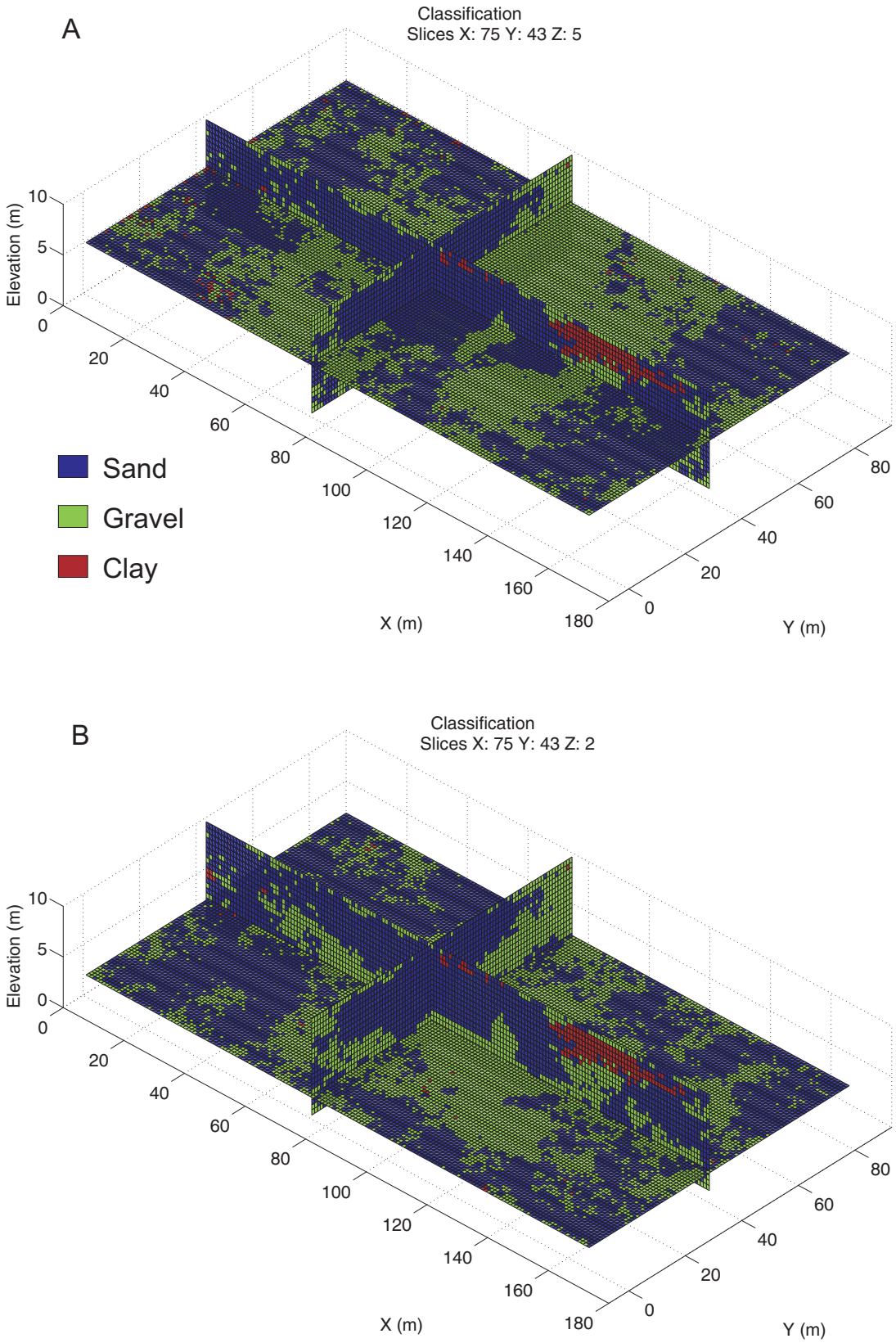

Figure 4.28: Classification of the elements according to the posterior probability at (A) 5 m and (B) 2 m above the bedrock for the training image with small bars. The training image influences clearly the classification.

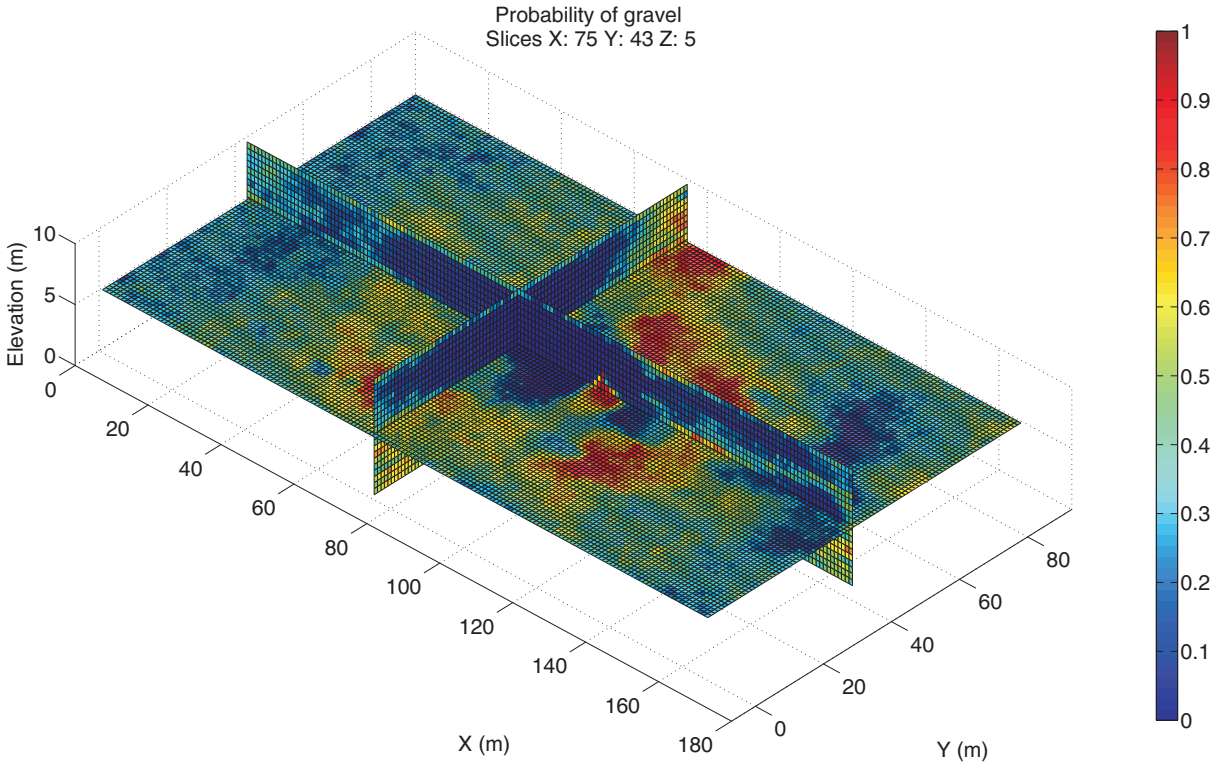

Figure 4.29: Posterior probability of gravel in the case of Hermalle-sous-Argenteau with hard and soft data and the big bars training image. The influence of the training image is visble on the posterior probability of gravel, compared to figure 4.23.

channels (figure 4.26). At the bottom of the models, almost all cells are classified as gravel and in the middle of the model, gravel occurrences in boreholes tend to be connected. The classification models with medium channels or bars have a less "erratic behavior" than the ones with small elements.

Even though the big bar training image was rated as the most probable according to geophysical data, its performance in the PPM algorithm is not perfect. As it was the case for the medium channel training image, the mean objective function for the 50 realizations (0.013) at the end of the 10 iterations is above the target (0.01) for calibration. Nevertheless, a minority of the models lies below this limit which shows that those training images are not incompatible with the observed drawdowns resulting from pumping. As stated previously, larger elements allow less variability in individual realizations since the training image imposes to reproduce large structures, additionally conditioned to hard and soft data. These large structures may have a stronger impact on calculated drawdowns than a combination of smaller structures, which have more "flexibility". This could also be related to the relative size of these structures compared to the size of the model and the choice of hydrogeological parameters.

However, the difference in the objective function compared to other cases remains relatively small. The synthetic benchmark taught us that alternative training images could perform as good as or even better than the actual one. Therefore, this observation *a posteriori* is not sufficient to reject training images with medium channels and big bars.

In this work, we have proposed a methodology to verify the consistency between training images and geophysical data, because geophysical tomographic methods contain indirect information on the spatial distributions of the deposits. However, the final aim being to produce reliable hydrogeological models, a methodology to analyze the consistency and the probability of training image-based scenarios with available hydrogeological data is also necessary. To achieve this, a similar methodology could be developed where the response of synthetic models based on various scenarios is compared to the true one (e.g. Park et al. 2013). The distance could be the Euclidean distance between individual response or any relevant distances. The probability resulting from such an analysis would likely be different from the one based on geophysical data and would be an interesting complement towards the identification of the most consistent training image(s).

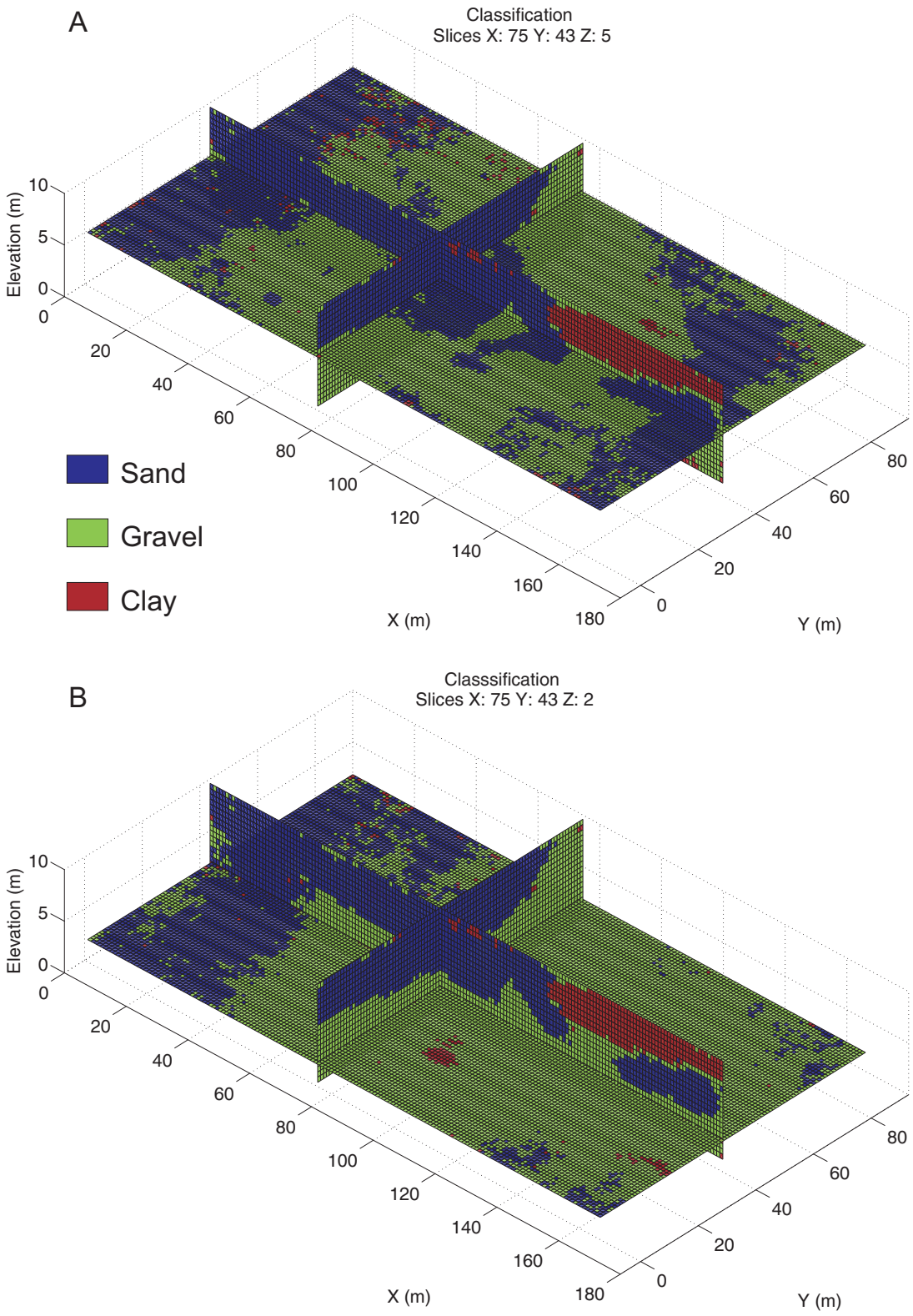

Figure 4.30: Classification of the elements according to the posterior probability at (A) 5 m and (B) 2 m above the bedrock for the training image with big bars. The training image influences clearly the classification.

Another possibility to analyze the reliability of the results for field case would be cross-validation. Part of the boreholes would be discarded in the hard data constrain. Then, they would be used to estimate the classification efficiency of the method. As seen with the synthetic benchmark, it could be useful to discriminate the best training image.

4.4.4.3 Final model

Considering the uncertainty involved at each step of the process, it is not possible nor coherent to favor one of the cases presented in the previous section. We thus propose to combine the posterior probability maps of the different cases according to the conditional probability of table 4.11. We used a linear combination of the posterior probability of each case to generate the final posterior probability maps (figure 4.31) and classification (figure 4.32).

These final results include geological data within the form of hard data deduced from borehole log descriptions and within the form of training images deduced from our expectation of the heterogeneity. The training images were weighted according to their consistency and conditional probability with geophysical data (electrical resistivity tomography) assessed with the multidimensional scaling approach. Electrical resistivity tomographies were further used to condition geostatistical simulations as soft data in the SNESIM multiple-point algorithm. Prior information was included in the form of bedrock position and vertical correlation length deduced from electromagnetic log measurements. Finally, the integration of hydrogeological data was ensured by the selection of model matching observed data through the PPM algorithm.

4.4.5 Summary of the field case

In this section, we have successfully applied the probability perturbation method to integrate pumping test hydraulic heads into multiple-point statistics simulations constrained by borehole logs and ERT models. The example has shown that the PPM algorithm was efficient to converge to calibrated solutions, but that a lot of aquifer models were able to explain the observed data.

The combined use of borehole logs and geophysical data, acting through prior model constraints, permits to reduce the number of possible models. Posterior probability maps show that parts of the model are rather well-constrained, with a relative low uncertainty.

However, the use of hydraulic heads only is not sufficient to constrain the geometrical features

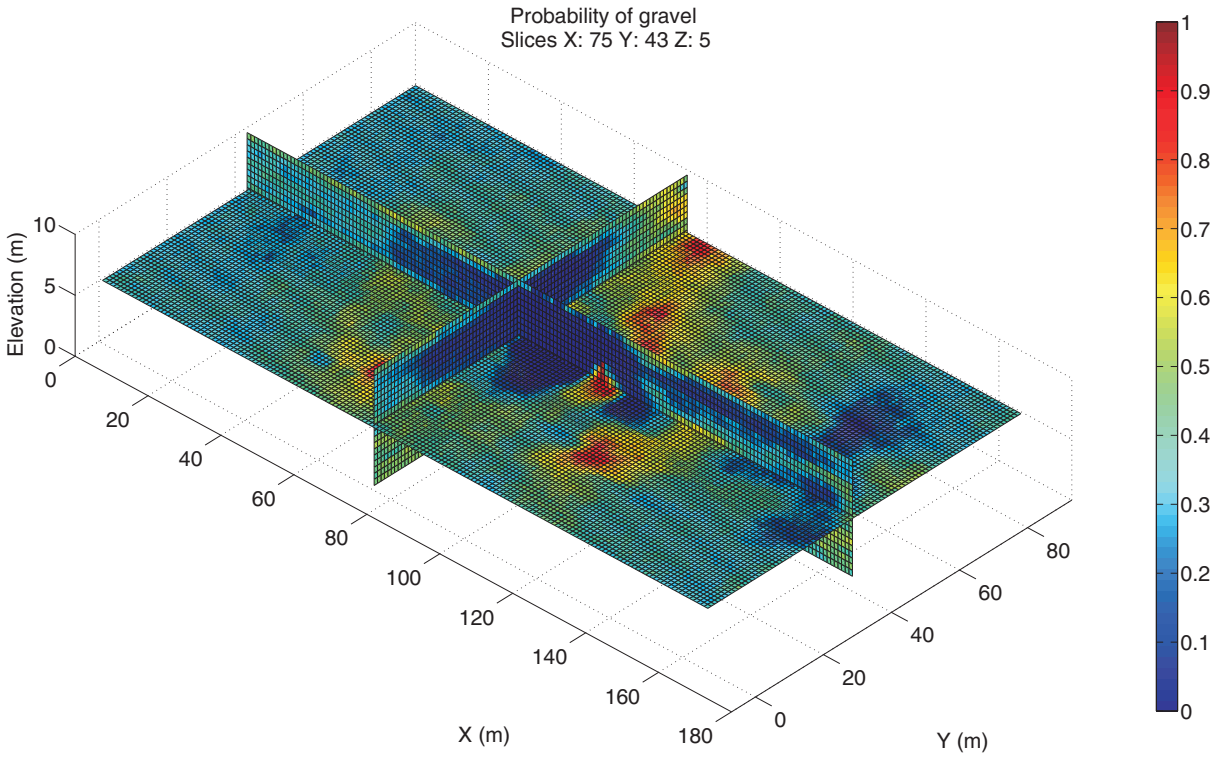

Figure 4.31: Posterior probability of gravel in the case of Hermalle-sous-Argenteau with hard and soft data calculated by combination of the four cases with different training images.

of the model. Such data does not contain enough information to locate precisely preferential flow paths (gravel channels or bars). The use of transient data, tracer tests for example, could be more appropriate to characterize local features of the aquifer (see next chapter). The set-up of such experiments could be based on a previous selection of models as it was done in this section. The classification maps could be used to select zones where preferential flow paths are expected or have a strong influence. The location of piezometers for tracer experiments would then be chosen to confirm or precise it. The probability perturbation method tackles the hydrogeological inversion problem as a data integration problem. It is thus perfectly suited to integrate tracer tests in a "history matching" procedure.

The uncertainty related to the training image remains high *a posteriori*. With the tools used in this study, it is impossible to unequivocally determine what is the best training image. In the synthetic benchmark, only an indicator based on the classification efficiency was able to retrieve the actual training image-based scenario. This indicator is impossible to use in field case studies since the true distribution is unknown. It could be assessed using a cross-validation procedure when the amount of hard data is sufficient. This highlights the need to develop new

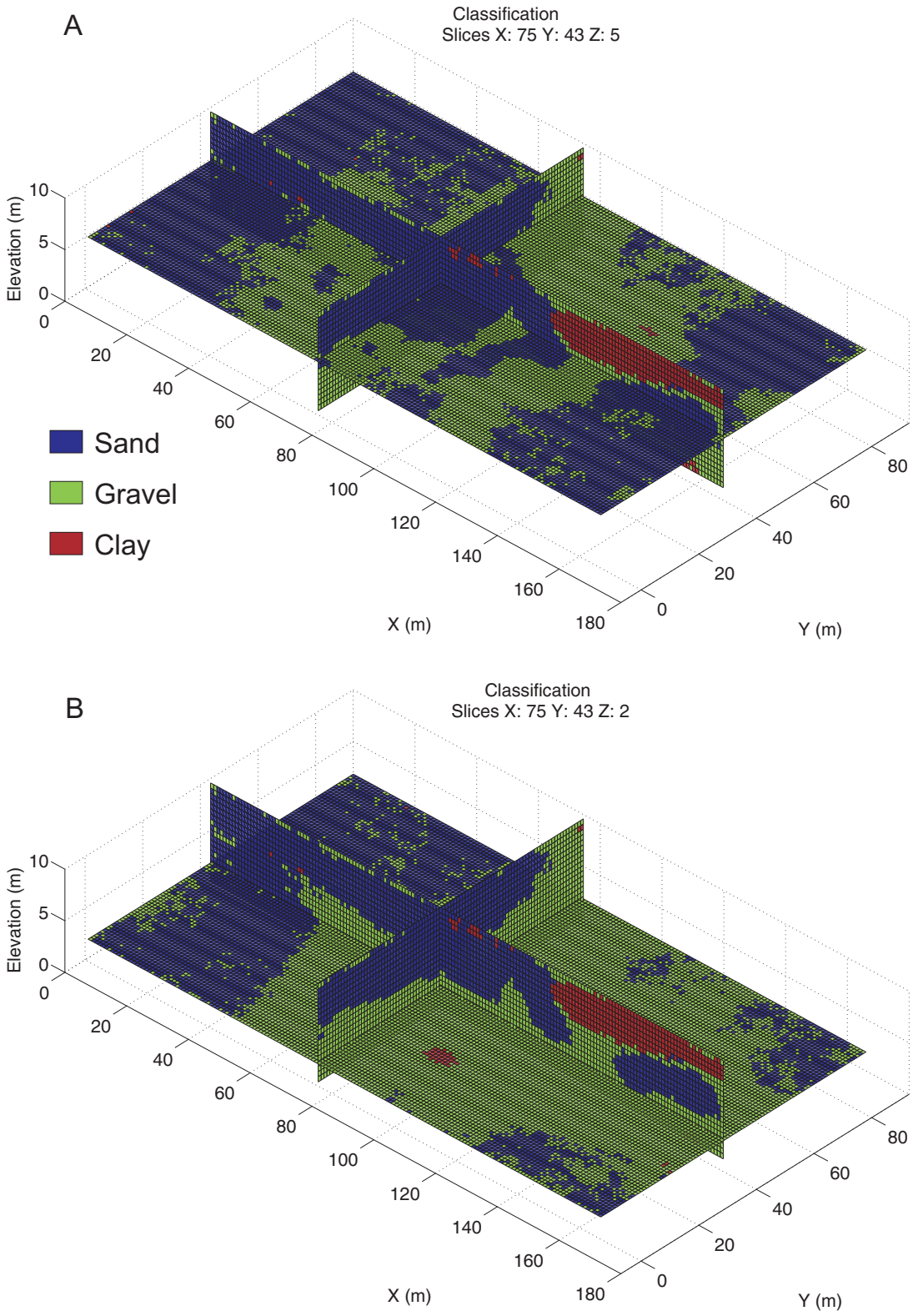

Figure 4.32: Classification of the elements according to the posterior probability at (A) 5 m and (B) 2 m above the bedrock for the combination of training images.

methodologies to estimate *a priori* the uncertainty related to training images in multiple-point statistics frameworks.

In the future, the methodology could be generalized to other contexts, such as fractured aquifers, where geophysical data can also bring relevant information to constrain aquifer models (Robert et al. 2011).

The example illustrated in this section is at the local scale, but the methodology could be used at other scales as long as the training images depicts the expected heterogeneity relative to this scale and that the resolution of the geophysical method is relevant.

Chapter 5

Acquisition of temporally and spatially distributed geophysical data: thermal tracing experiments

Note. The research material of this chapter is partially published in proceeding of international conferences and papers in international peer-reviewed journals.

Hermans T., Vandenbohede A., Lebbe L. and Nguyen F. 2012. A shallow geothermal experiment in a sandy aquifer monitored using electric resistivity tomography. Geophysics, 77(1), B11-B21, doi: 10.1190/GEO2011-0199.1.

Vandenbohede A., **Hermans T.**, Nguyen F. and Lebbe L. 2011. Shallow heat injection and storage experiment: Heat transport simulation and sensitivity analysis. Journal of Hydrology, 409, 262-272, doi: 10.1016/j.hydrol.2011.08.024.

Hermans T., Daoudi M., Vandenbohede A., Robert T., Caterina D. and Nguyen F. 2012. Comparison of temperature estimates from heat transport model and electric resistivity tomography during a shallow heat injection and storage experiment. Berichte der Geologischen Bundesanstalt, 93, 43-48.

Hermans T., Wildemeersch S., Jamin P., Orban P., Brouyère S., Dassargues A. and Nguyen

F. 2013. A heat injection and pumping experiment in a gravel aquifer monitored with crosshole electrical resistivity tomography. EarthDoc, Extended abstract Near Surface Geosciences 2013, TuS2a09, September 9-11, Bochum, Germany.

Hermans T., Wildemeersch S., Jamin P., Orban P., Brouyère S., Dassargues A. and Nguyen F. 2013.Quantitative temperature monitoring of a heat tracing experiment using cross-borehole ERT. Geothermics, submitted.

Robert T., **Hermans T.**, Dumont G., Nguyen F., Rwabuhungu D., 2013, Reliability of ERT-derived temperature : insigths from laboratory measurements. EarthDoc, Extended abstract Near Surface Geosciences 2013, TuS2a10, September 9-11, Bochum, Germany, EarthDoc.

Chapters 2 to 4 describe a methodology to integrate various data into multiple-point geostatistics. Geophysical data, considering ERT here, supposed a link between the geophysical parameter of interest (electrical resistivity) and the parameter used in the geostatistical model (here the facies). This relationship is built on the basis of static measurements. Similarly, the integration of hydrogeological data was made on the basis of steady-state flow conditions.

In practice, much information may be contained in transient and dynamical processes. Globally, absolute electrical resistivity values are poor indicator of the lithology. In chapter 4, we have seen that an overlapping exists between clay and gravel for example, which have a completely different hydrogeological behavior. This is due to the many factors influencing electrical resistivity: lithology, saturation, total dissolved solid content, porosity, tortuosity, clay content, temperature, etc. Static results, also known as characterization ERT, are thus often limited to a qualitative interpretation. When ERT is used as a monitoring tool, it is possible to interpret inversion results in terms of resistivity variations. This permits to study the investigated process more quantitatively if only the parameter of interest varies. As an example, during a saline tracer test, one will interpret the change of resistivity in terms of total dissolved solid content and will assume that temperature effects can be neglected. Time variations of lithology do not occur.

In the following sections, we investigate the potential of ERT to monitor temperature variations during heat injection experiments. After an introduction and review of the literature, the

methodology used to estimate temperature with ERT will be described (section 5.2). The reliability of the method is then successively demonstrated on two field cases: the first (section 5.3) uses a surface array and illustrates the limitation of the method for long term experiment, the second (section 5.4) uses a cross-borehole experimental set-up to achieve a better resolution. This chapter ends with conclusion and perspectives of further developments.

Data related to monitoring and tracing experiments, if reliable, should eventually be integrated to aquifer models through history matching in transient flow conditions. This will be the next step to develop in order to complete the proposed methodology.

5.1 Introduction

Groundwater contributes to a major part in the production of geothermal energy, which is increasingly growing worldwide. For instance, in 2010, geothermal heat pumps accounted for 47.2% of thermal energy use and 68.3% of total installed capacity in the world (Lund 2010). Geothermal energy resources therefore constitute an essential field of research and development in the diversification of energy resources to hinder global warming.

Very low temperature systems ($< 30°C$) are much more easily accessible and involve lower implementation costs than deeper high temperature systems. Moreover, very low temperature systems, such as shallow aquifers, are relatively abundant in alluvial or coastal plains where urban development concentrates. From 0 to less than 100 meters depth, groundwater has an average temperature ranging from 5 to $30°C$ and may be used for domestic or industrial cooling or heating (Allen and Milenic 2003, Haehnlein et al. 2010).

The two main techniques to exploit shallow geothermal energy systems are ground source heat pumps (GSHP), which are closed systems with a vertical or horizontal heat exchanger, and groundwater heat pumps (GWHP), which are open systems circulating groundwater between production and injection wells or towards surface water (e.g. Lund et al. 2005). Designing such systems requires a multidisciplinary approach including geological and hydrogeological aspects. The most common approach is to model the system using a coupled heat flow and transport simulator. However, such models require estimating parameters governing heat transport such as heat capacity, thermal conductivity and thermal diffusivity. Due to a lack of data, authors often have to rely on standard calculation charts, values found in the literature or default values

implemented in softwares (e.g. Busby et al. 2009, Lo Russo and Civita 2009, Liang et al. 2011, de Paly et al. 2012). In-situ tests, such as thermal response tests (Raymond et al. 2011, Mattsson et al. 2008), or laboratory measurements (e.g. Haffen et al. 2013) are sometimes possible but the deduced values may deliver only well-centered information or may not always be representative of in-situ conditions.

Besides the characterization of shallow geothermal systems themselves, their impact on groundwater temperatures in the aquifer may be important since their exploitation yields cold and hot plumes (Molson et al. 1992, Palmer et al. 1992, Warner and Algan 1984) which may influence aquifer properties and groundwater chemistry (e.g. Jesussek et al. 2013) and microbiology (Brielmann et al. 2009). Haehnlein et al. (2010) pointed out that, if laws and rules exist in some countries to limit the temperature difference caused by the use of geothermal systems, the development of anomalies is rarely monitored. With the growth of the demand for renewable energy, we can expect that regulations will become stricter and controls of installations more common. New monitoring technologies will be needed and ERT may play an important role to monitor spatially, i.e. not only in wells, the variations of temperature in the aquifer. For example, the temperature changes observed on operating GWHP systems (e.g. Vanhoudt et al. 2011) are typically in the range of temperature that could be detected by ERT.

Thermal tracing experiments are performed for decades in hydrogeology (Anderson 2005, Saar 2011). Such experiments are used to improve the characterization of hydrogeological parameters (e.g. hydraulic conductivity or dispersivity), but the same methodologies may be used to study the thermal properties of shallow geothermal systems (e.g. Vandenbohede et al. 2009, 2011, Giambastiani et al. 2013). However, the heterogeneity of geothermal and hydrogeological systems may be too complex to be fully caught by thermal or solute tracer experiments alone (e.g. Brouyère 2001).

In this context, electrical resistivity tomography (ERT) can bring relevant and spatially distributed information both on the heterogeneity of aquifers and on the temporal behavior of tracers. Indeed, ERT has proven its efficiency to image and/or monitor spatial phenomena (Vereecken et al. 2006) such as salt water intrusions (Nguyen et al. 2009, Hermans et al. 2012b), variations in moisture content (Binley et al. 2002), biodegradation of hydrocarbons (Atekwana et al. 2000) and salt tracer experiments (Kemna et al. 2002, Robert et al. 2012).

ERT aims at imaging the electrical resistivity distribution of the subsurface. Bulk electrical resistivity of soil/rock samples decreases with temperature (e.g. Revil et al. 1998, Hayley et al. 2007). This correlation reflects the change in conductivity of water contained in the pores but also in the surface conductivity of grains. The first effect is related to changes in the fluid viscosity, whereas the second is due to changes in the surface ionic mobility. In most studies, temperature effects are undesirable and may create artifacts in the interpretation. As a result, temperature corrections in time-lapse series may be necessary to correct electrical resistivity tomography results in order to avoid misinterpretation when explaining resistivity changes (e.g. Hayley et al. 2007, 2010, Ma et al. 2011, Sherrod et al. 2012).

A parallel can be made between temperature monitoring (Anderson 2005) and salt tracer test (Ptak et al. 2004). Temperature and salt concentration both have an effect on fluid and surface electrical conductivity (Revil et al. 1998). As shown recently by Singha et al. (2011), traditional chemically conservative tracers may not be electrically conservative due to phenomena like ion exchanges, mass transfers or surface conductance. Temperature may also modify chemical processes by changing equilibrium constants or reaction kinetics (Ketrane et al. 2009). Both effects modify the density of the fluid, but in an opposite way. Saline tracers can be used to generate very high contrasts (typically around 10 to 1), but an increase in salinity will increase water density and potentially lead the tracer to sink down the aquifer (e.g. Kemna et al. 2002). It is difficult to reach such a contrast with heat tracers, but an increase in temperature will decrease the density, which is favorable when monitoring from the surface, since the injected tracer will not sink. An analogy exists concerning the flow and transport model for both types of tracer (e.g. Anderson 2005, Langevin et al. 2010), but using thermal tracers enables the derivation of governing parameters for heat transport processes. The monitoring design with ERT will be similar for both cases, but the interpretation needs to use appropriate petrophysical relationships.

ERT has already been applied to study heat reservoirs where hydrothermal fluids generate high resistivity contrasts due to their temperature often exceeding $150°C$. In those situations, ERT can detect the reservoir itself, map preferential flow paths and be useful to characterize rock properties (e.g. Pérez-Flores and Gomez Trevino 1997, Bruno et al. 2000, Garg et al. 2007, Arango-Galvàn et al. 2011). Recently, several studies were carried out to image volcano

hydrothermal systems with very long resistivity cables, showing that ERT is a reliable tool to detect hydrothermal features (e.g. Revil et al. 2010, 2011). ERT has also been used to study seasonal changes in permafrost rock walls. A resistivity-temperature relationship was calibrated around and below the freezing point to give quantitative information on frozen rock temperatures (Krautblatter et al. 2010).

Time-lapse measurements were also used to monitor geothermal systems. Legaz et al. (2009) used ERT and self-potential measurements to image the effect of the variations in lake level of Inferno Crater Lake in New-Zealand. ERT highlighted a large decrease in resistivity as the water level in the lake decreased.

However, few studies used time-lapse ERT to monitor temperature changes directly. Ramirez et al. (1993) used cross-borehole time-lapse ERT to monitor a steam injection during a restoration process. Changes in resistivity were related to an increase in water and soil temperature, a displacement of pore water and changes in ionic content of this water.

LaBrecque et al. (1996b) monitored temperature changes in the context of Joule heating combined to vapor extraction during a remediation process with cross-borehole time-lapse ERT. They compared their results with temperature measurements but did not proceed to a conversion of ERT results into temperature. They analyzed the variation in conductivity between background and time-lapse series. After 7 days of heating, the mean temperature increased by $17°C$, they found mean temperatures in agreement with their expectations. After 14 days, the temperature reached $100°C$ and the change in conductivity was slightly smaller than expected by temperature effects only. It was explained by a decrease in saturation. After 28 days of heating, conductivity values were much below the background values showing an important loss of water produced by desaturation.

To our knowledge, few studies have used time-lapse surface ERT to estimate the characteristics of heat exchange and fluid transport during a geothermal tracer experiment at low temperature and small scale, typical of very-low enthalpy geothermal systems. Benderitter and Tabbagh (1982) carried out an experiment where injected heated water in a 4 to 7 m deep confined aquifer was monitored with DC resistivity measurements. The electrical current was injected into two electrodes and the potential was measured at a moving electrode with reference to a fixed one. The authors produced qualitative anomaly maps using percentage changes in

potential. Due to limited computing power, these maps were interpreted using electrical forward modeling of resistivity anomalies calculated for simple geometric subsurface models determined according to the injected volume. The existence of an electrical anomaly in bulk electrical resistivity (-33%) resulting from injection of heated water ($40°C$) was clearly demonstrated.

In this chapter, we first examine the potential of surface ERT to image a heat injection and storage experiment and its contribution in calibrating coupled flow and heat transport models in a homogeneous shallow aquifer. The results will be generalized to non-dimensional values according to the electrode spacing.

For deeper reservoirs, the rapid decrease in resolution and sensitivity of surface ERT becomes a major drawback (Caterina et al. 2013). It is then necessary to consider borehole ERT to improve resolution (Perri et al. 2012). As an example, Prevedel et al. (2009) installed deep (600 to 750 m) borehole electrodes to monitor the migration of CO_2 within a storage reservoir (Martens et al. 2012). For cross-hole ERT, the results obtained for a specific study are more easily extendable than for surface ERT because resolution patterns are not depth dependent.

In borehole ERT, electrodes are located under the ground surface, either fixed at the outer-edge of the casing or mounted on cables with the borehole fluid ensuring the electrical contact with the surrounding rock. In the latter case, borehole fluid is generally more conductive than the rock and may influence resistance measurements (Doetsch et al. 2010a). Using time-lapse ERT, the relative fluid effect will be almost similar at each time-step and should be insignificant in inversion results (Nimmer et al. 2008).

In a second step, this chapter will investigate the ability of cross-hole ERT to monitor temperature changes and follow thermal tracing experiments in a heterogeneous aquifer. In the next sections, the methodology to acquire, inverse and transform ERT results into temperature will be presented. Then, it will be applied on two field cases illustrating the ability of the method to monitor temperature changes in the considered context.

5.2 Methodology

5.2.1 Petrophysical relationships

The aim of the petrophysical relationship is to quantify the link between bulk electrical conductivity and temperature. Bulk electrical conductivity is generally expressed as a function

of porosity, grain size and tortuosity (often joined in a term called the formation factor F), saturation, fluid electrical conductivity and surface conductivity. Archie's law (equation 5.1) describes the link between F and the porosity ϕ through the cementation exponent m (Archie 1942)

$$\frac{1}{F} = \phi^m. \tag{5.1}$$

The formation factor is used to link the bulk and fluid electrical conductivity (equation 5.2) when surface conductivity can be neglected

$$\sigma_b = \frac{\sigma_f}{F} \tag{5.2}$$

where σ_b is the bulk electrical conductivity of the soil/rock expressed in $[S/m]$ and σ_f is the electrical conductivity of the fluid expressed in $[S/m]$.

When the matrix conductivity is non-negligible, in shaly and clayey sediments for example, additional terms are needed to take into account the surface conductivity of the solid. Equation 5.3 generalizes equation 5.2 to include the surface conductivity σ_s

$$\sigma_b = \frac{\sigma_f}{F} + \sigma_s. \tag{5.3}$$

Several authors (e.g. Waxman and Smits 1968, Revil et al. 1998) propose more complex equations to take into account the surface conductivity, using for example the cation exchange capacity.

In saturated sediments, equation 5.2 shows that the bulk electrical conductivity is directly proportional to the fluid electrical conductivity if we neglect the surface conductivity. Several authors (e.g. Revil et al. 1999, Revil and Linde 2006, Bolève et al. 2007, Leroy et al. 2008) showed that silica grains have a surface conductivity, which cannot be neglected if the water is fresh enough (e.g. Jardani et al. 2009). According to Revil and Linde (2006), the surface electrical conductivity increases when the diameter of the particles decreases (increase in the specific surface of the grains)

$$\sigma_s = \frac{6\Sigma_s}{d_o} \tag{5.4}$$

where Σ_s is the specific surface conductivity in $[S]$ and d_0 is the mean particle diameter in $[m]$. The specific surface conductivity of silica grains is about 4×10^{-9} S (Bolève et al. 2007).

In the unsaturated zone, Archie's law (equation 5.2) can be extended to account for water saturation S_w

$$\sigma_b = \frac{\sigma_f}{F} S_w^n \tag{5.5}$$

where n is an empirical exponent close to 2. In consequence, electrical conductivity changes in the unsaturated zone may be related to either saturation or temperature changes. In the following, we will consider only the saturated zone in absence of surface conductivity. This assumption will be justified later.

The formation factor F may vary spatially (both laterally and with depth), depending on the lithology. In the case of ERT monitoring studies, we measure bulk electrical resistivity at different time steps and compare it to a reference state, called the background. If we take the ratio of equation 5.2 between a specific time-step (state 2) and the reference background (state 1), we have

$$\frac{\sigma_{b1}}{\sigma_{b2}} = \frac{\sigma_{f1}}{\sigma_{f2}} \tag{5.6}$$

and the relation is not dependent on the formation factor. This can be done only if the formation factor is supposed to be independent from electrical conductivity, constant in time and that the surface conductivity is negligible. In equation 5.6, σ_{b1} and σ_{b2} are determined using ERT after inversion of resistance data and σ_{f1} is measured on a sample from formation water of the aquifer before the experiment. This is a requirement for quantitative interpretation. The only unknown in equation 5.6 is thus the fluid electrical conductivity at state 2 (σ_{f2}), which can be expressed as

$$\sigma_{f2} = \frac{\sigma_{b1}}{\sigma_{b2}} \sigma_{f1}. \tag{5.7}$$

Through equation 5.6, we see that the variation in bulk electrical conductivity in the saturated zone is related only to a variation of the fluid electrical conductivity. The latter can be caused by a change in fluid salinity or by a change in temperature. If we assume that the salinity

of the fluid remains constant during the experiment, the water electrical conductivity depends only on temperature. Later, we will see that a change in temperature may modify the chemical composition, and thus the salinity of water as well.

When limited temperature intervals are considered (a few tens of degrees), a linear dependence between water electrical conductivity and temperature can be assumed, it is called the ratio model. Equation 5.8 expresses the linear relation around a temperature of reference T_{ref} (e.g. Hayley et al. 2007):

$$\frac{\sigma_{f,T}}{\sigma_{f,T_{ref}}} = m_{f,T_{ref}}(T - T_{ref}) + 1 \tag{5.8}$$

where $\sigma_{f,T}$ is the fluid electrical conductivity at temperature T (in $°C$), $\sigma_{f,T_{ref}}$ is the fluid electrical resistivity at the temperature of reference, and $m_{f,T_{ref}}$ is the fractional change in electrical conductivity per degree Celsius for the temperature of reference. In the following, we will use $T_{ref} = 25°C$.

The value of $m_{f,25}$ can be experimentally determined and varies according to the composition of the fluid. A value between $0.018°C^{-1}$ and $0.025°C^{-1}$ is often found for $m_{f,25}$ (Hayley et al. 2007). Surface conductivity variations with temperature can be expressed by similar equations, with a different fractional change per degree $m_{s,25}$. Revil et al. (1998) found $m_{f,25}$ equal to $0.023°C^{-1}$ and $m_{s,25}$ around $0.04°C^{-1}$ on the temperature range $25-200°C$ during tests on shaly sands. The ratio of surface conductivity to the fluid conductivity increases with temperature and equation 5.8 does not apply for bulk conductivity. Hayley et al. (2007) applied the same model as Revil et al. (1998) on the temperature range $0 - 25°C$ and found $m_{s,25}$ around $0.018°C^{-1}$ and $m_{f,25}$ equal to $0.0187°C^{-1}$ (Hayashi 2004). These values are similar, leading globally to linear temperature dependence for the bulk electrical resistivity. When surface conductivity can be neglected, equation 5.8 can be directly incorporated in Archie's law.

For larger temperature intervals, an exponential model may be necessary to describe the relationship. An example is given by Corwin and Lesch (2005)

$$\sigma_{f,25} = \sigma_{f,T} \times \left[0.447 + 1.4034 \exp\left(-\frac{T}{26.815}\right)\right]. \tag{5.9}$$

In the temperature interval considered in the experiments presented in this chapter (10 to $45°C$) the linear relationship between temperature and fluid electrical conductivity can be

assumed (equation 5.8).

Introducing equation 5.8 into equation 5.7, we can express the temperature T (in $°C$) according to bulk electrical conductivity of the background and of the considered time-lapse section, to water electrical conductivity at the temperature of reference and at the temperature of the background and to the fractional change per degree Celsius

$$T = \frac{1}{m_{f,25}} \left[\frac{\sigma_{b2,T}}{\sigma_{b1}} \frac{\sigma_{f1}}{\sigma_{f,25}} - 1 \right] + 25 \tag{5.10}$$

where $\sigma_{b2,T}$ represents the bulk electrical conductivity at the time-step for which we try to determine the temperature.

Since ERT provides a spatial model of the distribution of bulk electrical conductivity in the subsurface, time-lapse ERT proposes, under a few assumptions, a unique way to assess spatial and temporal temperature variations in the subsurface.

5.2.2 Time-lapse inversion procedure

In electrical resistivity tomography, the solution of the inverse problem is non-unique (see chapter 2). A common way to solve such inverse problems is to add a regularization constraint to the least-square problem (Tikhonov and Arsenin 1977). The problem is then to minimize, through an iterative process an objective function of the form of equation 2.17. See section 2.1 for more details.

With time-lapse data sets, we are more interested in the change in electrical conductivity than in the absolute value of conductivity. Generally, the process of inversion is adapted in order to improve inversion results. Three main procedures, with several variants, exist to invert for time-lapse ERT data (e.g. Miller et al. 2008): namely independent inversion, time-constrained or reference model inversion and difference inversion. In the first one, inversion results obtained separately are simply substracted, which should eliminate systematic errors but amplify uncertainties in the data. For temporally constrained schemes, a regularization operator is added in the time dimension (under the form of a reference model) in addition to the space dimensions, to minimize changes between successive sections (e.g. Karaoulis et al. 2011). In this study, we used the difference inversion scheme (Kemna et al. 2002) where the problem is formulated in terms of variations for both data and model. Equation 2.17 becomes

$$\psi(\mathbf{m}) = \|\mathbf{W}_d(\mathbf{d} - \mathbf{d}_0 + f(\mathbf{m}_0) - f(\mathbf{m}))\|^2 + \|\mathbf{W}_m(\mathbf{m} - \mathbf{m}_0)\|^2 \tag{5.11}$$

where $\mathbf{d}_0$ and $\mathbf{m}_0$ are respectively the data set and the model corresponding to the background state. The results obtained for the background are thus used as a reference for subsequent inversions. This method should reduce the systematic error and provide a faster convergence (LaBrecque and Yang 2001).

To compare the successive models in the monitoring study, it is important that all data sets are inverted with the same level of data misfit corresponding to the expected noise level. Indeed, over-fitting the data may create artifacts of inversion in the corresponding image, whereas the contrary would result in an over-smoothed inverted section (LaBrecque et al. 1996a). To achieve this, the iteration process is stopped when the root-mean-square (ϵ_{RMS}) value of error-weighted data misfit is equal to one (equation 2.15).

The results are presented as percentage change of resistivity

$$\Delta\rho = \frac{\rho_i - \rho_{BG}}{\rho_{BG}} \times 100 \tag{5.12}$$

where ρ_i is the resistivity of the time-lapse section and ρ_{BG} is the resistivity of the background section. A negative value corresponds to a decrease in resistivity (or increase of conductivity) and a positive value corresponds to an increase in resistivity.

We used the code CRTomo (Kemna 2000) to invert our data. This code is a 2.5D inversion code; it means that the electrical conductivity distribution is assumed to be constant in the direction perpendicular to the section and that the effect of boreholes themselves cannot be taken into account (Nimmer et al. 2008, Doetsch et al. 2010a). Effects caused by boreholes are of more concern when the investigated site is located in high resistive rocks. They may also be, at least partly, avoided with time-lapse inversion. Indeed, we can expect that, if they exist, 3D artifacts will be compensated because present in both background and monitoring states (Nimmer et al. 2008). This is also true for surface arrays. Bowling et al. (2007) explained that the effect of a quarry cliff of infinite resitivity was only perceived within 5 m of an electrical tomography profile (48 electrodes with an electrode spacing of 2 m). This signifies that distortions due to true 3D resistivity distributions are limited using $2.5D$ imaging. However, in both studied cases, the targeted plume of heated water is $3D$ and some distortions could occur using a $2D$ survey

leading to errors in the estimated magnitude of the anomaly (e.g. Bentley and Gharibi 2004). A possible 3D effect when imaging a contrasting moving plume (as it will be the case during the injection and pumping experiment) is that the plume is imaged even though it is outside the image plane. The reason is that the 3D heterogeneity caused by the moving tracer is not taken into account in the 2.5D inversion scheme (Nimmer et al. 2008). This may result in bias in the breakthrough curve, leading to an apparent more diffuse behavior of tracers (Vandenborght et al. 2005). This effect is also called "the shadow effect".

Assessing the quality of an ERT image and the reconstruction of electrical resistivity is a major point when interpreting imaging results. As the parameter resolution matrix of the inverse problem (Alumbaugh and Newman 2000) is computationally expensive to calculate, we used the error weighted cumulative sensitivity matrix (Kemna 2000, see equation 2.21). A high value of sensitivity for a parameter signifies that changing its value of resistivity will strongly influence the data. In contrast, a low value of sensitivity is characteristic of a parameter having less influence on the predicted data. Such a low sensitivity zone will most likely be badly resolved in the inverted section. However, it has to be noted that high sensitivity does not necessarily mean high resolution.

5.3 Field Case 1 : Heat injection and storage experiment

5.3.1 Field site and heating procedure

The field experiments took place on the campus De Sterre of Ghent University (figure 5.1). It corresponds to the Ghent site of chapter 2. Figure 5.2 shows a schematic cross-section of the site with lithological characteristics and the position of the water level, together with the well description. The upper layer lies from 0 to -2 m and corresponds to unsaturated fine sands. From -2 m down to -4.4 m, the same sands are found at saturation. These sands constitute homogeneous Quaternary deposits, as evidenced by nearby boreholes (W02 and W03 on figure 5.1). Below -4.4 m, a clay layer of Tertiary age is found, forming a low permeability layer. The injecting well was drilled down to -4.4 m, it is made of a PVC casing with a screen of 90 cm at the bottom of the Quaternary layer. Calibrated sands were poured around the well along the screen, and bentonite cement was used to fill the upper part of the drilling hole as a hydraulic seal. The water table lies at -2 m and is nearly flat on the site; a gradient of

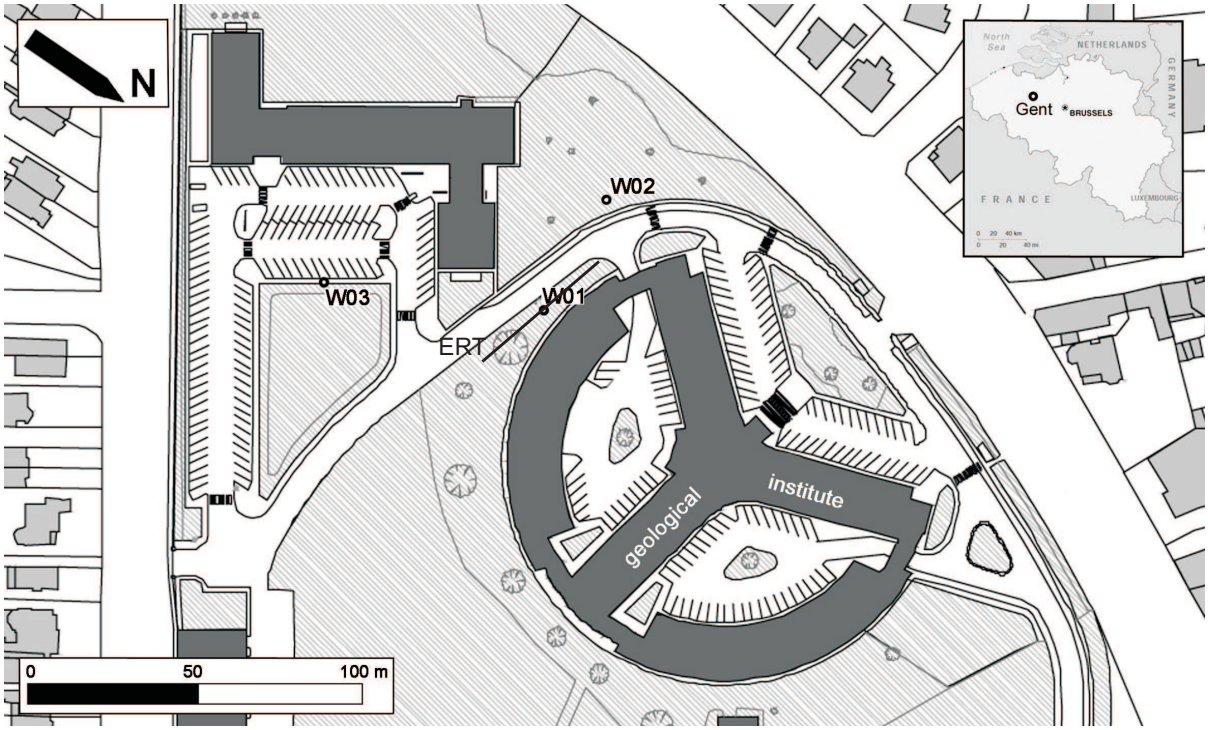

Figure 5.1: The study area is located on the campus De Sterre of Ghent University. W01 gives the position of the injection well, W02 and W03 the position of two wells used to described the water level. The black line shows the position of the ERT profile next to the geological institute.

0.005 m/m towards the south-southwest was derived from three wells (W01, W02 and W03 on figure 5.1). The temperature in the aquifer was $10.5°C$.

The layer where heated water is injected is composed of fine sands. Assuming a specific surface conductivity of 4×10^{-9} S (Bolève et al. 2007) and a mean particle size diameter for the fine sands of 200 μm, we find a surface conductivity of 1.2×10^{-4} S/m, which is three orders of magnitude below the water electrical conductivity on the site, which is around 10^{-1} S/m. The role of the sediment surface electrical conductivity was thus neglected.

In the clays of Tertiary age, equation 5.3 should be used to take into account the change in surface conductivity. Interpretation in terms of temperature was not considered in the clays since the surface conductivity effect cannot be neglected. Clay acts as an impermeable barrier avoiding convection processes, but conduction is still possible, leading to an increase in temperature of the clay.

A slug test was performed in the injection well to estimate possible injection rates. A volume of 10 l was injected and the evolution of the hydraulic head was followed with a pressure transducer. For a water temperature of $10.5°C$, a maximum rate of 70 l/h was estimated.

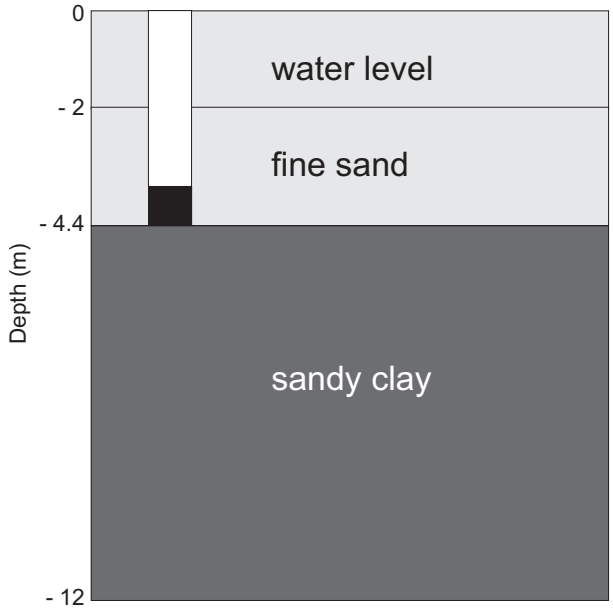

Figure 5.2: The 4.4 first meters of the field site consist of fine sands. These sands cover a sandy clay layer which is less permeable. The water level lies at $-2\ m$. The injection well is drilled in the fine sands and is screened between -3.5 and $-4.4\ m$.

However, for water at $48°C$, the decrease in water viscosity enabled to inject at a rate of 87 l/h.

For practical reasons, it was not possible to heat the formation water directly. This would have required two new pumping wells and would have lead to logistics problems: control of pumping rates during all the experiment and storage of pumped formation water in containers outside of the building in cold air conditions before heating. Access to the unconfined aquifer was only possible in the injection well. Other wells intersecting the unconfined aquifer were located on the other side of the road (figure 5.1). The use of a resistance to heat the water through Joule dissipation (e.g. LaBrecque et al. 1996b) was not considered, since it would lead only to conduction and no convection.

Tap water was thus used for the injection. Its temperature fluctuated between 9 and $14°C$. After passing through a heating system consisting of two electrical boilers having a capacity of 200 l and a power of 2200 W, water temperatures varied between 45 and $49°C$, with an average of $48°C$. Injection of heated water lasted for 70 h.

In the $10-50°C$ temperature interval considered for this experiment, a linear relationship can describe the link between temperature and water electrical conductivity (figure 5.3). Applying equation 5.8 for water electrical conductivity, we obtain a fractional change in conductivity $m_{f,25}$ equal to $0.02125°C^{-1}$. This value is comprised between the values obtained by Hayashi (2004)

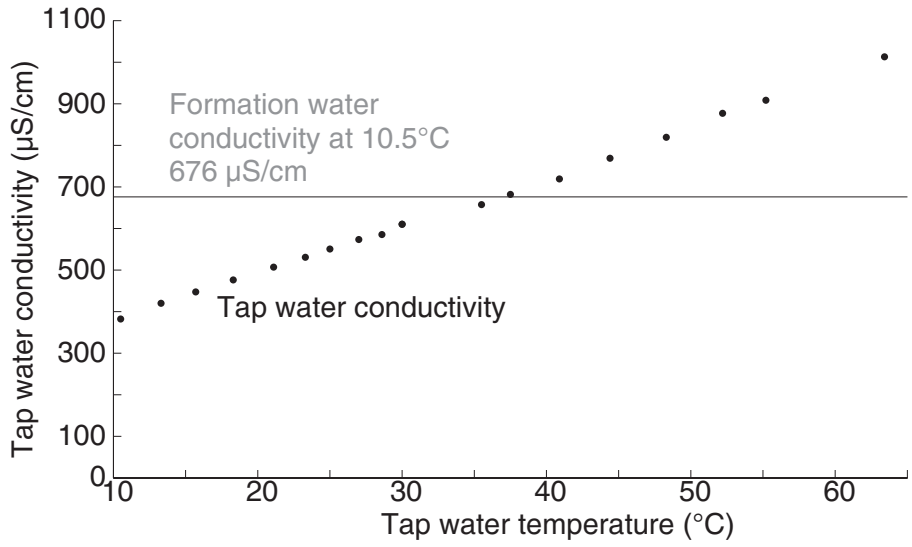

Figure 5.3: Electrical conductivity of the injected water increases linearly with temperatures (points) according to our laboratory measurements, the fractional change per degree Celcius is about 2.1%. The formation water at temperature of the aquifer (i.e. $10.5°C$, line) is more conductive than the injected water.

in the interval $0 - 25°C$ (0.0187) and by Revil et al. (1998) on the interval $25 - 200°C$ (0.023).

At $10.5°C$, tap water, which is used for injection, electrical conductivity is 374 $\mu S/cm$ whereas formation water conductivity is 676 $\mu S/cm$ (figure 5.3). At $48°C$, the average injection temperature, tap water electrical conductivity reaches 818 $\mu S/cm$. If both waters had the same conductivity, the increase in temperature would have led to an increase in water electrical conductivity, and thus in bulk electrical conductivity according to equation 5.2, of 120%. However, the increase in temperature from 10.5 to $36°C$ first balances this difference of 302 $\mu S/cm$ in specific electrical conductivity instead of producing an electrical conductivity anomaly, what appears only above 676 $\mu S/cm$. Only the increase from 36 to $48°C$ contributes to produce an electrical anomaly in the sand layer. In consequence, the maximum increase in bulk electrical conductivity is equal to 21%, the corresponding decrease in bulk electrical resistivity is 17%.

To interpret ERT time-lapse series in terms of temperature variations in the aquifer, we cannot directly use equation 5.10. Indeed, it is necessary to take into account the difference in conductivity between formation and tap water. The injection was simulated with the calibrated hydrogeological model (see section 5.3.4). We started from an aquifer filled with formation water and then simulated the injection during 70 h of a solution whose conductivity was equal to the one of tap water, at a rate of 87 l/h. The dispersivity was set at 0.2 m and was chosen according

to results in similar Quaternary deposits (Vandenbohede and Lebbe 2002, Vandenbohede et al. 2011). This neglects the increase of hydraulic conductivity with temperature. The transition between water electrical conductivity in $[S/m]$ and concentration C in $[mg/L]$, was made using Keller and Frischknecht (1966) relationship

$$\sigma_f \approx \frac{C}{5000}. \tag{5.13}$$

Then, a temperature correction was applied according to the simulated conductivity of the water at the end of the injection. If the conductivity was equal to the conductivity of tap water, no correction was applied and we can apply equation 5.10 to derive the temperature directly. If the conductivity was equal to the one of formation water, a correction of $-25.5°C$ was applied. This enables to take into account the fact that formation water has the same electrical conductivity as tap water when its temperature is $25.5°C$ lower. Doing so, we assume that the fractional change in electrical conductivity per degree Celsius m is the same for the formation water. Between these two conductivity limits, a linear variation was used to calculate the temperature correction, i.e. if the conductivity was equal to the mean between tap and formation water, a correction of $-12.25°C$ was applied.

5.3.2 ERT measurements

We used an ABEM SAS 1000 Terrameter (single channel) with 64 take-outs and stainless steel electrodes with copper wire connectors. Dipole-dipole arrays generally lead to better results in terms of imaging but have a lower signal to noise ratio (Dahlin and Zhou 2004). On the field site, the level of noise was quite high. We attribute the origin of the ambient noise to the urban nature of the area (figure 5.1). As a second choice, we used a Wenner-Schlumberger array with $n \leq 6$ and an unlimited a factor with an electrode spacing of 0.75 m. This array type has a higher signal to noise ratio than the dipole-dipole array. The average repeatability error was below 0.1%. The array used to collect the data had 62 electrodes and 823 measurements points.

The ERT profile was centered on the well W01, which is located at the abscissa 23.5 m on the profile, and parallel to the geological institute building (figure 5.1). The total length was equal to 45.75 m.

The estimation of the data quality for ERT (noise level) is very important since the inverse

electrical problem is non-linear and can lead to large amplifications of data noise in the electrical image. An overestimation of the level of noise can lead to a smoothed final image. In contrast, when the noise level is underestimated, the inversion algorithm will generate rough and irregular structures to reproduce noisy data (LaBrecque et al. 1996a).

We used reciprocal measurements to assess the error level in the data (LaBrecque et al. 1996a). To minimize acquisition time for the reciprocal measurements, 200 points were sampled out of the 823 with both normal and reciprocal measurements randomly chosen for each pseudo-depth. Obviously, we kept all of the 823 normal measurements to invert our data sets.

We derived an error model according to the procedure of Slater et al. (2000). The absolute reciprocal error $|e_{N/R}| = R_N - R_R$, where R_N and R_R are the normal and reciprocal resistance in $[Ohm]$, is modelled as

$$|e_{N/R}| = a + bR \tag{5.14}$$

where a represents the minimum absolute error in $[Ohm]$ and b defines the relative increase of the error with the mean resistance R in $[Ohm]$. These parameters are determined by the envelope that contains all the points after removal of outliers. This is illustrated on figure 2.2 for the 200 sample points. Obvious outliers were removed. The best fit for the envelope was found with a minimum absolute value of 0.001 Ohm and a relative error of 2.5%.

5.3.3 Monitoring results

Before the heated water injection started, a background image was collected to serve as a reference for subsequent time-lapse series.

Standard smoothness constraint regularization was first used to invert the data. The error model of equation 5.14 was used to weight the data. It yielded a smooth model with gradual changes from high surface resistivity corresponding to the unsaturated sand to low resistive clay (figure 5.4A). The transitions between unsaturated and saturated zones or sand and clay are not clearly observable.

To take into account available prior information and to better define the saturated sand which is the zone of injection, additional structural constraints (see section 2.4) deduced from borehole evidences were included to improve the solution. At $-2\ m$ and $-4.5\ m$, where we know

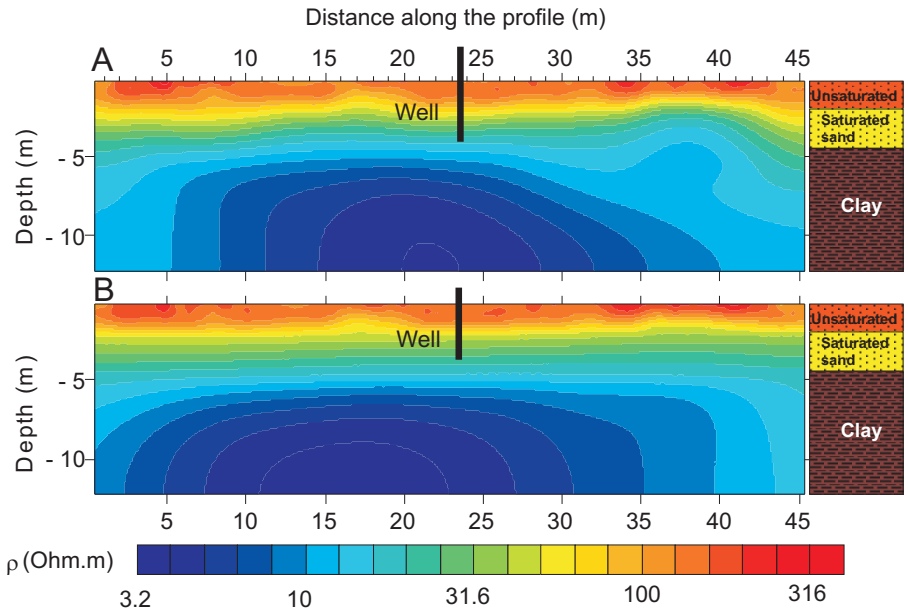

Figure 5.4: The correspondence between ERT and borehole data is improved when structural constraints are added (B) to the standard smoothness constraint (A). The saturated sands are better described, which is important as it constitutes the zone of injection.

that a horizontal limit exists, the horizontal/vertical anisotropy ratio β_x/β_z in the smoothness constraint inversion was set at $1000:1$, i.e. the smoothing effect of the inversions is 1000 lower vertically than horizontally. It permits to reduce vertical smoothing effects at these locations and therefore to avoid smoothing effects between unsaturated and saturated zones and sands and clays, respectively. It yields the background image (figure 5.4B). The comparison between the two models (Tikhonov regularization and with structural constraints) shows that the layers boundaries are sharper.

The lithological/hydrological layering is clearly visible on the ERT image. The first layer, corresponding to unsaturated sand in the upper 2 m, displays resistivity values between 100 and 200 $Ohm.m$, decreasing from the surface to the bottom with the increasing saturation (see equation 5.5). At abscissae 5, 35 and 40 m, resistivity increases up to 300 $Ohm.m$, this is due to the presence of indured sands in the upper part of the sand layer. From 2 m below the surface down to -4.4 m, the sands are saturated; we thus observe a decrease in resistivity down to about 30 $Ohm.m$. At the depth of 4.4 m, the resistivity values decrease again, with values below 10 $Ohm.m$, due to the presence of sandy clay.

Using the background resistivity model (figure 5.4B) as a starting model and reference model (equation 5.11), resistance changes were inverted to reproduce resistivity models 24, 48 and 72 h

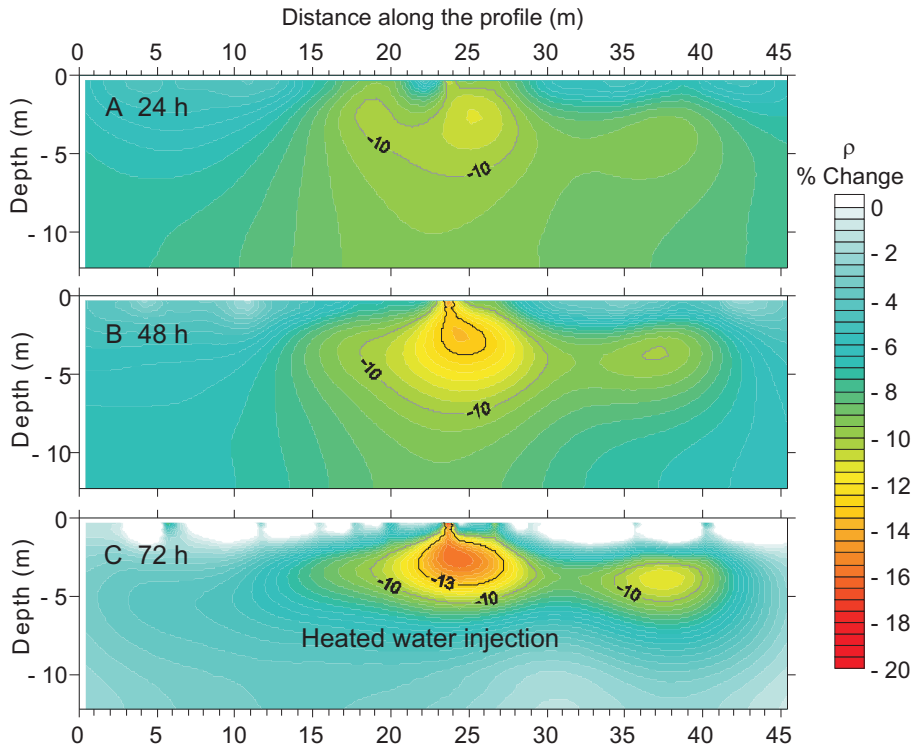

Figure 5.5: The plume of heated water is detected as an increasing negative anomaly (i.e. decrease in bulk electrical resistivity) in the time-lapse series after (A) 24 h, (B) 48 h and (C) 72 h. The minus 13% isoline is highlighted in black, it illustrates the growing heated water anomaly. The minus 10% isoline is highlighted in grey. Below this value, changes are not directly interpretable due to the noise and changing weather conditions.

after the beginning of injection of heated water. We used the same noise level for all the data. The results are displayed in figure 5.5 in terms of percentage change in bulk electrical resistivity.

Since ERT is a non-linear inverse problem, the injection of heated water and subsequent modification of the bulk electrical resistivity distribution can modify the resolution and sensitivity pattern in time and space (Singha and Gorelick 2006). In this case, a small increase in sensitivity is expected since the new distribution of bulk resistivity will display a zone of smaller resistivity in the center of the profile due to the presence of the plume of heated water. This zone will focus current lines and improve the sensitivity.

To ensure that we avoid interpreting anomalies related to differential resolutions, we analyzed the cumulative sensitivity distribution (equation 2.21) for the different time frames. As an example, we compared the cumulative sensitivity before (background) and after 48 h of injection (figure 5.6).

Changes in sensitivity are visible but are mostly limited to the deepest layers of the site,

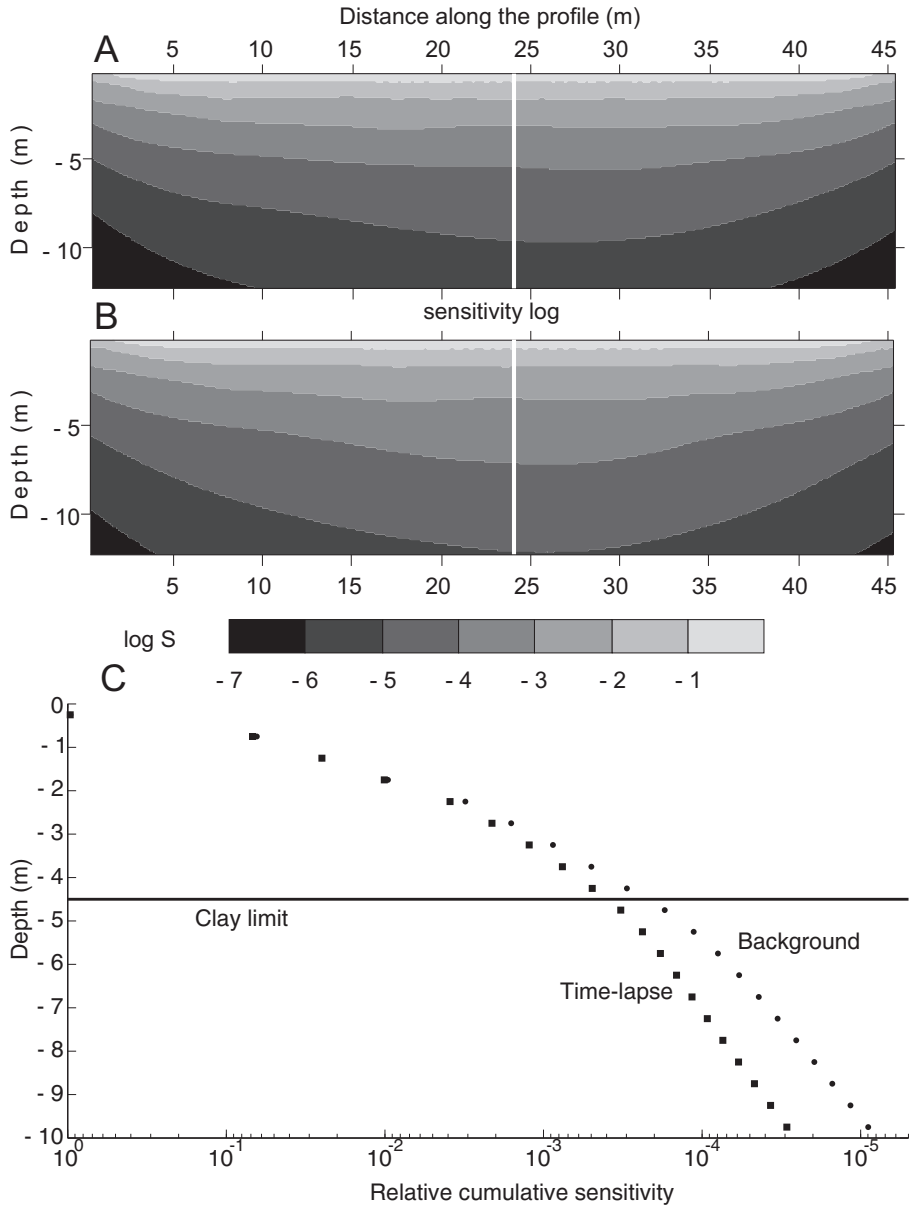

Figure 5.6: The cumulative sensitivity before the test (A) and during the test (B) remain similar in the zone of injection (between -2 and $-4.5\ m$), artifacts due to different resolutions should be avoided. A log of sensitivity at the position of the well (C) enabled to appreciate quantitatively this similarity. The maximum difference in the zone of injection is found at the bottom of the sand where the sensitivity is 8×10^{-3} for the background and 5×10^{-3} after 48 hours.

which are not concerned by the heated water injection, as shown by the comparison of the sensitivity logs at the position of the well (figure 5.6C). For the zone concerned by this injection, from $-2\ m$ to $-4.5\ m$, sensitivity values remain within the same range and changes in resistivity from the background to the time-lapse series due to differential resolutions should be avoided.

The heated water plume is detected at the location of the injection well at the different times as an increasing negative electrical resistivity change anomaly, in agreement with the petrophysical model presented above, as illustrated by the minus 13% change in bulk electrical resistivity isoline on figure 5.5. The maximum amplitude change is detected at the end of injection at the centre of the plume (figure 5.5C). As explained previously, the maximum decrease in resistivity is around -17%, which is lower than expected, because injection water is more resistive (less conductive) than formation water at the same temperature (figure 5.3). If both waters would have had similar electrical conductivity, the maximum decrease would have been around -54%. Due to the smoothing effect of inversion, the plume is enlarged, the decrease in resistivity concerns a bigger volume than expected and the maximum decrease is likely underestimated. 3D effects can also reduce the maximum decrease in resistivity.

After 24 h (figure 5.5A), a change of -12% in bulk electrical resistivity is detected at the well. At this time, the volume of heated water injected in the well was limited to 2.1 m^3, yielding a small anomaly that ERT can barely image. After 48 h (figure 5.3B), the anomaly is enlarged and the change in resistivity is higher (-15%). Since the volume of heated water injected is doubled (4.2 m^3), ERT managed to image the plume in more details. At the end of injection (figure 5.3C), the decrease in resistivity reaches its maximum (-17%). The geophysical inversions show that the plume extension is limited in depth by the clay layer. This result is also in accordance with the hydrogeology of the site since this layer is considered as impermeable.

A decrease of electrical resistivity is observed above the top of the screen in the aquifer, between -2 and $-3.5\ m$, where the bentonite seal was placed. This variation corresponds to an increase in temperature, as shown by temperature logs (figure 5.7) carried out after the injection phase (Vandenbohede et al. 2011). Such an important increase in temperature could not be explained only by heating due to thermal conduction from the PVC casing (thermal conductivity of 0.17 $W/m°C$). This phenomenon can be explained if the bentonite seal used to prevent leakage of injection water was not properly set up, inducing injection of heated water to

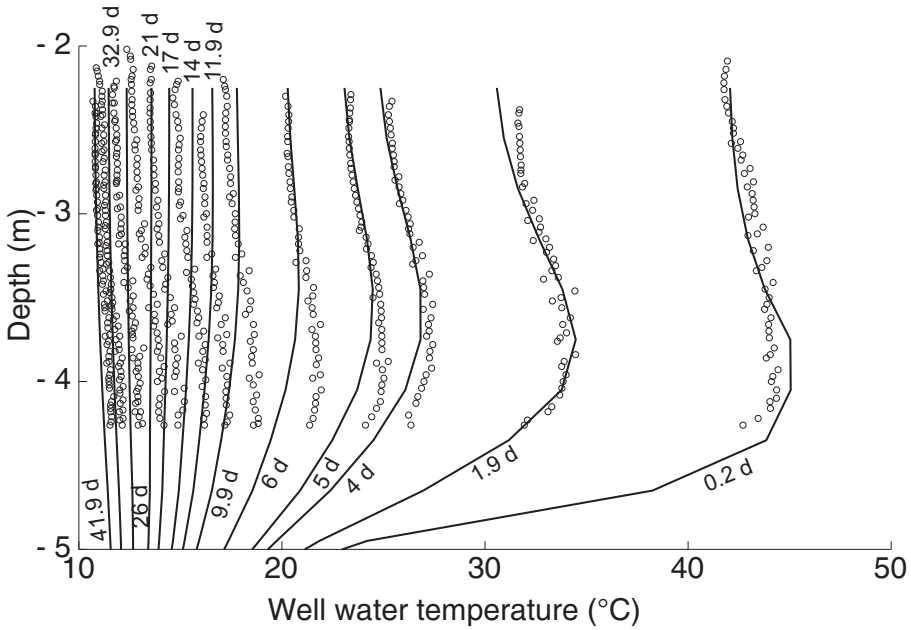

Figure 5.7: Temperature logs were taken after the injection in the injection well (W01) to control the temperature in the aquifer and to calibrate the thermo-hydrogeological model. The misfit between observed (o) and calculated (-) temperature logs can be appreciated at different observation times (Vandenbohede et al 2011).

reach the upper part of the aquifer. Another anisotropy ratio, with a greater vertical component, could have a similar effect. However, even a forward flow and transport simulation with a $1:1$ anisotropy ratio is not able to produce temperatures similar to the one observed with the logs. We thus favor the former hypothesis. In addition, we observe a bulk electrical resistivity decrease in the unsaturated zone along the well, which could be caused by thermal conduction through the pipe.

On figures 5.5A and B, we see an almost systematic lowering of -5% in bulk electrical resistivity across the entire image. In contrast, in figure 5.5C, significant changes are limited to the zone of injection; elsewhere, variations are around -3% at maximum. It is important to recall that all the inversions were run with the same level of noise, determined once with the reciprocal error. However, we think that the data quality (noise level), which was estimated only once after the injection, varied during the three days of injection (e.g. Miller et al. 2008). During the background, the weather was dry with air temperature above $0°C$. For the following two days, air temperature decreased below $0°C$ and snow fell. Surface conditions were thus completely different, which influenced the contact resistance at electrodes and therefore the noise level. This change might affect the overall quality of the image also at depth and might

be reflected in the difference inversion through enhanced/reduced smoothing effect. As a result, the -10% isoline seems larger after 48 h than after 72 h. At the end of injection, temperature was again above zero and weather conditions were closer to the one of the background.

To assess the minimal changes in temperature that could be detected by the electrical survey, which depends mainly on the electrical resistivity distribution, on the estimated signal to noise ratio and on the array design, we generated an ensemble of 100 geoelectrical data sets by adding a Gaussian random noise to the field data (standard deviation of 2.5%). That was used to compute the background image (figure 5.4). This ensemble was then inverted with the same inversion parameters (Kemna et al. 2007). We found that the distribution of each parameter follows a Gaussian distribution. The generated artificial electrical resistivity changes are around 3 to 5%, when considering changes between the average resistivity and the average resistivity minus one standard deviation. This would correspond to temperature variations of about 2 to $3°C$. As a result, we considered only changes two times greater than the noise-related changes (10% in magnitude) as significant.

An anomaly is also present at 37 m from the beginning of the profile. At this position, there was a big tree. Barker and Moore (1998) showed the influence of roots in the saturation of sands and this tree could explain why resistivities below 100 $Ohm.m$ are found less deep than elsewhere in the section (figure 5.4). However, the cause of the 10% decrease in resistivity below the water table at this position is unclear.

5.3.4 Heat flow and transport model

Parameters responsible for heat transport in the aquifer are of special interest when studying geothermal systems. We carried out thermo-hydrogeological modeling to identify those parameters and to assess their reliability. Temperature logs were taken before and after the test, as well as during the storage phase, i.e. after the end of injection. A complete description of this modeling can be found in Vandenbohede et al. (2011).

To simulate heat transport, the US Geological Survey computer program SEAWAT version 4 (Langevin et al. 2007) was used. This is a finite-difference solver, coupling MODFLOW-2000 (Harbaugh et al. 2000) with MT3DMS (Zheng and Wang 1999). SEAWAT is capable of simulating heat transport and takes into account density and viscosity changes.

We simulated the test with a 3D model constituted of 80 rows and 80 columns of 0.25 m each (20 m by 20 m) and 23 layers. The 8 first layers are 0.3 m thick and represent Quaternary deposits and the top of the model corresponds to the water table. The remaining layers represent clay deposits. The thicknesses are 0.3 m thick for layers 9 to 13, 0.4 m for layers 14 and 15, 0.5 m for layers 16 and 17, 0.6 m for layers 18 and 19, 0.7 m for layers 20 and 21, 0.8 m for layer 22 and 0.9 m for layer 23. The geological building (figure 5.1) is represented by the first 30 columns of the upper 4 layers which are inactive. The hydraulic gradient of 5×10^{-3} was imposed between eastern and western boundaries with constant head boundaries.

Constant temperature boundary conditions are applied in the first layer and in cells bordering the inactive cells which represent the building. This temperature depends on air temperature and temperature of the groundwater recharge which are subject to seasonal changes. We approximated this variation with a sinusoidal function calibrated thanks to temperature measurements in W01 and W02 as done by Suzuki (1960) for instance. The influence of the building was taken into account by increasing the mean temperature of the aquifer next to it. With this seasonal model, we simulated the initial conditions for the heat injection test; details can be found in Vandenbohede et al. (2011).

A horizontal hydraulic conductivity of 0.5 m/d was derived from slug tests performed in the well. The slug test was interpreted using guidelines given by Butler (1998) and interpreted with the KGS model (Hyder et al. 1994). For Tertiary deposits, we estimated a horizontal hydraulic conductivity of 0.1 m/d from previous studies (Lebbe et al. 1992). Vertical conductivity was taken ten times smaller for both cases and we estimated an effective porosity of 0.35, which is a typical value for these sediments. These values are based on our knowledge of the lithology and results from previous experiments in similar Quaternay sediments (Vandenbohede and Lebbe 2002, 2003, 2006). The groundwater recharge was estimated at 150 $mm/year$. Thermal properties of the medium are summed up in table 5.1.

The injection phase, the phase of interest for comparison with geophysical data, is simulated with one stress period of 70 h (2.92 days) subdivided in 300 time steps. The storage phase is simulated with 45 stress periods of one day subdivided in 10 time steps. The model was calibrated by trials and errors.

In our initial modeling attempt, the injection rate was concentrated at the screen position.

Parameter	Value for simulation
reference temperature	10°
fluid density - temperature relation	$\delta\rho/\delta T = -0.375\ kg/(^{\circ}m^3)$
reference viscosity	$\mu_0 = 0.001\ kg/(ms)$
porosity	$\phi = 0.35$
solid matrix density	$\rho_s = 2640\ kg/m^3$
specific heat of the fluid	$c_F = 4183\ J/(kg^{\circ}C)$
specific heat of the solid	$c_S = 710\ J/(kg^{\circ}C)$
distribution coefficient for temperature	$K_{DT} = 1.69 \times 10^{-4}\ m^3/kg$
thermal conductivity of the fluid	$\lambda_F = 0.58\ W/m^{\circ}C$
thermal conductivity of the solid	$\lambda_S = 3\ W/m^{\circ}C$
bulk thermal conductivity	$\lambda_b = 2.153\ W/m^{\circ}C$
bulk thermal diffusivity	$D_T = 0.127\ m^2/d$

Table 5.1: Model parameters used in the SEAWAT model (Langevin et al. 2010, Vandenbohede et al. 2011).

To account for the geophysical observations, which show a temperature increase all along the well, it was necessary to spread the injection rate over the complete length of the well in the thermo-hydrogeological model. Figure 5.7 shows, in support of the geophysical images, increased temperatures in the injection well (corresponding to downhole temperature profiles) above the screen during the storage phase. This reflects the failure of the bentonite to seal the annular space of the well. We assume that these temperatures are in equilibrium with water outside of the borehole.

Resistivity values from ERT images were converted into temperature (called hereafter ERT-derived temperature) using equation 5.10 and the correction term. The main difficulty was to account for the difference in electrical conductivity of formation water and tap water.

The comparison (figure 5.8) shows that the horizontal and vertical positions of the plume after 72 h are correctly imaged, but the plume itself is enlarged. Before 72 h, the volume of heated water is not big enough to be correctly imaged. The enlargement of the plume can be easily explained by the smoothness constraint used to regularize the model differences in the inversion process and was also observed by Vanderborght et al. (2005) for a saline tracer.

The ERT-derived temperature image also shows changes near the surface in the unsaturated zone, between 0 and -2 m depth. Here, saturation variations can also explain smaller resistivity values. The temperature values given in figure 5.8B in the unsaturated zone are not reliable as they assume similar saturations for the background and the time-lapse series.

Temperatures monitored with ERT are quite consistent with the thermo-hydrogeological modeling after 72 h. The maximum temperature deduced from ERT is $45^{\circ}C$ which is only $3^{\circ}C$

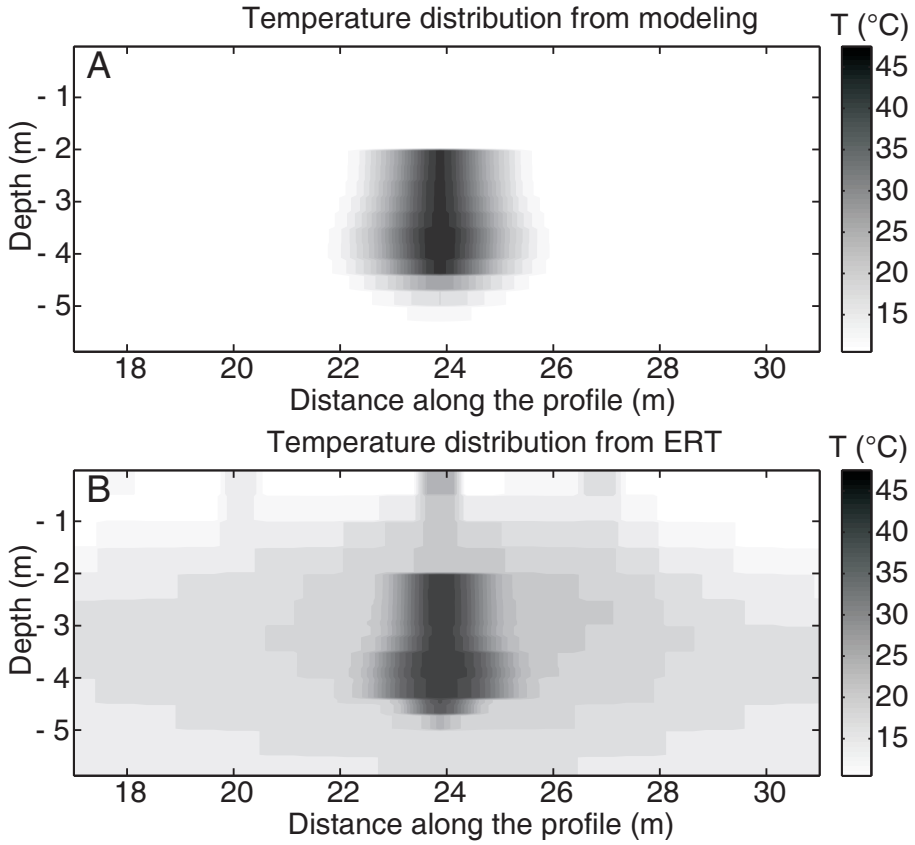

Figure 5.8: Petrophysical laws enabled to transform resistivity values into temperatures. The plume detected with ERT (B) is in accordance with the plume calculated with a calibrated thermo-hydrogeological model (A).

below the mean temperature of injection. The width and thickness of the plume are also satisfactory. Note that the smoothing effect of the regularization is in part counterbalanced by the spatial distribution of the proportion of tap and formation water obtained from hydrogeological simulations.

5.3.5 Focus on the storage phase

During this first experiment, only the injection phase was monitored, the main aim being to study the feasibility of using ERT to monitor temperature changes. To overcome the limitations of this first test and to monitor the storage phase, the experiment was restarted (Daoudi 2011). In addition, in order to increase the detected contrast in electrical resistivity, cold tap water was injected in the well for two weeks before the injection of heated water, which lasts 6 days instead of 3. This will also allow the use of equation 5.10 to transform ERT results into temperature.

The data acquisition sequence was also modified. The spacing between electrodes was reduced to 60 cm with 48 electrodes centered on the injection well. The resulting geometrical factors being reduced, this allowed to use a dipole-dipole configuration ($a = 3$ and all possible n values) which has a higher lateral resolution than the Wenner-Schlumberger.

During the storage phase, ERT is able to highlight the decrease in temperature of injected water, which corresponds to a decrease in the resistivity anomaly. The decrease in resistivity is maximum at the end of injection; then, it tends progressively to zero. Figure 5.9 shows this anomaly after 4 (figure 5.9A) and 9 days (figure 5.9B) of cooling. At this time, a decrease in resistivity of -25% compared to the background is still visible. The plume is enlarged due to the smoothing effect of the regularization. In this case, the effect would also be visible in an ERT-derived temperature section (in contrast with figure 5.8), because the effect is not counterbalanced by the contrast of conductivity between formation and injection water. Note also the increase of resistivity in the upper part of the image, due to the desaturation of the unsaturated area which was almost saturated for the background due to a rainfall event.

The obtained resistivity values were validated with borehole measurements. We performed electromagnetic measurements in the well with an EM39 device (McNeill 1986) to obtain a conductivity log (figure 5.10A). The results are very similar four days after the end of injection, which proves that ERT is a reliable tool to predict electric conductivity in this particular

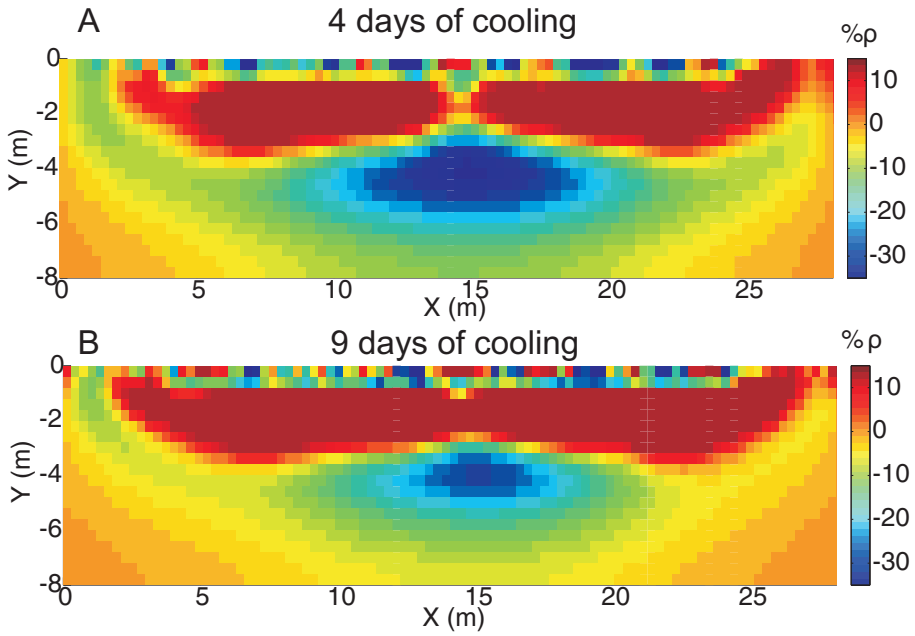

Figure 5.9: ERT time-lapse images show, as expected, a decrease of the resistivity anomaly during the cooling phase between 4 (A) and 9 (B) days of cooling. In the upper part of the model, an increase in resistivity due to a change of saturation in the unsaturated zone related to changing weather conditions (for the background, the soil was almost saturated due to strong precipitations) is also visible.

experiment.

However, when we look at the correspondence with temperature logs (figures 5.10B and C), we see that the results are much worse than in figure 5.8. Since electric conductivity seems to be correctly resolved, we assume that the discrepancy results from the transformation of electric conductivity to temperatures.

Figure 5.9A is taken 10 days after the beginning of injection. Some other phenomena may be responsible for a change in electric conductivity other than the temperature effect for mid- and long-term sections. These could be related to modifications of the TDS content related with different phenomena:

1. Assuming that formation water is in equilibrium with the sediments, injecting tap water will break this equilibrium. The specific electrical conductivity of injected tap water is likely to change during the experiment. This effect will be mostly visible in the well after the end of injection, which corresponds to the end of advection.

2. An effect of diffusion is also possible between formation water at the outer edge of the injected plume and the bell of injection water since a gradient of concentration exists.

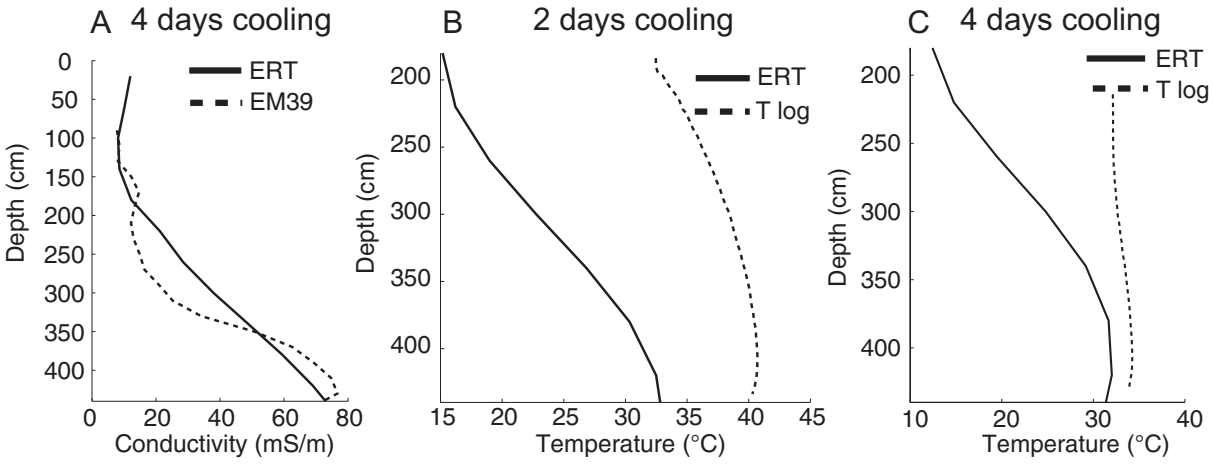

Figure 5.10: ERT measurements were validated using electromagnetic conductivity logs (A). In the zone of injection, ERT is really closed to EM39 data. Once transformed in temperatures, we observe a gap between ERT and temperatures logs after both 2 days (B) and 4 days of cooling (C). Since, this gap was not observed for the injection phase (figure 5.8), a more complex petrophysical relationship may be necessary to understand the phenomenon.

3. Physico-chemical processes are affected by temperature variations. The equations driving chemical processes are generally related to an equilibrium constant which is temperature dependent. A change in temperature may consequently induce precipitation/dissolution or adsorption/desorption processes.

5.3.6 Laboratory investigations

The physico-chemical aspects in the link between electrical resistivity and temperature were investigated during a laboratory experiment. Sand and water samples were collected on the Ghent site to reproduce a heat and storage experiment in a saturated soil column. The sand was first dried in a drying oven and its granulometry was assessed using a series of sieves (figure 5.11). The size-distribution curve is dominated by fine to very fine sands (between 100 μm and 400 μm). This justifies the value estimated for the surface conductivity of the fine sands. However, about 4% of the grain have a size smaller than 63 μm and could be clay particles. The sample was then homogenized to fill the measurement columns.

The column used for electrical resistivity monitoring has a diameter of 8 cm and a heigth of 30 cm. The current electrodes used for injection are connected to bronze porous plates in order to have a homogeneous current inside the column (parallel current lines). Potential electrodes are punctual copper electrodes. The spacing between potential electrodes is 10 cm

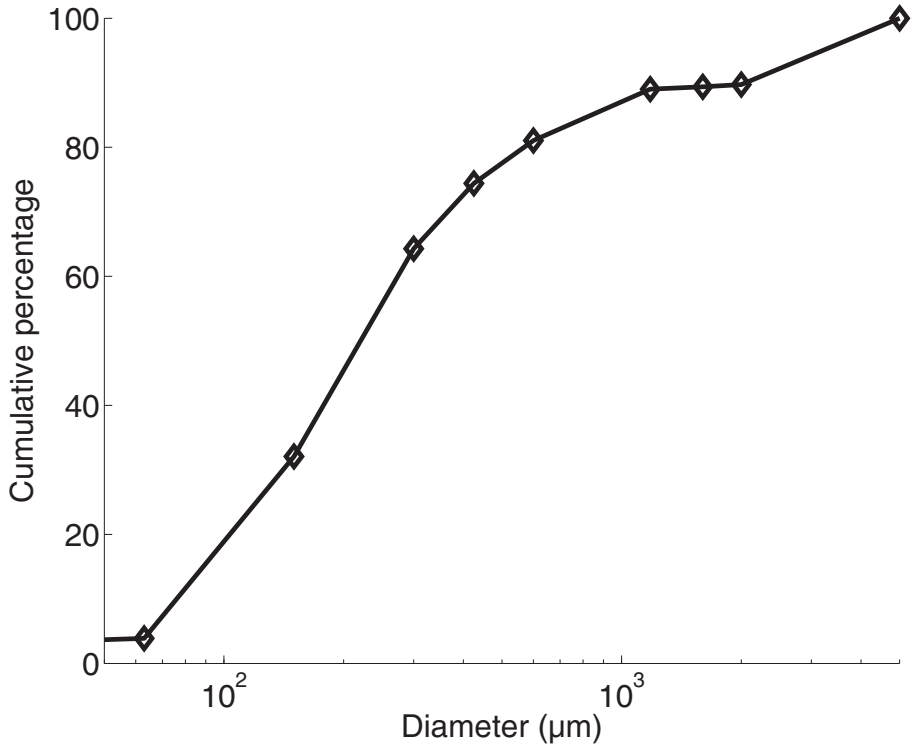

Figure 5.11: The cumulative size-sistribution curve of the Ghent size is dominated by particles between 100 μm and 400 μm.

and they are centered in the column so that the spacing with current electrodes is also 10 cm such as in a Wenner configuration. The column was calibrated using 3 $NaCl$ solutions of known resistivity at different concentration in order to derive the geometrical factor. The geometrical factor (equation 2.4) is the ratio between electrical resistivity and measured resistance. The geometrical factor was measured with a standard deviation of 0.0001 m.

A first sample was used to assess Archie's law in the presence of clay (equation 5.3). The sample was successively saturated with distilled water solution of increasing $NaCl$ concentrations. For very resistive water, most conductivity is related to surface conductivity. It is thus possible to estimate the surface conductivity of the sample. For more conductive water, the relative importance of surface conductivity decreases and it is possible to estimate the formation factor. We found a surface conductivity between 0.0018 and 0.0038 S/m. This is one order of magnitude above the estimation from the mean diameter of the grain, but it remains two orders of magnitude below the electrical conductivity of water. Neglecting surface conductivity is still a reasonable assumption. The estimated formation factor is comprised between 2.5 and 3.3, which is a reasonable value for sands.

Parameter	Before experiment	After experiment
Ca^{2+} (mg/l)	168	133
$HC0_3^-$ (mg/l)	371	192
Langelier index	0.6	0
σ_w $(\mu S/cm)$	1045	960

Table 5.2: Chemical analysis of water before and after the test.

The heating experiment consists in increasing the temperature of the column from $20°C$ (ambient temperature) to $64°C$. The latter temperature was maintained for a few hours before stopping the experiment. The experiment was performed on a column filled with formation water in equilibrium with the soil and a column whose formation water was replaced by tap water just before the heating experiment. A third column was used to monitor the temperature continuously.

What happens in the column with tap water is quite complex because several processes are superimposed. The resistivity decreases rapidly with an effect more important than expected from temperature only. Tap water becomes more conductive at the contact of the soil which was first saturated with formation water. This is confirmed by water sample analysis before and after the test, which shows a higher TDS content after the experiment.

The monitoring of the column with formation water also shows a decrease in resistivity with the increase of temperature (figure 5.12A). However, we would have expected that the resistivity stabilizes at its minimum when the temperature reaches the plateau, at about $64°C$. On the contrary, just before reaching the plateau, resistivity increases to stabilize at an intermediate level. This signifies that for a given resistivity, two ERT-derived temperatures are possible (figure 5.12B). The same behavior was also observed in the tap water column.

Figure 5.12 compares the observed behavior during the test and the expected behavior according to equation 5.10. Up to $30°C$, the decrease in resistivity is coherent with the proposed law. Then, the error becomes more and more important, the calculated resistivity is too low compared to the observed one. The reason for this behavior may lie in the decrease in solubility of calcium carbonates. Chemical analysis of formation water (table 5.2) shows that its saturation index before the experiment is greater than 0, the sample thus has a tendency to precipitate. Increasing the temperature will additionally favor the precipitation by reducing the solubility constant. However, the process of precipitation is also limited by the kinetics of the reaction.

At this point, we assumed that when temperature increases, the kinetics make the precipi-

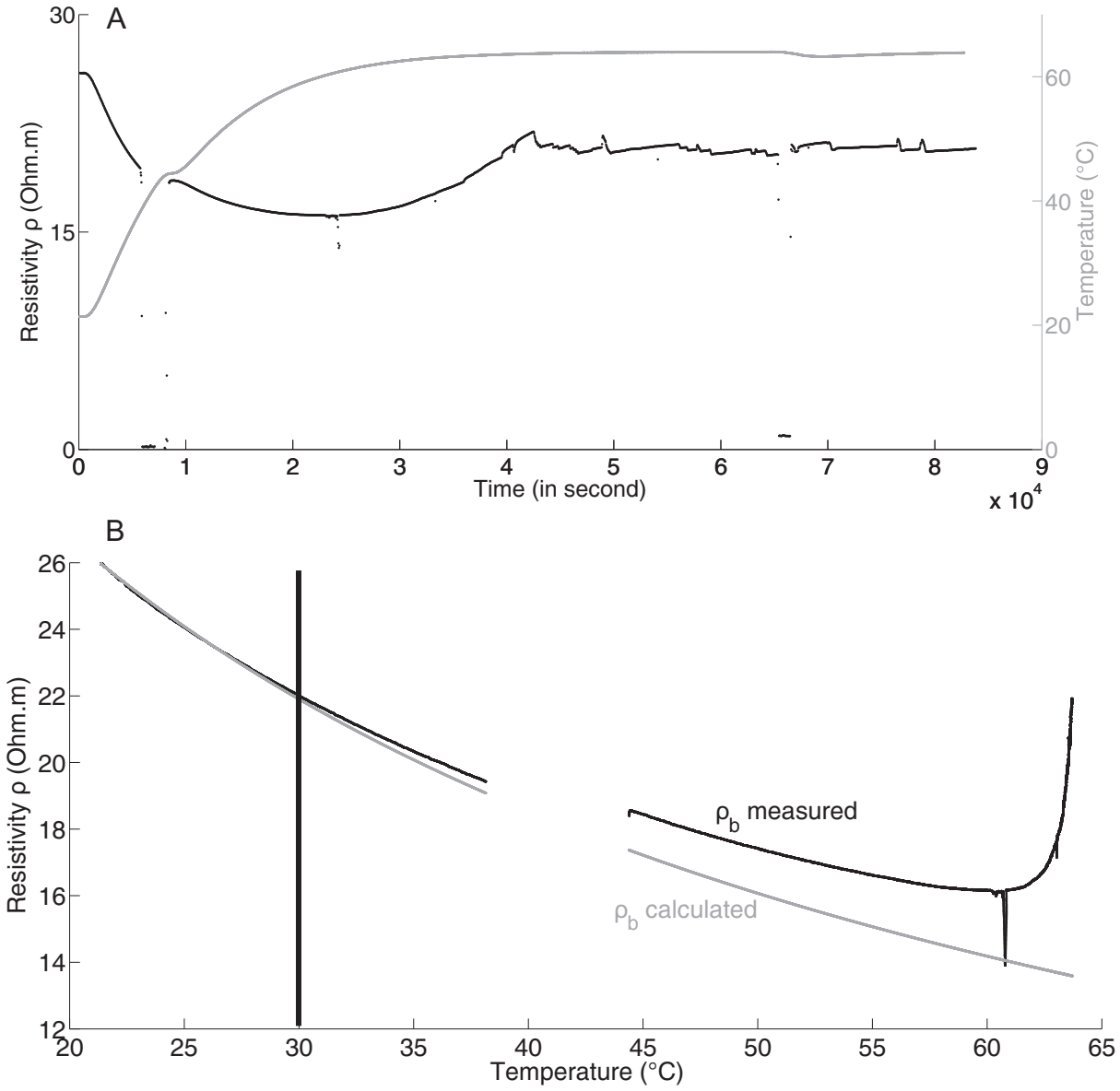

Figure 5.12: (A) The resistivity of the column first decreases as expected with temperature, but it reaches a minimum before the temperature plateau. (B) The calculated resistivity (equation 5.10) is not coherent with the measured resistivity due to chemical reactions in the sample.

tation of calcite possible. This phenomenon tends to reduce the total dissolved solid content of water, leading to a decrease of its specific electrical conductivity. Consequently, at a constant temperature, resistivity tends to increase as observed in figure 5.12A. Part of the increase in resistivity during the temperature plateau could be explained by desaturation at the top of the column. Water samples analysis confirms the reduction of carbonates in the water after the experiment (table 5.2). However, more tests are needed to fully understand and quantify what happens in the column. This requires to take kinetics and chemical equilibria into account.

5.4 Field Case 2 : Heat injection and pumping experiment

5.4.1 Field site and heating procedure

The study site is located on the site of Hermalle-sous-Argenteau (figure 2.21). It lies on the alluvial aquifer of the Meuse River. A pumping well and 8 piezometers were already present on the site since the 1980's and 11 new piezometers were drilled in June 2012 together with an injection well. They were arranged in three different panels crossing the main flow direction between the injection well and the pumping well in order to study the spatial variability during tracing experiments (Pz10 to 20, figure 5.13).

Previous investigations enabled to globally divide the deposits in four different units (see section 4.4). The first layer consists of loam and clay with a thickness between 1 and 1.5 m. The second layer is composed of gravel in a silty matrix. The bottom of this layer is found at depth between 2 and 3.2 m. These two first layers have little importance in this study because they are located in the unsaturated zone. The water table lies at approximately 3.2 m depth, with a small natural gradient towards the northeast which is the main direction of flow (figure 5.13). The third unit is composed of gravel and pebbles in a sandy matrix. The quantity of sand decreases with depth, whereas the size of the pebbles increases with depth. A vertical variability is thus expected. Lateral variability in the grain size distribution of the deposits is also expected in this heterogeneous aquifer, leading to variable hydrogeological parameters. Between 9.7 and 10.1 m, the Carboniferous bedrock composed of folded shales and sandstones is found. In the saturated zone, the grain size distribution is dominated by gravel with very few fine sediments. Surface conductivity (equation 5.3) was thus neglected given its low value for coarse grains (equation 5.4).

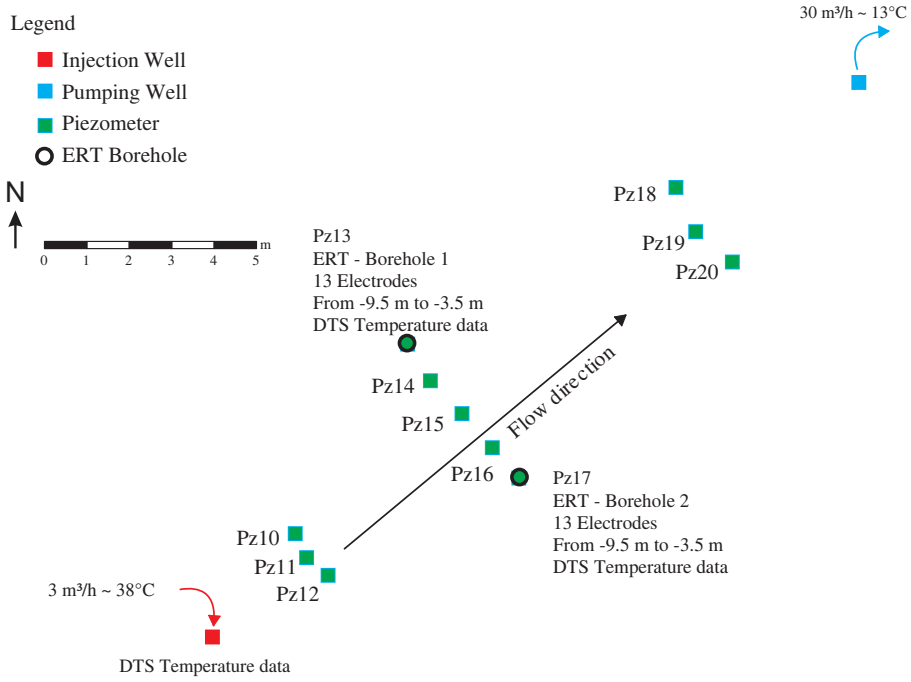

Figure 5.13: The new piezometers are arranged in three different panels crossing the expected flow direction between an injection and a pumping well. Pz 10-12, Pz 14-16 and Pz 18-20 are equipped with groundwater temperature loggers at two different levels. On the middle panel, the outer piezometers were equipped with a DTS system and with electrodes.

In the middle panel, the outer piezometers are screened on the whole thickness of the alluvial aquifer. This is also the case for the injection and pumping wells. Except for the latter, they were equipped with a distributed temperature sensing (DTS) system to monitor the temperature during the experiment (e.g. Leaf et al. 2012 and references therein) with a spatial resolution of 0.25 m. Pz14 and Pz16 were screened at two different levels, with a 2 m length screen between 4 and 6 m depth and a 1 m screen between 8.5 and 9.5 m. All other piezometers were screened at two different levels, with a 1 m screen between 4.5 and 5.5 m depth and a 2 m screen between 8 and 10 m depth. In the middle of each screened zone, a groundwater temperature logger was placed to monitor the temperature and the pressure during the whole experiment.

Previous studies have shown that the gravel aquifer is very permeable. Calibrated hydraulic conductivity values were found previously between 1.2×10^{-1} and 2×10^{-3} m/s (Dassargues 1997, Derouane and Dassargues 1998, Brouyère 2001). With such values, it is possible to inject at a rate much higher than in the test performed in Ghent which was limited by the low hydraulic conductivity of fine sands and the small thickness of the aquifer.

The experiment consists in an injection and pumping test. The groundwater is pumped from

the pumping well, located in the northeastern part of the site, downstream from the injection well. We used a pumping rate of 30 m^3/h. Given the high hydraulic conductivity values of the aquifer, the corresponding drawdown is only 5 cm in the pumping well and 4 cm in Pz19 (5 m upgradient from the well). The pumping process ensures that the main direction of flow will cross the three intermediate panels. Pumping was started one day before the beginning of the injection of heated water, to reach far in advance a steady-state flow, and continued after the end of injection.

We used a mobile water heater (AQUAMOBIL DH6 system) to heat the water injected in the aquifer. It can work at a maximum rate of 3 m^3/h with a difference in temperature of about 30°C. Given the high hydraulic conductivity of the aquifer, we decided to inject at this maximal rate. During the injection phase, 3 m^3/h of the pumped water were derived in a stocking tank, passed through the water heater and injected in the injection well. The mean temperature of the extracted water at the time of the experiment (October-November 2012) was 13°C. With the maximum injection rate, the temperature of the injected water reached a stabilized mean value of 38°C.

Injection started on October 30^{th} and lasted for 1 day, resulting in the injection of 72 m^3 of heated water. Using groundwater also for injection, the transformation of ERT results into temperatures will be direct and only require a unique petrophysical relationship (equation 5.10). However, the heterogeneity of the aquifer and the advection component make the experimental set-up more complex than in Ghent.

A water sample was taken on the site and relation 5.8 was verified experimentally in the laboratory (figure 5.14). Figure 5.14 shows the results up to 20°C (temperature encountered in the middle panel), but the trend remains the same until 40°C. Fitting a linear curve to the experimental points, we found $m_{f,25}$ equal to 0.0194 and the conductivity at the reference temperature (25°C) is equal to 0.0791 S/m. The value for the fractional change per degree Celsius is in the same range as observed by Hayley et al. (2007) and in the first field case.

5.4.2 ERT measurements

The two outer piezometers of the middle panel (Pz13 and Pz17 on figure 5.13) were equipped with borehole electrode cables with 0.5 m spacing. Each borehole has thus 13 electrodes made

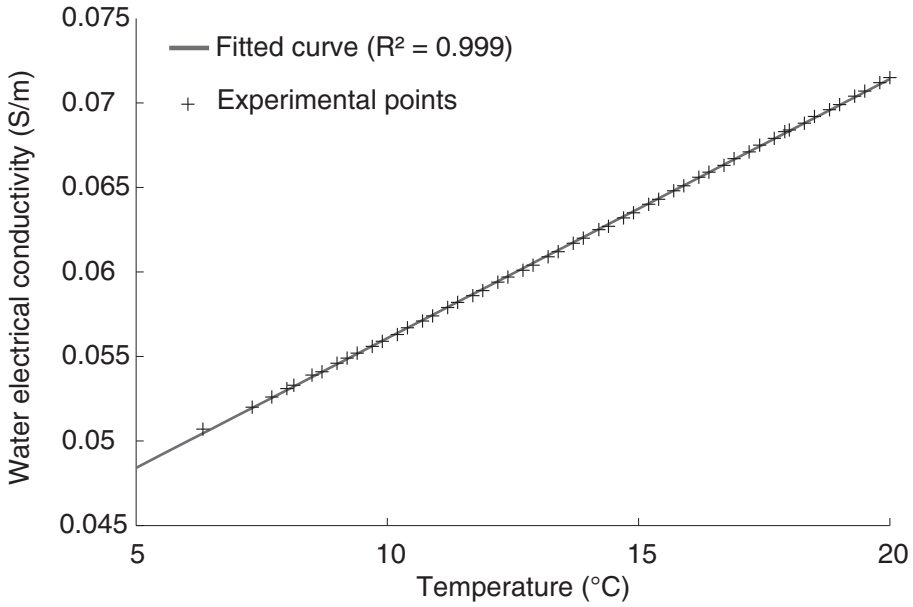

Figure 5.14: Water electrical conductivity increases linearly with temperature (points). Parameters of equation 5.8 were fitted with a fractional change per degree Celsius, m_f, equal to 0.0194 and the electrical conductivity at $25°C$ is 0.0791 S/m.

of stainless steel located from 3.5 to 9.5 m depth. The first electrode is located just below the water table whereas the last electrode is located just above the bedrock.

The two boreholes are separated horizontally by 4.5 m. The thickness covered by the electrodes is 6 m. The aspect ratio, i.e. the ratio of the separation between boreholes and the length of the equipped borehole is thus equal to 0.75. This value is often considered as the maximum acceptable value to obtain a sufficient resolution. Optimal resolution is generally achieved with an aspect ratio of 0.5 (LaBrecque et al. 1996b).

We used a combination of bipole-bipole (also called AM-BN) and dipole-dipole (AB-MN) configurations as measuring sequence. The first one has one injection electrode and one potential electrode in each well. Injection and potential bipoles are parallel to each other. This configuration has a better signal-to-noise ratio, but a lower resolution (Zhou and Greenhalgh 2000). The dipole-dipole has the two injection electrodes in the same borehole, and the two potential electrodes also in the same borehole. For bipole-bipole measurements, we measured every possible configuration. For the dipole-dipole, we only kept the cross-borehole measurements, using a dipole spacing ranging from 0.5 to 5 m and measuring dipoles sharing one electrode. The complete data set contains 969 possible measurements.

We used an ABEM Terrameter LS to acquire the data with an acquisition delay of 0.5 s

and an acquisition time of 1 s. We used a standard deviation limit of 1% on the repeatability error after 3 stacks to filter the data. For almost each time step, we collected both normal and reciprocal measurements to assess the error level on the data. Acquiring a complete data set took about 45 minutes (normal and reciprocal measurements).

The error level was estimated using both the methods of Slater et al. (2000) and Koestel et al. (2008). They both used the reciprocal error to derive a linear relationship between the mean measured resistance R_m and the absolute reciprocal error $e_{N/R}$. Slater et al. (2000) considered the envelope curve as error model, which can be considered as conservative, since the mean error is overestimated. Koestel et al. (2008) worked with standard deviation of logarithmic bins to determine the coefficients. This method may result in a mean error model, less conservative.

Nguyen et al. (2013) have shown that the noise level characterization is of great importance in time-lapse studies and should always be investigated carefully. If the noise levels are too different between time-steps, it may prevent a quantitative interpretation of monitoring data. If noise levels are almost similar, one should choose a common error model to invert all data sets. We calculated error models for both methods and each time-step. We chose a common error model with an absolute error of 0.002 Ohm and a relative error of 0.5%. We tested different error levels around these values, with few differences in the final images, both qualitatively and quantitatively.

The aim of cross-hole electrical resistivity was to detect the first arrival of the tracer and the maximum temperature reached in the middle panel and to image vertical and lateral variations in the temperature distribution. Data sets were collected about every six hours during the injection and the day after. For the next days, we increased the time-steps to about 18 h, with one or two sections per day. The total monitoring time was 6 days, time at which the resistivity distribution had almost returned to the background distribution. For comparison, a DTS system was set in both boreholes to control the temperature directly and assess the ability of ERT to derive reliable temperature results.

We used a grid with square elements of 0.25 m $\times$ 0.25 m in order to have two elements between electrodes, extended laterally and in depth for inversion. ERT-borehole 1 is located at abscissa 1 m and ERT-borehole 2 at abscissa 5.5 m on the grid.

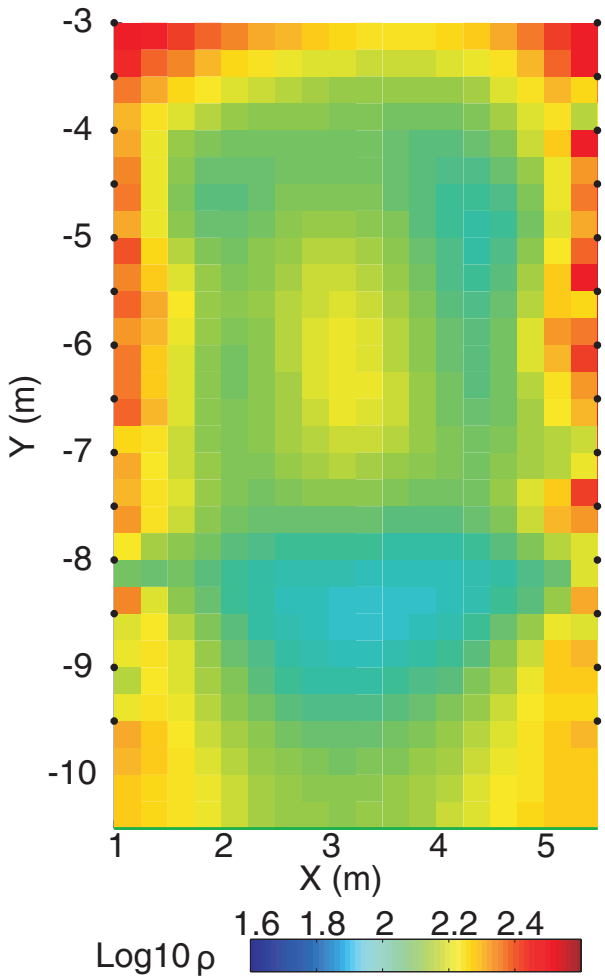

Figure 5.15: The background inverted section shows resistivity values varying between 100 and 200 $Ohm.m$. The panel is slightly heterogeneous.

5.4.3 Monitoring results

The background image was obtained using equation 2.17, corresponding to the smoothness-constrained solution (figure 5.15). In the zone between the boreholes, we see that the resistivity lies between 100 and 200 $Ohm.m$, with lower resistivities at the bottom of the section. These resistivity values are characteristic of saturated sand and gravel. The lower resistivity observed at the bottom of the aquifer may correspond with coarser gravel and a lower sand content, which is coherent with borehole logs (see chapter 4).

The sensitivity pattern is typical of cross-borehole measurements (figure 5.16). The sensitivity is high in the neighborhood of the boreholes and decreases towards the middle part of the section. The sensitivity is lower in two opposite triangles in the upper and bottom part of the saturated zone, due to a smaller coverage of data points in this zone. The lowest sensitivity

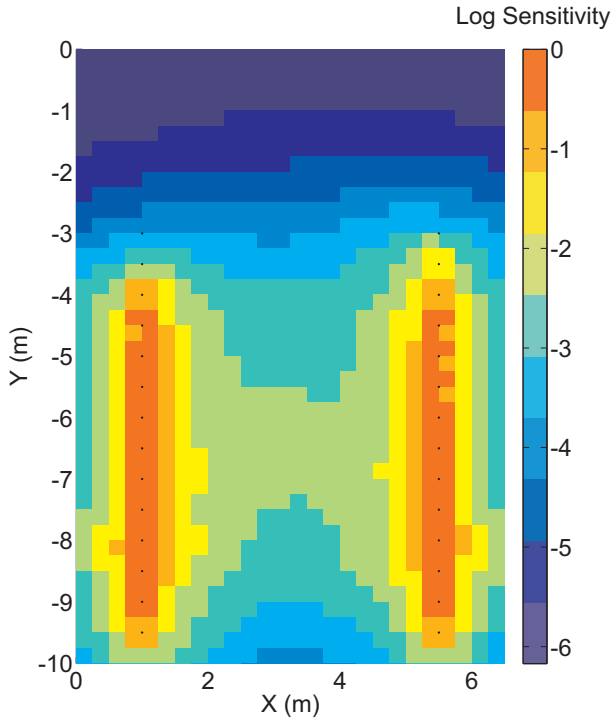

Figure 5.16: The sensitivity pattern is typical of cross-borehole measurements, with smaller sensitivity values in the middle part of the section, especially at the top and bottom of the model.

values are found in the unsaturated zone. The electrical contact through borehole electrodes was not possible because the borehole is not filled with water in this part; no surface electrodes were used to improve the resolution, because the aim is to image temperature changes in the saturated zone. Given the sensitivity values and the aspect ratio, we assume that the chosen configuration is sufficient to monitor temperature changes within the section.

Before looking at inverted data, it is important to qualitatively check if the acquired data contains some information about the monitored process. We calculated the mean resistance of each data set after removing points with repeatability error higher than 1% (870 points remaining). The mean resistance for the background data set is 14.31 Ohm. The first monitoring set was taken after 7 h of injection, the mean resistance slightly increases, but not significantly (figure 5.17). This is likely an effect of noise on the data. We can state that temperature changes are too small to influence the measured resistance. The same effect can be observed on individual measurements. The first arrival of tracer is detected after 12 h. The mean resistance then decreases with time to reach a minimum value of 13.76 Ohm (a decrease of about 4%) after 30 to 35 h after the beginning of injection, which corresponds to 6 to 11 h after the end

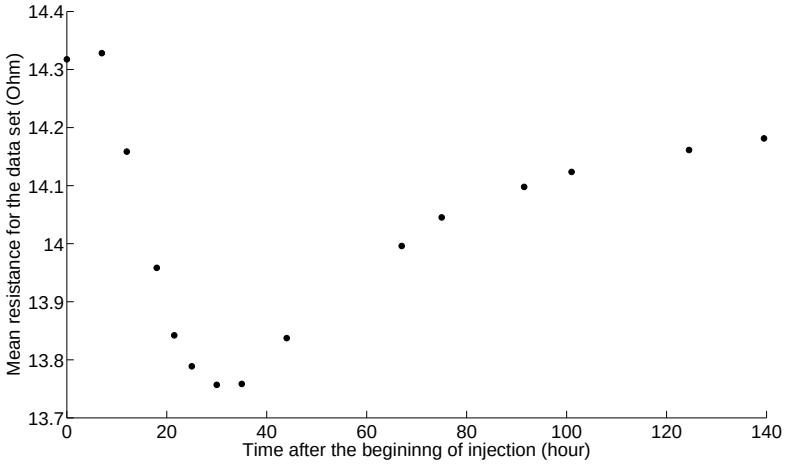

Figure 5.17: The mean resistance of the global data set first decreases with time as the plume of heated water approaches, it reaches a minimum after 30 to 35 h and then starts to increase slightly.

of injection. After the minimum, the mean resistance starts to increase and slightly tends to its initial state, even if it is not totally reached at the end of the monitoring process.

Figure 5.17 can be seen as a qualitative mean breakthrough curve of the heat tracing experiment. It enables to derive two important parameters: the first detected arrival of heat, which occurs between 7 and 12 h, and the maximum change, which occurs between 30 and 35 h. In this experiment, we did not achieve a better time resolution, but the material and methods used should allow achieving a time resolution of half an hour.

The time-lapse data sets were inverted using equation 5.11, i.e. the results of figure 5.15 are used as a reference and we inverted data differences to derive model perturbations. We kept the same error model for all inversions and we reached a value of ϵ_{RMS} equal to 1 for all inversions, ensuring that all models are fitted to the same level of noise.

Except for small variations due to propagation of data noise in the inverted section, only negative changes related to an increase in temperature are expected.

The inverted time-lapse sections (figure 5.18) show a general behavior of the plume similar to the one observed from the mean resistance. After 7 h (not shown), changes in resistance are low and under the level of noise, yielding a section with no changes, i.e. the background model is sufficient to explain the data. After 12 h, changes of resistivity about -5% appear. This level is considered to be the minimum level of changes that can be attributed to temperature. Indeed, small changes of resistivity may result of noise in the data and cannot be clearly correlated with

temperature. In the same way, increases in resistivity are not expected and are whitened on the figure. Increases above 5% are not observed, which seems to legitimate the limit of 5%. However, changes in the range 3 to 5% are only observed in the unsaturated zone, where the sensitivity is very low. The limit of 5% is thus a conservative limit that could be lowered to about 3%. Then, the decrease in resistivity becomes stronger and reaches a maximum between 25 and 35 h. Afterwards, the contrast becomes less strong and after 90 h, almost all changes are below 5%. It signifies that their level becomes too low to be interpreted quantitatively. However, their spatial distribution is coherent with previous time steps, so it could mean that the aquifer has not returned to its initial state yet, which is confirmed by the mean resistance.

The apparent decrease in resistivity observed in the 101 h section is likely due to an artifact of inversion since it is not physically plausible and does not appear in any other sections. The fact that all other anomalies observed in the sections are recurrent for all time steps and that their behavior follows the expected behavior of a tracer validate the results of inversion. If some anomalies were related to artifacts of inversion, they would be more randomly distributed for the different time-steps (except if caused by noise in the background section).

The advantage of crosshole ERT compared to direct measurements is to provide a spatial distribution of the changes occurring in the aquifer. Figure 5.18 clearly shows that the changes in resistivity are not homogeneously distributed in the aquifer. Most important changes are observed below -7.5 m depth. This part of the alluvial aquifer is dominated by very coarse gravel with pebbles and a limited amount of sandy matrix. The hydraulic conductivity of the bottom part is higher and the flux is greater, so a major part of the tracer is flowing in this zone of the aquifer. In the upper part, the flow is slower and the maximum change in temperature is much lower, below the minimum change that ERT could detect. Laterally, we also see variations that are not expected. The maximum change was expected to occur in the middle of the panel, along the supposed main flow direction. Here, we see that the maximum change is located closer to ERT-borehole 1. The resistivity changes are smaller in the middle part, whereas they are a little bit higher in the neighborhood of ERT-borehole 2.

The lateral variations observed in the ERT sections suggest a degree of heterogeneity that was not clearly distinguishable on borehole logs. Zones of preferential flows may modify the expected flow direction and result in sections showing a complex spatial behavior. In the next

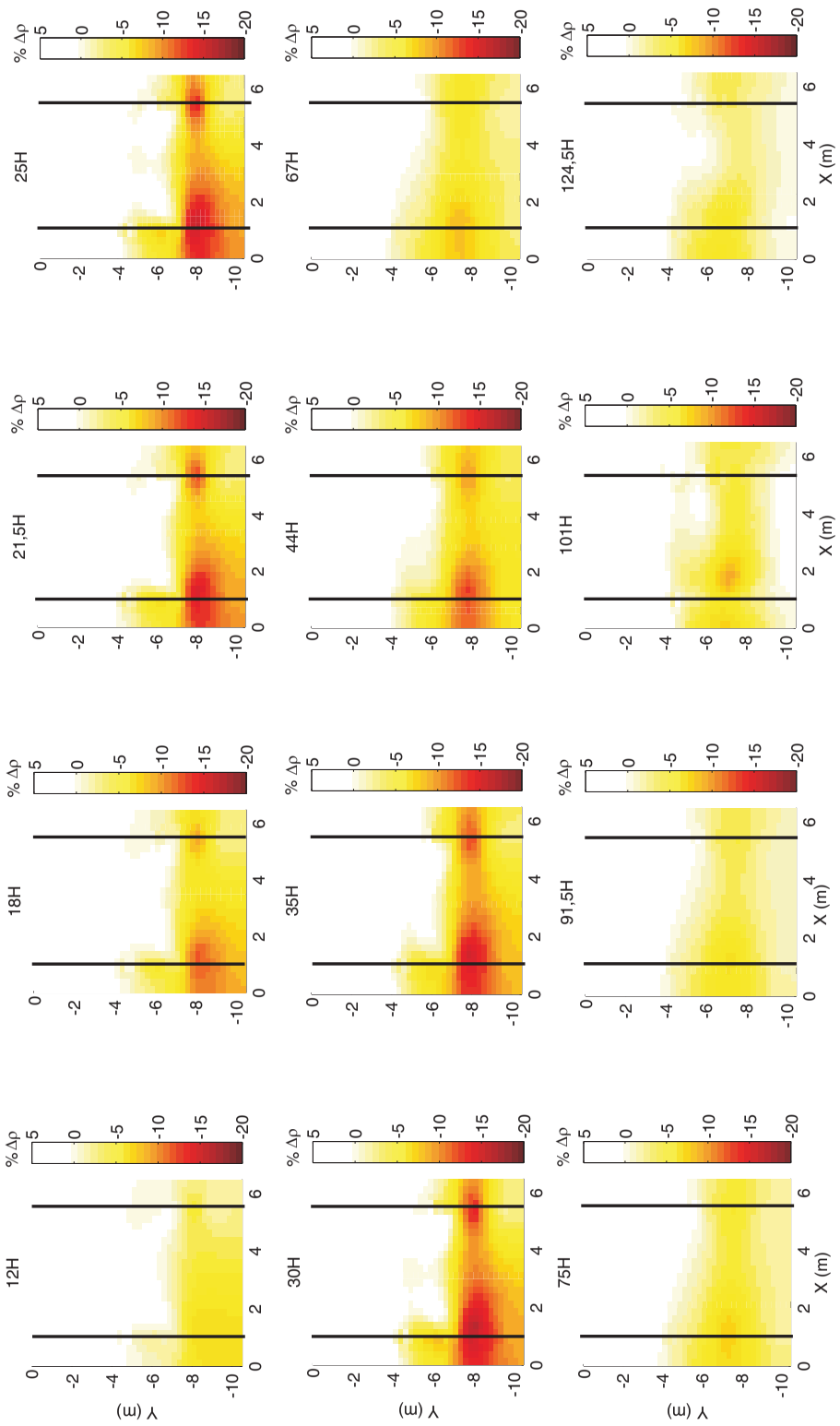

Figure 5.18: The inverted sections evolve in time with the arrival of the plume. Maximum changes are observed between 30 and 35 h in the surrounding of ERT borehole 1. These sections highlight the spatial heterogeneity of the aquifer. Time is given from the beginning of injection.

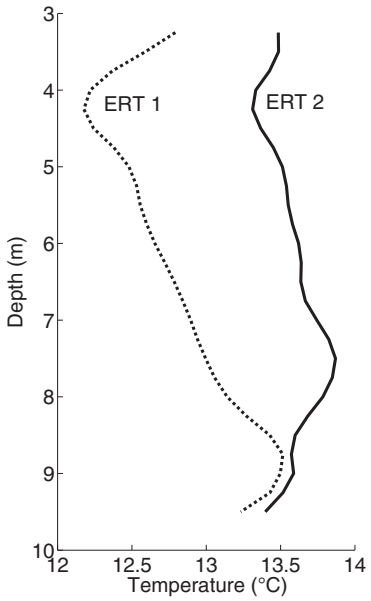

Figure 5.19: Temperature profiles in the two ERT boreholes are not similar. The temperature varies with depth and the mean temperature is different in the two boreholes: $12.8°C$ in ERT-borehole 1 and $13.6°C$ in ERT borehole-2.

section, we will see that these observations are confirmed by direct measurements in borehole.

5.4.4 Comparison with direct measurements

In the saturated zone, if we assume that all variations in electrical resistivity are related to temperature, it is possible to deduce the spatial distribution of temperature for each time step using equation 5.10. However, there remains an undetermined parameter in equation 5.10 which is the electrical conductivity of water for the background state σ_{f1}. Since we have derived a relation temperature/conductivity (equation 5.8) and that the temperature in the aquifer is known through direct measurements at borehole locations, this value can be deduced.

DTS measurements in borehole show that the temperature profile is not constant everywhere in the aquifer and in the ERT panel (figure 5.19). In ERT-borehole 1, a maximum temperature difference of $1.3°C$ is observed between the top and the bottom of the aquifer. It is slightly less in ERT-borehole 2. The mean temperature in the two boreholes is also different: $12.8°C$ in ERT-borehole 1 (Pz13) and $13.6°C$ in ERT-borehole 2 (Pz17).

For simplicity, we decided to use a unique value of σ_{f1} to transform the ERT images into temperature sections. We took the mean temperature of both ERT-boreholes ($13.2°C$) and derived with equation 5.8 a water electrical conductivity of 0.061 S/m. Another solution would

have been to interpolate temperatures between boreholes, but it would have made the process more complex without ensuring an improvement of the results. Doing so, we know that the ERT-derived temperature contained a mean error of $0.4°C$, but that the error may be up to $1°C$. Given that ERT is an indirect way of measurement for temperature, this value is still acceptable.

The spatial distribution of temperature (figure 5.20) is similar to electrical resistivity changes (figure 5.18). Maximum changes of temperature are observed in the neighborhood of ERT-borehole 1, with a maximum temperature of $21°C$, which corresponds to an increase of about $8°C$. However, we know that the background temperature in ERT-borehole 1 is slightly below the mean value chosen to draw these sections. Considering that the electrical resistivity variations below -3% are only indicative and that water electrical conductivity increases about $2\%/°C$, we may say that absolute temperature in the range $13 - 14.5°C$ are only indicative of a small raise in temperature, but that the exact value cannot be derived. In addition, we have a mean error interval of $\pm 0.4°C$ related to the mean water electrical conductivity used in equation 5.10.

The layout of the study site enabled to make a lot of direct measurements in piezometers, at different levels in the aquifer. To compare with ERT results, we have DTS measurements in ERT-boreholes 1 and 2, and groundwater temperature loggers at two levels in the three intermediate piezometers Pz14 to Pz16.

The quicker arrival of the tracer in the bottom part of the aquifer (figures 5.18 and 5.20) is confirmed in intermediate piezometers (figure 5.21 for Pz15). In the upper part, the arrival is very slow and a clear arrival of the tracer is only visible after 2 days. Note that the oscillations in the signal are disturbances due to dynamic sampling of water from the piezometer. The amplitude of the signal remains very small, below $1°C$ at the end of the test. Actually, the peak would only be observed after 10 days with an amplitude of about $1.15°C$. The same is observed in Pz16 ($1°C$ after 10 days). In Pz14, the change is slightly higher ($2°C$ after 4 days). In the bottom part, the arrival of the tracer is quicker, after a few hours, with a range of temperature above the limit of quantification of ERT. This is totally in agreement with the ERT sections. Spatially, the temperatures observed with ERT are also coherent with direct measurements. The temperatures observed in the bottom part of Pz14 to 16 have a trend of decrease from Pz14 to Pz16, which is also evident from ERT sections where the zone near ERT-borehole 1 is hotter

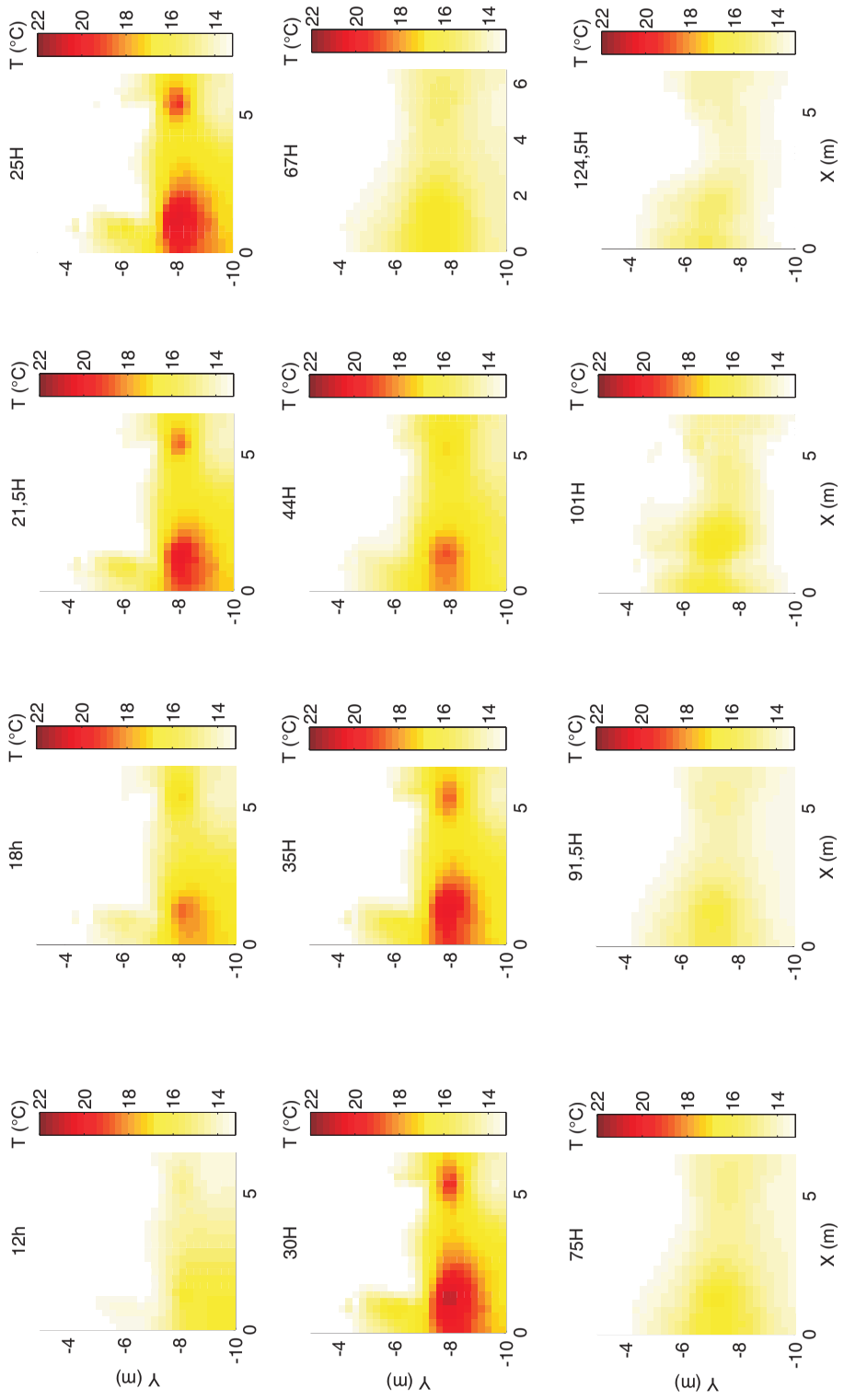

Figure 5.20: The ERT-derived temperature sections show that the maximum temperature reached in the panel is around $21°C$ in the neighborhood of ERT-borehole 1. The sections are limited to the saturated zone, because equation 5.10 is not valid in the unsaturated zone.

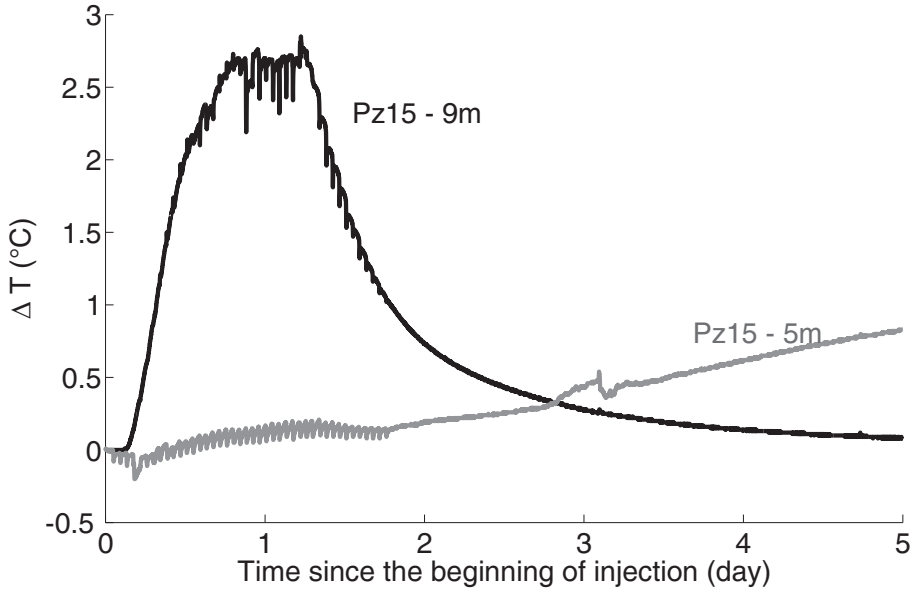

Figure 5.21: The temperature monitored at two different levels in Pz15 shows that the arrival of the tracers is much quicker and with much higher amplitude in the bottom part of the aquifer than in the upper part.

than the middle of the panel. As an example, the maximum ΔT in Pz14 is $4.2°C$, whereas it is only $2.9°C$ in Pz15. We can conclude that the qualitative observations on the spatial and temporal distribution of the heat tracer are confirmed by direct measurements.

To verify the ability of ERT measurements to quantify temperature, we rely on two different indicators. First, we can draw breakthrough curves at the location of groundwater temperature loggers to compare the direct measured curve with the ERT-derived curve. This will give insights on the ability to quantify temporally temperature changes. Secondly, we may compare temperature logs at ERT-borehole 1 and 2, to investigate quantitatively the spatial distribution of temperature.

Figure 5.22 shows the breakthrough curves in the bottom part of Pz14 (A) and Pz15 (B) for both direct measurements and ERT. We used the temperature measured in the corresponding boreholes to determine σ_{f1} in equation 5.10. For both piezometers, ERT does not detect directly that some tracer is arrived, because the changes are small, below the sensitivity of the method. However, the rising part of the curve is well resolved. The ERT-derived temperatures are almost equal to direct measurements. The maximum is overestimated, with an error of about $0.5°C$ in Pz14. The maximum change being $4°C$, it represents an error of about 12.5%. In Pz15, the fit is less good, but the maximum change is lower and the spatial smoothing of the inversion

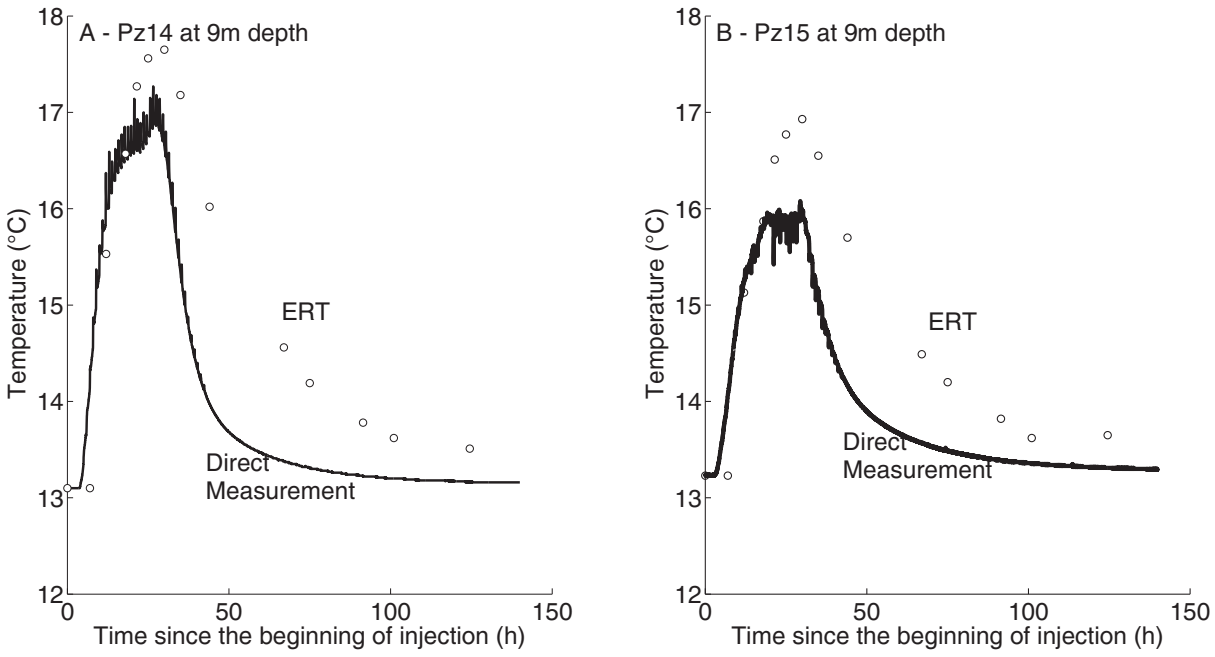

Figure 5.22: Breakthrough curves for ERT-derived temperatures and direct measurements in Pz14 (A) and Pz15 (B) show a good temporal agreement, but temperature are overestimated for the maximum and the tail of the curve.

process may yield an overestimation of the temperature. For both cases, the tail of the curve is overestimated by ERT-derived temperatures. This effect would lead to an overestimation of the dispersion parameters of the aquifer if ERT results were used alone. This could be related to a 3D effect (shadow effect), because the maximum of the plume, even if not in the panel anymore, is still influencing measurements. We must also keep in mind that the volume investigated by ERT and direct measurements is not the same. Groundwater temperature loggers give a very local measurement inside the piezometer which is itself a singularity inside the aquifer. ERT inversion results give a mean resistivity over the surface of the corresponding cell (here $0.25\ m \times 0.25\ m$).

Looking at the breakthrough curves of figure 5.22, it also appears that ERT is able to detect tiny changes in temperature between successive time steps. Indeed, even though the absolute deduced temperature may have an error of the order of $1°C$, the trends towards an increase or a decrease are always correctly assessed from time-lapse ERT, despite that changes in temperature are smaller than $0.5°C$.

Temporally, the results are very satisfactory because the raising part, the maximum and the tailing of the curve are imaged at correct times. In this specific case, the time resolution of ERT is only of a few hours, but given the material used, we could achieve a time resolution of half an

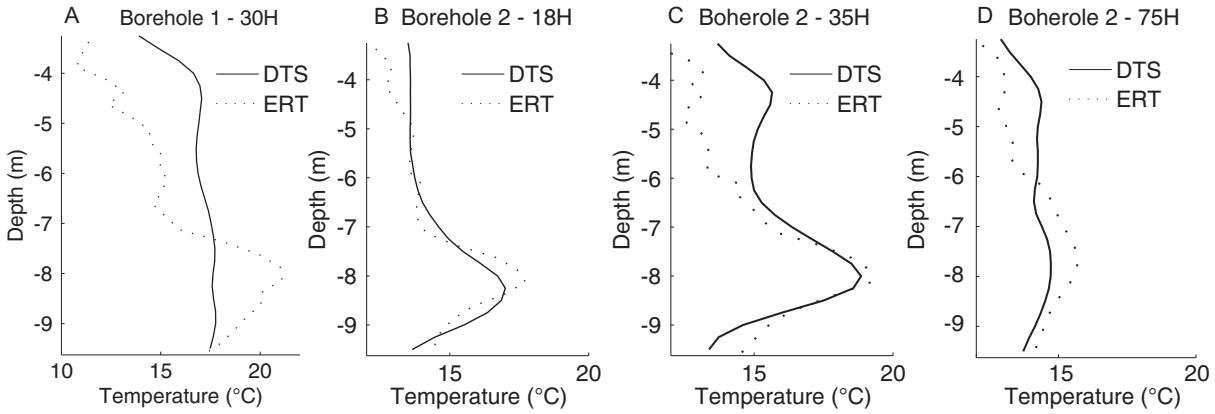

Figure 5.23: ERT-derived temperature profiles are not consistent with DTS measurements in ERT-borehole 1 (A), but show a very good agreement in ERT-borehole 2 (B, C and D). The almost constant temperature observed with DTS in ERT-borehole 1 may be due to some mixing of water in and around the well.

hour. It signifies, for example, that we cannot expect to detect the first arrival with precision.

The comparison of ERT-derived temperatures with DTS measurement in the two ERT-boreholes yields contrasted results and conclusions (figure 5.23). The temperatures measured with the DTS for the background profile were used to derive a specific value of σ_{f1} for each depth level. In addition, DTS measurements were averaged on the time interval corresponding to the duration of a complete ERT data acquisition. Consequently, the match would be perfect if we would derive temperatures for the background ERT profile using equation 5.10.

In ERT-borehole 1 (figure 5.23A), ERT results show the same behavior as observed in figure 5.20, with higher temperatures in the bottom part of the aquifer, and smaller in the upper part. In contrast, DTS measurements yield an almost constant temperature on the whole thickness of the aquifer. This is a quite surprising observation since all direct measurements made on the site have shown a clear contrast in tracer behavior between the bottom and upper parts of the aquifer. We thus doubt that DTS measurements in this borehole are reliable. A possible explanation is that the water in the well suffers from some mixing in and around the well. Multilevel well sampling remains challenging in geosciences. ERT measurements, even if influenced by the borehole fluid, are sensitive to the variations outside the borehole itself. This effect may also explain why temperature near ERT-borehole 1 seems to be higher in figure 5.20 in the upper part of the aquifer whereas it is not the case in the middle part of the section.

In ERT-borehole 2 (figure 5.23B, C and D), the agreement between ERT-derived temperatures and DTS logs is almost perfect in the bottom part, whereas ERT slightly underestimates

DTS temperatures in the upper part. It confirms that the hot spot observed near this borehole in figure 5.18 is not an artifact of inversion but is related to an increase in temperature. Globally, DTS measurements show slightly less contrast than ERT, maybe also due to some mixing in the well. Quantitatively, ERT-derived temperatures are close to DTS temperatures for the rising and maximum part of the breakthrough curve (figure 5.23B and C), but suffer from an overestimation for the tail (figure 5.23D), as it was observed in figure 5.22. Such an effect would be reduced in a storage experiment with conditions of no flow.

The good agreement of ERT results with direct measurements confirms that the alluvial aquifer is heterogeneous and complex. Instead of a unique plume of tracer in the middle part of the section, we observed two separated arrivals of the tracer with a minimum temperature observed in the middle.

5.5 Conclusion and perspectives

The growing demand for renewable energy leads to an increase in the development of geothermal energy projects. Heat has become a common energy storage system and a common tracer in hydrology and hydrogeology. The variation of electrical resistivity/conductivity of water, soils and rocks is a well-known phenomenon and has been studied for several decades. However, the potential of ERT, a method mapping the electrical resistivity of the subsurface, to monitor and quantify temperature was barely approached in the literature.

From our results, electrical resistivity tomography appears to be a reliable tool to image injection and storage of heated water and should therefore be further studied to complement thermal response tests.

First, we mapped the extent of a geothermal plume around a borehole, in unfavorable field conditions (varying surface conditions). Changes in resistivity can be interpreted qualitatively to follow the evolution of the plume of heated water in the subsurface and quantitatively to estimate the temperature change. At shallow depths, ERT was able to detect leakage in the bentonite seal and appears as a reliable tool to check in situ geothermal installations, their efficiency and possible heat losses.

Then, we investigated the ability of crosshole ERT to monitor a heat tracing experiment in a complex heterogeneous alluvial aquifer. The studied section was located along the main

direction of flow to cross the plume of heated water. The results highlight the ability of ERT to qualitatively monitor the variations of temperature in the aquifer. Spatially, it enabled to map the horizontal and vertical extent of the plume, as well as the zones of maximum temperatures, what would not be feasible with costly and limited direct measurements.

Laboratory measurements, site specific petrophysical relationships and direct measurements of temperature at some points in the aquifer enabled the quantitative interpretation of ERT results in terms of temperature in the aquifer. Such volumetric information, in contrast with temperature logs, could be of great importance to calibrate thermo-hydrogeological models which often rely on integrated and localized information to calibrate volumetric parameters.

In the second field case, the temperatures estimated from ERT were relatively close to the ones observed directly during the rise and maximum part of the curve. An overestimation, likely related to 3D effects, was observed for the tail of the breakthrough curve. The error can be estimated to be between 10 to 20%, which is a fair value for indirect measurements. The precision of the method may be better in more favorable cases, for example in no or low flow conditions. 3D imaging procedure using more than two wells should also improve the reliability of electrical resistivity monitoring results, yielding a better characterization of temperature distribution.

In the first specific case, the difference in conductivity between formation and injection waters limited the use of inferred temperatures directly in the thermo-hydrogeological model, even if they appear to be reliable. However, geophysics was used to conceptualize the source term of the thermo-hydrogeological model. At present, few techniques address the in-situ characterization of low enthalpy geothermal systems and a specific methodology could be developed including ERT and other geophysical methods sensitive to temperature changes. A method to correct ERT-derived temperatures is also proposed to account for the different electrical resistivity of injected water. This correction can be applied when it is not possible to inject formation water or in a methodology where heat tracing is combined to traditional solute tracing: solute tracers would be used to derive traditional transport parameters and to calculate the correction term, then the corrected temperatures would be used to derive heat flow and transport parameters.

The limit of quantification of temperature changes depends on the noise level observed on the site. ERT asks for an error assessment in order to avoid artifacts in the inverted sections. The higher the noise level, the lower the resolution of ERT to derive temperature changes. In the

second case, the experimental conditions enabled to estimate those parameters. After inversion, we observed positive changes of electrical resistivity up to 3% in the saturated zone. Those changes were not physically related to the tracing experiments and enabled us to estimate a limit of quantification for ERT around $1.5°C$ for temperature changes. However, breakthrough curves show that smaller temperature changes are imaged between successive time steps. The method seems sensitive to temperature changes below 0.5°.

A limitation of surface ERT is its loss of resolution with depth. We imaged correctly with surface ERT measurements a $35°C$ temperature change, corresponding to a decrease of 17% in bulk electrical resistivity, using an electrode spacing a of 0.75 m, a 2.5 m thick, 3 m width and 3 m deep heat water plume. We can generalize these features using non-dimensional numbers linked to the electrode spacing a: thickness of $3.33a$, width and depth of $4a$. These values can serve as guidelines for further studies and application to deeper reservoirs.

In contrast with surface ERT, the resolution of cross-hole ERT is not depth-dependent but depends mostly on the aspect ratio and the distance from the boreholes. The results obtained in this study could be easily extended to other experiments keeping the same aspect ratio. The resolution could even be refined using better aspect ratio or more electrodes. For larger experiments, it would require larger distances between electrodes and boreholes.

A limitation to quantify directly hydrogeological and heat transport parameters with ERT results seems to be the regularization method used to invert the data. It could be interesting to combine forward electrical modeling and hydrogeological modeling in a coupled-inversion scheme in order to avoid the regularization, and thus the smoothing. It is also interesting to develop new regularization operators for time-lapse inversions, based for example on the minimum-gradient support or geostatistical approaches.

For long-term storage experiment, careful attention must be paid to possible variations in the chemical composition of the water. When the injected water is not the formation water, a new equilibrium with the formation must be reached which will affect the specific conductivity of water. Diffusion effects are also possible.

Temperature variations in the aquifer will also modify chemical equilibria. As an example, an increase in temperature will reduce the solubility of calcite. A risk of precipitation exists when temperature increases what will modify the chemistry of water, but possibly also the petrophys-

ical relationship itself (through the formation factor, equation 5.1). In addition, an increase in temperature may accelerate the kinetics of reaction, which can be the main factor influencing carbonates precipitation. More laboratory experiments are needed to fully understand the relationship resistivity-temperature for long-term experiments when chemical reactions cannot be ignored.

The road ahead is to perform a more quantitative integration of our geophysical data and results in the thermo-hydrogeological modeling if modeling is performed, and to refine the geophysical imaging, if imaging is needed. As an example, ERT monitoring results could be used as an additional soft constraint in MPS simulations (see chapter 3) if the evolution of the electrical resistivity during monitoring is showed to be dependent on the facies distribution, through preferential flow paths. ERT-derived temperatures could also be integrated directly as dynamical data (see chapter 4) in the inversion of hydrogeological model with PPM (e.g. Castro 2007).

The results presented in this chapter suggest that ERT should be considered when designing heat tracing experiments to derive the parameters governing heat flow and transport in the subsurface or geothermal systems. It should also be used to assess the complexity of the concerned reservoirs. It also appears that ERT could be a useful tool to monitor and control geothermal systems once they are in operation. Our approach should contribute to the development of in-situ techniques in order to characterize groundwater and porous matrix properties governing heat transfer in the subsurface and to monitor shallow geothermal resources exploitation.

Chapter 6

General conclusions and perspectives

In this work, we have proposed and developed a methodology for the integration of near-surface geophysical, geological and hydrogeological data through multiple-point geostatistics. The method was demonstrated within the context of alluvial aquifers, both in a synthetic benchmark and in a field case, namely on the site of Hermalle-sous-Argenteau. The method can be divided in three main steps:

1. The definition of the parameters used for building aquifer models (in this case we chose the facies, based on a scale of hydraulic conductivity), the transposition of available geological data (i.e. borehole logs) into the chosen parameter and the creation of training image(s) representing the expected geological heterogeneity. This step consists to make the inventory of available data. This is the creation of the prior, which sums up the spatial constraints of the model and hard data (chapter 3).

2. The acquisition and inversion of geophysical data (in this case we chose electrical resistivity tomography) sensitive to the parameter of interest. The geophysical model must be compared to direct observations in order to derive the likelihood to observe the geophysical parameter given the studied parameter. This methodology enables to avoid the definition of a petrophysical relationship which assumes a deterministic link between geophysics and the modeled parameter. Here, a probabilistic relationship is assumed which is in accordance with the choice of a stochastic method for simulation. The likelihood contains the uncertainty related to geophysics which is an indirect method of observation (chapter 3). However, it was shown that it is possible to increase the informative content of geophysi-

cal inversions by including available prior information (i.e. information independent of the acquisition of ERT data) during the inversion process (chapter 2). Geophysical models may then be used as soft data in the multiple-point algorithm to reduce the uncertainty related to the prior.

3. The integration of dynamical hydrogeological data (in this case we used hydraulic heads) into models is done through an inversion method: the probability perturbation method. A model explaining hydrogeological data is iteratively obtained by perturbing the current model. The algorithm was implemented to use SNESIM geostatistical realizations as input models and HydroGeoSphere as forward water flow simulator. This ensures that the final model is consistent with every data concerned by the methodology (chapter 4).

What have been done in this study for alluvial aquifer may be extended for any type of reservoir as long as we are able to propose a reliable training image. Similarly, we demonstrate the method using ERT as geophysical data. Other geophysical methods may be used as well, the key point being to prove that the method is sensitive to the simulated parameter. Spectral-induced polarization for example has a great potential given its correlation with hydraulic conductivity (Kemna et al. 2012). However, its field application still needs further developments. It is also possible to integrate two or more different geophysical methods if they provide insights on the distribution of the parameter. Finally, we limited our investigations to the incorporation of "steady-state" hydrogeological data. The extension of the method to transient data is straightforward, it only requires to define an adapted objective function.

The inherent non-uniqueness of the solution of the geophysical inversion is a major concern in the domain. Several methodologies were developed in the last two decades to go beyond standard smoothness constraint inversion. In the literature, the proposed new methods were generally compared to the smoothness constraint method and the improvement demonstrated on a synthetic case only. In this work, we selected three different methods, easily implementable in inversion algorithms and compared them in three different field cases. This process shows us that it is almost impossible to find a perfect method of inversion given the large variety of geological contexts. However, it is possible to propose the method the most adapted to a given geological context. When sharp contrasts are expected and their position relatively well-known, it is possible to add the structure in the inversion in order to improve the reconstruction of

the geophysical parameter. In contrast, when the expected model is more diffuse, a covariance function to describe the spatial correlation is able to overcome the main drawback of standard Occam inversion: the extreme smoothness of the model. Even in poorly known sites, the simple addition of a reference model can yield largely improved results by adding information in low sensitivity zones of the model.

The analysis made in this work indicates that it is always worth to try to integrate prior information in the inversion. Especially, the regularized geostatistical inversions is well suited to replace the smoothness constrained inversion. Indeed, this constraint is applied on the whole section and influences the results in a similar way as the smoothness constraint. In all considered cases, it yields improvements of the results and in the worst cases results as good as the smoothness constraint. This philosophy at the scale of geophysical inversions is then reproduced at the scale of the hydrogeological model where the integration of various sources of information aids to reduce the uncertainty. As many methodologies as geophysicists may exist, but the important point is to encourage interpreters to take prior information into account at the step of inversion and not to consider only cooperative interpretation of the data.

Some existing methodologies could be combined to the ones selected in this thesis to further improve the results. For example, it could be interesting to weight the reference model according to the uncertainty of the estimates differently. Indeed, reference models are often based on borehole data and their uncertainty increases when we move away from the borehole location. Another improvement to the method would be to make the choice of the best solution on an objective basis. The choice most often relies on a visual inspection which may be user-dependent. Going towards more objectivity would strengthen the method.

We have also seen that the incorporation of prior information influences the poorly resolved or low-sensitivity zones mostly. Common image appraisal tools are used to select zones of the model that are interpretable or not. However, the use of prior information will improve the results of these zones without affecting the resolution or sensitivity patterns strongly. Image appraisal tools then become a way to describe where the prior information becomes more important than the data itself, and not a way to limit the interpretation anymore. These tools should then be adapted to integrate this observation.

In this work, we concentrate our efforts on the improvement of static images. However, the regularization of time-lapse images suffers from the same drawbacks, where changes of parameters are smoothed, which may not be representative of the actual process. As an example, transport in fractured or in preferential flow paths may be characterized by limited smoothing. It is thus needed to generalize the results obtained for the static inversions to the time-lapse inversions. It may be possible during a monitoring test to derive a time-dependent correlation length, based on borehole logs for example, and use it to constrain the difference inversion with a covariance matrix. Future research in time-lapse monitoring methods will probably include new regularization operators adapted for the incorporation of prior information.

In this project, we also propose a data base of training images to be used in the alluvial plain of the Meuse River. Training images used in this work remains relatively simple and general. This is related to the poor sedimentological knowledge of the alluvial deposits of the Meuse River. To get more precise and better defined training images, geological and sedimentological studies are needed.

The direct consequence of this observation is that the uncertainty related to training images is high. This is not a unique case. Indeed, in many contexts, two geologists will have a different interpretation of the geology and would provide different training images to the modeler. Deciding which training image is the most appropriate or quantify this uncertainty is difficult and very few studies have tackled this problem yet. We propose a methodology using available geophysical data to verify the consistency of the proposed training images and estimate the probability of the different scenarios. It requires to compare synthetic models from the training image with true models acquired on the field. These models are then mapped using multi-dimensional scaling based on their distance to each other. Synthetic models form a distribution. The assumption of the method is that if true model(s) fall(s) in this distribution, it proves the consistency of the training image. It is then possible to analyze the sensitivity of the parameters used to build the training images and even to assess the probability of each scenario.

This method being new, it still needs to be validated on various cases in different contexts and many developments are possible. First,the results are sensitive to the Euclidean distance, which is location dependent. This is a drawback of the method. However, it is possible to use another distance calculation and it would be interesting to investigate alternative distances and

see if others perform better to evaluate the consistency of training image. A possible direction of research is to borrow tools from image analysis. Another possibility is to take into account the sensitivity patterns of tomographic methods, which is spatially dependent, to weight differently well and poorly resolved parts of the section.

A current limitation of the method is that it was based on 2D sections whereas training images are 3D. The use of sections from all directions reduces the effect, but it would be more robust to generalize the methodology in 3D. The transposition is straightforward, but the limitation comes mainly from geophysics. Acquiring 3D data sets is costly and time-consuming and remains limited for field cases. Moreover, when available for a specific site, the 3D model is unique and may not be sufficient to derive average and robust conclusions.

The method used to transform geophysical models into probability maps is classic. It is based on the direct comparison between facies and geophysics in boreholes. However, the application for more than two facies within the context of multiple-point statistics using a potential geophysical method (ERT) is new. These methods suffer from double resolution dependence. First, the relation is dependent on the spacing between sensors, in this case between electrode. Secondly, the resolution pattern is also depth-dependent. In the future, it may be worth to investigate the improvement that would be brought by considering this decrease of resolution with depth. Soft data would be more informative near the surface, and its information would decrease with depth. This could be taken into account by an increasing standard deviations of the likelihood for deeper layers.

The direct comparison approach is simple and easy to implement. However, in some cases, more complex strategies may deliver better results. For example, Caers and Ma (2002) proposed a neural network approach to calculate the probability distribution.

The probability perturbation method, i.e. the hydrogeological inversion method that we proposed to use in this work, is perfectly suited to include hydrogeological data into our geostatistical models. Its philosophy with MPS contrasts with standard optimization methods which generally aim to optimize the value of the parameter given some zonation. Here, the algorithm will seek, from an initial model, the perturbation of the geometry of the deposits that will maximize the fitting with observed data, given a value of the parameter for each facies. The question could be, do we have a better knowledge of the geometry of the deposits or a better knowledge

of the order of magnitude of hydraulic conductivity? We have shown that the latter could be investigated through a simple sensitivity analysis. A major advantage of the PPM is to propose a geostatistical and stochastic framework to solve the problem. The posterior distribution will be investigated by generating several models all explaining the same data. Geological and geophysical data are integrated in the geostatistical framework to reduce the uncertainty of the prior model which will subsequently improve the prediction capacity of the models.

The methodology is of course well adapted for complex reservoir whose geological heterogeneity is difficult to catch with sparse direct observation and indirect geophysical data. The role of geophysics in the process was clearly illustrated. By the additional knowledge of the deposits that it brings, the sets of possible initial models are reduced (decreased uncertainty of the prior). This accelerates the convergence of the PPM algorithm, i.e. less iteration are required to reach the targeted objective function. Of course, this additional information is also reflected in the posterior distribution maps, where geophyiscs-derived probability maps aid to fill the gap between direct observations points. The effect is less clear than for deterministic methodologies (where the geophysical parameter would be directly used as an estimate of the hydrogeological parameter), but present.

Within the context of this work, we limited our application to a simple pumping test in steady-state conditions, on a site of limited extension. However, the method does not have any limitation on the size of the models or the complexity of the data to fit. Clearly, the method can be used to integrate transient pumping test data, or transport experiment data (such as tracer tests for example). We have shown that ERT is a reliable monitoring tool to follow heat injection and tracing experiments. Two field experiments have proved that both surface and borehole ERT were efficient to qualitatively image the zones the most affected by temperature variations during heat injection experiments. It enabled in one case to detect a defect in the injecting well, and in the other case to highlight preferential flow paths in the alluvial aquifer. The use of laboratory calibrated petrophysical relationships, rigorously verified simplifying assumptions as well as a few direct measurements allow to transform resistivity changes into quantitative temperature estimates. This makes ERT an available spatio-temporal tool for the monitoring of heat injection experiments, heat tracing tests and geothermal systems. ERT should thus be integrated in the calibration of models during the designing phase of geothermal installations and during their

exploitation. For long-term application, laboratory investigations will be needed to understand the complex behavior of geological systems regarding temperature changes. This must include physical-chemical reactions as well as kinetics of reaction. This should allow to better understand the link between electrical resistivity and temperature and improve quantitative estimates from ERT.

The integration of transient data sets should further aid to reduce the uncertainty about the geometry of the deposits, by revealing preferential flow paths more sharply than pumping tests. This only requires to run the forward simulator in transient conditions and to adapt the objective function. The combination of geophysical monitoring results and thermo-hydrogeological model is possible through history matching methodologies like PPM and a further research development would be to integrate spatio-temporal geophysical data within the framework developed in this work as it is done for 4D seismic survey (e.g. Castro 2007).

Similarly, the proposed methodology can be applied for the site-specific scale, to the local, regional or basin scale. Only the training image should be adapted to correspond to the scale of the problem. The method could also be combined to upscaling and downscaling approaches to deal with scaling issues. However, the application of the whole methodology for large scale studies may be limited by the acquisition of geophysical data at a large scale. For local model, it is possible to acquire relatively high-resolution geophysical data on the entire site. This would become difficult for large scale, considering time, cost and logistic constraints. However, it remains possible to acquire lower resolution data as long as it is informative for the parameter of interests. As an example, for regional or basin scale studies, the use of airborne geophysics is able to provide a dense spatial distribution of geophysical parameters to constrain models. It is also possible to focus geophysical acquisition on a limited part of the model where the reduction of uncertainty is more crucial or to develop multiple scale approaches where geophysical data would be integrate at the scale at which its resolution is relevant.

Bibliography

Allen, A. and D. Milenic (2003). Low-enthalpy geothermal energy resources from groundwater in fluvioglacial gravels of buried valleys. *Applied Energy 74*, 9–19.

Alumbaugh, D. and G. Newmann (2000). Image appraisal for 2-D and 3-D electromagnetic inversion. *Geophysics 65*, 1455–1467.

Anderson, M. (2005). Heat as a ground water tracer. *Ground Water 43*, 951–968.

Anderson, M. and W. Woessner (1992). *Applied groundwater modeling. Simulation of flow and advective transport*. Elsevier Academic Press, San Diego.

Arango-Galvàn, C., R. Prol-Ledesma, E. Flores-Màrquez, C. Canet, and R. V. Estrada (2011). Shallow submarine and subaerial, low-enthalpy hydrothermal manifestations on Punta Banda, Baja California, Mexico: geophysical and geochemical characterization. *Geothermics 40*, 102–111.

Archie, G. (1942). The electrical resistivity log as an aid in determining some reservoir characteristics. *Transactions AIME 146*, 54–62.

Arpat, G. and J. Caers (2007). Conditional simulation with patterns. *Mathematical Geology 39*(2), 177–203.

Aster, R., B. Borchers, and C. Thurber (2005). *Parameter estimation and inverse problems*. Elsevier Academic Press, Amsterdam.

Atekwana, E., W. Sauck, and D. Werkema (2000). Investigations of geoelectrical signatures at a hydrocarbon contaminated site. *Journal of Applied Geophysics 44*, 167–180.

Auken, E. and A. V. Christiansen (2004). Layered and laterally constrained 2D inversion of resistivity data. *Geophysics 69*(3), 752–761.

Barker, R. and J. Moore (1998). The application of time-lapse electrical tomography in groundwater studies. *The Leading Edge 17*, 1454–1458.

Battle-Aguilar, J. (2008). *Groundwater flow and contaminant transport in an alluvial aquifer: in-situ investigation and modelling of a brownfield with strong groundwater - surface interactions*. Ph. D. thesis, University of Liege, Faculty of Applied Sciences.

Bayer, P., P. Huggenberger, P. Renard, and A. Comunian (2011). Three-dimensional high resolution fluvio-glacial aquifer analog: Part 1: Field study. *Journal of Hydrology 405*, 1–9.

Bélanger, C., B. Giroux, E. Gloaguen, and R. Lefebvre (2010). GPR, ERT and CPT data integration for high resolution aquifer modeling. In *13th International Conference on Ground Penetrating Radar*.

Benderitter, Y. and J. Tabbagh (1982). Heat storage in a shallow confined aquifer: geophysical tests to detect the resulting anomaly and its evolution with time. *Journal of Hydrology 56*, 85–98.

Bentley, L. and M. Gharibi (2004). Two- and three-dimensional electrical resistivity imaging at a heterogeneous remediation site. *Geophysics 69*, 674–680.

Berendsen, H. (2007). Fluvial system. Utrecht University. `http://www.geo.uu.nl/fg/palaeogeography/results/fluvialstyle`.

Berendsen, H. and E. Stouthamer (2001). *Paleogeographic development of the Rhine-Meuse delta, The Netherlands*. Assen, Van Gorcum.

Bersezio, R., M. Giudici, and M. Mele (2007). Combining sedimentological and geophysical data for high-resolution 3D mapping of fluvial architectural elements in the Quaternary Po plain (Italy). *Sedimentary Geology 202*, 230–248.

Binley, A., P. Winship, L. West, M. Pokar, and R. Middleton (2002). Seasonal variation of moisture content in unsaturated sandstone inferred from borehole radar and resistivity profiles. *Journal of Hydrology 267*, 160–172.

Blakely, R. (1995). *Potential theory in gravity and magnetic applications*. Cambridge University Press, Cambridge.

Blaschek, R., A. Hördt, and A. Kemna (2008). A new sensitivity-controlled focusing regularization scheme for the inversion of induced polarization data based on the minimum gradient support. *Geophysics 73*(2), F45–F54.

Blouin, M., R. Martel, and E. Gloaguen (2012). Accounting for aquifer heterogeneity from geological data to management tools. *Ground Water 51*(3), 421–431.

Bolève, A., A. Crespy, A. Revil, F. Janod, and J. Mattiuzzo (2007). Streaming potentials of granular media: Influence of the Duhkin and Reynolds numbers. *Journal of Geophysical Research 112*, B08204.

Borg, I. and P. Groenen (2005). *Modern multidimensional scaling - Theory and applications* (2nd ed.). Springer Series in Statistics. Springer, New York.

Bouchedda, A., M. Chouteau, A. Binley, and B. Giroux (2012). 2-D joint structural inversion of cross-hole electrical resistance and ground penetrating radar data. *Journal of Applied Geophysics 78*, 52–67.

Bowling, J., D. Harry, A. Rodriguez, and C. Zheng (2007). Integrated geophysical and geological investigation of a heterogeneous fluvial aquifer in Colombus Mississippi. *Journal of Applied Geophysics 62*, 58–73.

Bowling, J., A. Rodriguez, D. Harry, and C. Zheng (2005). Delineating alluvial aquifer heterogeneity using resistivity and GPR data. *Ground Water 43*(6), 890–903.

Bridge, J. (2003). *Rivers and floodplains. Forms, processes and sedimentary record*. Oxford Blackwell Publishing.

Brielmann, H., C. Griebler, S. Schmidt, R. Michel, and T. Lueders (2009). Effects of thermal energy discharge on shallow groundwater ecosystems. *FEMS Microbiology Ecology 68*, 273–286.

Brouyère, S. (2001). *Etude et modélisation du transport et du piégeage des solutés en milieu souterrain variablement saturé*. Ph. D. thesis, University of Liege, Faculty of Applied Sciences.

Bruno, P., V. Paoletti, M. Grimaldi, and A. Rapolla (2000). Geophysical exploration for geothermal low enthalpy resources in Lipari island, Italy. *Journal of Volcanology and Geothermal Research 98*, 173–188.

Busby, J., M. Lewis, H. Reeves, and R. Lawley (2009). Initial geological considerations before installing ground source heat pump systems. *Quaternaly Journal of Engineering Geology and Hydrogeology 42*, 295–306.

Butler, J. (1998). *The design, performance, and analysis of slug tests.* Lewis Publishers, New York.

Caers, J. (2001). Geostatistical reservoir modeling using statistical pattern recognition. *Journal of Petroleum Science and Engineering 29*, 177–188.

Caers, J. (2003). History matching under training-image based geological model constraints. *Society of Petroleum Engineers Journal 8*(3), 218–226.

Caers, J. (2007). Comparing the probability perturbation method with the gradual deformation method. *Mathematical Geology 39*(1), 27–52.

Caers, J. (2011). *Modeling Uncertainty in the Earth Sciences.* Wiley-Blackwell, Chichester, UK.

Caers, J. and T. Hoffman (2006). The probability perturbation method: a new look at bayesian inverse modeling. *Mathematical Geology 38*(1), 81–100.

Caers, J. and X. Ma (2002). Modeling conditional distributions of facies from seismic using neural nets. *Mathematical Geology 34*(2), 143–167.

Calembert, L. (1968). Constitution de la plaine alluviale de la meuse en aval de Liège, à Herstal, Jupille, Wandre, Cheratte et Vivegnis. Technical report, Service Géologique de Belgique.

Cardarelli, E. and F. Fischanger (2006). 2D data modelling by electrical resistivity tomography for complex subsurface geology. *Geophysical Prospecting 54*(2), 121–133.

Carrera, J., A. Alcolea, A. Medina, J. Hidalgo, and L. Slooten (2005). Inverse problem in hydrogeology. *Hydrogeology Journal 13*, 206–222.

Carrera, J. and S. Neuman (1986a). Estimation of aquifer parameters under transient and steady state conditions: 1. Maximum likelihood method incorporating prior information. *Water Resources Research 22*(2), 199–210.

Carrera, J. and S. Neuman (1986b). Estimation of aquifer parameters under transient and steady state conditions: 2. Uniqueness, stability, and solution algorithms. *Water Resources Research 22*(2), 211–227.

Cassiani, G., G. Böhm, A. Vesnaver, and R. Nicolich (1998). A geostatistical framework for incorporating seismic tomography auxiliary data into hydraulic conductivity estimation. *Journal of Hydrology 206*(1), 58–74.

Castro, S. (2007). *A probabilistic approach to jointly integrate 3D/4D seismic, production data and geological information for building reservoir models*. Ph. D. thesis, Stanford University.

Caterina, D., J. Beaujean, T. Robert, and F. Nguyen (2013). A comparison study of image appraisal tools for electrical resistivity tomography. *Near Surface Geophysics 11*, 639–657.

CEEW (2007). Rapport analytique sur l'état de l'environnement wallon 2006-2007. Cellule Etat de l'Environnement Wallon, Ministère de la Région wallonne - DGRNE, Namur. `http://etat.environnement.wallonie.be/index.php?page=le-rapport-analytique-2006-2007`.

Chasseriau, P. and M. Chouteau (2003). 3D gravity inversion using a model of parameter covariance. *Journal of Applied Geophysics 52*, 59–74.

Comunian, A., P. Renard, J. Straubhaar, and P. Bayer (2011). Three-dimensional high resolution fluvio-glacial aquifer analog - part 2: Geostatistical modeling. *Journal of Hydrology 405*, 10–23.

Constable, S., R. Parker, and C. Constable (1987). Occam's inversion: a practical algorithm for generating smooth models from electromagnetic sounding data. *Geophysics 52*(3), 289–300.

Corwin, D. and S. Lesch (2005). Apparent soil electrical conductivity measurements in agriculture. *Computers and Electronics in Agriculture 46*, 11–43.

Coz, M., P. Genthon, and P. Adler (2011). Multiple-point statistics for modeling facies heterogeneities in a porous medium: The Komadugu-Yobe alluvium, lake Chad basin. *Mathematical Geosciences 43*(7), 861–878.

Dafflon, B., J. Irving, and K. Holliger (2009). Simulated-annealing-based conditional simulation for the local-scale characterization of heterogeneous aquifer. *Journal of Applied Geophysics 68*(1), 60–70.

Dahlin, T. and B. Zhou (2004). A numerical comparison of 2D resistivity imaging with ten electrode arrays. *Geophysical Prospecting 52*, 379–398.

Daoudi, M. (2011). Geophysical monitoring of a thermal response test. Master's thesis, University of Liege, Faculty of Applied Sciences.

Dassargues, A. (1997). Modeling baseflow from an alluvial aquifer using hydraulic conductivity data obtained from a derived relation with apparent electrical resistivity. *Hydrogeology Journal 5*, 97–108.

Davis, R. (1983). *Depositional systems: a genetic approach to sedimentary geology*. Prentice hall Inc., Englewood Cliffs, New Jersey.

Day-Lewis, F. D. and J. Lane (2004). Assessing the resolution-dependent utility of tomograms for geostatistics. *Geophysical Research Letters 31*, L07503.

de Groot-Hedlin, C. and S. Constable (1990). Occam's inversion to generate smooth, two dimensional models from magnetotelluric data. *Geophysics 55*, 1613–1624.

de Groot-Hedlin, C. and S. Constable (2004). Inversion of magnetotelluric data for 2D structure with sharp resistivity contrasts. *Geophysics 69*(1), 78–86.

de Marsily, G., G. Lavedan, M. Boucher, and G. Fasanino (1984). Interpretation of interference tests in a well field using geostatistical techniques to fit the permeability distribution in a reservoir model. In G. Verly, M. David, A. Journel, and A. Marechal (Eds.), *Proceedings of Geostatistics for Natural Resources Characterization*, pp. 831–849. D. Reidel Pub. Co.

de Paly, M., J. Hecht-Méndez, M. Beck, P. Blum, A. Zell, and P. Bayer (2012). Optimization of energy extraction for closed shallow geothermal systems using linear programming. *Geothermics 43*, 57–65.

dell'Arciprete, D., R. Bersezio, F. Felletti, M. Giudici, A. Comunian, and P. Renard (2012). Comparison of three geostatistical methods for hydrofacies simulation: a test on alluvial sediments. *Hydrogeology Journal 20*, 299–311.

Derouane, J. and A. Dassargues (1998). Delineation of groundwater protection zones based on tracer tests and transport modelling in alluvial sediments. *Environmental Geology 36*(1-2), 27–36.

Deutsch, C. (2002). *Geostatistical reservoir modeling*. Oxford University Press, New York.

Doetsch, J., I. Coscia, S. Greenhalgh, N. Linde, A. Green, and T. Günther (2010a). The borehole-fluid effect in electrical resistivity imaging. *Geophysics 75*(4), F107–F114.

Doetsch, J., N. Linde, I. Coscia, S. Greenhalgh, and A. Green (2010b). Zonation for 3D aquifer characterization based on joint inversions of multimethod crosshole geophysical data. *Geophysics 75*(6), G53–G64.

Doetsch, J., N. Linde, M. Pessognelli, A. Green, and T. Günther (2012). Constraining 3-D electrical resistance tomography with GPR reflection data for improved aquifer characterization. *Journal of Applied Geophysics 78*, 68–76.

Doherty, J. (2003). Ground water model calibration using pilot points and regularization. *Ground Water 41*(2), 170–177.

Doherty, J. (2004). *PEST: Model-independent parameter estimation, user manual, version 5*. Brisbane, Australia: Watermark Numerical Computing.

Dubreuil-Boisclair, C., E. Gloaguen, D. Marcotte, and B. Giroux (2011). Heterogeneous aquifer characterization from ground-penetrating radar tomography and borehole hydrogeophysical data using nonlinear bayesian simulations. *Geophysics 76*(4), J13–J25.

Eidsvik, J., O. Henning, T. Mukerji, G. Mavko, P. Avseth, and N. Hydro (2002). Seismic

reservoir prediction using bayesian integration of rock physics and markov random fields: A north sea example. *The Leading Edge 21*(3), 290–294.

Elwaseif, M. and L. Slater (2010). Quantifying tomb geometries in resistivity images using watershed algorithms. *Journal of Archaeological Science 37*(7), 1424–1436.

Engdahl, N., G. Weissmann, and N. Bonal (2010). An integrated approach to shallow aquifer characterization: combining geophysics and geostatistics. *Computer and Geosciences 14*(2), 217–229.

European Environment Agency (2010). The european environment - state and outlook 2010. European Environment Agency. `http://www.eea.europa.eu/soer`.

Ezzedine, S., Y. Rubin, and J. Chen (1999). Bayesian method for hydrogeological site characterization using borehole and geophysical survey data: Theory and application to the Lawrence Livermore National Superfund site. *Water Resources Research 35*(9), 2671–2683.

Farquharson, C. and D. Oldenburg (1998). Nonlinear inversion using measures of data misfit and model structure. *Geophysical Journal International 134*, 213–227.

Feyen, L. and J. Caers (2006). Quantifying geological uncertainty for flow and transport modeling in multi-modal heterogeneous formations. *Advances in Water Resources 29*, 912–929.

Gallardo, L. and M. Meju (2003). Characterization of heterogeneous near-surface materials by joint 2D inversion of DC resistivity and seismic data. *Geophysical Research Letters 30*(13), 1658–1661.

Garambois, S., P. Sénéchal, and H. Perroud (2002). On the use of combined geophysical methods to assess water content and water conductivity of near-surface formations. *Journal of Hydrology 259*, 32–48.

Garg, S., J. Pritchett, P. Wannamaker, and J. Combs (2007). Characterization of geothermal reservoirs with electrical surveys: Beowave geothermal fields. *Geothermics 36*, 487–517.

Geosciences Australia (2013). Groundwater in australia: alluvial aquifers. Australian Government. `http://www.ga.gov.au/groundwater/groundwater-in-australia.html`.

Giambastiani, B., N. Colombani, and M. Mastrocicco (2013). Limitation of using heat as a groundwater tracer to define aquifer properties: experiment in a large tank model. *Environmental Earth Sciences 70*, 719–728.

Gloaguen, E., M. Chouteau, D. Marcotte, and R. Chapuis (2001). Estimation of hydraulic conductivity of an unconfined aquifer using cokriging of GPR and hydrostratigraphic data. *Journal of Applied Geophysics 47*, 135–152.

Goovaerts, P. (1997). *Geostatistics for natural ressources evaluation*. Oxford University Press, New York.

Gouw, M. (2008). Alluvial architecture of the holocene Rhine-Meuse delta (the Netherlands). *Sedimentology 55*(5), 1487–1516.

Gouw, M. and G. Erkens (2007). Architecture of the holocene Rhine-Meuse delta (the Netherlands) - a result of changing external controls. *Netherlands Journal of Geosciences - Geologie en Mijnbouw 86*(1), 23–54.

Guardiano, F. and R. Srivastava (1993). Multivariate geostatistics: beyond bivariate moments. In *Geostatistics Troia '92*.

Günther, T. and C. Rücker (2006). A general approach for introducing information into inversion and examples from DC resistivity inversion. In *Near Surface 2006 - 12th european meeting of EAGE*, Helsinki.

Haddouchi, B. (1987). *Etude géologique et hydrogéologique de la plaine alluviale de la Meuse en Belgique*. Ph. D. thesis, University of Liege, Faculty of Applied Sciences.

Haehnlein, S., P. Bayer, and P. Blum (2010). International legal status of the use of shallow geothermal energy. *Renewable and Sustainable Energy Review 14*, 2611–2625.

Haffen, S., Y. Geraud, M. Diraison, and C. Dezayes (2013). Determination of fluid-flow zones in a geothermal sandstone reservoir using thermal conductivity and temperature logs. *Geothermics 46*, 32–41.

Hansen, T. M., A. G. Journel, A. Tarantola, and K. Mosegaard (2006). Linear inverse gaussian theory and geostatistics. *Geophysics 71*(6), R101–R111.

Harbaugh, A., E. Banta, M. Hill, and M. McDonald (2000). Modflow-2000, the u.s.s. geological survey modular ground-water model: user guide to modularization concepts and the ground-water process. US Geological Survey Open-File Rep., 00-92.

Hayashi, M. (2004). Temperature-electrical conductivity relation of water for environmental monitoring and geophysical data inversion. *Environmental Monitoring and Assessment 96*, 119–128.

Hayley, K., L. Bentley, M. Gharibi, and M. Nightingale (2007). Low temperature dependence of electrical resistivity: Implications for near surface geophysical monitoring. *Geophysical Research Letters 34*, L18402.

Hayley, K., L. Bentley, and A. Pidlisecky (2010). Compensating for temperature variations in time-lapse electrical resistivity difference imaging. *Geophysics 75*(4), WA51–WA59.

Henderson, R. D., F. D. Day-Lewis, E. Abarca, C. F. Harvey, H. N. Karam, L. Liu, and J. W. Lane (2010). Marine electrical resistivity imaging of submarine groundwater discharge: sensitivity analysis and application in Waquoit Bay, Massachusetts, USA. *Hydrogeology Journal 18*(1), 173–185.

Hermans, T. (2010). The use of *a priori* information in electrical resistivity tomography for salt water intrusion studies at the Belgian coast. Master's thesis, University of Liege, Faculty of Applied Sciences.

Hermans, T., A. Vandenbohede, L. Lebbe, R. Martin, A. Kemna, J. Beaujean, and F. Nguyen (2012a). Imaging artificial salt water infiltration using electrical resistivity tomography constrained by geostatistical data. *Journal of Hydrology 438-439*, 168–180.

Hermans, T., A. Vandenbohede, L. Lebbe, and F. Nguyen (2012b). A shallow geothermal experiment in a sandy aquifer monitored using electric resistivity tomography. *Geophysics 77*(1), B11–B21.

Hill, M. and C. Tiedeman (2007). *Effective groundwater model calibration. With analysis of data, sensitivities, predictions and uncertainty.* John Wiley and Sons, New Jersey.

Hoffman, B. and J. Caers (2005). Regional probability perturbations for history matching. *Journal of Petroleum Science and Engineering 46*, 53–71.

Hoffman, B., X. Wen, S. Strebelle, and J. Caers (2005). Geologically consistent history matching of a deepwater turbidite reservoir. In *SPE Annual Technical Conference and Exhibition*. Society of Petroleum Engineers.

Holliger, K., J. Tronicke, H. Paasche, and B. Dafflon (2008). Quantitative integration of hydrogeophysical and hydrological data: geostatistical approaches. In C. Darnault (Ed.), *Overexploitation and contamination of shared groundwater resources*, pp. 67–82. Springer Netherlands.

Horta, A., P. Correia, L. M. Pinheiro, and A. Soares (2013). Geostatistical data integration model for contamination assessment. *Mathematical Geosciences 45*(5), 575–590.

Hu, L. and T. Chugunova (2008). Multiple-point geostatistics for modeling subsurface heterogeneity: A comprehensive review. *Water Resources Research 44*, W11413.

Hu, W., A. Abubakar, and T. M. Habashy (2009). Joint electromagnetic and seismic inversion using structural constraints. *Geophysics 74*(6), R99–R109.

Huang, T., L. De-Tang, X. Li, and L. Wang (2013). GPU-based SNESIM implementation for multiple-point statistical simulation. *Computer and Geosciences 54*, 75–87.

Huysmans, M. and A. Dassargues (2009). Application of multiple-point geostatistics on modelling groundwater flow and transport in a cross-bedded aquifer (Belgium). *Hydrogeology Journal 17*(8), 1901–1911.

Huysmans, M. and A. Dassargues (2012). Modeling the effect of clay drapes on pumping test response in a cross-bedded aquifer using multiple-point geostatistics. *Journal of Hydrology 450-451*, 159–167.

Hyder, Z., J. Butler, C. McElwee, and W. Liu (1994). Slug tests in partially penetrating wells. *Water Resources Research 30*(11), 2945–2957.

Hyndman, D., J. Harris, and S. Gorelick (2000). Inferring the relation between seismic slowness and hydraulic conductivity in heterogeneous aquifers. *Water Resources Research 36*(8), 2121–2132.

Irving, J. and K. Singha (2010). Stochastic inversion of tracer test and electrical geophysical data to estimate hydraulic conductivities. *Water Resources Research 46*, W11514.

Issaks, E. and R. Srivastava (1989). *Applied geostatistics*. Oxford University Press, New Yprk.

Jardani, A., A. Revil, W. Barrash, A. Crespy, E. Rizzo, S. Straface, M. Cardiff, B. Malama, C. Miller, and T. Johnson (2009). Reconstruction of the water table from self-potential data: a bayesian approach. *Ground Water 47*, 213–227.

Jesussek, A., S. Grandel, and A. Dahmke (2013). Impacts of subsurface heat storage on aquifer hydrogeochemistry. *Environmental Earth Sciences 69*(6), 1999–2012.

Johnson, T., P. S. Routh, T. Clemo, W. Barrash, and W. P. Clement (2007). Incorporating geostatistical constraints in nonlinear inversion problems. *Water Resources Research 43*, W10422.

Journel, A. (1993). Geostatistics: Roadblocks and challenges. In *Geostatistics Troia '92*.

Journel, A. (2002). Combining knowledge from diverse sources: an alternative to traditional data independence hypothesis. *Mathematical Geology 34*(5), 573–596.

Journel, A. and C. Huijbregts (1978). *Mining Geostatistics*. Academic Press London, New York.

Kaipio, J. P., V. Kolehmainen, M. Vauhkonen, and E. Somersalo (1999). Inverse problems with structural prior information. *Inverse Problems 15*, 713–729.

Karaoulis, M., J. Kim, and P. Tsourlos (2011). 4D active time constrained resistivity inversion. *Journal of Applied Geophysics 73*, 25–34.

Kelkar, M., G. Perez, and A. Chopra (2002). *Applied geostatistics for reservoir characterization*. Society of Petroleum Engineers, Richardson.

Keller, G. and F. Frischknecht (1966). *Electrical methods in geophysical prospecting*. Oxford.

Kemna, A. (2000). *Tomographic inversion of complex resistivity - Theory and application*. Ph. D. thesis, Ruhr-University of Bochum.

Kemna, A., A. Binley, G. Cassiani, E. Niederleithinger, A. Revil, L. Slater, K. Williams, A. Flores-Orozco, F. Haegel, A. Hördt, S. Kruschwitz, V. Ledoux, K. Titov, and E. Zimmermann (2012). An overview of the spectral induced polarization method for near-surface applications. *Near Surface Geophysics 10*, 453–468.

Kemna, A., F. Nguyen, and S. Gossen (2007). On linear model uncertainty computation in electrical imaging. In *SIAM Conference on Mathematical and Computational Issues in the Geosciences, Santa Fe, March 19-22*, pp. 82.

Kemna, A., J. Vanderborght, B. Kulessa, and H. Vereecken (2002). Imaging and characterization of subsurface solute transport using electrical resistivity tomography (ERT) and equivalent transport models. *Journal of Hydrology 267*, 125–146.

Ketrane, R., B. Saidini, O. Gil, L. Leleyter, and F. Baraud (2009). Efficiency of five scale inhibitors on calcium carbonate precipitation from hard water: Effect of temperature and concentration. *Desalination 249*, 1397–1404.

Khodabakhshi, M. and B. Jafarpour (2013). A bayesian mixture-modeling approach for flow-conditioned multiple-point statistical facies simulation from uncertain training images. *Water Resources Research 49*(1), 328–342.

Koestel, J., A. Kemna, M. Javaux, A. Binley, and H. Vereecken (2008). Quantitative imaging of solute transport in an unsaturated and undisturbed soil monolith with 3-D ERT and TDR. *Water Resources research 44*, W12411.

Krautblatter, M., S. Verleysdonk, A. Flores-Orozco, and A. Kemna (2010). Temperature-calibrated imaging of seasonal changes in permafrost rock walls by quantitative electrical resistivity tomography (Zugspitze, German/Austrian alps). *Journal of Geophysical Research 115*, F02003.

Krishnan, S., A. Boucher, and A. Journel (2005). Evaluating information redundancy through the tau model. In *Geostatistics Banff 2004*.

LaBrecque, D., M. Miletto, W. Daily, A. Ramirez, and E. Owen (1996a). The effects of noise on Occam's inversion of resistivity tomography data. *Geophysics 61*(2), 538–548.

LaBrecque, D., A. Ramirez, W. Daily, A. Binley, and S. Schima (1996b). ERT monitoring of environmental remediation processes. *Measurement Science and Technology 7*, 375–383.

LaBrecque, D. and X. Yang (2001). Difference inversion of ERT data: a fast inversion method for 3-D in-situ monitoring. *Journal of Environmental and Engineering Geophysics 6*, 83–90.

Langevin, C., A. Dausman, and M. Sukop (2010). Solute and heat transport model of the Henry and Hilleke laboratory experiment. *Ground Water 48*(5), 757–770.

Langevin, C., D. Thorne, A. Dausman, M. Sukop, and W. Guo (2007). Seawat version 4: a computer program for simulation of multi-species solute and heat transport. US Geological Survey Technical Methods, Book 6, US Geological Survey, Reston, VA.

LaVenue, A., B. RamaRao, G. de Marsily, and M. Marietta (1995). Pilot point methodology for automated of an ensemble of conditionally simulated transmissivity fields 2. Application. *Water Resources Research 31*(3), 495–516.

Leaf, A., D. Hart, and J. Bahr (2012). Active thermal tracer tests for improved hydrostratigraphic characterization. *Ground Water 50*(5), 726–735.

Lebbe, L. (1978). *Hydrogeologie van het duingebied ten westen van De Panne*. Ph. D. thesis, University of Ghent.

Lebbe, L. (1999). Parameter identification in fresh-saltwater flow based on borehole resistivities and freshwater head data. *Advances in Water Resources 22*(8), 791–806.

Lebbe, L., M. Mahouden, and W. D. Breuck (1992). Execution of a triple pumping test and interpretation by an inverse numerical model. *Applied Hydrogeology 4*, 20–34.

Legaz, A., J. Vandenmeulebrouck, A. Revil, A. Kemna, A. Hurst, R. Reeves, and R. Papasin (2009). A case study of resistivity and self-potential signatures of hydrothermal instabilities, Inferno Crater Lake, Waimangu, New Zeland. *Geophysical Research Letters 36*, L12306.

Lelièvre, P., D. Oldenburg, and N. Williams (2009). Integrating geologic and geophysical data through advanced constrained inversions. In *ASEG Annual Meeting Extended Abstracts*.

Leopold, L. and M. Wolman (1957). River channel patterns: Braided, meandering and straight. *US Geological Survey Professional Paper 282-B*, 39–85.

Leroy, P., A. Revil, A. Kemna, P. Cosenza, and A. Ghorbani (2008). Complex conductivity of water-saturated packs of glass beads. *Journal of Colloid and Interface Science 321*, 103–117.

LGIH (1990). Modélisation mathématique des écoulements souterrains de la nappe alluviale de la Meuse entre Monsin et Lanaye ainsi que des interations entre le Canal Albert et la Meuse. Technical Report MTP 901, University of Liege.

Li, T. and J. Caers (2008). Solving spatial inverse problems using the probability perturbation method: An S-GEMS implementation. *Computers and Geosciences 34*, 1127–1141.

Liang, J., Q. Yang, L. Liu, and X. Li (2011). Modeling and performance evaluation of shallow ground water heat pumps in Beijing plain, China. *Energy and Buildings 43*, 3131–3138.

Linde, N., A. Binley, A. Tryggvason, L. Pedersen, and A. Revil (2006). Improved hydrogeophysical characterization using joint inversion of cross-hole electrical resistance and ground-penetrating radar traveltime data. *Water Resources Research 42*(12), W04410.

Liu, Y. (2006). Using the SNESIM program for multiple-point statistical simulation. *Computer and Geosciences 32*(10), 1544–1563.

Liu, Y., A. Harding, W. Abriel, and S. Strebelle (2004). Multiple-point simulation integrating wells, three-dimensional seismic data, and geology. *American Association of Petroleum Geologists Bulletin 88*(7), 905–921.

Lochbühler, T., G. Pirot, J. Straubhaar, and N. Linde (2013). Conditioning of multiple-point statistics faceis simulations to tomographic images. *Mathematical Geosciences In Press*.

Loke, M., I. Acworth, and T. Dahlin (2003). A comparison of smooth and blocky inversion methods in 2D electrical imaging surveys. *Exploration Geophysics 34*, 182–187.

LoRusso, S. and M. Civita (2009). Open-loop groundwater heat pumps development for large buildings: a case study. *Geothermics 38*, 335–345.

Lund, J. (2010). Direct utilization of geothermal energy. *Energies 3*, 1443–1471.

Lund, J., D. Freeston, and T. Boyd (2005). Direct application of geothermal energy: 2005 worldwide review. *Geothermics 34*, 691–727.

Ma, R., A. McBratney, B. Whelan, B. Minasny, and M. Short (2011). Comparing temperature correction models for soil electrical conductivity measurement. *Precision Agriculture 12*, 55–66.

Maharaja, A. and A. Journel (2005). Hierarchical simulation of multiple-facies reservoirs using multiple-point geostatistics. In *SPE Annual Technical Conference and Exhibition*. Society of Petroleum Engineers.

Mariethoz, G., P. Renard, and J. Straubhaar (2010). The direct sampling method to perform multiple-point geostatistical simulations. *Water Resources Research 46*(11), W11536.

Martens, S., T. Kempka, A. Liebscher, S. Lüth, F. Möller, A. Myrttinen, B. Norden, C. Schmidt-Hattenberger, M. Zimmer, and M. Kün (2012). The Ketzin group, 2012. Europe's longest-operating on-shore $C0_2$ storage site at Ketzin, Germany: a progress report after three years of injection. *Environmental Earth Sciences 67*, 323–334.

Mattsson, N., G. Steinmann, and L. Laloui (2008). Advanced compact device for the in situ determination of geothermal characteristics of soils. *Energy and Buildings 40*, 1344–1352.

Maurer, H., K. Holliger, and D. Boerner (1998). Stochastic regularization: smoothness or similarity? *Geophysical Research Letters 25*, 2889–2892.

McNeill, J. (1986). *Geonics EM39 borehole conductivity meter - Theory of operation*. Geonics Limited. Geonics Limited technical note TN-20.

Meerschman, E., G. Pirot, G. Mariethoz, J. Straubhaar, M. V. Meirvenne, and P. Renard (2013). A practical guide to performing multiple-point statistical simulations with the direct sampling algorithm. *Computer and Geosciences 52*, 307–324.

Menke, W. (1984). *Geophysical data analysis: Discrete inverse theory*. Elsevier, New-York.

Michael, H., H. Li, A. Boucher, T. Sun, J. Caers, and S. Gorelic (2010). Combining geologic-process models and geostatistics for conditional simulation of 3-D subsurface heterogeneity. *Water Resources Research 46*, W05527.

Miller, C., P. Routh, T. Brosten, and J. McNamara (2008). Application of time-lapse ERT imaging to watershed characterization. *Geophysics 73*(3), G7–G17.

Molson, J., E. Frind, and C. Palmer (1992). Thermal energy storage in an unconfined aquifer 2. Model development, validation and application. *Water Resources Research 28*, 2857–2867.

Monjoie, A. (1970). La plaine alluviale de la Meuse à Tihange. Technical report, Service géologique de Belgique.

Monjoie, A., A. Lox, and P. Anthonus (1987). Etude de la nappe alluviale de la Meuse au barrage de Lixhe à la frontière avec les Pays-Bas. Technical Report MTP 982, Rapport des laboratoires de géologie de l'ingénieur, d'hydrogéologie et de prospection géophysique de l'Université de Liège.

Nanson, G. and J. Croke (1992). A genetic classification of floodplains. *Geomorphology 4*, 459–486.

Nguyen, F., S. Garambois, D. Jongmans, E. Pirard, and M. Loke (2005). Image processing of 2D resistivity data for imaging fault. *Journal of Applied Geophysics 57*(4), 260–277.

Nguyen, F., A. Kemna, A. Antonsson, P. Engesgaard, O. Kuras, R. Ogilvy, J. Gisbert, S. Jorreto, and A. Pulido-Bosch (2009). Characterization of seawater intrusion using 2D electrical imaging. *Near Surface Geophysics 7*, 377–390.

Nguyen, F., A. Kemna, T. Robert, T. Hermans, M. Daoudi, and A. Flores-Orozco (2013). A new approach to data error quantification in time-lapse ert. *Near Surface Geophysics*, Accepted pending revision.

Nimmer, R., J. Osiensky, A. Binley, and B. Williams (2008). Three-dimensional effects causing artifacts in two-dimensional, cross-borehole, electrical imaging. *Journal of Hydrology 359*, 59–70.

Oh, S. (2013). Geostatistical integration of seismic velocity and resistivity data for probabilistic evaluation of rock quality. *Environmental Earth Sciences 69*(3), 939–945.

Oldenburg, D. W. and Y. Li (1994). Subspace linear inverse method. *Inverse Problems 10*, 915–935.

Oldenburg, W. and Y. Li (1999). Estimating depth of investigation in DC resistivity and IP surveys. *Geophysics 64*(2), 403–416.

Paasche, H. and J. Tronicke (2007). Cooperative inversion of 2D geophysical data sets : a zonal approach based on fuzzy c-means cluster analysis. *Geophysics 72*(3), A35–A39.

Paasche, H., J. Tronicke, K. Holliger, A. Gree, and H. Maurer (2006). Integration of diverse physical-property models: Subsurface zonation and petrophysical parameter estimation based on fuzzy c-means cluster analyses. *Geophysics 71*(3), H33–H44.

Paciorek, C. and M. Schervish (2006). Spatial modelling using a new class of nonstationary covariance functions. *Environmetrics 17*, 483–506.

Palmer, C., D. Blowes, E. Frind, and J. Molson (1992). Thermal energy storage in an unconfined aquifer 1. Field injection experiment. *Water Resources Research 28*, 2845–2866.

Parasnis, D. (1988). Reciprocity theorem in geoelctric and geoelectromagnetic work. *Geoexploration: International Journal of Mining and Technical Geophysics and Related Subjects 25*, 177–198.

Park, H., C. Scheidt, D. Fenwick, A. Boucher, and J. Caers (2013). History matching and uncertainty quantification of facies models with multiple geological interpretations. *Computer and Geosciences 17*, 609–621.

Pérez-Flores, M. and E. Gomez-Trevino (1997). Dipole-dipole resistivity imaging of the Ahuachapan-Chipilapa geothermal field, El Salvador. *Geothermics 26*, 657–680.

Perri, M., G. C. I. Gervasio, R. Deiana, and A. Binley (2012). A saline tracer test monitored via both surface and cross-borehole electrical resistivity tomography: Comparison of time-lapse results. *Journal of Applied Geophysics 79*, 6–16.

Pidlisecky, A., E. Haber, and R. Knight (2007). RESINVM3D: A 3D resistivity inversion package. *Geophysics 72*(2), H1–H10.

Pilkington, M. and J. Todeschuk (1991). Naturally smooth inversion with a priori information from well logs. *Geophysics 56*, 1811–1818.

Press, W., S. Teukolsky, W. Vetterling, and B. Flannery (1992). *Numerical recipes in C*. Cambridge University Press, Cambridge.

Prevedel, B., L. Wohlgemuth, B. Legarth, J. Henninges, H. Schütt, C. Hattenberger, B. Norden, A. Förster, and S. Hurter (2009). The CO_2 SINK boreholes for geological CO_2-storage testing. *Energy Procedia 1*, 2087–2094.

Ptak, T., M. Piepenbrink, and E. Martac (2004). Tracer tests for the investigation of heterogeneous porous media and stochastic modelling of flow and transport - a review of some recent developments. *Journal of Hydrology 294*, 122–163.

Rahman, A., F.-C. Tsai, C. White, D. Carlson, and C. Wilson (2008). Geophysical data integration, stochastic simulation and significance analysis of groundwater responses using ANOVA in the Chicot Aquifer system, Louisiana, USA. *Hydrogeology Journal 16*(4), 749–764.

Ramirez, A., W. Daily, D. LaBrecque, E. Owen, and D. Chesnut (1993). Monitoring an underground steam injection process using electrical resistance tomography. *Water Resources Research 29*, 73–87.

Raymond, J., R. Therrien, L. Gosselin, and R. Lefebvre (2011). A review of thermal response test analysis using pumping test concepts. *Ground Water 49*, 932–945.

Remy, N., A. Boucher, and J. Wu (2009). *Applied geostatistics with SGEMS: a user's guide*. Cambridge University Press.

Renard, P., J. Straubhaar, J. Caers, and G. Mariethoz (2011). Conditioning facies simulations with connectivity data. *Mathematical Geosciences 43*(8), 879–903.

Rentier, C. (2003). *Méthode stochastique de délimitation des zones de protection autour des captages d'eau - Conditionnement par des mesures de conductivité hydraulique K, de hauteur piézométrique h et de résistivité ρ.* Ph. D. thesis, University of Liege, Faculty of Applied Sciences.

Revil, A., L. Cathles, S. Losh, and J. Nunn (1998). Electrical conductivity in shaly sands with geophysical applications. *Journal of Geophysical Research 103*, 23925–23936.

Revil, A., A. Finizola, T. Ricci, E. Delcher, A. Peltier, S. Barde-Cabusson, G. Avard, T. Bailly, L. Bennati, S. Byrdina, J. Colonge, F. D. Ganga, G. Douillet, M. Lupi, J. Letort, and E. T. H.

Sun (2011). Hydrogeology of Stromboli volcano, Aeolian islands (Italy), from the interpretation of resistivity tomograms, self-potential, soil temperature and soil CO_2 concentration measurements. *Geophysical Journal International 186*, 1078–1094.

Revil, A., T. Johnson, and A. Finizola (2010). Three-dimensional resistivity tomography of vulcan's forge, Vulcano island, southern Italy. *Geophysical Research Letters 37*, L15308.

Revil, A. and N. Linde (2006). Chemico-electrochemical coupling in microporous media. *Journal of colloid and interface sciences 302*, 682–694.

Revil, A., H. Schwaeger, L. Cathles, and P. Manhardt (1999). Streaming potential in porous media 2. Theory and application to geothermal systems. *Journal of Geophysical Research 104*, 20033–20048.

Robert, C. and G. Casella (2004). *Monte Carlo Statistical methods* (Second edition ed.). Springer.

Robert, T., D. Caterina, J. Deceuster, O. Kaufmann, and F. Nguyen (2012). A salt tracer test monitored with surface ERT to detect preferential flow and transport paths in fractured/karstified limestones. *Geophysics 77*(2), 42–53.

Robert, T., A. Dassargue, S. Brouyère, O. Kaufmann, V. Hallet, and F. Nguyen (2011). Assessing the contribution of electrical resistivity tomography (ERT) and self-potential (SP) methods for a water well drilling program in fractured/karstified limestones. *Journal of Applied Geophysics 75*, 42–53.

Ronayne, M., S. Gorelick, and J. Caers (2008). Identifying discrete geologic structures that produce anomalous hydraulic response: An inverse modeling approach. *Water Resources Rresearch 44*, W08426.

Rubin, Y. and S. Hubbard (2005). Stochastic forward and inverse modelling. In Y. Rubin and S. Hubbard (Eds.), *Hydrogeophysics*, pp. 487–511. Springer, Dordrecht, the Netherlands.

Saar, M. (2011). Review: Geothermal heat as a tracer of large-scale groundwater flow and as a mean to determine permeability fields. *Hydrogeology Journal 19*, 31–52.

Sasaki, Y. (1994). 3D inversion using the finite-element method. *Geophysics 59*, 1839–1848.

Saunders, J., J. Herwanger, C. Pain, M. Worthington, and C. de Oliveira (2005). Constrained resistivity inversion using seismic data. *Geophysical Journal International 160*, 785–796.

Sherrod, L., W. Sauck, and D. Werkema (2012). A low-cost, in-situ resistivity and temperature monitoring system. *Ground Water Monitoring and Remediation 32*, 31–39.

Singha, K. and S. Gorelick (2006). Effects of spatially variable resolution on field-scale estimates of tracer concentration from electrical inversions using Archie's law. *Geophysics 71*(3), G83–G91.

Singha, K., L. Li, F. Day-Lewis, and A. Regberg (2011). Quantifying solute transport processes: Are chemically "conservative" tracers electrically conservative? *Geophysics 76*, F53–F63.

Slater, L., A. Binley, W. Daily, and R. Johnson (2000). Cross-hole electrical imaging of a controlled saline tracer injection. *Journal of Applied Geophysics 44*, 85–102.

Smith, D. (1983). Anastomosed fluvial deposits: Modern examples from western canada. In J. Collinson and J. Lewin (Eds.), *Modern and Ancient Fluvial Systems*, pp. 155–168. Oxford, Blackwell.

Smith, T., M. Hoversten, E. Gasperikova, and F. Morrison (1999). Sharp boundary inversion of 2D magnetotelluric data. *Geophysical Prospecting 47*(4), 469–486.

SPW-DGO3 (2013). Etat des nappes d'eau souterraine de wallonie. Service Public de Wallonie, DGO 3 (DGARNE), Belgique. `http://environnement.wallonie.be/de/eso/atlas/versions.htm`.

Straubhaar, J., P. Renard, G. Mariethoz, R. Froidevaux, and O. Besson (2011). An improved parallel multiple-point algorithm using a list approach. *Mathematical Geosciences 43*(3), 305–328.

Straubhaar, J., A. Walgenwitz, and P. Renard (2013). Parallel multiple-point statistics algorithm based on list and tree structures. *Mathematical Geosciences 45*(2), 131–147.

Strebelle, S. (2000). *Sequential simulation drawing structures from training images*. Ph. D. thesis, Stanford University.

Strebelle, S. (2002). Conditional simulation of complex geological structures using multiple-point statistics. *Mathematical Geology 34*(1), 1–21.

Strebelle, S., K. Payrazyan, and J. Caers (2003). Modeling of a deep water turbidite reservoir conditional to seismic data using principal component analysis and multiple-point geostatistics. *SPE Journal 8*(3), 227–235.

Strebelle, S. and N. Remy (2005). Post-processing of multiple-point geostatistical models to improve reproductions of training patterns. In *Geostatistics Banff 2004*.

Strebelle, S. and T. Zhang (2005). Non-stationary multiple-point geostatistics models. In *Geostatistics Banff 2004*.

Suzuki, S. (1960). Percolation measurements based on heat flow through soil with special reference to paddy fields. *Journal of Geophysical Research 65*(9), 2883–2885.

Tarantola, A. (1987). *Inverse problem theory*. Elsevier, Amsterdam.

Tarantola, A. and B. Valette (1982). Generalized non-linear problems solved using the least-squares criterion. *Review of Geophysics and Space Physics 20*, 219–232.

Telford, W., L. Geldart, and R. Sheriff (1990). *Applied Geophysics*. Cambridge University Press, Cambridge.

Therrien, R., R. McLaren, E. Sudicky, and S. Panday (2010). *HydroGeoSphere: A three-dimensional numerical model describing fully-integrated subsurface and surface flow and solute transport*. Groundwater Simulations Group.

Tikhonov, A. and V. Arsenin (1977). *Solution of ill-posed problems*. Winston and Sons, Washington.

Trainor, W. (2010). *On the value of information for spatial problems in the earth sciences*. Ph. D. thesis, Stanford University, California.

Tran, T. (1994). Improving variogram reproduction on dense simulation grids. *Computer and Geosciences 20*(7-8), 1161–1168.

Tronicke, J. and K. Holliger (2005). Quantitative integration of hydrogeophysical data: conditional geostatistical simulation for characterizing heterogeneous alluvial aquifers. *Geophysics 70*(3), H1–H10.

van den Berg, J. (1995). Prediction of alluvial channel pattern of perennial rivers. *Geomorphology 12*(4), 259–279.

Vandenbohede, A., T. Hermans, F. Nguyen, and L. Lebbe (2011). Shallow heat injection and storage experiment: heat transport simulation and sensitivity analysis. *Journal of Hydrology 409*, 262–272.

Vandenbohede, A. and L. Lebbe (2002). 3D density dependent numerical model of a tracer test performed in the Belgian coastal plain. *Aardkundige Mededelingen 12*, 223–226.

Vandenbohede, A. and L. Lebbe (2003). Combined interpretation of pumping and tracer tests: theoritical considerations and illustration with a field test. *Journal of Hydrology 277*, 134–149.

Vandenbohede, A. and L. Lebbe (2006). Double forced gradient tracer test: performance and interpretation of a field test using a new solute transport model. *Journal of Hydrology 317*, 155–170.

Vandenbohede, A., L. Lebbe, S. Gysens, K. Delecluyse, and P. DeWolf (2008). Salt water infiltration in two artificial sea inlets in the Belgian dune area. *Journal of Hydrology 360*, 77–86.

Vandenbohede, A., A. Louwyck, and L. Lebbe (2009). Conservative solute versus heat transport in porous media during push-pull tests. *Transport in Porous Media 76*, 265–287.

Vandenborght, J., A. Kemna, H. Hardelauf, and H. Vereecken (2005). Potential of electrical resistivity tomography to infer aquifer transport characteristics from tracer studies: A synthetic case study. *Water Resources Research 41*, W06013.

Vanhoudt, D., J. Desmedt, J. V. Bael, N. Robeyn, and H. Hies (2011). An aquifer thermal storage system in a Belgian hospital: Long-term experimental evaluation of energy and cost savings. *Energy and Buildings 43*, 3657–3665.

Vereecken, H., A. Binley, G. Cassiani, A. Revil, and K. Titov (2006). *Applied Hydrogeophysics*. Number IV Earth and Environmental Sciences in Nato Science Series. Springer.

Vesnaver, A., R. Bridle, B. Henry, R. Ley, R. Rowe, and A. Wyllie (2006). Geostatistical integration of near-surface geophysical data. *Geophysical Prospecting 54*(6), 763–777.

Warner, D. and U. Algan (1984). Thermal impact of residential ground-water heat pumps. *Ground Water 22*, 6–12.

Waxman, M. and L. Smits (1968). Electrical conductivities in oil-bearing shaly sands. *Society of Petroleum Engineers Journal 8*, 107–122.

Wijns, C., F. Boschetti, and L. Moresi (2003). Inverse modelling in geology by interactive evolutionary computation. *Journal of Structural Geology 25*(10), 1615–1621.

Wu, J., A. Boucher, and T. Zhang (2008). A SGEMS code for pattern simulation of continuous and categorical variables: Filtersim. *Computers and Geosciences 34*(12), 1863–1876.

Yang, X. and D. LaBrecque (1998). Stochastic inversion of 3D ERT data. In EEGS (Ed.), *Symposium on the application of geophysics to engineering and environmental problems*, Volume 11, pp. 221–228. EEGS.

Yeh, T.-C. J. and S. Liu (2000). Hydraulic tomography: Development of a new aquifer test method. *Water Resources Research 36*(8), 2095–2105.

Yeh, T.-C. J., S. Liu, R. Glass, K. Baker, J. Brainard, D. Alumbaugh, and D. LaBrecque (2002). A geostatistically based inverse model for electrical resistivity surveys and its applications to vadose zone hydrology. *Water Resources Research 38*(12), 1278.

Yeh, T.-C. J., J. Zhu, A. Englert, A. Guzman, and S. Flaherty (2006). A successive linear estimator for electrical resistivity tomography. In H. Vereecken, A. Binley, G. Cassiani, A. Revil, and K. Titov (Eds.), *Applied hydrogeophysics*, Volume 71 of *NATO science series - IV Earth and Environmental sciences*, pp. 45–74. Springer.

Zhang, T., P. Switzer, and A. Journel (2006). Filter-based classification of training image patterns for spatial simulation. *Mathematical Geology 38*, 63–80.

Zheng, C. and P. Wang (1999). Mt3dms, a modular three-dimensional multispecies model for simulation of advection, dispersion and xhemical reactions of contaminants in groundwater systems: documentation and user's guide. US Army research and development center contract report, SERDP-99-1. Vicksburg, MI.

Zhou, B. and S. Greenhalgh (2000). Cross-hole resistivity tomography using different electrode configurations. *Geophysical Prospecting 48*, 887–912.